Synthèse en flux continu de nanocristaux de semi-conducteurs

Ranjana Yadav

THÈSE

Pour obtenir le grade de

DOCTEUR DE L'UNIVERSITÉ GRENOBLE ALPES

École doctorale : CSV- Chimie et Sciences du Vivant
Spécialité : Chimie inorganique et Bio inorganique
Unité de recherche : Systèmes Moléculaires et Nano Matériaux pour l'Énergie et la Santé

Synthèse En Flux Continu De Nanocristaux De Semi-conducteurs

Continuous Flow Synthesis of Semiconductor Nanocrystals

Présentée par :

Ranjana YADAV

Direction de thèse :

Peter REISS DIRECTEUR DE RECHERCHE, CEA Grenoble	Directeur de thèse

Rapporteurs :

Sandrine ITHURRIA
MAITRE DE CONFERENCES, École Supérieure de Physique et de Chimie Industrielles Paris
François RIBOT
DIRECTEUR DE RECHERCHE, CNRS, Sorbonne Université Paris

Thèse soutenue publiquement le **23 février 2023**, devant le jury composé de :

Peter REISS DIRECTEUR DE RECHERCHE, CEA Grenoble	Directeur de thèse
Sandrine ITHURRIA MAITRE DE CONFERENCES, École Supérieure de Physique et de Chimie Industrielles Paris	Rapporteure
François RIBOT DIRECTEUR DE RECHERCHE, CNRS, Sorbonne Université Paris	Rapporteur
Fabien DELPECH PROFESSEUR DES UNIVERSITES, Université de Toulouse	Examinateur
Kuntheak KHENG PROFESSEUR DES UNIVERSITES, Université Grenoble Alpes	Présidente

I would like to dedicate this thesis

to my Nani

Acknowledgement

First and foremost, I would like to express my gratitude to the members of my PhD thesis jury, Prof. Sandrine Ithuria, Prof. François Ribot, Prof. Fabien Delpech, and Prof. Kuntheak Kheng, for their valuable time, expertise, and constructive feedback on my thesis. Their critical evaluation, insightful comments, and suggestions have helped me improve my work and make it more comprehensive. Thank you for your dedication and commitment to ensuring the quality of my research.

I express my sincere gratitude to my thesis supervisor, Dr. Peter Reiss, for giving me the opportunity to pursue my Ph.D. thesis in his group. I am grateful to him for his trust in me and for allowing me to explore the world of nanomaterials. Without his support and guidance, I would not have been able to undertake this endeavor, and his suggestions and meticulous corrections were invaluable in giving the final shape to this manuscript.

I would like to thank Céline Rivaux for helping with the continuous flow platform and ICP-AES measurements. I would like to thank Dr. Dmitry Aldakov for his support and the scientific discussion during group meetings and CSI. I am grateful to Dr. Pascal Chenevier for motivating me and helping me with corrections during my thesis writing. I would like to thank Dr. Winnie for helping with TEM measurements. I would like to thank Pierre-Alain Bayle for help with NMR spectroscopy and Dr. Stéphanie Pouget for assistance with powder X-ray diffraction. Big thanks to Rachel Mauduit for helping me with administrative processes.

Many thanks to my officemate Mr. Tuan (soon to be Dr. Tuan) for the long philosophical discussion about life, science, history, and so on. I can’t thank him enough for helping me during my thesis. I would like to thank my present and former labmates Yuze, Antik, Omar, Yongju, Avijit, Pierre, Anu, and Zafer for the motivation and scientific discussion. I enjoyed our long coffee break talking about the most absurd things possible. It was indeed a pleasure working alongside you all. I am grateful to all the present and former STEP team members with whom I had the opportunity to meet, especially Marc, Claire, Guilhem, Guillaume, and Caroline, for making my last three years enjoyable and exciting.

I would like to thank Dr. Valid and Louis for all the entertainment, food, and scary trips to abandoned places. My heartfelt thanks to Shifali, Vaibhav, Harinder and Ronit for their support throughout my stay in Grenoble, especially during COVID-19. I cannot imagine my life without them in Grenoble.

I will always be indebted to my IISER friends Komal, Supriya, and Sukanya for keeping in touch and motivating me.

I owe my deepest gratitude to all my teachers for showing me the path, motivating me, and forming me who I am now.

Last but not least, I would like to thank my family, especially my wonderful parents and my boyfriend Amit for their unconditional love and emotional support. Their belief in me has kept my spirits and motivation during these years. I thank all the people who have contributed from near and far to the completion of this thesis.

Table of contents

Chapter I

Introduction

1.1. Nanotechnology: "There's plenty of room at the bottom"

1.1.1. Definition

The term *nano* originates from the Greek word *nanos* meaning dwarf. In modern scientific or non-scientific literature, this term is often associated with two events. The first instance was in 1959 when Nobel prize laureate physicist Richard Feynman introduced the idea of nanotechnology during his famous lecture titled "there's plenty of room at the bottom".[1] Later, in 1974, Norio Taniguchi first defined the term nanotechnology as "mainly consists of the processing of separation, consolidation, and deformation of the materials by one atom or one molecule".[2]

Nanomaterials have emerged as building blocks in nanotechnology. Objects that have at least one dimension nanometre-sized (10-9 m) belong to this class of material. Their nanoscale structural organization provides them with unique properties different from their bulk counterparts. According to Pokropivny and Skorokhod, nanomaterials can be classified depending on the movement of the electron along the dimensions such as 0D, 1D, 2D and 3D nanomaterials.[3] In recent decades, semiconductor and metal nanoparticles (NPs) have been the most developed, optimized, and commercialized materials for different applications.[4-5]

1.1.2. History

The use of nanomaterials can be traced back to far earlier in human history. We can find various shreds of evidence where nanocrystals were empirically used in manufacturing glasses, ceramics, and medical applications. Throughout the centuries, colored glasses were manufactured by adding metal nanoparticles (Cu, Co, specifically Au). The synthesis of metallic nanoparticles can be dated back to the 13th century BC when Egyptians and Mesopotamians started manufacturing metal-containing glasses.[6] The red glass found in Frattesina di Rovigo, Italy dates back to 1200-1000 BC. These glasses were colored by adding Cu nanoparticles, from which the red color originates. The 4th-century Roman glass cage known as the Lycurgus cup (conserved in the British Museum) represents a masterpiece of glass during that era.[7] In addition to being an important symbol in Greek mythology, it has a very interesting behavior. The Lycurgus cup appears red under transmitted light but green under reflected light (Figure 1.1a). Recent studies show that dichroic behavior arises due to the addition of silver and gold nanoparticles throughout the material. Red and green colors arise from the absorption and scattering of light by gold-silver nanoparticles present in the glass. During the 17th and 18th centuries,

the production of gold ruby glass expanded in Europe mainly due to the significant attention it received among rich families. Meanwhile, in France, the Manufacture royale de Sèvres developed a solution-based technique for manufacturing gold ruby enamels on ceramics, popularly known as the Rose Pompadour series (Figure 1.1b).[8] Similar to glasses, ceramics were also prepared by creating layers of metallic nanocrystals with different shapes and sizes. One of the earliest examples of luster ceramic dates back to the 10th century AD.[9] A recent finding shows that luster ceramic was produced by creating different layers of Ag and Cu nanocrystals. Transmission electron microscopy (TEM) analysis of these ceramics shows a double-layered structure, Ag NPs with 5-10 nm in the outer layers and the larger NPs (10-20 nm) in the inner layer with an interlayer distance of around 430 nm. The most remarkable aspect of multilayered structures relies on angle-dependent coloration. The scattered light from the outer layer goes through a phase shift due to the scattering of the light by the inner layer, creating an angle-dependent scattering (Figure 1.1c). Using a similar technique, Satsuma glasses were manufactured in Japan in the early 19th century where Cu NPs were used to brighten/imbue the glass with the ruby color.

Figure 1.1: (a) Image of the Lycurgus cup in transmitted light (red) and reflected light (green).[7] (b) A vase from 'Famille rose' (conserved in the Guimet Museum, Paris).[8] (c) Luster ceramic from fustat.[9]

Several examples can be found where nanoparticles were used for beauty and medical purposes in ancient times. For example, a lead nanoparticle-based chemical was used for hair coloration in ancient Egypt. Researchers found that the PbS nanoparticles of size around 5 nm can be used for dying hair black while retaining its mechanical properties.[10] It is probably one of the earliest examples of

semiconductor nanoparticles. In ancient India, an eye cosmetic 'Kajal' made of carbon nanoparticles (~100 nm) was used for antifungal properties.[11]

1.2. Quantum Dots: small wonders

When a semiconductor absorbs a photon, it creates a quasiparticle known as an 'exciton' which is a bound state between the electron promoted to the conduction band and the hole in the valence band. The distance between the electron and the hole pair is known as the excitonic Bohr radius, a characteristic of the bulk semiconductor. As the size of the material becomes smaller than the excitonic Bohr radius, the charge carriers start to be confined in one or more dimensions. This effect is called the quantum confinement effect and the nanoparticles exhibiting such an effect are known as quantum dots. Due to quantum confinement, an increase in the band gap with a decrease in the QDs size is observed. Hence, it is entirely possible to modify the band gap simply by changing the size of the particles.

1.2.1. Quantum confinement effect

The 'quantum confinement' term deals with the energy of confined electrons or excitons. To recall the formation of energy bands, nearly continuous bands are formed due to an increase in the energy states when atoms are brought together in the bulk material. The electron-hole pair is bound with an excitonic Bohr radius(r_B) (Equation 1.1).[12]

$$r_B = \frac{h\varepsilon}{4\pi e^2}\left(\frac{1}{m_e^*} + \frac{1}{m_h^*}\right) \qquad \textit{Eq.1.1}$$

where ε is the static dielectric constant of the given material, e is the unit charge of the electron, h is the Planck constant, and m_e^* and m_h^* are the effective masses of electron and hole, respectively.

As the size of the semiconductor particle approaches the point where it becomes comparable to or smaller than the excitonic Bohr radius, spatial confinement of excitons occurs. Consequently, a transition from continuous to discrete energy levels becomes apparent (Figure 1.2). This phenomenon is known as the quantum confinement effect. One of the most important consequences of quantum confinement is that the semiconductors exhibit size-dependent electronic and optical properties.

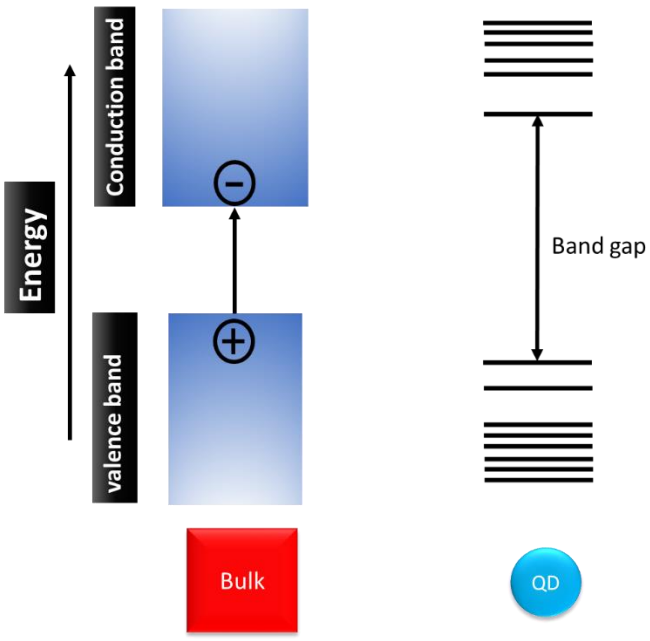

Figure 1.2: Scheme of the electronic states in the bulk semiconductor material and a quantum dot.

According to the effective mass approximation model, in the strong confinement regime where the particle size is much smaller than the Bohr radius, electrons and holes are considered independent particles, and the band gap energy is given by the following equation (1.2).[12] Whereas when the particle size is in the order of the Bohr excitonic radius or slightly smaller, a weak confinement effect can be observed and the energy is given by the following equation (1.3).[13-14]

$$E_g = E_g^{bulk} + \frac{h^2}{8}\left(\frac{1}{m_e^*} + \frac{1}{m_h^*}\right)\frac{\pi^2}{R^2} - 1.786\frac{e^2}{\varepsilon R} \qquad \textit{Eq. 1.2}$$

$$E_g = E_g^{bulk} + \frac{2.6}{\varepsilon * R}\left(2.74\frac{r_B}{R} - 1\right) \qquad \textit{Eq. 1.3}$$

Here E_g^{bulk} is the bulk band gap and R is the radius of the semiconductor QDs. The second term in equations 1.2 and 1.3 shows a $1/R^2$ dependence on the band gap. The third term stands for the Coulombic interaction energy of excitions having $1/R$ dependence. Consequently, the band gap energy of the quantum-confined particles will always increase with a decrease in size.

Table 1.1: Different classes of semiconductor materials and their bulk band gaps obtained from the literature. The band gaps are direct unless indicated otherwise.

Group	Semiconductor materials	Bulk band gap (eV)
IV	Ge	0.66 (indirect)
	Si	1.12 (indirect)
	SiC	2.39(indirect)
II-VI	HgTe	-0.13
	HgSe	-0.06
	HgS	0.54
	CdTe	1.51
	CdSe	1.66
	CdS	2.38
	ZnTe	2.28
	ZnSe	2.70
	ZnO	3.37
	ZnS	3.77
	MnSe	3.40
	MnS	3.80
	MgTe	3.50
	MgSe	3.59
	MgS	4.45
IV-VI	PbSe	0.27
	PbS	0.37
III-V	InSb	0.17
	InAs	0.35
	InP	1.35
	InN	0.76
	GaSb	0.73
	GaAs	1.42
	GaP	2.27(indirect)
	GaN	3.24
	AlSb	1.62 (indirect)
	AlAs	2.16 (indirect)
	AlP	2.49 (indirect)
	AlN	6.16
I-III-V_2	$CuInS_2$	1.2
	$AgInS_2$	1.87
	$CuFeS_2$	0.6
Perovskite	$CsPbCl_3$	3.06
	$CsPbBr_3$	2.25
	$CsPbI_3$	1.70

1.2.2. Optical properties

1.2.2.1. Absorption

Due to the quantum confinement, the energy level of QDs becomes discrete near the band edges like in the case of atoms. Therefore, when a QD absorbs a photon with higher energy than its band gap, a distinct characteristic peak is observed in the absorption spectra. This characteristic peak is generally known as the first excitonic peak (Figure 1.3). The first excitonic peak position depends on the band gap of the material and also on the size and shape of the QDs. The full width at half maximum (FWHM) of this peak is influenced by the size distribution of the QDs. If a sample has a high polydispersity then a broad excitonic peak (shoulder) is observed on the absorbance spectrum. In the absorption onset, a shift to lower energy (red-shift) in the first excitonic is observed with an increase in the QDs size due to the confinement effect. The absorbance of the quantum dots is higher in the blue region offering a wide range of excitation possibilities that provide an advantage over traditional organic dyes.

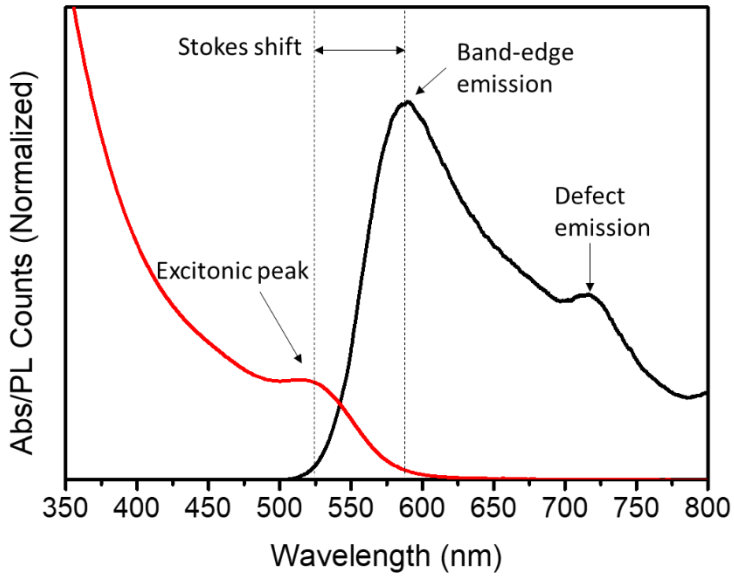

Figure 1.3: Absorption and photoluminescence spectra of InP QDs.

1.2.2.2. Photoluminescence

As discussed above, when a QD is excited, it creates excitons and the system can relax to the ground state by radiative or nonradiative recombinations. The radiative recombination process results in luminescence which may arise from band-edge or defect-related states (Figure 1.3). The radiative recombination between the conduction band and the valance band is known as band-edge emission. Generally, however, a Stokes shift is classically observed, which can have different reasons depending on the material. If the absorbed energy during the excitation is greater than the band gap, then relaxation via phonons (dissipation of heat) of the excited electron takes place to the lowest excited state, from which deexcitation via photon emission (luminescence) can occur. As the band gap is size dependent, the line width of the band-edge emission strongly depends on the size distribution of the QDs. The

emission efficiency is called photoluminescence quantum yield (PLQY) which is calculated from the ratio of absorbed and emitted number of photons. Due to the large surface-to-volume ratio, surface passivation plays an important role to achieve a high PLQY. The emission intensity of pristine QDs is often very low due to surface defects that give rise to nonradiative recombination. Many methods have been explored to achieve surface passivation including the use of appropriate organic ligands or the growth of an epitaxial shell of a higher bandgap semiconductor material. Shell growth is the most common and successful method for improving the PLQY, photostability and for protecting the core from oxidation.[15-17]

1.2.3. Colloidal synthesis of quantum dots

The early 1980s witnessed the birth of quantum dots in the semiconductor research field. The first quantum confinement effect was observed in CdS additives in the glass.[18] In 1993, this field was stormed after a report on the colloidal synthesis of highly crystalline and monodisperse CdS, CdSe, and CdTe nanoparticles by Bawendi et al.[19] In the years after this publication, the colloidal synthesis saw a rapid acceleration, and the research was extended to other semiconductor nanocrystals and metal nanoparticles.

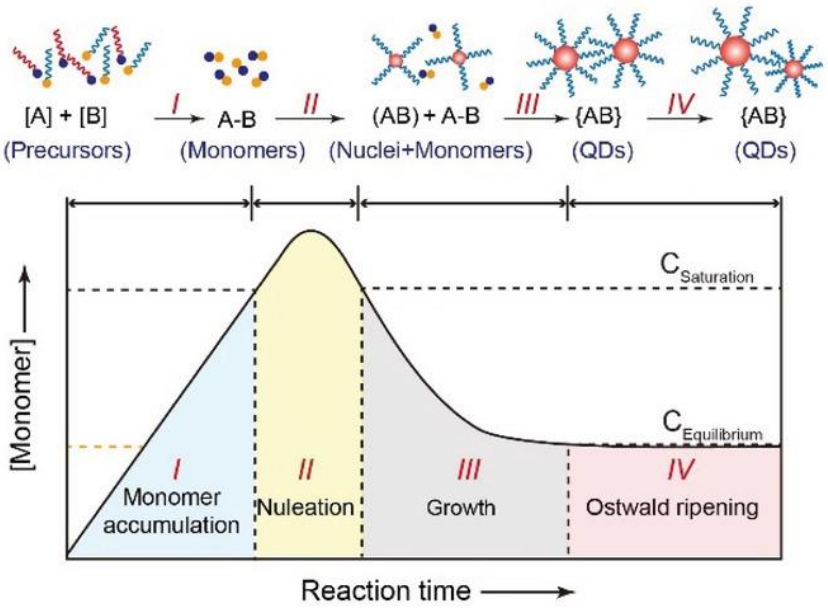

Figure 1.4: The LaMer plot depicts the separation of nucleation and growth for the colloidal synthesis of nanocrystals. This plot shows the degree of monomer saturation against the reaction time.[4]

In 1950, Victor LaMer proposed a model explaining the formation of uniform-sized hydrosols. According to the LaMer model, the synthesis of uniform colloids requires a temporal separation of nucleation and the growth of the nuclei.[20] The LaMer plot (Figure 1.4) consists of four stages; (I) Monomers, either existing in the reaction medium or constantly being deployed from the exterior, accumulate in the reaction medium. (II) When the monomer concentration overcomes the

supersaturation limit, stable nuclei are formed. Subsequently, due to the fast consumption of monomers, the monomer concentration decreases below the supersaturation limit, which terminates the nucleation process. (III) The remaining monomers then start to deposit on the existing nuclei, corresponding to the growth of the nanocrystals. (IV) Afterward, when the concentration of the monomers enters the equilibrium regime, smaller particles dissolve and redeposit on the surface of the larger particles (Ostwald ripening). Generally, Ostwald ripening leads to a minimum size distribution of 15-20%, and hence the QDs synthesis should be stopped before the ripening. The quenching can be achieved by chilling the reaction very fast.

Colloidal QDs can be synthesized using a variety of precursors in both aqueous and organic solvents. For organic-based synthesis, high boiling point organic solvents are mainly utilized since they provide flexibility in working with different reaction temperatures. Non-coordinating solvents such as octadecene can provide control over the diffusion rate of reactants whereas coordinating solvents such as oleylamine and trioctylphosphine oxide bind with the surface of the QDs, acting as surfactants. In the synthesis of QDs, surfactants called ligands play an important role in controlling the reaction kinetics, shape, size, and colloidal stability.

1.2.4. Core-shell quantum dot heterostructures

Generally, for colloidal stability and size control, one or more types of ligands are used for stabilizing the QDs. These surfactants may not completely passivate the surface trap states arising from the incomplete coordination sphere of surface atoms that favor the non-radiative recombination of excitons, which significantly reduces the PLQY. Therefore, the original strategy to improve the PL efficiency is overcoating the QDs with another semiconductor material. These types of QDs are commonly referred to as core-shell QDs (CSQDs). Moreover, depending on the core size, shape, and composition, the valence and conduction band positions can be altered upon shell growth, which offers another method to tune their optical properties. Depending on the relative band positions of core and shell materials, CSQDs are mainly categorized into type-1, inverse type-1, type-2, inverse type-2, and quasi type-2 as shown in Figure 1.5.

For type-1 CSQDs, the shell material's band gap is larger than that of the core QDs. In this configuration, both electrons and holes are confined within the core. In this case, the formation of an inorganic shell passivates the surface traps of the core QDs, enhancing their photoluminescence and photostability. Although in this case, while the confinement of electrons and holes is unaffected by the shell growth, the leakage of wave functions into the shell can occur due to finite energy offset between the core and the shell. As a result, slightly redshifted absorption and emission spectra are observed with shell growth. ZnS-capped CdSe QDs are one of the earliest examples of type 1 CSQDs that have been developed.[21] Some other popular examples of type-1 CSQDs are CdSe/CdS QDs,[22] InP/ZnS QDs,[23] InAs/ZnSe, and PbSe/PbS QDs.[24]

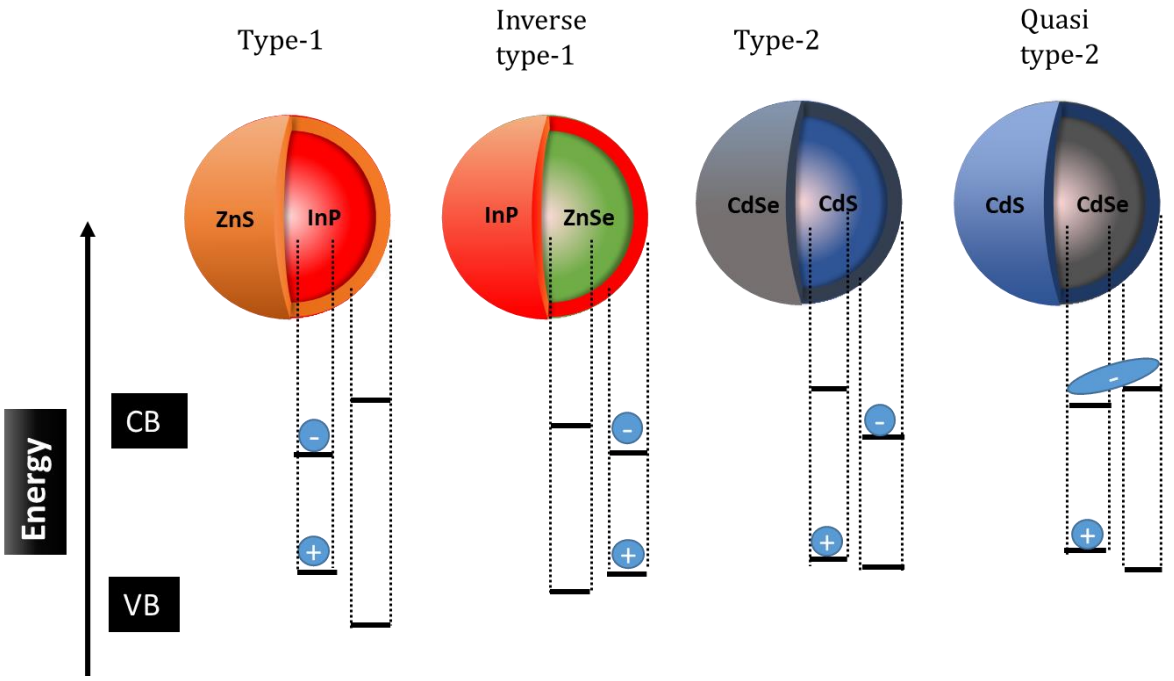

Figure 1.5: Schematic of core-shell types quantum dots, their band alignment, and spatial localization of the carriers.

In the case of reverse type-1 CSQDs, the band gap of the shell material lies completely within that of the core QDs and the carriers are thus localized in the shell. A significant red shift of the emission could be achieved in inverse type-1 ZnSe/InP CSQDs by controlling the shell thickness.[25-26] In type-2 CSQDs control of the emission wavelength can be achieved by tuning the shell thickness and the core sizes because in such cases the electrons and the holes have spatial confinement in the core and shell separately. In this type of CSQDs, significantly redshifted emission spectra with a prolonged lifetime are observed upon shell growth.[27] Additionally, type-2 CSQDs exhibit a large shift between the absorption and emission maxima (Stokes shift).[27-29] Moreover, the effective band gap of the type-2 CSQDs depends on the core and shell band offset. For example, CdSe/ZnTe QDs show emission energy smaller than the bandgap of both CdSe and ZnTe.[29] Furthermore, one of the carriers can be delocalized over the entire core-shell structure if the conduction or valence band offset between the core and shell is small. These specific structures are known as quasi-type-2 CSQDs. For example, when a small CdSe core is overcoated with thick CdS shell, due to a small conduction band offset, it exhibits a quasi-type-2 CSQDs band alignment.[30] In this class of heterostructure, Auger recombination is suppressed due to reduced overlap between electron-hole wavefunctions.[31] Additionally, the bi-exciton lifetime is also prolonged making them suitable for photovoltaic and photocatalytic applications.[31]

Besides the band gap alignment in core/shell structures as abovementioned, an important requirement for shell growth is a small lattice mismatch between core and shell materials. A large lattice mismatch introduces interfacial reconstruction caused by lattice strain at the core/shell interface, which contributes to emission spectral broadening.[32] Moreover, it also generates defects and favors alloying

or cation exchange.[33] Therefore, to create a core/shell structure, both the band gap alignment and lattice mismatch should be carefully considered.

1.2.5. Quantum dots on demand: Applications

Quantum dots have been explored in a variety of applications like light-emitting diodes (LEDs), photovoltaics, bioimaging, catalysis, etc.[34-35] Some of these applications such as TV sets where QDs are used in the white backlight are now commercially produced, and have become part of our daily lives.[36]

1.2.5.1. Light-emitting diodes (LEDs) and display applications

Displays and LEDs are the most invested fields in QDs-based technology due to QDs solution processability and their narrow, tunable emission covering the visible and near-infrared regions.[15, 34, 37-39] Compared to organic-based LEDs, it is possible to obtain all three primary colors (red, green, and blue) just by changing the size of the quantum dots. Moreover, inorganic materials usually have higher thermal stability than organic materials.

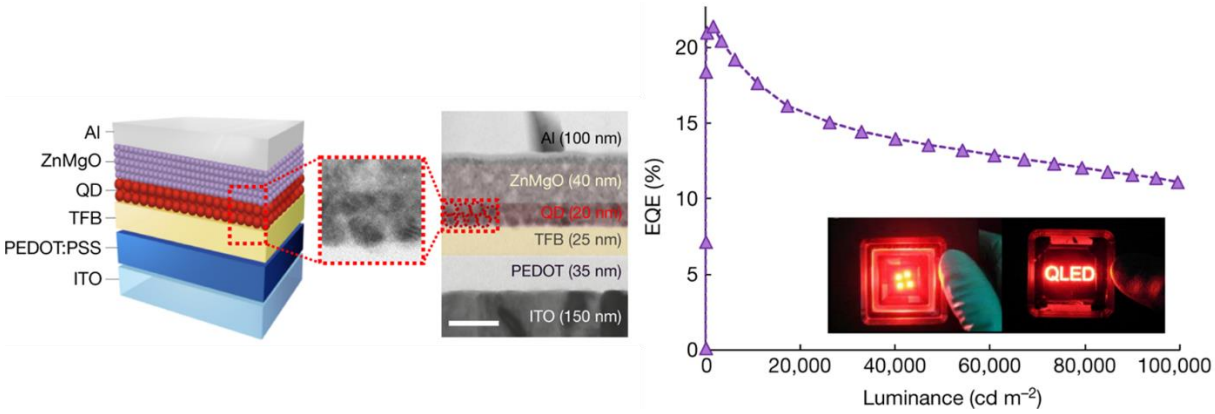

Figure 1.6: Illustration of device fabrication (left) and EQE–luminance profile (right).[15]

Early LED applications were mainly based on III-V QDs such as InAs/GaAs heterostructure, which was grown on a semiconductor substrate by molecular beam epitaxy (MBE).[40] In recent years, InP QDs are being widely explored in LEDs and display applications.[27, 41] Jang et al. developed a highly efficient (external quantum efficiency - 21.4%) QLED with a maximum brightness of 100 000 cd/m^2 and a long lifetime (Figure 1.6). The InP QDs film is sandwiched between two layers assuring electron and hole injection; Figure 1.6 presents the device architecture system. A high PLQY of the applied QDs (~100%) was achieved by etching the InP QDs surface with HF and subsequent multi-shell growth of ZnSe and ZnS.[15] Using QDs with different sizes, it is possible to obtain LEDs emitting in all colors. However, the challenges on these types of devices remain the improvement in color purity and blinking.[15, 42] QDs-based commercial television displays are already available in the market.

1.2.5.2. Photoconductors and photodetectors

The demand for photodetector and photoconductor devices is increasing for their use in automation, communications, and military industries, particularly in NIR spectrum detection. Traditional photodetectors were mainly composed of III-V semiconductors such as InGaAs and InGaP. However, the high fabrication cost limited their reach. A large number of materials were investigated, among which QDs gained enormous attention due to their solution processability and strong confinement effect. Various QDs such as PbS were employed in IR detectors as early as the 1940s.[43] [44] PbS shows a large range of tunable band gaps (0.6–1.6 eV), a high, broadband molar absorption coefficient ($\approx 10^6$ M^{-1} cm^{-1}), and a large Bohr exciton radius (~18 nm), and the advantages of low-cost, easy solution processabilities and high stability in air.[44] Therefore, PbS QDs-based devices are increasingly used in the IR region as broadband photoconductors and photodetectors. However, PbS QD-based photodetectors are mainly limited by the toxicity of the materials.

1.2.5.3. Biological applications

Currently, a great amount of research is being invested in the development of QDs for biological applications such as bioimaging and biosensors. QDs offer several advantages over traditional dyes, which were used for most biological imaging in the past due to their low toxicity.

- QDs have a higher absorption coefficient, less photobleaching, and a broad excitation window.
- The cell autofluorescence covers the completely visible region that sometimes masks the signals from dyes. NIR-emitting QDs can be utilized to avoid signal masking by autofluorescence from cells.
- QDs also show better stability within cell environmental conditions for example at varying pH.
- It is possible to modulate the emission wavelength for the same excitation wavelength using different sizes of the QDs to visualize simultaneously different areas of interest. This technique is known as multiplexing.
- With QDs it is possible to functionalize the surface with chemical functions of different nature whereas with an organic fluorophore a single function can generally be attached. In addition, the properties of the fluorophores will be more sensitive to the addition of this function.

For in vitro imaging (test in tube, outside the living organism), the photostability of the QDs compared to organic fluorophores is one of the main advantages. In vivo imaging (on a living organism) imposes more constraints because of the absorbance of tissues and body fluids. Therefore, QDs must have absorption and emission wavelengths in the near infrared range (IR) between 700 and 900 nm or between 1000 and 1350 nm where tissues, water and (oxy-)hemoglobin absorb and scatter less light. The QDs are therefore very good candidates for applications in NIR wavelength ranges. To be used in in vivo imaging, NCs must be smaller than 100 nm to be able to cross biological barriers and should not contain toxic substances.[45]

Exploiting the advantages of the QDs, a few studies were done *in vivo* and *in vitro*.[46-47] Recently, $CuInS_2$/ZnS QDs demonstrated improved biocompatibility and low nonspecific binding to the cells making them promising for bioimaging.[48] Figure 1.7 shows the in vitro imaging of cancer cells using In-based QDs in various organs of mice at different durations.[49] It was found that the InP QDs antibody probes were non-cytotoxic to cells cultures. Also, they can target HepG2 cells and liver cancer tumors for recognition and labeling. These findings demonstrate the potential of InP QDs for in vivo tumor-targeted imaging in cancer diagnosis and other clinical applications.

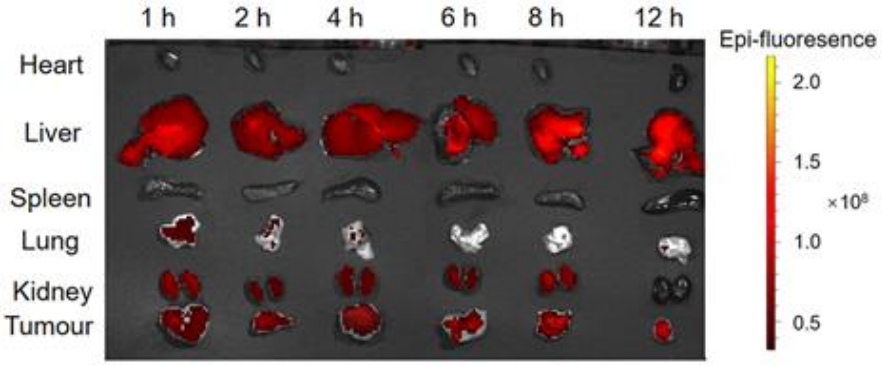

Figure 1.7. In vitro imaging of cancer cells using InP QDs in various organs of mice at different durations.[49]

1.2.6. Investment in the quantum dots research

As the high demand for quantum dots for various applications was discussed in the previous section, it is clear that both academic and industrial research are playing significant roles in the research and development of quantum dots, thereby stimulating commercialization and funding. It is almost impossible to present up-to-date data considering all the latest progress and new applications.

1.2.6.1. Academic research

In the last decades, quantum dots synthesis, characterization, and application in modern technologies have been highly active topics of research. Numerous laboratories worldwide focus their research in the very field and produced a large body of research papers reaching more than 2500 publications in 2019 alone (Web of Science). Figure 1.8 shows the growth in the number of publications of CdSe, CdS, and InP QDs in recent times. We can see the number of research publications of CdSe and CdS QDs already reached a plateau during 2012-2015 and then started to decline possibly due to the limitation over toxic materials by the Restriction of Hazardous Substance Directive (RoHS). A drop between 2020-2021 was expected as many laboratories were shut down during the COVID-19 pandemic. Earlier research was predominantly centered on the II-VI group, but III-V and I-III-VI-based QDs are getting attention as more environmentally benign materials.

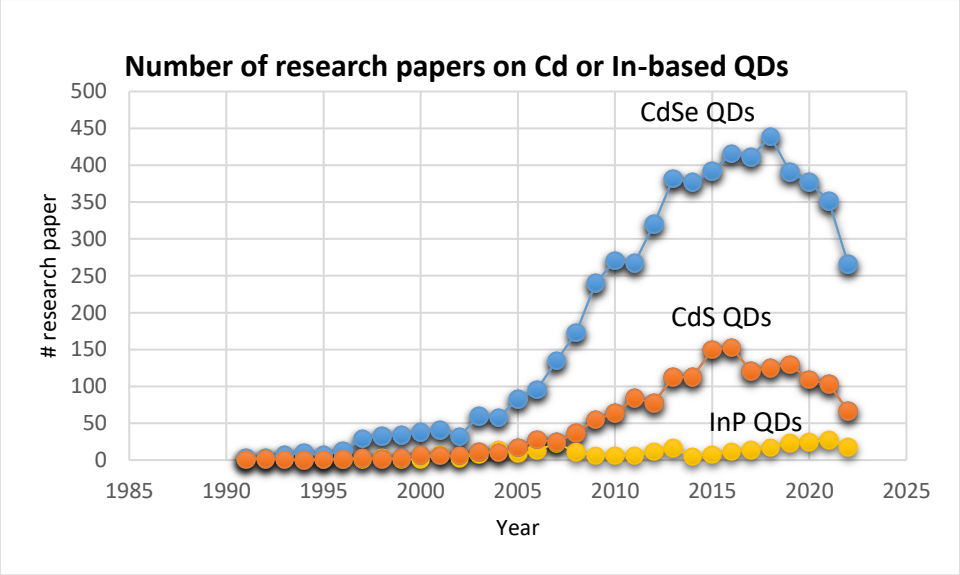

Figure 1.8. Estimate the number of publications on CdSe (blue), CdS (orange), and InP (yellow) quantum dots published in the last 20 years. The data is collected from the 'Web of Science' by using the keyword of CdSe, CdS and InP QDs or nanocrystals.

1.2.6.2. Industrial research

Growing demand for smart electronic devices is expected to enhance the growth of the QDs market. According to the Business Research Company's research report, the quantum dots market size is likely to expand from $4.70 billion (2021) to $6.03 billion (2022) at a compound annual growth rate (CAGR) of 26.35% and reach $14.68 billion in 2026. Many big companies are exploring new quantum dots-based technologies such as light-emitting diodes (LEDs), photovoltaics, photodetectors, etc. In October 2020, Samsung Advanced Institute of Technology (SAIT) developed blue Quantum Dot light-emitting diodes (QLEDs). These quantum dots deliver improved luminous efficiency by 20.2%, having a maximum luminance of 88,900 nits and a 16,000-hour QLED lifetime.

1.3. Indium phosphide (InP) quantum dots

In past decades, II-VI- and IV-VI-based QDs such as CdSe and PbS have been highly investigated due to their excellent optical and electronic properties and ease of preparation. Nonetheless, considering the significant intrinsic toxicity of Cd and Pb-based materials, practical applications in daily life become a major concern. Additionally, in the last decade, the Restriction of Hazardous Substance Directive (RoHS) 2002 /95/EC (formulated by the European Union) set criteria for using toxic material (CdSe (0.01%), mercury (0.1%)) in electrical and electronic applications.[50] As a replacement for CdSe, InP nanocrystals (NCs) have gained attraction due to their low intrinsic toxicity and comparable optoelectronic properties.[51-53] Likewise InAs QDs are developed for replacing PbS.

InP QDs belong to the III-V family of semiconductor NCs. InP has a bulk band gap of 1.35 eV and is mainly found in the zinc blende crystal structure. With the large excitonic Bohr radius of 11.5 nm and

a suitable band gap, InP QDs offer a wide range of tunability covering the whole visible to the near-infrared region by changing the particle size.[5, 54]

1.3.1. The birth of colloidal InP QDs

In 1989, Healy et al. reported the first synthesis of InP NCs by an organometallic reaction involving a reaction between indium (III) chloride ($InCl_3$) and tris(trimethylsilyl) phosphine [$P(SiMe_3)_3$]. The reaction was performed in vacuum and under high-temperature conditions.[55] Later, in 1995, Wells et al. synthesized InP NCs by thermal decomposition and annealing of the black powder obtained from silyl cleavage reactions.[56] Wells' dehalosilylation reaction was the most common route to synthesize InP QDs. However, this reaction needed a long reaction time (7-9 days)[57] and consisted of multiple annealing processes at high temperatures which caused irreversible particle aggregation. The prepared InP NCs were poorly confined, leading to poor emission properties compared to II-VI semiconductor NCs. Subsequently, direct synthesis approaches such as hot injection, heat-up methods, and seeded growth methods were developed to overcome this problem.

1.3.2. Direct methods to prepare InP QDs

1.3.2.1. Hot-injection method

In 1993, Murray et al. developed the hot-injection technique to synthesize monodisperse CdE (E=S, Se, Te) QDs in the coordinating solvent trioctylphosphine oxide (TOPO).[19] The hot-injection method works by swiftly injecting one precursor into a hot reaction mixture containing the other precursor(s) or, injecting all precursors into a hot solvent simultaneously (Figure 1.9a). The rapid injection of precursors triggers a burst nucleation followed by a sudden drop in the reaction temperature and monomer concentration, hindering any further nucleation and leading to size-focused growth. However, the synthesis of InP QDs via this route is more complicated due to the low solubility of existing indium and phosphorous precursors in non-polar solvents such as octadecene (ODE). In 2002, Peng et al. developed a synthesis of InP QDs by injecting $P[Si(Me_3)_3]$ into ODE at 270 ºC. The coordinating solvent TOPO was replaced by ODE and different chain lengths of fatty acids (lauric, myristic, palmitic, and steric acid) were examined as surface ligands for controlling the reaction kinetics (Figure 1.9b).[58] In comparison to previous methods, this novel synthesis method was much faster and more economical. Henceforth, it has been one of the most developed methods for synthesizing InP QDs of low-size distribution.

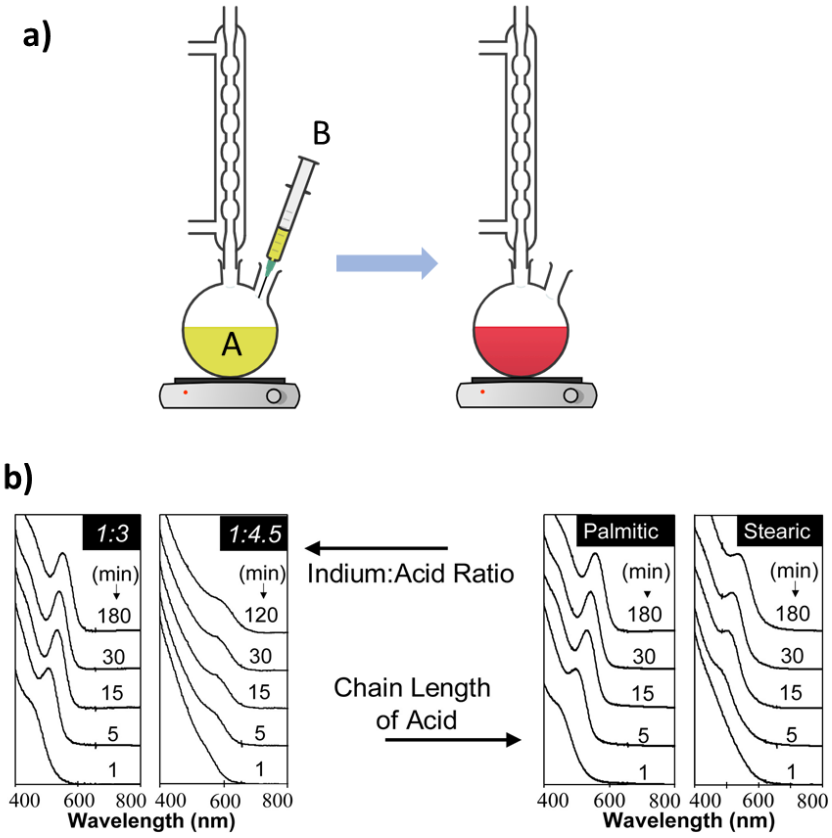

Figure 1.9: (a) Schematic of the hot injection method; (b) Absorption data of InP QDs prepared using the hot-injection method by injecting P[Si(Me_3)$_3$] into ODE at 270 ^oC.[58]

1.3.2.2. Heat-up approach

One of the drawbacks of the hot-injection method is the trade-off between scalability and particle quality. To circumvent such problems, the heat-up method was developed in which all the precursors, the solvent, and the ligands are added at room temperature and heated to high temperatures. The subsequent heating increases the monomer concentration, leading to a long nucleation period along with the growth. In earlier studies, a single precursor In($PtBu_2$)$_3$ was heated in a coordinating solvent, however, it resulted in poor size distribution with inferior optical properties. In 2008, in our laboratory, a single-step heat-up method was reported to synthesize high-quality InP/ZnS QDs with a narrow emission peak (FWHM = 40-60 nm) and 68% PLQY (Figure 1.10a-c).[59] In 2010, in our laboratory, it was found that the presence of Zn enhances the size uniformity (represented by the sharpness of the exciton peak in the absorption spectrum) of the InP QDs.[60] In further mechanistic studies, they found that Zn was forming a stable intermediate complex with P which controls the extreme reactivity of P($SiMe_3$)$_3$ and leads to better size-focused growth.[61]

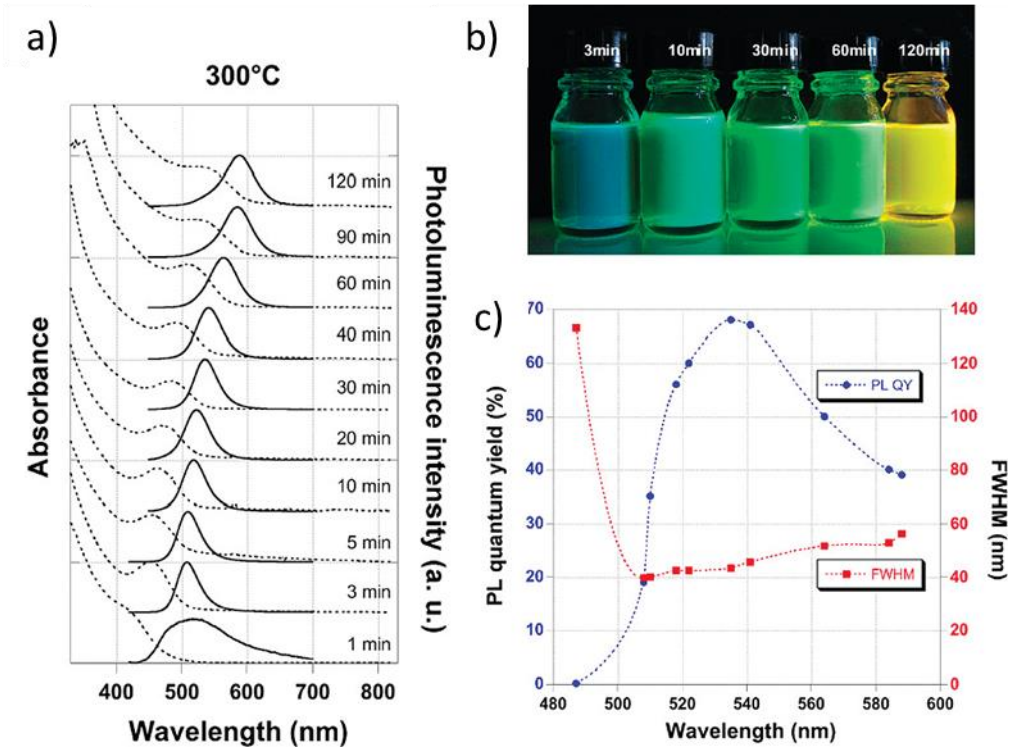

Figure 1.10: (a) Photoluminescence and absorption spectra of InP/ZnS QDs with reaction time. (b) Photographs of selected samples under UV light. (c) Fluorescence QY and PL linewidth profiles of InP/ZnS QDs.[59]

1.3.3. Template-based synthesis

1.3.3.1. Seed-assisted growth

In the seed-mediated or seed-assisted growth method, the nucleation of the NCs is initiated from external seeds. According to Gibbs's free energy theory, the energy barrier for homogeneous nucleation and heterogeneous nucleation is given by the following equations.[54]

$$\Delta G_{homo} = \frac{16\pi\gamma^3}{3\Delta G_v^2} \qquad \textit{Eq. 1.4}$$

$$\Delta G_{hetero} = \left(\frac{2-3\cos\theta+cos^2\theta}{4}\right) * \Delta G_{homo} \qquad \textit{Eq. 1.5}$$

Where G_v is the change in the free energy per unit volume of the nucleus, γ is the increase in the free energy per unit surface area of the nucleus, and θ is the contact angle of the nucleus on the seed substrate. In the case of the 90° contact angle, according to Eq. 1.4 and 1.5, the energy barrier for the heterogeneous nucleation is half of that of the homogeneous nucleation. This reduction in energy barrier favors the deposition of the monomers on seeds leading to controllable growth. Figure 1.11a shows the Gibbs free energy plot against the size of the particles.

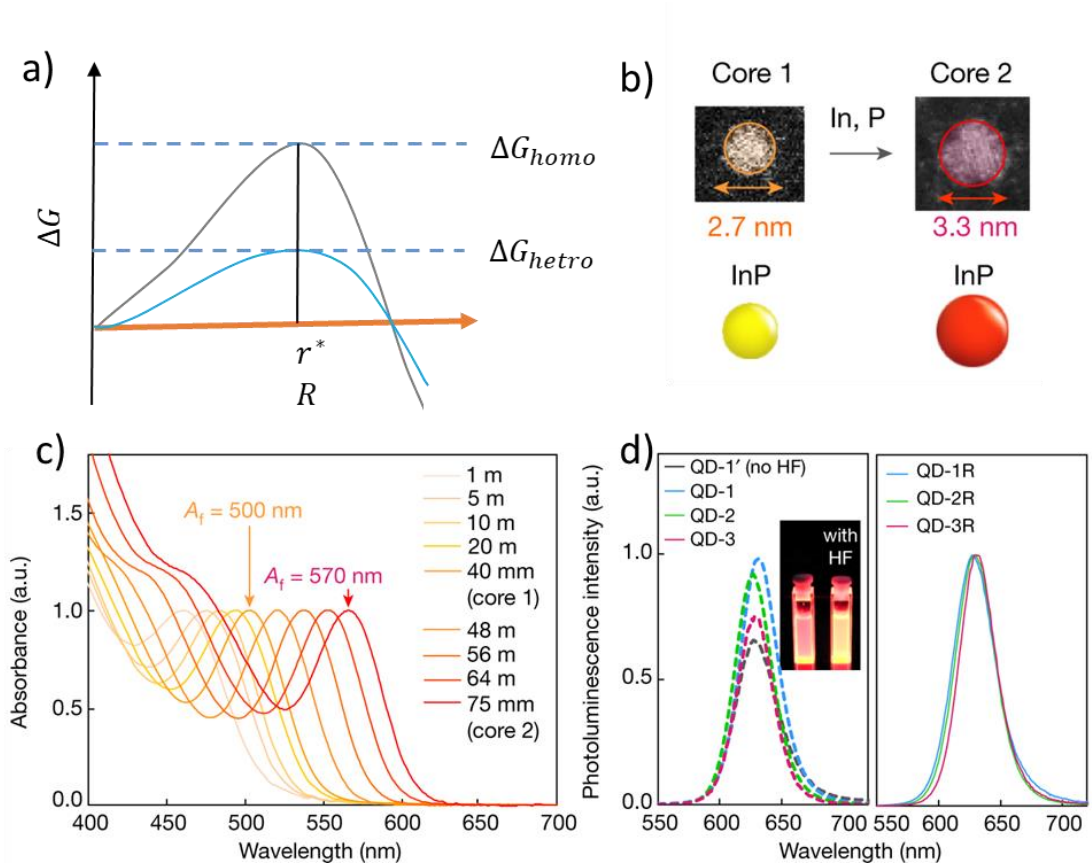

Figure 1.11: (a) The plot of Gibbs free energy versus the size of the QDs. The grey curve shows homogeneous and the blue curve shows heterogeneous nucleation. (b) Scheme for the preparation of different InP core QDs.[15] (c) Absorption spectra of InP QDs at different reaction times.[15] (d) Photoluminescence spectra of InP/ZnSe/ZnS QDs without (QD-1') and with (QD-1, QD-2, QD-3) HF treatement.[15]

Due to the high reactivity of the most employed P precursors, separating nucleation and growth has been a challenge. Specifically, $P(SiMe_3)_3$ is consumed extremely fast leading to growth in the Ostwald ripening regime. Despite several attempts to reduce and control the reactivity of the precursors, the size dispersity of InP QDs remained the same.[62-64] Later, Ramasamy et al. developed a seed-mediated method to prepare monodisperse InP QDs (QY <10%) where oxide-free 1.9 nm InP seeds were used to synthesize large (4.5 nm) particles by continuous injection of Zn-In-P complexes (Figure 1.11b-c).[65] Recently, Won et al. reported monodisperse (FWHM = 35 nm) and near-unity PLQY InP/ZnSe/ZnS multi-shell QDs using the seed-mediated hot injection method (Figure 1.11d).[15] Although seed-mediated synthesis is more complex than the direct synthesis methods, it enables better control over the reaction kinetics.

1.3.3.2. Cation exchange method

The cation exchange reaction has emerged as an alternative to direct synthesis. During cation exchange, the initial cation is rapidly replaced by a targeted cation while preserving the QDs size and morphology.

Ion exchange is driven by Lewis acid-base interaction and solvation energy. Moreover, it is a post-synthetic process and does not need any special equipment.

In 2012, Beberwyck et al. demonstrated the cation exchange method to prepare monodisperse and crystalline III-V semiconductor NCs. InP NCs were prepared by introducing cadmium pnictide (Cd_2P_3) NCs in a trioctylphosphine (TOP) and $InCl_3$ solution at a high temperature (270 ^oC).[66] Recently, Banin et al. achieved luminescent wurtzite InP NCs via a cation exchange reaction from hexagonal copper phosphide ($Cu_{3-x}P$) NCs templates (Figure 1.12). As-prepared InP NCs exhibit a well-resolved absorption spectrum with a narrow emission linewidth of 80 meV, and a photoluminescence quantum yield of up to 40%.[67]

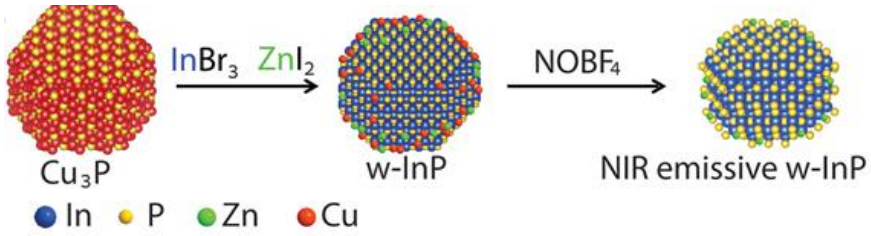

Figure 1.12: Scheme describing the cation exchange of Cu_3P to InP and the surface treatment with NOBF4.[67]

1.3.4. Large-scale synthesis of InP QDs

Undoubtedly, there has been significant development in the direct synthesis method for preparing high-quality InP QDs although they enable only gram-scale production. The large-scale production of high-quality InP QDs is largely limited and remained one of the main challenges for their utilization in the applications. Mainly, there have been two methods for large-scale production of InP-based QDs; i) microwave-assisted and ii) microfluidic-based.

1.3.4.1. Microwave-assisted large-scale production

Microwave-assisted synthesis enables better control of reaction conditions over hot-injection or heat-up methods. Due to efficient and rapid heating in the microwave, QDs synthesis can be achieved within minutes compared to the several hours needed for conventional methods.[68] Additionally, microwave enables uniform heating, unlike conventional heating mantle where a gradient in the reaction temperature is evident. The microwave-assisted technique has been applied in various syntheses such as for metal NPs, chalcogenide NPs, and perovskite NPs, etc.[69-70]

Strouse et al. first reported the microwave-assisted production of highly crystalline InP QDs, obtaining 4% PLQY.[71] They improved the PLQY further up to 47% with the presence of a fluorinated ionic liquid during synthesis. They found that the growth of InP QDs in the presence of the ionic liquid 1-hexyl-3-methyl-imidazolium tetrafluoroborate produces etched particles enhancing the PLQY. Moreover, in situ formed F^- ions passivate the as-synthesized QDs at low concentrations whereas a high fluoride ion

concentration leads to faster etching resulting in the loss of InP QDs. Therefore, a balance between etching and growth needs to be maintained to optimize the synthesis of InP QDs.

Despite exhibiting a great potential for scalability, microwave-assisted synthesis is still challenging for the in-situ characterization of products and synthesizing core-shell heterostructures.

1.3.4.2. Microfluidic-based synthesis

Another method that has been developed for large-scale production is microfluidic-based synthesis. This technique utilizes a microreactor which consists of multiple pumps for the continuous injection of precursors, a precursor mixing chamber, and multiple heaters. It also consists of in-line absorption and PL detectors providing the additional advantage of in-situ monitoring of the reaction kinetics.[72] In 2009, deMello et al. first reported a microfluidic method for preparing InP QDs.[73] They found that the flow rate was an important parameter to tune the optical properties of InP QDs. By adjusting the flow rate and the heating time, they could achieve up to 7% PLQY, however, the size distribution of the InP QDs remained very poor. Recently, Vikram et al. reported a modular millifluidic reactor-based continuous and multi-step synthesis of InP/ZnSeS core-shell QDs for gram-scale production (Figure 1.13a).[74] After the optimization of temperature and reaction time for the synthesis, they achieved up to 67% PLQY with good reproducibility. Moreover, by adjusting the conditions for shelling, they tuned the emission wavelength of InP QDs from 480 to 650 nm (Figure 1.13b-d).

Despite having the potential for large-scale production and significant benefits over conventional synthesis, microfluidic-based synthesis is yet to be fully developed for InP QDs.

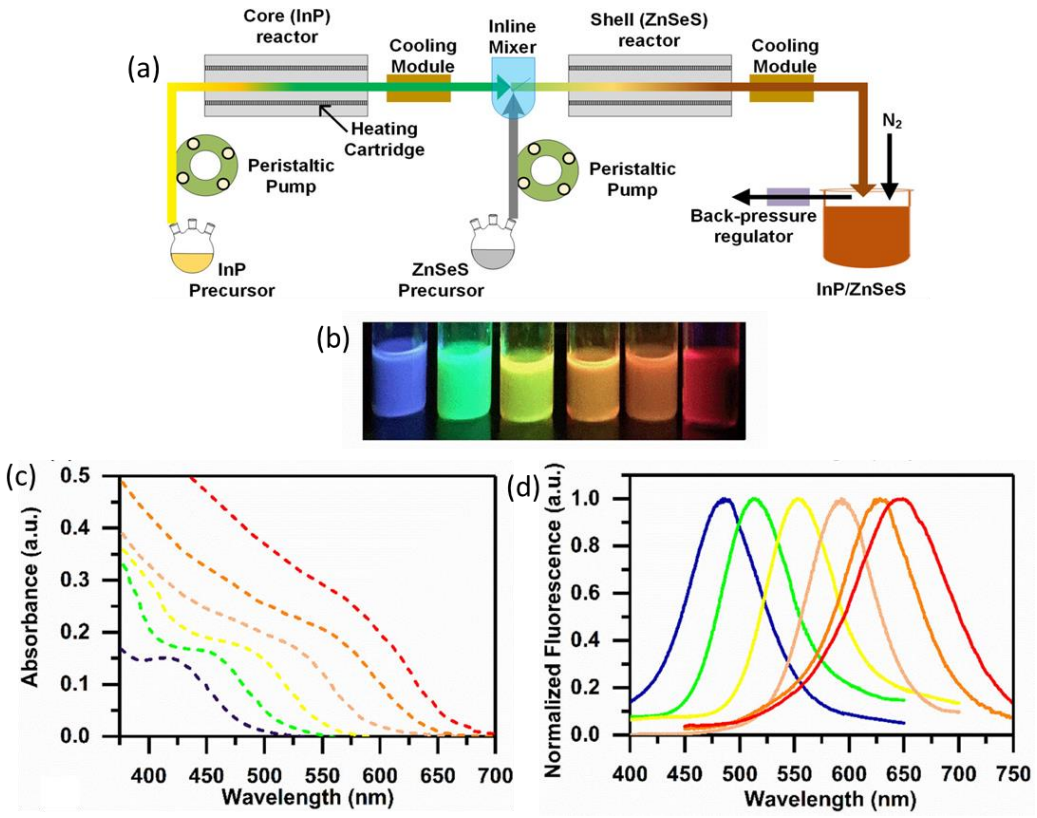

Figure 1.13: Schematic of microflow reactor for InP/ZnSeS production. (b) Photograph of as-synthesized InP/ZnSeS QDs under UV-light. (c) and (d) Absorbance and emission spectra of InP/ZnSeS QDs, respectively.[74]

1.3.5. Development toward more economical and safer synthesis

To date, $P(TMS)_3$ has been used in the majority of InP syntheses as the source of the P precursor. Despite being very expensive and pyrophoric in nature, it is still the most necessary component for obtaining monodispersed and highly emissive InP QDs. Meanwhile, other economical alternatives such as P_4,[75] PH_3,[76] and PCl_3[77] pose a major concern in terms of the quality of the obtained QDs. In recent studies, tris(dialkyl)aminophosphines are emerging as an economical and much safer P precursor to produce InP-based QDs with similar optical properties as those prepared using $P(TMS)_3$.[78-80]

1.3.5.1. Aminophosphine-based synthesis of InP QDs

In 2013, Song et al. first developed a hot-injection method to produce InP QDs with tunable emission (532 nm to 610 nm) by introducing tris(dimethylamino)phosphine [$P(NMe_2)_3$] in a mixture of $InCl_3$ and $ZnCl_2$ in oleylamine at 220 ^oC (Figure 1.14a-c).[79] Addition of $ZnCl_2$ was found to be beneficial in improving the size distribution of the InP QDs. In many reports, introducing Zn precursor in the core synthesis is an important step for the formation of high-quality InP QDs in terms of emission linewidth and PLQY.[81] In one study, it was found that Zn forms a relatively less reactive Zn-In complex in situ, providing better control over reaction kinetics and size distribution.[81] The location of zinc in the QDs depends on the reactivity of the zinc precursor used; highly reactive zinc acetate forms Zn_3P_2

incorporated into the InP lattice whereas higher carbon chain Zn-carboxylate precursors work as surfactants leading to better size distribution by limiting the particle growth.[81]

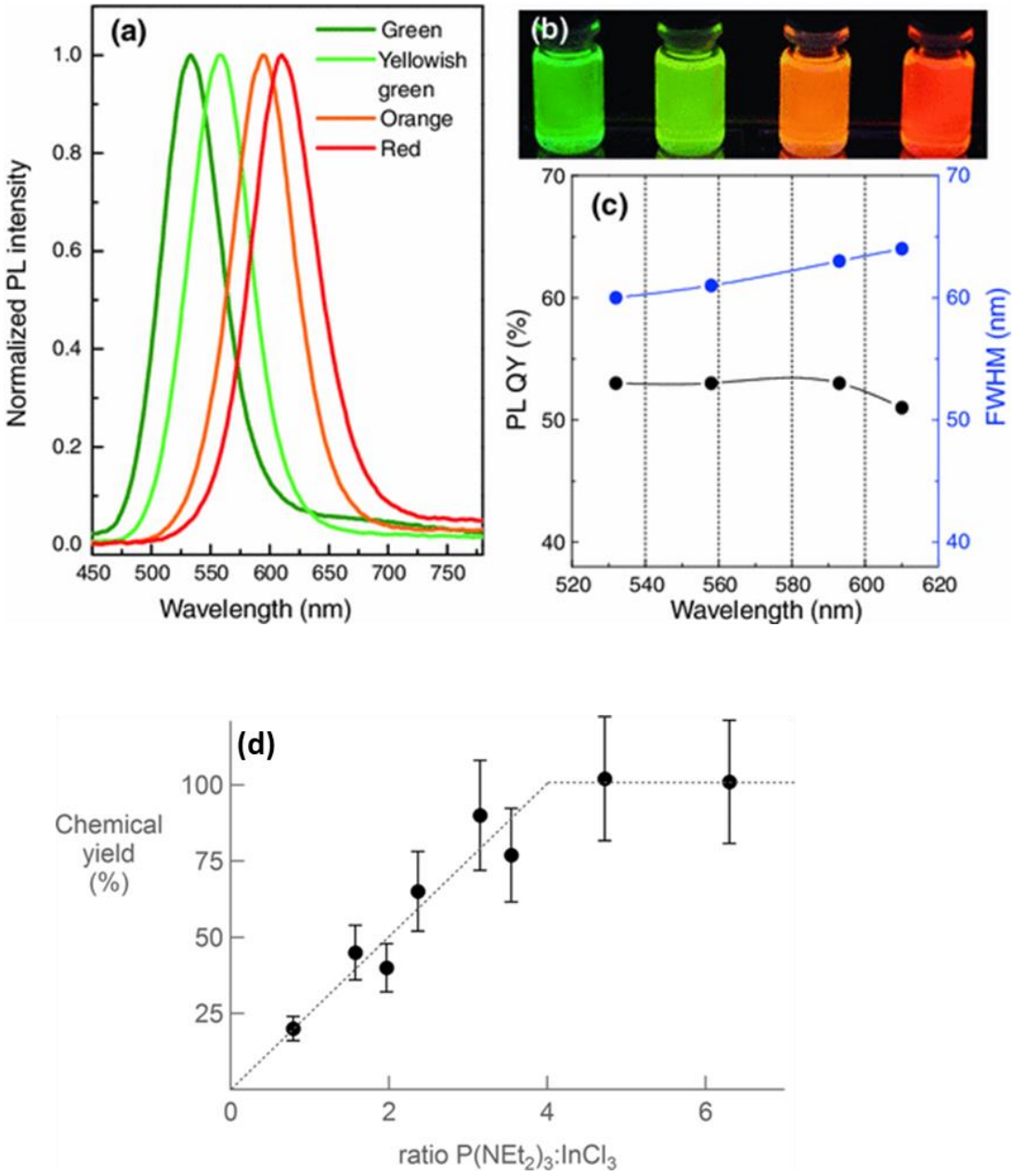

Figure 1.14: (a) Emission spectra of InP/ZnS QDs synthesized using the aminophosphine route.[79] (b) Photograph of InP/ZnS QDs under UV light.[79] (c) Photoluminescence quantum yield (PLQY) and emission linewidth (FWHM) of InP/ZnS QDs synthesized using the aminophosphine route.[79] (d) Change in the chemical yield of InP QDs with different P:In ratios.[82]

Furthermore, detailed mechanistic studies of the reaction between aminophosphine precursor and indium halides in the presence of primary amines were proposed by Buffard et al.[80] and Tessier et al.[82] In a typical aminophosphine-based synthesis, first, transamination occurs between $P[(NMe_2)_3]$ and the primary amine present as the solvent (oleylamine) along with diethylamine gas evolution (*Eq. 1.6*), followed by reaction between transaminated phosphine with indium halide yielding InP QDs and

aminophosphonium salt as a by-product (*Eq. 1.7*). Thus aminophosphine acting as both P source and the reducing agent and that explains the need of higher amount of P (1 In 4 P) to obtain 100% chemical yield (Figure 1.14d).

$$4\ P(NEt_2)_3 + 12\ NH_2R \longrightarrow 4\ P(NHR)_3 + 12\ Et_2NH \qquad \textit{Eq. 1.6}$$

$$InCl_3 + 4\ P(NHR)_3 \longrightarrow InP + 3P(NHR)_4Cl \qquad \textit{Eq. 1.7}$$

1.3.6. Surface passivation

Pristine InP QDs contain a large amount of surface traps and are highly susceptible to surface oxidation leading to poor optical properties (5% PLQY). A general strategy to overcome this is to suppress the quenching effect by ion passivation or shell passivation of both cationic and anionic surfaces by an inorganic shell. We have discussed in detail the different types of core-shell structures in section 1.2.4.

ZnS is the most popular shell material for surface passivation due to its proper band alignment and chemical robustness, despite its rather large lattice mismatch (Figure 1.15b). The earliest InP/ZnS core/shell structure was inspired by well-developed CdSe/ZnS-based core/shell systems. In an attempt to prepare InP/ZnS QDs, Weller et al. found that the shell formation was not complete and formed ZnS islands on the InP QDs surface, resulting in only 23% PLQY.[23] In 2008, in our laboratory, a one-pot method was developed to produce highly luminescence InP/ZnS QDs (PLQY 60%) by treating the surface with zinc before ZnS shelling.[59] This method is still a very popular technique to produce highly emissive InP/ZnS on a large scale.

Despite ZnS being the most developed shell material, the lattice mismatch between InP and ZnS is comparably large (7.7%). The large misfit creates core-shell interface defects leading to PL reduction. Therefore, other shell materials of lower lattice mismatch (Figure 1.15b) such as ZnSe and GaP were investigated. In a comparative study, Tessier et al. found that InP/ZnSe QDs showed a narrower emission linewidth (FWHM = 48 nm) than that of InP/ZnS QDs (FWHM = 56 nm, Figure 1.15a).[78] On the other hand, the smaller conduction band offset between InP and ZnSe led to the delocalization of the core charge carriers over the shell. Consequently, there was a reduction in PLQY in the case of InP/ZnSe (50%) compared to InP/ZnS (60%).[78] Later, InP/ZnSeS,[17] InP/ZnCdSe alloyed shell or InP/ZnSe/ZnS,[15] InP/ZnSeS/ZnS, InP/GaP/ZnS[38] multi-shell structures were explored to minimize the lattice mismatch and provide strong confinement. In 2019, Jang et al. proposed a class of InP/ZnSe/ZnS multi-shell QDs prepared at high temperatures. The recorded PLQY after ZnSe and ZnS shell growth was 95%, the highest value achieved for green-emitting InP QDs.[83] In the same year, InP/ZnSe/ZnS core/shell QDs having PLQY of 100% at 630 nm (FWHM of 35 nm) were reported by the same group,[15] albeit the core InP QDs were prepared with $P(TMS)_3$ in both examples. The photoluminescence was improved by in situ surface etching of the InP particles using HF followed by ZnSe and ZnS shell growth. Recently, Avermaat et al. prepared InP/ZnSeS/ZnS QDs and achieved near-unity PLQY by

saturating the ZnSe surface with zinc acetate before ZnS growth (Figure 1.15c). To date, this is the best report for aminophosphine-based InP QDs in terms of quantum efficiency, however, the emission linewidth (FWHM = 45 nm) is larger than that of $P(TMS)_3$-based reports (FWHM = 35 nm). Table 1.2 shows the state of the art of InP CSQDs prepared using different In and P precursors.

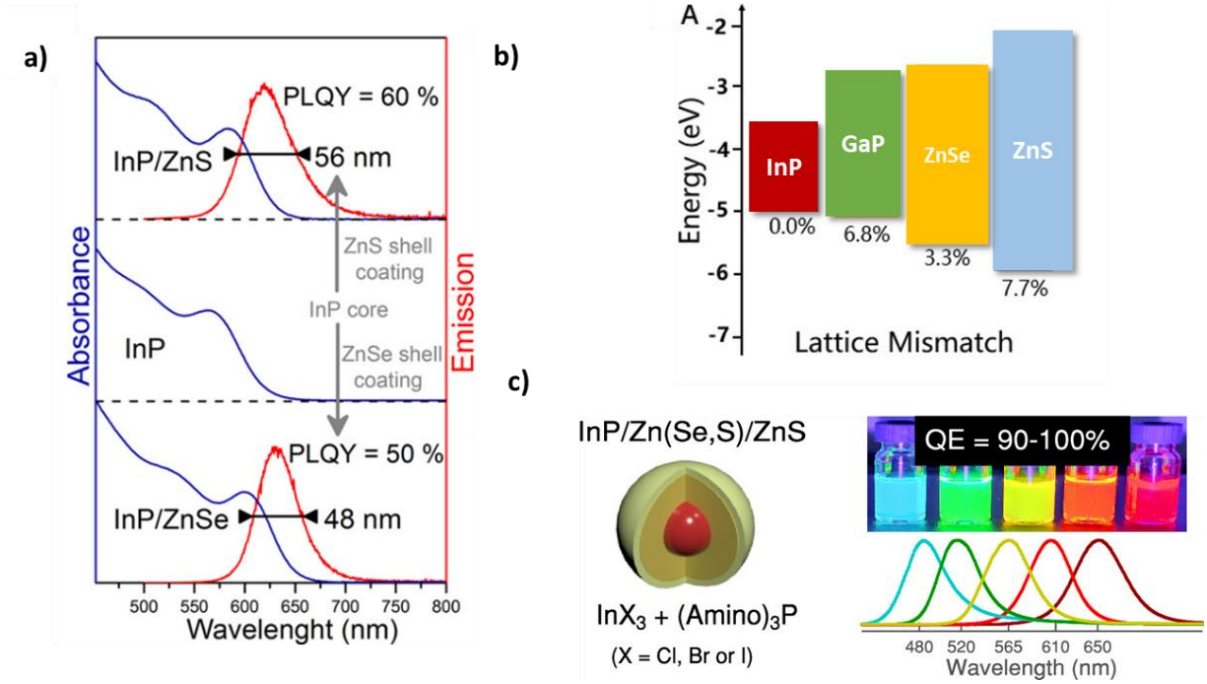

Figure 1.15: (a) Absorption and emission spectra of InP, InP/ZnS, and InP/ZnSe QDs.[78] (b) Schematic of band alignment of different materials. (c) InP/ZnSeS/ZnS QDs exhibiting near-unity PLQY.[84]

Table 1.2: List of the different InP core-shell-based QDs with high PLQY from literature.

QDs	Core precursors	Shell precursors	Emission peak (nm)	FWHM (nm)	PLQY (%)
InP/ZnS[59]	$InMy_3$, $ZnSt_2$, DDT, $P(TMS)_3$	$ZnSt_2$, DDT,	535	40	70
InP/ZnSe[78]	InCl3, $ZnCl_2$, $P(DMA)_3$	$ZnSt_2$, TOP-Se	630	48	50
InP/ZnSe/ZnS[42]	$InMy_3$, $P(TMS)_3$	$Zn(COOR)_2$, ODE-Se/S	535/618	35/42	90/93
InP/ZnSe/ZnS[15]	$In(PA)_3$, $P(TMS)_3$, HF	$ZnOA_2$, TOP-Se/S	630	35	98
Ga-InP/ZnSe/ZnS[85]	InI_3, $ZnCl_2$, $P(DMA)_3$	GaI_3, $ZnSt_2$, TOP-Se/S	525	37	97
InP/ZnSe/ZnS[86]	$InCl_3$, $ZnCl_2$, NaOCP	$ZnSt_2$, TOP-Se/S	533	36	97
InP/ZnSeS/ZnS[16]	InI_3, $ZnBr_2$, $P(DMA)_3$	$ZnSt_2$, TOP-Se/S	510	45	95
InP/ZnSe/ZnS[87]	$InBr_3$, $ZnCl_2$, $P(DMA)_3$	$Zn(Pa)_2$, TOP-Se/S	621	44	86
InP/Zn(Se,S)/ZnS[84]	InX_3, ZnX_2 (X = Cl, Br, I), $P(DEA)_3$	$ZnOA_2$, $ZnAc_2$, TOP-Se/S	480–630	45	90-100

My = myristate, St = stearate, OA = oleate, R = alkyl chain, DMA = dimethylamino, PA= palmitate

1.4. Outline of the Ph.D. thesis

As summarized in this chapter, various colloidal synthesis methods have been developed for preparing high-quality InP QDs which is a promising candidate as a less toxic replacement of Cd-based QDs. Nevertheless, poor size distribution, low PLQY, and the inability to large-scale production of InP QDs remained a major concern for their utilization in commercial applications.[88] It is within this context that the objective of this thesis was designed.

Chapter 2 deals with developing the large-scale continuous flow synthesis of InP QDs while maintaining a good size distribution. This chapter consists of two parts. For continuous flow synthesis, one of the main limitations is the solubility of the precursors, in-situ gas formation and poor mixing. Therefore, we first optimized the synthesis of InP QDs in batch and investigated different indium and phosphorous precursors and solvents compatible with the flow reactor. Further, we optimized various reaction conditions to improve the size distribution and developed InP/ZnS core-shell structures to improve the PLQY and photostability. In the second part, we transferred the batch-developed methods to continuous flow routes for large-scale production of high-quality InP QDs and InP/ZnS QDs with good reproducibility.

During the development of continuous flow synthesis (Chapter 2), we found that the addition of Zn in the core InP was an important parameter for size focusing. However, several issues were encountered

regarding the room temperature solubility of the Zn precursor. Therefore, next, we developed a Zn-free synthesis of InP QDs which is described in Chapter 3. In this chapter, we developed a novel protocol to prepare large-sized InP QDs by using indium (I) halide and aminophosphine. Moreover, we performed ^{31}P NMR and mass spectroscopy to understand the underlying reaction mechanism. To improve the emission properties, we explored room-temperature etching using in-situ generated HF and InP/ZnS core-shell growth at low temperatures.

In Chapter 4, we attempted a template-based method to synthesize InP nanoplatelets. InP nanoplatelets offer precise control over the optical properties of the InP NCs, one of the main goals of the thesis. First, we synthesized and characterized ZnSe NPLs which are further used as a template for the layer-by-layer growth method of anisotropic InP NCs.

Chapter 5 is an independent study. Here, we have synthesized Ga_2S_3 quantum dots which can be of great interest as blue emitters for example in blue-LEDs applications. We have studied the origin of the blue emission in this material and further improved the PLQY by coating it with ZnS shell.

Each Chapter contains its experimental section and characterization methods.

Chapter II

Continuous flow synthesis of InP-based quantum dots

2.1. Introduction

Colloidal semiconductor quantum dots (QDs) are promising candidates for various applications including photovoltaics,[38, 89] catalysis,[90] bioimaging and biosensing[45] due to their size-tunable properties. Widely studied cadmium- and lead-based semiconductor QDs exhibit excellent optical properties such as narrow emission and high quantum yield.[91] However, the issue of intrinsic toxicity of Cd and Pb remains a major disadvantage for their practical applications.[91] Due to their toxicity, cadmium and lead are restricted in many countries, including the European Union (EU). Therefore, academics and industrial research are shifting towards more environment-friendly alternatives. Among non-toxic/less toxic replacements, indium phosphide (InP) quantum dots are of significant interest due to their broad emission tunability, large absorption coefficient and large Bohr radius.[5, 54, 92]

In the past decade, there has been significant development in the batch synthesis of InP QDs reaching 20-95% quantum yield and emission FWHM of 35-80 nm after ZnSeS/ZnS multi-shell growth.[15, 59] Despite the advancement, there are several challenges in the InP QDs synthesis.[88] One of the main obstacles is the lack of precise control over size distribution while maintaining high PLQY.[92] Unlike II-VI class of QDs, in which the reaction kinetics is dependent on the precursor conversion,[93-94] InP QDs synthesis thus far has failed to obtain a well-defined LaMer type growth.[62, 95-96] The second challenge is the scarcity of safer and cost-effective phosphorous precursors. To date, in the majority of the InP QDs synthesis, highly hazardous and costly tris(trimethylsilyl)phosphine [$P(TMS)_3$] has been used as the phosphorus precursor and the developments for InP QDs synthesis have been revolving around this compound. $P(TMS)_3$ shows a high reactivity towards indium carboxylate complexes (e.g. indium myristate, indium palmitate) with the formation of Si-O bonds being the driving force of the reaction. However, the rapid depletion of monomers during the synthesis leads to a comparatively high polydispersity due to a ripening-type growth.[96-97] Furthermore, it prevents the preparation of larger (> 5 nm) InP QDs without multiple precursor injections. In more recent studies, safer and more economical aminophosphine-based phosphorus precursors have been explored as alternatives to $P(TMS)_3$.[78-80] Recently, up to 95% PLQY was reported with InP QDs synthesized via the aminophosphine route, albeit the PL FWHM (45 nm/151 meV)[16, 84] was broader than the best values reported with $P(TMS)_3$-based syntheses (35 nm /110 meV).[98]

Undoubtedly, the aminophosphine route provides a much greener route for preparing InP QDs. However, in conventional batch synthesis, the scalability is obstructed by problems with precursor mixing, temperature control, and reproducibility. To overcome the abovementioned challenges, microwave-based and flow chemistry-based syntheses have been developed.[72, 99-101] Compared to traditional flask-based synthesis, continuous flow reactors enable better heat and mass transfer. Additionally, they allow better control over reaction parameters, enabling high reproducibility. Most flow reactors are designed with inline detectors for *in situ* monitoring of the absorption and photoluminescence properties, which provides an additional advantage over traditional methods to study real-time kinetics.[101] Recently, we have demonstrated the efficiency of the continuous flow platform where ternary Ag-In-S and Ag-In-S/ZnS QDs were prepared in aqueous medium with high reproducibility and short reaction time (8-15 min). Under optimized conditions, up to 83% of PLQY was achieved for the core/shell systems.[102]

In one of the earliest attempts to develop a microfluidic method for preparing InP QDs, deMello et al. found that the flow rate was an important parameter to tune the optical properties of InP QDs.[73] The flow system was combined with one or two injection pumps, one oil bath and one flow cell. However, they could achieve up to 7% PLQY and the size distribution of the InP QDs remained very poor. Recently, Vikram et al. studied a modular millifluidic reactor-based continuous and multi-step synthesis of InP/ZnSeS core-shell QDs for gram-scale production.[74] With optimization of temperature and reaction time for the synthesis, they achieved up to 67% PLQY with good reproducibility. Moreover, by adjusting the conditions for shelling, they tuned the emission of InP QDs from 480 to 650 nm with a best emission line width of 72 nm. It is noteworthy that all of the abovementioned syntheses were performed using $P(TMS)_3$.

While this thesis was in progress, very recently, Lignos et al. developed a high-temperature continuous stirred-tank reactor cascade method to synthesize InP/ZnS QDs, using the safer aminophosphine route.[101] They tuned the emission of InP/ZnS QDs between 520–610 nm and reached up to 42% PLQY. Nevertheless, the emission line width (46-64 nm) remained broader compared to that of the $P(TMS)_3$-based syntheses.

This chapter of my thesis deals with developing a protocol for continuous flow synthesis of InP-based QDs using the safer and more economical aminophosphine route. First, we have optimized a synthesis protocol in batch where along with the standard tris(diethylamino)phosphine precursor, we also investigated transaminated tris(oleylamine)phosphine ($P(RNH)_3$ R= $C_{18}H_{35}$)) as the P precursor. While aminophosphine syntheses generally use oleylamine as the solvent, we also investigated InP QDs synthesis in the non-coordinating solvent octadecene (ODE), which is compatible with high pressure and temperature. Finally, we developed a continuous flow route to prepare InP and InP/ZnS core-shell QDs. In optimized conditions, we reached up to 53% PLQY with line widths comparable to the batch

synthesis. We have also demonstrated the efficiency of the continuous flow approach for producing InP QDs at the gram-scale.

2.2. Experimental section

2.2.1. Materials

Tris(diethylamino)phosphine ($(DEA)_3P$, 98%), indium chloride ($InCl_3$, 99.99%), zinc chloride ($ZnCl_2$, 99.99%), oleylamine (OLA, 98%), octylamine (OCA, 99%), hexadecylamine (HDA, 99%), trioctylamine (TOA, 90%), pyrrolidine (Pyrr, 99%), octadecene (ODE, 90%), trioctylphosphine (TOP, 90%) and zinc diethyldithiocarbamate ($Zn(DDTC)_2$, 97%) were purchased from Sigma-Aldrich and were used as received.

2.2.2. Batch syntheses

2.2.2.1. Synthesis of InP QDs using $P(DEA)_3$

The InP QDs were synthesized using the previously optimized standard protocol.[78] In a three-neck round bottom flask, 66 mg (0.3 mmol) $InCl_3$, 220 mg (1.6 mmol) $ZnCl_2$ and 7 mL oleylamine were added. The reaction mixture was kept under vacuum for 30 min. Afterward, it was switched under argon and the temperature was raised to 180 ^oC. At 180 ^oC, 324 μL (1.2 mmol) tris(diethylamino)phosphine diluted in 0.5 mL of ODE was swiftly injected. Shortly after the injection of the P precursor at high temperature, the reaction color changed to yellow and subsequently to orange and deep red. The reaction mixture was kept for 30 min at 180 ^oC and then the synthesis was quenched by lowering the temperature. The synthesized InP QDs were washed with mixture of methanol, chloroform and acetone (1V/1V/2V) by centrifugation at 8000 RPM for 5 min. Washed InP QDs were then dispersed in toluene for further use.

For the synthesis of InP QDs using octylamine, hexadecylamine and trioctylamine, a similar protocol was followed by replacing oleylamine with the desired amines with the same volume.

2.2.2.2. Synthesis of InP QDs using tris(oleylamino)phosphine $P(NHR)_3$

In a three-neck round bottom flask, 66 mg (0.3 mmol) $InCl_3$, 220 mg (1.6 mmol) $ZnCl_2$ and 7 mL oleylamine were added. The reaction mixture was kept under vacuum for 30 min. The reaction was switched under argon and the temperature was raised to 180 ^oC. Then 1.5 mL pre-prepared tris(oleylamino)phosphine (details in section 2.2.4.1.) was swiftly injected into the reaction mixture. Shortly after the injection of P precursor at high temperature, the reaction color changed from yellow to orange and then red. The reaction was kept for 30 min and then quenched by lowering the temperature. A similar washing procedure was followed as explained in the previous section.

2.2.2.3. Synthesis of InP QDs in non-coordinating solvent

In a three-neck round bottom flask, 66 mg (0.3 mmol) $InCl_3$, 220 mg (1.6 mmol) $ZnCl_2$, 2 mL TOP, and 5 mL ODE were added. The reaction mixture was kept under vacuum for 60 min. The reaction was

switched under argon and the temperature was raised to 180°C. At this temperature, previously synthesized 1.5 mL $P(NHR)_3$ (see section 2.2.4.1. for details) was swiftly injected. Shortly after the injection of the P-precursor at high temperature, the reaction color changed from colorless to yellow and with time changed to deep red. The reaction was kept for 30 min and then quenched by lowering the temperature. The as-prepared InP QDs were washed with mixture of methanol, chloroform, and acetone (1/1/2V) by centrifugation at 8000 RPM for 5 min. This step was repeated twice and washed InP QDs were dispersed in toluene for further use.

2.2.2.4. Synthesis of InP QDs using $P(OCA)_3$/$P(Pyrr)_3$

A similar synthesis method as 2.2.2.3 was followed for synthesizing InP QDs using $P(OCA)_3$ or $P(Pyrr)_3$. In all the syntheses P:In 4:1 feed ratio was used and the amount of aminophosphines was calculated accordingly.

2.2.2.5. Synthesis of InP/ZnS core/shell QDs

ZnS shelling was performed using as-synthesized InP QDs without purification to avoid any surface oxidation. In a typical ZnS shelling reaction, 1 mL of InP QDs, 2 mL single molecular $Zn(DDTC)_2$ (0.2 M/OLA) precursor and 2 mL of ODE were added in a three neck round bottom flask and heated to 160 °C with a slow heating rate of 2 °C/min. The reaction was held at this temperature for 2 hours and then cooled down to room temperature. The InP/ZnS QDs were purified using the same method as mentioned in section 2.2.2.1.

2.2.3. Continuous flow experimental set-up

Figure 2.1 shows the photograph of the continuous flow system purchased from Asia flow chemistry by Syrris®. The flow system is configured with two syringe pumps, two automated injectors with sample loops of 5 mL each, one stainless steel tubular heater (4/16 mL) with an inner diameter of 1 mm, one backpressure controller, and an automated collector. The continuous flow system can be used in two modes. i) Automatic mode, in which the residence time (reaction time) can be fixed and the flow rate is calculated automatically by the system, and ii) manual mode where all the parameters such as flow rate, heating temperature, and pressure can be changed manually during the synthesis. The flow setup is also equipped with an in-line UV-vis detector for in situ characterization, however, this feature could not be used in the present experiments, as the optical path was too long, which led to the saturation of the signal.

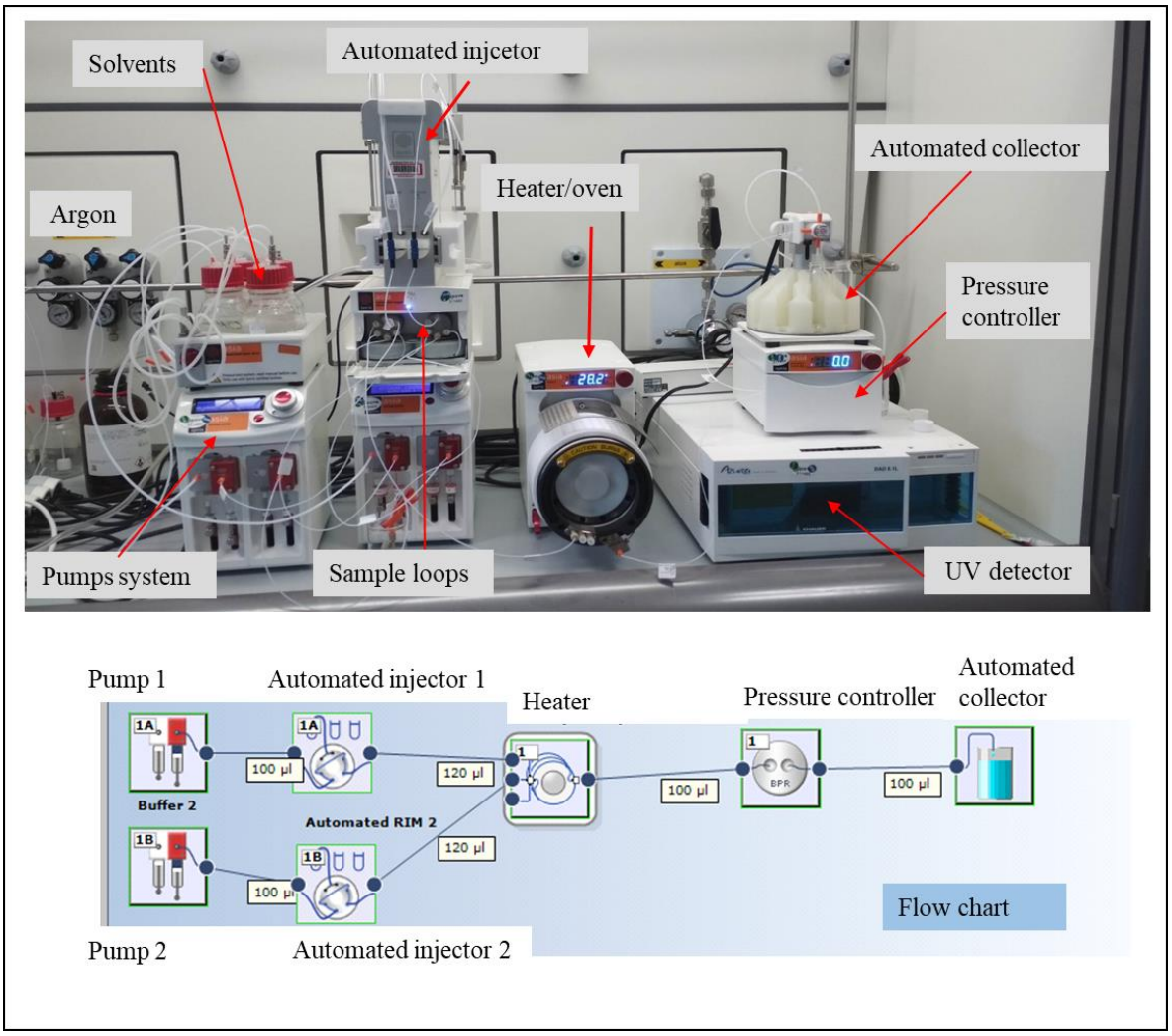

Figure 2.3. Photograph of the continuous flow system (top) and schematic of the flow chart (below).

2.2.4. Preparation of stock solutions of the precursors for flow

2.2.4.1. P precursor

For the preparation of $P(NHR)_3$, 12 mL (44 mmol) of $P(DEA)_3$ (**1**) and 46 mL (133 mmol) of pre-degassed oleylamine were added together in a 100 mL round-bottom flask. The reaction mixture was increased to 100 °C. Shortly after the reaction reached 100 °C, bubble formation was observed due to the evolution of diethylamine gas during the transamination process (Scheme 2.1).[80] The reaction was kept for 13-15 h and then cooled down to room temperature.

Using a similar molar ratio but decreasing the reaction time to 5-7 h, a mixture of $P(NHR)_3$ (**2**) and bisubstituted $P_2(NHR)_4NR$ was prepared (cf. Scheme 2.1). We note that the heterocyclic compound $P_2(NHR)_2(NR)_2$ (**3'**) is also formed, however, in very small quantity. For the preparation of tris(octylamine)phosphine ($P(OCA)_3$), and tris(pyrrolidinyl)phosphine ($P(Pyrr)_3$), we replaced oleylamine with octylamine and pyrrolidine respectively while all other parameters were kept same as in the case of $P(NHR)_3$. The final transaminated products were analyzed using ^{31}P NMR spectroscopy

in each case. All the pre-prepared P precursors were stable and were stored inside the glove box as prepared for further use.

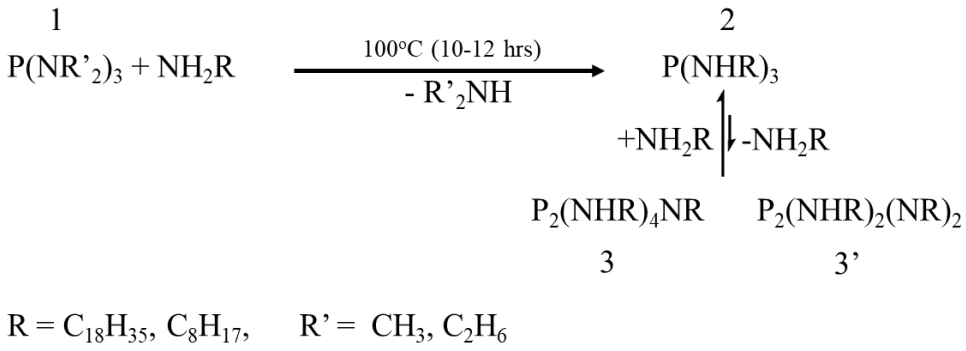

Scheme 2.1: Transamination reaction of $P(DEA)_3$ or $P(MEA)_3$ with OLA or OCA.[80]

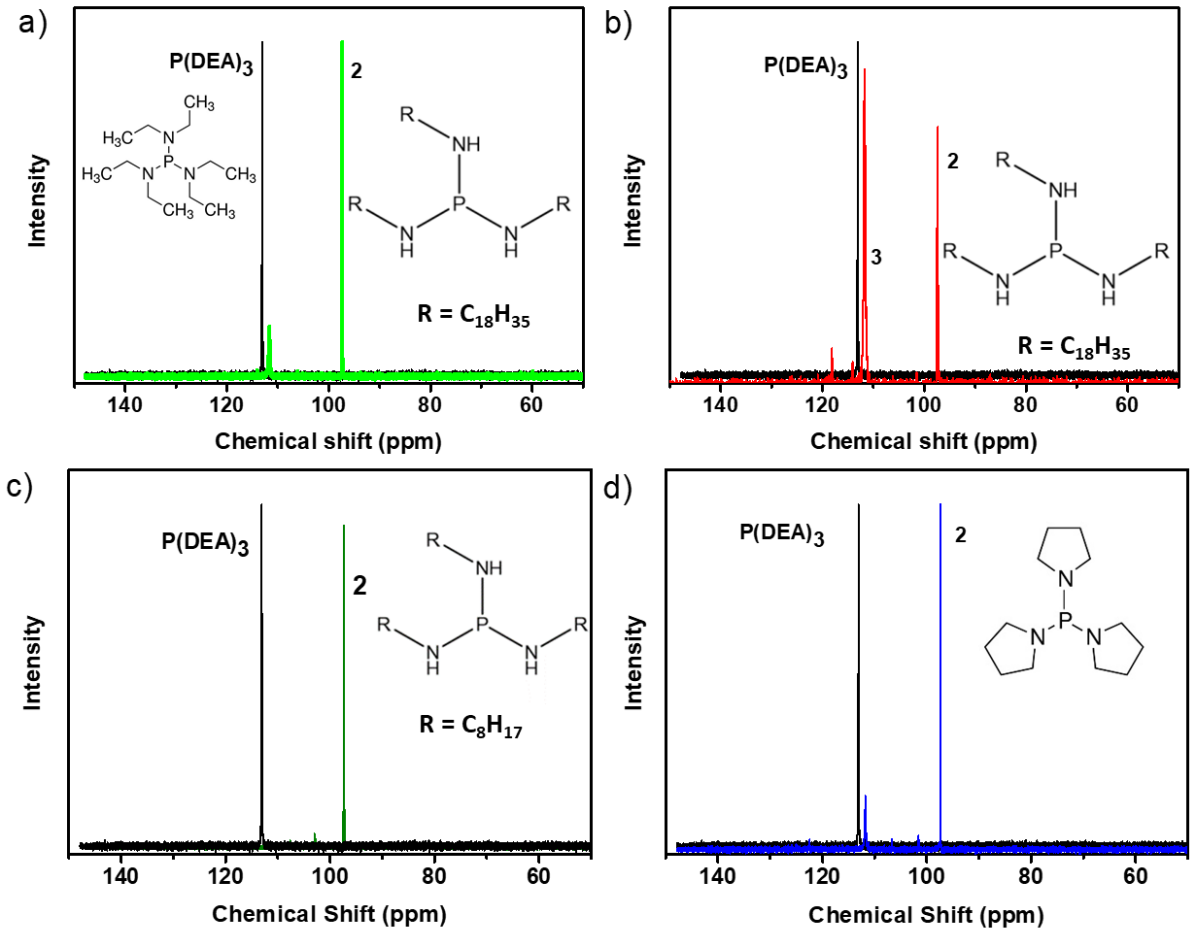

Figure 2.2: ^{31}P(proton-coupled) NMR spectra of the transaminated pre-prepared phosphorous precursors. (a) $P(NHR)_3$ (b) $P(NHR)_3$ and $P_2(NHR)_4(NR)$ (c) $P(OCA)_3$ and (d) $P(Pyrr)_3$. **2** symbolizes the trisubstituted aminophosphines, **3** (in b) the bisubstituted compound $P_2(NHR)_4(NR)$.

^{31}P NMR analysis

Figure 2.2a shows the ^{31}P NMR spectrum of $P(NHR)_3$. A shielded peak at 97 ppm compared to $P(DEA)_3$ (113 ppm) was observed confirming to the transamination reaction. Figure 2.2b shows the NMR spectra of the sample prepared at a lower reaction time (5-7 hours). In this case, two peaks at 111 ppm and 97 ppm were observed corresponding to the bisubstituted product $P_2(NHR)_4NR$ and the trisubstituted product $P(NHR)_3$ with a ratio of 3:2. Figures 2.2c and 2.2d show peaks at 97.2 ppm and 97.5 ppm corresponding to $P(OCA)_3$ and $P(Pyrr)_3$ respectively. All the peaks were assigned based on data from previous studies.[80, 82]

2.2.4.2. In precursor

The indium precursor was prepared inside a glove box. In a 100 mL bottle, 3 mmol $InCl_3$, 9 mmol $ZnCl_2$, 20 mL TOP and 50 mL previously degassed ODE were added. The reaction mixture was heated at 50 ^{o}C under magnetic stirring overnight.

2.2.4.3. ZnS precursor

Similar to the batch synthesis, the single molecular $Zn(DDTC)_2$ precursor was prepared for the flow synthesis. In a 100 mL bottle, 14 mmol $Zn(DDTC)_2$ and 70 mL previously degassed oleylamine were added inside a glove box. The reaction mixture was heated at 50 ^{o}C overnight to obtain a clear solution. It should be noted that the final solution turned muddy white in two weeks. Therefore, the solubility of the precursor was insured by stirring it for 30 min prior to usage to avoid any clogging in the tubes.

2.2.5. Characterization

Absorption spectra were measured on a Hewlett Packard 8452A UV-VIS spectrometer. The emission spectra were obtained using a Fluorolog FL3-22 spectrometer, which was equipped with 150 W xenon lamp (for steady-state measurements). A NanoLED laser diode from Horiba with a wavelength of 455 or 350 nm (1 MHz repetition rate) was used for time-correlated single-photon counting (TCSPC). Absolut photoluminescence quantum yield (PLQY) measurements were performed at room temperature using an integration sphere, Hamamatsu Quantaurus. Powder X-ray diffraction (XRD) patterns were recorded using a Bruker D8 powder diffractometer equipped with a copper anode (lKa1=1.5406 A, lKa2=1.5444 A) and an X' celerator 1D detector. The elemental compositions were analyzed using a Zeiss Ultra 55+ scanning electron microscope equipped with a Bruker QUANTAX energy dispersive X-ray (EDX) probe. The samples for XRD and EDX measurements were prepared by drop-casting concentrated InP QDs dispersed in toluene on a cleaned silicon substrate (disoriented Si for XRD). The substrate was kept under argon and toluene was allowed to evaporate. TEM grids were prepared by drop-casting nanocrystal suspensions onto a 400-mesh copper transmission electron microscopy grid covered with an ultrathin carbon film and the solvent was allowed to evaporate. Transmission electron microscopy was performed at cryogenic temperature and images were collected with an FEI Tecnai F20

microscope. For ^{31}P NMR spectroscopy, in a typical preparation, 50 μL of the sample and 500 μL of toluene *d8* were added to the NMR tube. ^{31}P (proton-coupled) spectra were collected on a Bruker NEO nanobay spectrometer at a frequency of 161.9MHz (50 scans, relaxation delay = 3 sec). Chemical shifts were internally referenced to H_3PO_4 (δ = 0 ppm).

2.3. Results and discussion

In an earlier attempt of continuous flow synthesis of InP QDs via the aminophosphine route in our laboratory, it was found that the use of tris(diethylamino)phosphine ($P(DEA)_3$) was not suitable in the flow reactor. It caused uncontrollable pressure rise during the synthesis due to the in-situ formation of diethylamine gas (*Eq. 2.1.*).[103] Besides safety issues, the gas formation during a flow synthesis causes inconsistent flow rates. To avoid these problems, we have pre-synthesized the transaminated P-precursor tris(oleylamino)phosphine ($P(NHR)_3$). The experimental details regarding the preparation of $P(NHR)_3$ are presented in Section 2.2.4.1.

$$InCl_3 + 4\,(PNEt_2)_3 + 12\,RNH_2\ (R= C_{18}H_{35}) \longrightarrow InP + 3P(NHR)_4Cl + 12\,HNEt_2\uparrow$$

Eq. 2.1

2.3.1. Batch syntheses: tris(diethylamino)phosphine/tris(oleylamino)phosphine

InP QDs were synthesized using tris(diethylamino)phosphine $P(DEA)_3$ via the standard hot-injection method. Four equivalents of $P(DEA)_3$ were swiftly injected into the reaction mixture containing $InCl_3$, $ZnCl_2$ and oleylamine at 180 ^oC. The role of zinc addition during the core synthesis will be discussed in the next section. Figure 2.3a shows the absorption spectra of the aliquots collected between 2-30 min of the reaction. A clear evolution of a well-defined excitonic peak can be observed in the absorption spectra, which is continuously tuned from 418 to 567 nm (Figure 2.3b) with the reaction time. The red shift in the first excitonic peak position is associated with the increase in the particle size with reaction time. To analyze the size dispersity, the line width (FWHM) of the first excitonic was calculated by fitting the absorption peak with a Gaussian function. Figure 2.3b shows the change in the line width of the absorption peaks of the aliquots collected at different reaction times. A clear decrease in the FWHM of the first excitonic from 87 to 59 nm can be observed with the increase in the reaction time. Figure 2.3c shows the UV-vis spectra of InP QDs synthesized using pre-prepared $P(NHR)_3$ in the same synthetic conditions as $P(DEA)_3$. The absorption spectra were taken by collecting the aliquots at different reaction times (1 – 45 min). Unexpectedly, the excitonic peak was only tuned from 430 to 556 nm during the reaction time when $P(NHR)_3$ was used as the P precursor. Moreover, the first excitonic became much broader in the case of $P(NHR)_3$ compared to $P(NEt_2)_3$. Comparing the FWHM of the absorption peak for the sample collected at 30 min, a significant increase (71 nm vs. 59 nm) was observed in the case of $P(NHR)_3$ (Figure 2.3d) implying a broader size distribution.

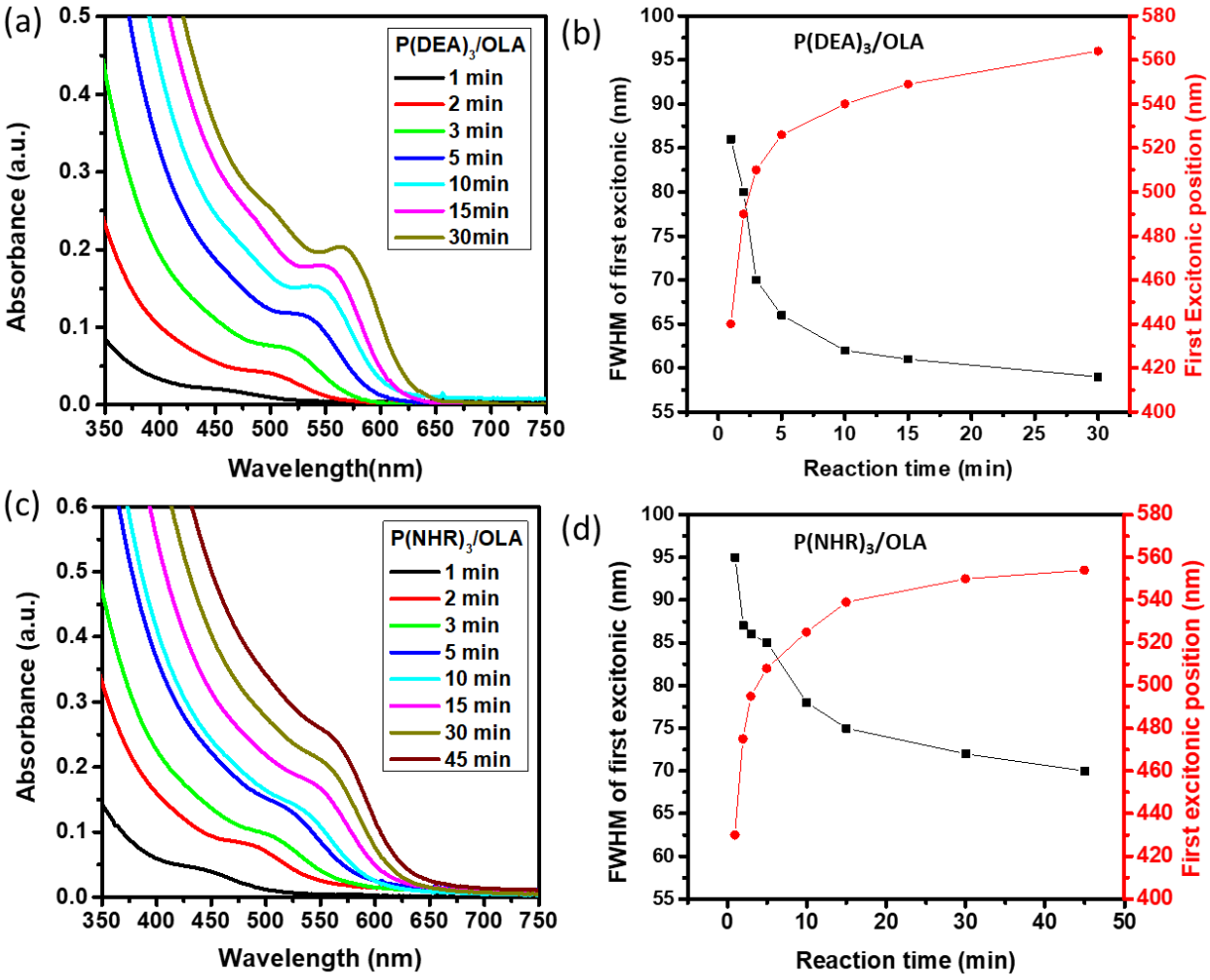

Figure 2.3: (a) Absorption spectra of InP QDs synthesized using $P(DEA)_3$ (standard aminophosphine synthesis). (b) The shift in the first excitonic peak position and change in the line width (FWHM) with the reaction time for InP QDs synthesized using $P(DEA)_3$. (c) Absorption spectra of InP QDs synthesized using pre-prepared $P(NHR)_3$. (d) Evolution of the excitonic peak position and the line width (FWHM).

2.3.1.1. Size evolution and chemical yield

In order to gain insight into the reaction kinetics, we calculated the particle size and chemical yield in the case of $P(NHR)_3$ and $P(DEA)_3$. The size is calculated from the following equation (*Eq. 2.2*) which correlates the first excitonic peak position and the size of the particles.[80, 104]

$$d = (-3.7707 * 10^{-12})\lambda^5 + (1.0262 * 10^{-8})\lambda^4 - (1.0781 * 10^{-5})\lambda^3 + (5.4550 * 10^{-3})\lambda^2 - (1.3122)\lambda + 119.9 \quad \textit{Eq. 2.2}$$

Where λ is the wavelength of the first excitonic peak determined from UV-vis spectra.

The chemical yield (CY) was calculated using an empirical formula (*Eq. 2.3*) which estimates the particle concentration.[80, 104] Since phosphorous was used in excess, In is the reaction limiting factor and therefore, the chemical yield was calculated with respect to indium. For the UV-vis measurements,

samples were directly collected from the reaction mixture without any purification process. A known amount of aliquot was taken and dissolved in a known amount of toluene to record the absorption spectra.

$$CY = \frac{A(350\,nm)}{[-1749.00465d^3 + (2.4413 * 10^6)d^2 - (9.00637 * 10^6)d + 1.05893 * 10^6]} * \frac{V_s * 16\pi R^3 * V_t}{V_a * 3a^3} \Big/ M(In)$$

$Eq.\ 2.3$

where A is the absorbance of the InP QDs at 350 nm wavelength, d is the diameter (nm) of the particles, V_s and V_a are the volumes (m^3) of the solvent and the aliquots respectively, V_t is the total volume of the synthesis, R is the radius of the particles, a is the lattice parameter and $M(In)$ is the molar amount of indium used in the synthesis. The calculated values were found to be in good agreement with analyses by inductively coupled plasma atomic emission spectroscopy (ICP-AES) measurements.

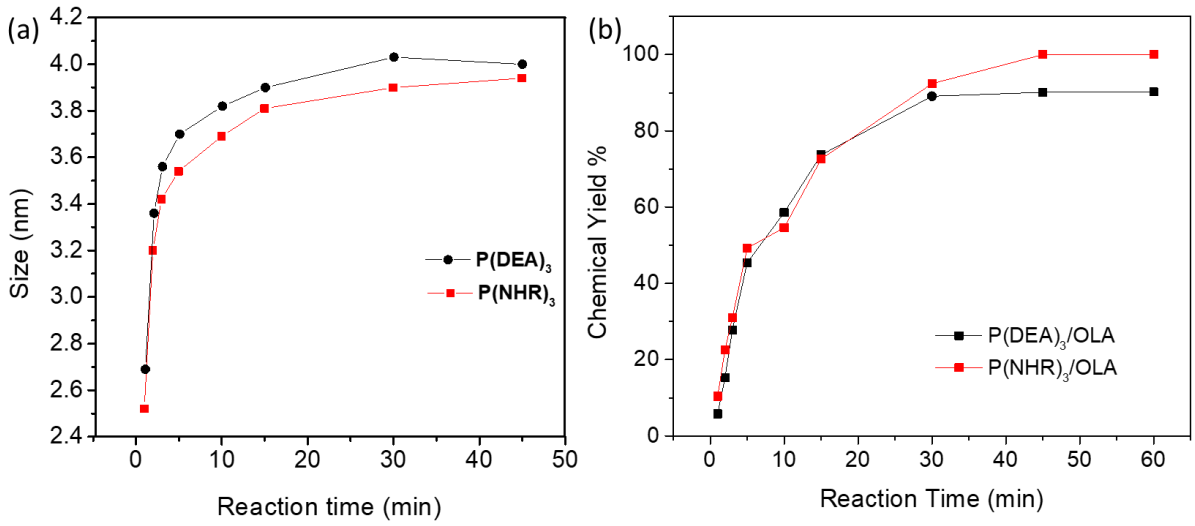

Figure 2.4: (a) Evolution of particle size and (b) Change in chemical yield with the reaction time of the InP QDs synthesized using $P(DEA)_3$ (black) and $P(NHR)_3$ (red).

Figures 2.4a and 2.4b show the increase in the size and the chemical yield of InP QDs prepared using $P(DEA)_3$ and $P(NHR)_3$ respectively. In both cases, a continuous increase in the particle size and the chemical yield was observed during the reaction. By comparing the particle size at early reaction times (0-2 min), we found that $P(NHR)_3$ produced smaller particles (2.5 vs 2.7 nm) with higher chemical yield (10 vs 5%). This indicates that $P(NHR)_3$ is more reactive leading to a rapid nucleation process of a larger number of nuclei followed by Ostwald ripening leading to size defocusing. Decoupling the transamination process before the nucleation stage might lead to faster reaction kinetics compared to $P(DEA)_3$ where in-situ transamination slows down the kinetics. After 30 min of the reaction, we observed a slight increase in the chemical yield reaching up to 98% in the case of $P(NHR)_3$ compared to 90% in the case of $P(DEA)_3$ again confirming the higher reactivity in the first case.

Figure 2.5 shows the X-ray diffraction patterns of InP QDs synthesized using $P(DEA)_3$ and $P(NHR)_3$. For both samples, the XRD pattern of InP QDs matches well the bulk InP reference (retrieved from JCPDS # 00-032-0452) suggesting a zinc blende structure. The XRD peaks are indexed to the (111), (220), and (311) reflections of the zinc blende cubic phase. The peak broadening is attributed to the small size (3 - 4 nm) of the InP QDs.

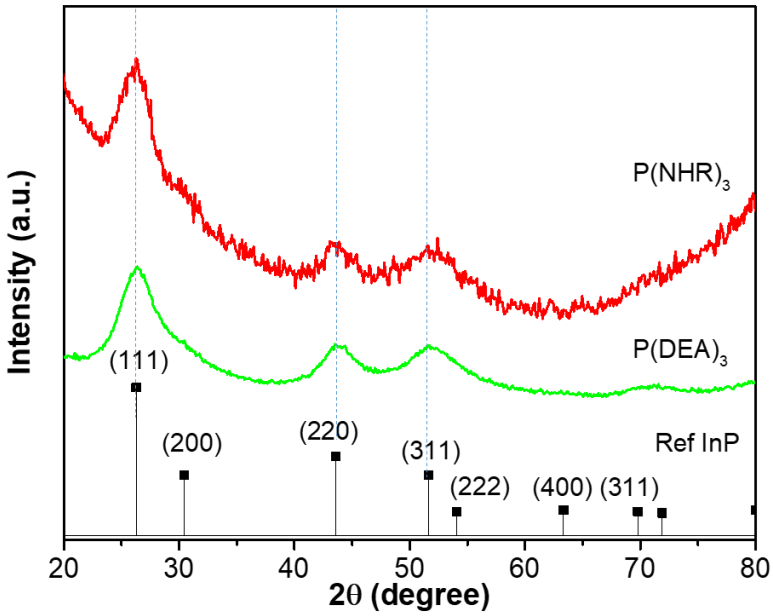

Figure 2.5: X-ray diffractograms of InP QDs synthesized using $P(DEA)_3$ and $P(NHR)_3$. The InP bulk reference retrieved from JCPDS # 00-032-0452 (black vertical lines) is given for comparison.

2.3.1.2. Effect of diethylamine addition

In the synthesis of InP QDs with $P(DEA)_3$, the formation of in-situ diethylamine gas is considered the driving force for the transamination reaction.[80] To study the effect of diethylamine presence on the reaction kinetics, we introduced diethylamine along with $P(NHR)_3$ in the reaction mixture during the synthesis. InP QDs were synthesized in two conditions where diethylamine was injected pre-nucleation and post-nucleation of InP. We found that the absorption spectra were blue-shifted when diethylamine and $P(NHR)_3$ were added together (Figure 2.6) compared to when only $P(NHR)_3$ was used suggesting a smaller-sized particle formation in the first case. Moreover, when diethylamine was added post nucleation (10-60 sec), slightly red-shifted (5-10 nm) absorption spectra were observed. However, in both cases, the size dispersity of the synthesized InP QDs remained broader than those obtained in the standard reaction with $P(NEt_2)_3$. These results suggest that the in-situ formation of diethylamine does affect the reaction kinetics of the InP QDs. Due to the very low boiling point (56 ^oC) of diethylamine, we were not able to further study the effect of diethylamine reactivity towards indium and phosphorous precursor.

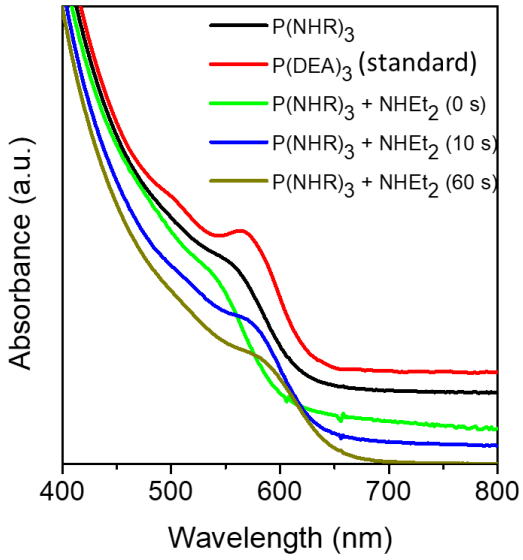

Figure 2.6: Absorption spectra of InP QDs synthesized using $P(NHR)_3$ and diethylamine. Diethylamine was added simultaneously (green), 10 sec after (blue) and 60 sec after injection of $P(NHR)_3$. Absorption spectra are shifted vertically for clarity.

2.3.1.3. Effect of amine-substituted species

As we have discussed previously, $P(DEA)_3$ undergoes rapid transamination upon injection into oleylamine at high temperatures. We performed a systematic study using ^{31}P NMR spectroscopy to gain real-time knowledge of the transamination and consumption process during the synthesis. For the ^{31}P NMR measurements, aliquots were collected at different reaction times ranging from 20 sec – 30 min after injection of $P(DEA)_3$. Shortly (0-2 sec) after the injection of $P(DEA)_3$, fully transaminated species $P(NHR)_3$ (**2**) and bisubstituted $P_2(NHR)_4(NR)$ (**3**) and $P_2(NHR)_4(NR)_2$ (**3'**) were observed at 97 ppm, 111 ppm and 181 ppm, respectively, in the ^{31}P NMR spectra (Figure 2.7a, Scheme 2.1). Figure 2.7b shows the change in transaminated species throughout the reaction. The percentage of different species is estimated from ^{31}P NMR spectra. Comparing the reactivity of species **2** and **3**, it is clear that species **3** is more reactive than species **2** since 26% (2*13%) of species 3 (vs 9% of species 2) is consumed during 2 min of the reaction.

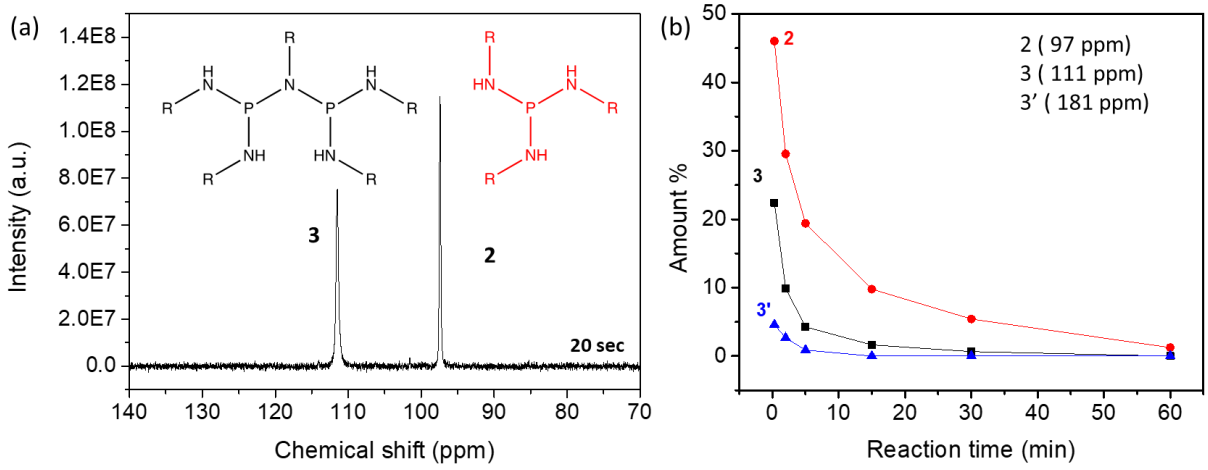

Figure 2.7: (a) Proton-coupled ^{31}P NMR spectra of the reaction mixture at 20 sec of the reaction after injection of $P(DEA)_3$ into the In precursor solution at 180 ^{o}C. (b) Change in the amount of transaminated P species **2, 3** and **3'** during the synthesis.

Next, we investigated the effect of the OLA:$P(DEA)_3$ ratio on the different transaminated species. Table 2.1 shows the change in the percentage when the ratio between $P(DEA)_3$ and oleylamine changed from 1:5 to 3:5. We can see that when the amount of $P(DEA)_3$ decreased, the formation of the fully transaminated species **2** is favored. Likewise an increase in species **3** can be observed with the increase in $P(DEA)_3$. We found that species **3'** was only formed in a very small amount (<8%) in all cases.

Table 2.1: Effect of $P(DEA)_3$ and oleylamine ratio on the amount of the transaminated aminophosphine species.

Ratio ($P(DEA)_3$/ OLA)	**181 ppm (3')**	**111 ppm (3)**	**97 ppm (2)**	**Ratio (2/3)**
1:5	5	29	66	2.3
2:5	6	39	55	1.4
3:5	8	45	47	1

In the literature, there have been many studies where two precursors with different reactivity were utilized for controlling the nucleation and growth of the particles. Recently, Cossairt et al. controlled the reaction rate of the InP QDs by employing $P(SiPh_3)_3$ and $P(SiMe_3)_3$ together.[62] They observed that when only $P(SiMe_3)_3$ was used, a broad size distribution resulted due to the poor control over nucleation and growth. On the contrary, when $P(SiPh_3)_3$ was combined with $P(SiMe_3)_3$, a clear LaMer-type growth was observed. It was suggested that the less reactive precursor acts as a monomer reservoir for the growth of the nuclei initially formed by the more reactive precursors. The standard synthesis of InP QDs with pristine aminophosphine $P(DEA)_3$ seems to follow the two-precursor behavior as observed in the ^{31}P NMR spectra where two different reactive species **2** and **3** are formed in situ. This explains why a broader size distribution was observed when only $P(NHR)_3$ was used in place of $P(DEA)_3$ as P

precursors. To confirm this point, we performed a control synthesis of InP QDs using a mixture of species **2** and **3**. The ratio between phosphorous and indium (P:In = 4:1) was maintained. Figure 2.8a shows the absorption spectra of InP QDs synthesized using a mixture of $P(NHR)_3$ and $P_2(NHR)_4NR$. Indeed, the first excitonic peak became sharper confirming a better size distribution. Moreover, the first excitonic was red-shifted from 560 to 590 nm compared to the case when only $P(NHR)_3$ was used (Figure 2.8b). It can be concluded that the ratio between species **2** and **3** strongly influences the reaction kinetics of the InP QDs and to achieve a better size distribution both species are required. Similar to the previous cases, we hypothesize that species **2** acts as monomer reservoir for the growth of the nuclei formed by the more reactive species **3** leading to better-controlled nucleation and growth than when only species **2** is used.

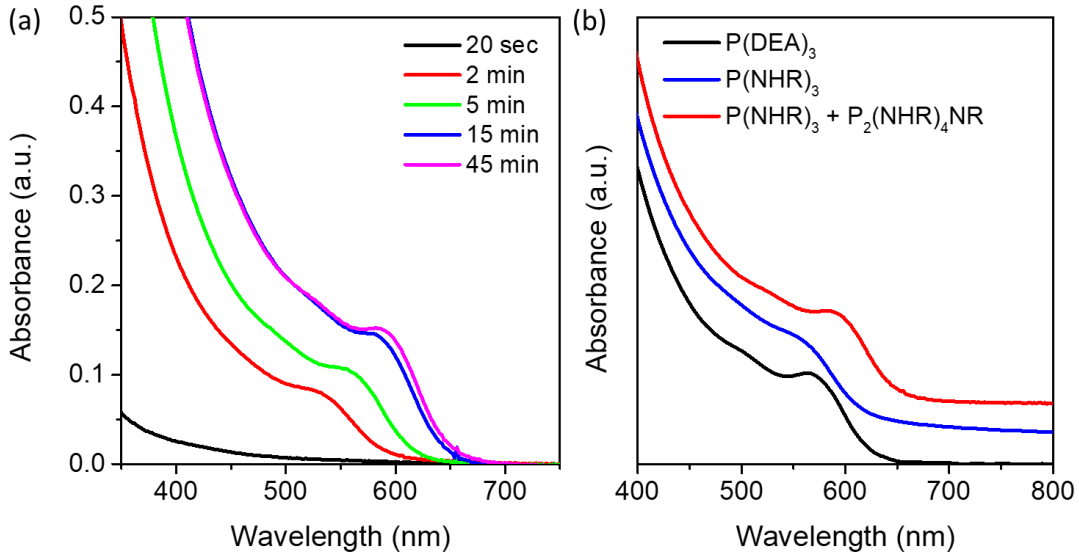

Figure 2.8: (a) Absorption spectra of InP QDs synthesized using mixture of $P_2(NHR)_4NR$ and $P(NHR)_3$ precursor. (b) Absorption spectra of InP QDs synthesized using $P(DEA)_3$, $P(NHR)_3$ and $P_2(NHR)_4NR$ + $P(NHR)_3$ for comparison.

2.3.1.4. Effect of Zn addition

Next, we studied the effect of zinc addition during the core InP synthesis. InP QDs with different In/Zn ratios were synthesized in similar reaction conditions by keeping the amount of $InCl_3$ the same while changing the amount of $ZnCl_2$. Figure 2.9 shows the absorption spectra of InP QDs prepared with and without $ZnCl_2$. It was observed that the first excitonic was blue-shifted after the addition of Zn similar to previous reports.[79] For $P(TMS)_3$-based syntheses of InP QDs, it was reported that Zn precursors form a stable intermediate complex with the P precursor, slowing down the reaction kinetics and producing smaller-sized particles with a better size distribution.[81] From absorption spectra (Figure 2.9) it can be observed that the addition of Zn strongly influences the size distribution as better pronounced excitonic features were observed for In:Zn = 1: 5. We point out that although 1-5 equivalences of $ZnCl_2$ were

added during the core synthesis, only 4-12 % of Zn was recorded in the EDX analysis of the final samples (Table 2.2).

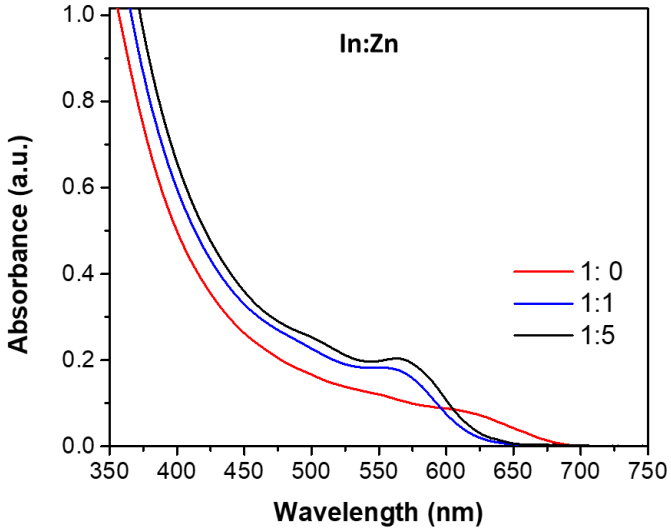

Figure 2.9: Absorption spectra of InP QDs synthesized using different In:Zn ratios.

Table 2.2: Effect of $P(DEA)_3$ and oleylamine ratio on the amount of the transaminated aminophosphine species.

Feed ratio of In:Zn	In (Atomic %)	P (Atomic %)	Zn (Atomic %)	Cl (Atomic %)
1:0	44	43	-	13
1:1	43	44	4	10
1:5	43	34	11	12

In accordance with the literature,[105] we also hypothesize that the refinement of the excitonic peak is partially due to the passivation of the surface traps by $ZnCl_2$, which also acts as a Z-type ligand. Unfortunately, due to the smaller size of the particles, we were not able to locate the zinc in the InP QDs. In studies done with $P(TMS)_3$, alloy formation was observed after addition of zinc carboxylate resulting in a shift of the XRD peaks to larger angles.[105-106] Since no change in XRD pattern was observed in our case and we carried out the reaction at comparably low temperature we conclude the formation of alloyed In(Zn)P did not take place. However, the possibility of surface doping cannot be excluded. In a detailed study of $P(TMS)_3$-based synthesis, Kirkwood et al. reported that in the majority of the cases, zinc was bound located on the surface of the QDs.[105] It was found that a small amount of Zn was doped into the InP lattices depending on the reactivity of the Zn precursor and the temperature. Considering the improvement in the size distribution, we decided to continue the addition of $ZnCl_2$ for our further study.

2.3.2. InP QDs synthesis in non-coordinating solvent

We have seen in the previous section that when tris(diethylamino)phosphine is injected into the reaction mixture, it undergoes in-situ transamination with the amines. Therefore, primary or secondary amines are obligatory for the formation of InP QDs via the aminophosphine route. Additionally, since amines are coordinating solvents, they coordinate with indium halide and zinc halide precursors during the synthesis making soluble complexes. Oleylamine, widely applied in NP synthesis,[107] is known to contain a number of impurities that can have a strong influence on the reaction behavior and reproducibility,[108] therefore, we attempted to replace it with alternative solvents. Since we already decoupled the transamination step by preparing tris(oleylamino)phosphine, using amines as a solvent is no longer an obligation. Using $P(NHR)_3$ as the P precursor provided us with the ability to investigate the influence of non-coordinating solvents such as octadecene (ODE) rather than oleylamine which until now, has remained a necessity for InP QD syntheses based on the aminophosphine route.

As the metal halides are not directly soluble in ODE, we added trioctylphosphine (TOP) to the reaction mixture to ensure the solubility of all the salt precursors. The lone pair of phosphorous in TOP, in principle, can coordinate with metals forming metal-TOP complex. Recently, in a $P(TMS)_3$-based synthesis, Peng et al. utilized TOP to prepare a TOP-In-$(stearate)_3$ complex to optimize the nucleation and growth of the InP QDs.[109] In addition, TOP has been widely used as ligand in various syntheses.[109-111] In the next section, the formation of In-TOP and Zn-TOP complexes will be investigated in detail.

2.3.2.1. In-TOP complex formation

Generally, indium is known to have four or six coordination number.[112] It has been seen previously that despite of being ionic in nature, $InCl_3$ does not dissociate while forming In-TOP complex.[112]

To investigate the coordination of TOP with the In metal center, five samples with the molar ratio of In:TOP = 1:0.5, 1:1, 1:2, 1:3 and 1:4 were prepared by stirring $InCl_3$, TOP and ODE in a vial at room temperature overnight. Next, we performed ^{31}P NMR experiments to study the interaction between $InCl_3$ and TOP. Figure 2.10 shows the ^{31}P NMR spectrum of the samples prepared using different In:TOP molar ratios. One reference sample with TOP was prepared for which a single peak at -32 ppm was observed in the ^{31}P NMR spectra (Figure 2.10). In the case of In:TOP = 1:0.5 the peak corresponding to TOP disappeared and a downfield-shifted single sharp peak was observed at 12 ppm corresponding to the complex **1** Cl_2-In-$(TOP)_2$. The observed downfield shift in NMR is attributed to the change in the electron density around the phosphorous of TOP due to its coordination with the In center. In the case of In:TOP = 1:1, a broad peak at –2 ppm was observed. We assigned this peak to the formation of the complex **3** Cl_3-In-$(TOP)_3$ because ^{31}P NMR becomes more shielded as a higher number of TOP was coordinated to In, which led to an increase in the electron density around phosphorous. The peak broadening was observed in the case of complex **3** which is attributed to the steric hindrance of the complex based on the previous study[112,109]. The samples obtained with In:P = 1:2, 1:3 and 1:4, the peak

at –2 ppm remained and a more downfield-shifted single sharp peak appeared at 37 ppm. We assign this peak to the complex **1** Cl_3-In-TOP. It should be noted that complex **1** and **2** are only formed in minor amount (< 5%) compare to complex **3**. For the sample using In:TOP = 1:3 and 1:4, a peak corresponding to non-coordinated TOP was observed at –31 ppm. The peak broadening and slight downfield shift are likely due to the interaction between free TOP and the $InCl_3$/TOP complex that stabilize the complex.[110]

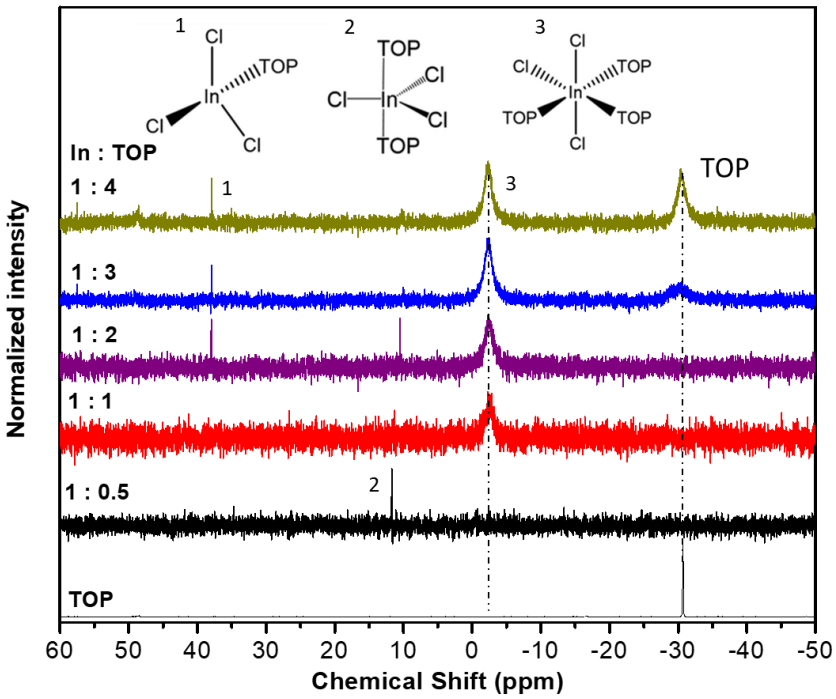

Figure 2.10: ^{31}P NMR spectra showing the evolution of In-TOP complex with the change in In:TOP ratios.

2.3.2.2. Zn-TOP complex formation

Similar to In-TOP, the Zn-TOP complex was also prepared using different molar ratios of Zn and TOP. In this case, we prepared two samples with Zn:TOP = 1:2 and Zn:TOP = 1:3 molar ratios. Figure 2.11 shows the ^{31}P NMR spectra of the evolution of the Zn-TOP complex with the change in the ratios of Zn and TOP. A downfield peak at -19 ppm can be observed for both samples associated with the formation of a Cl_2-Zn-$(TOP)_2$ complex. Moreover, in the sample prepared with a larger excess of TOP (Zn:TOP = 1:3), a stronger peak corresponding to free TOP can be observed at -32 ppm.

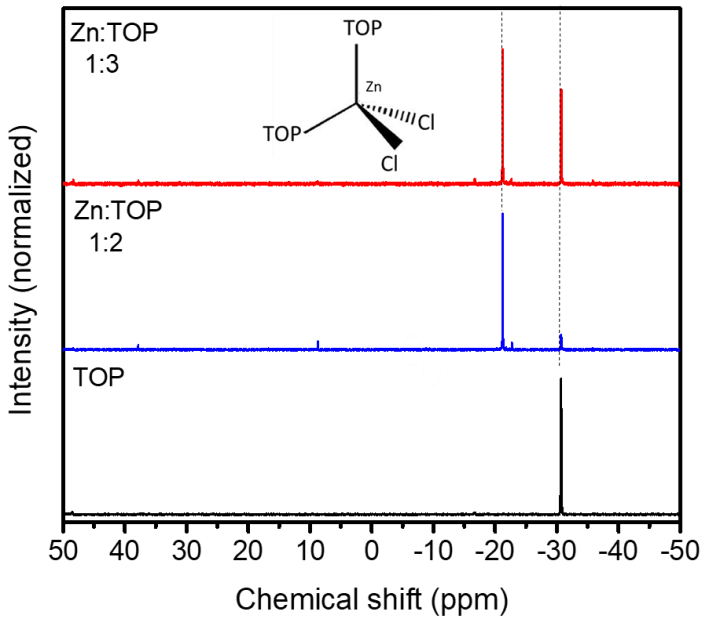

Figure 2.11: ^{31}P NMR spectra showing the formation of the Zn-TOP complex for different Zn:TOP ratios. The spectrum of free TOP is also given for reference.

2.3.2.3. Optical and structural properties

As discussed in the previous section, the problem of the insolubility of metal halides in ODE was solved by forming In-TOP and Zn-TOP complexes. Next, we performed the batch synthesis of InP QDs with the newly prepared In and Zn precursors in similar conditions to that of oleylamine and using $P(NHR)_3$ as the P precursor. Figure 2.12a shows the absorption spectra of the aliquots collected at different reaction times (1-60 min). An evolution of the excitonic peak position from 410 to 520 nm can be observed throughout the reaction time (Figure 2.12b). The absorption peak of the InP QDs prepared in ODE shows a blue shift of 40-47 nm compared to that of the InP QDs synthesized using oleylamine at 30 min of the reaction. It is noteworthy that after 30 min of the reaction no change in the absorption peak position was observed possibly due to the depletion of the In precursor. Importantly, unlike the reaction with oleylamine, the spectral shape was retained for longer reaction times (> 30 min), indicating that no Ostwald ripening occurred. The FWHM analysis of the first excitonic peak (Figure 2.12b) reveals that the size distribution of the synthesized InP QD was significantly improved compared to the reaction in oleylamine. Similar as before, we also performed an experiment with the mixture of $P_2(NHR)_4NR$ + $P(NHR)_3$, which had, however, no effect on the size distribution of the InP QDs. Nonetheless, a red shift in the absorption spectra from 520 to 570 was observed showing a similar trend as in the oleylamine case (Figure 2.12c).

The size and the chemical yield were calculated using the same method as explained earlier (section 2.3.1.1.). Figure 2.12d shows the change in the size and the chemical yield of the InP QDs with the reaction time. A continuous increase in the size can be observed from 2.1 to 3.5 nm, concomitant with the increase in the chemical yield (3-88%). Compared to the reaction with oleylamine, smaller-sized

particles (3.5 vs 3.9 nm) were obtained in the case of ODE. In the latter case, the smaller size can be attributed to the binding of TOP on the InP surface which slows down the particle growth. If we compare the size at lower reaction time (0-5 min) for OLA/$P(NHR)_3$ and ODE/$P(NHR)_3$, it becomes evident that the nucleation and growth processes are better controlled in the case of ODE/$P(NHR)_3$ resulting in better size distribution.

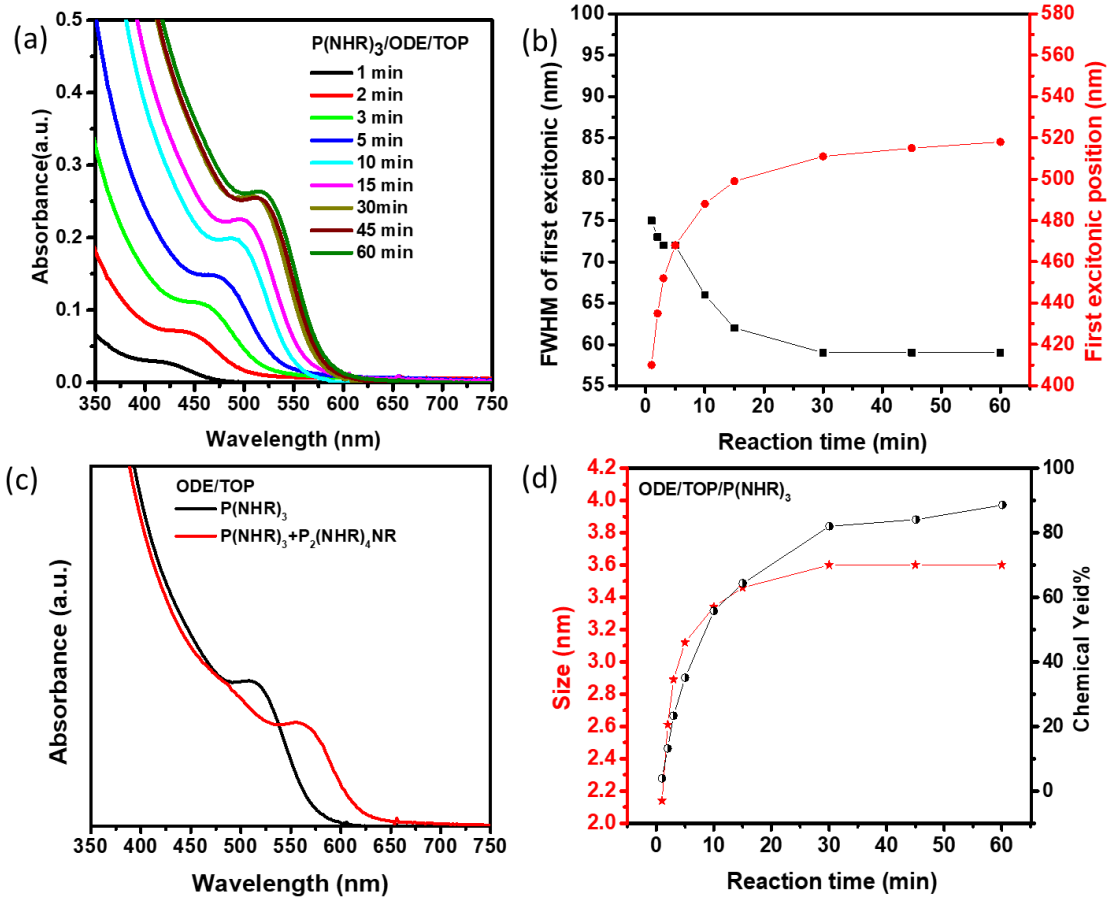

Figure 2.12: (a) Absorption spectra of InP QDs synthesized using $P(NHR)_3$ in ODE/TOP. (b) Change in FWHM and the position of the first excitonic with reaction time. (c) Absorption spectra of InP QDs synthesized using $P_2(NHR)_4NR$ + $P(NHR)_3$. (d) Change in the particle size and the chemical yield of InP QDs with reaction time.

Figure 2.13a shows the TEM image of InP QDs synthesized using $P(NHR)_3$ in presence of TOP and ODE. The calculated average size is 3.5 ± 0.5 nm showing a narrow size distribution (14%). It should be noted that no size-selective precipitation was performed prior to the TEM measurements. The size obtained from TEM is in good agreement with the value determined from the calculation using the absorption peak. Figure 2.13b shows the X-ray diffraction pattern of the InP QDs where all the peaks well matched with the given reference for bulk InP retracted from JPCDS # 00-032-0452. The pronounced peaks corresponding to the (111), (200), (220), and (311) planes in XRD confirm that the InP QDs have the zinc blende cubic crystal structure.

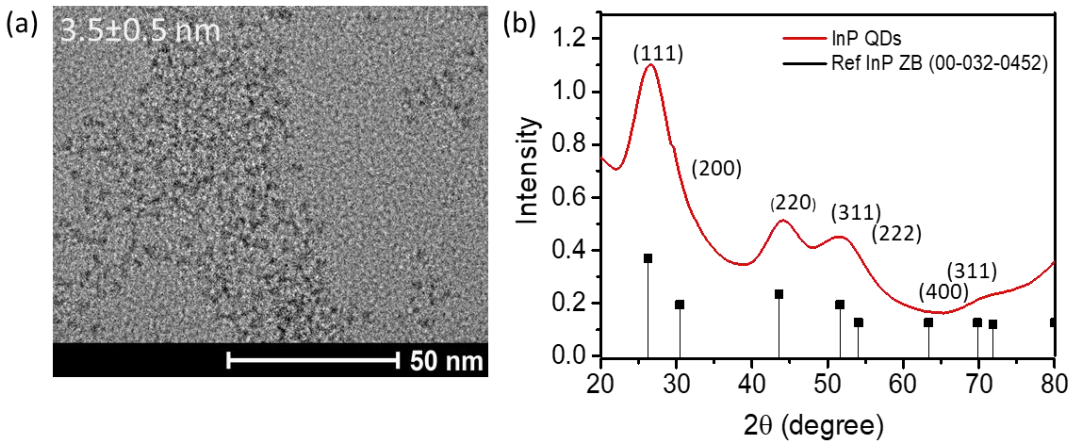

Figure 2.13: (a) Transmission electron microscopy (TEM) image of InP QDs synthesized in ODE/TOP. (b) XRD of the InP QDs synthesized in ODE/TOP. The bulk reference JCPDS # 00-032-0452 (vertical line) is given for reference.

2.3.2.4. Effect of the $P(NHR)_3$ derivatives

Different aminophosphine derivatives could be used to adjust the reaction kinetics of the InP QDs formation. The chain length of the amines influences their steric hindrance and reactivity with the indium precursor. Two transaminated P-precursors were prepared by reacting $P(NEt_2)_3$ either with octylamine or with the secondary cyclic amine pyrrolidine affording, tris(octylamino)phosphine ($P(OCA)_3$), and tris(pyrrolidinyl)phosphine ($P(Pyrr)_3$). It should be noted that for simplicity, the abbreviations OCA and Pyrr were used here for the deprotonated substitutents. The synthesis of InP QDs was performed in similar reaction conditions as with $P(NHR)_3$ and the ratio between In and P was kept the same. Figure 2.14a shows the absorption spectra of the InP QDs synthesized using $P(OCA)_3$. A red shift in the absorption spectra was observed implying the formation of a larger-sized particles. However, the size distribution is broader than with $P(NHR)_3$ as the absorption spectral features became less pronounced. In the case of $P(Pyrr)_3$, syntheses at lower temperature (< 200 °C) do not yield InP QDs. In a synthesis performed at 220 °C, a red color product was formed after injection of $P(Pyrr)_3$, however, the as-prepared InP QDs were not colloidally stable and stuck to the bottom of the reaction flask (Figure 2.14b). Due to this solubility issue, no further characterization could be performed for the samples obtained in this case.

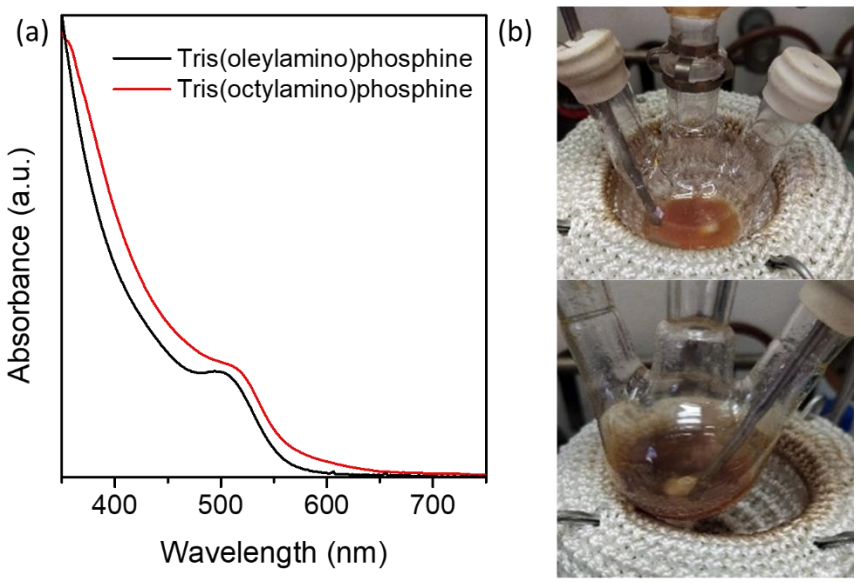

Figure 2.14: (a) Absorption spectra of InP QDs synthesized using tris(octylamino)phosphine ($P(OCA)_3$) in comparison with tris(oleylamino)phosphine ($P(NHR)_3$). (b) Photograph of the reaction flask after the synthesis using tris(pyrrolidinyl)phosphine ($P(Pyrr)_3$).

2.3.3. Batch optimization of the InP/ZnS core-shell synthesis

As synthesized InP QDs show very low photoluminescence (PL) (< 1%). InP QDs prepared with aminophosphines are well known for their surface defects responsible for non-radiative recombination (PLQY<1%). Generally, surface passivation with larger band gap semiconductor materials (ZnSe, ZnS, GaP) is an effective strategy to overcome this problem. Tessier et al. achieved up to 60% PLQY after ZnS and 50% PLQY after ZnSe shell growth with a comparably narrow linewidth of 46-63 nm.[78] The most popular approach for ZnS shell growth utilizes zinc carboxylate precursors (e.g., zinc stearate or oleate) and elemental sulfur in tertiary phosphines (e.g., TOP) or thiols (e.g., dodecanethiol) and require the use of comparably high temperatures (220 – 300 °C) due to the low reactivity of these precursors. The main problem with the abovementioned zinc precursors is that they are very viscous or solid at room temperature and hence not suitable for flow chemistry. Therefore, we decided to use the single molecular zinc diethyldithiocarbamate ($Zn(S_2CNEt_2)_2$/$Zn(DDTC)_2$) precursor which is soluble at room temperature in oleylamine. $Zn(DDTC)_2$ contains four S atoms and one Zn atom, and therefore, generally zinc stearate or zinc acetate are added to balance the ratio.[113] However, in our case, we already added excess $ZnCl_2$ during the core synthesis and hence we did not add any additional zinc precursor. Figure 2.15a and 2.15b show the absorption and PL emission spectra of InP/ZnS QDs where ZnS shelling was performed using a heat-up method with a slow heating rate of 2 °C/min to avoid any secondary nucleation of ZnS. Three aliquots were collected at 140, 180 and 200 °C respectively. A red shift of 10 nm was observed in the absorption spectra for the aliquot collected at 140 °C, indicating the leakage of exciton in the shell layer. The enhanced sharpness of the first excitonic peak can be attributed to the

passivation of shallow surface trap states after ZnS deposition (Figure 2.15a). The improved passivation also leads to a strong increase in the PL intensity (Figure 2.15b). We found that the absorption spectra systematically started to blue-shift for aliquots collected at higher temperatures (>180 °C). Similar to the absorption spectra, a blue shift was also observed in the PL spectra for the samples collected at 180 and 200 °C. Additionally, a spectral broadening was observed for the aliquots collected at 180 and 200 °C compared to that of 140 °C. These results suggest that at higher temperature, Zn starts to diffuse into the lattice of the InP core leading to an increase in the energy band gap.[114] Alternatively, the blue-shift could be explained by the compressive strain exerted by the ZnS shell (having a smaller lattice constant than InP) on the InP core. The spectral broadening is attributed to particle-to-particle variations in the shell thickness.

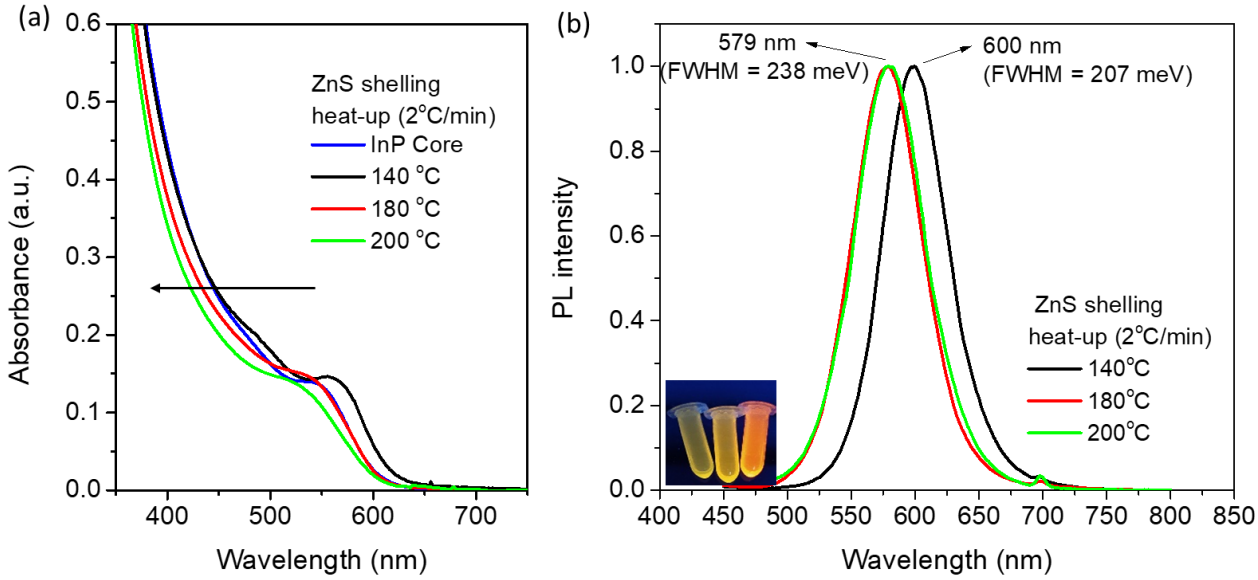

Figure 2.15: (a) Absorption and (b) PL spectra of InP/ZnS QDs synthesized at different ZnS shelling temperatures.

In the following, ZnS shelling was optimized at lower temperature to minimize the spectral broadening. Figure 2.16a shows the absorption and emission spectra of InP/ZnS QDs synthesized at 160 °C and 2 hours of the ZnS shelling time. Up to 52% of PLQY, a FWHM of 59 nm and Stokes shift of 147 meV were recorded for the InP/ZnS QDs synthesized using the optimized conditions. These values are similar to the state of the art for InP/ZnS QDs prepared with the aminophosphine route.[78, 87]

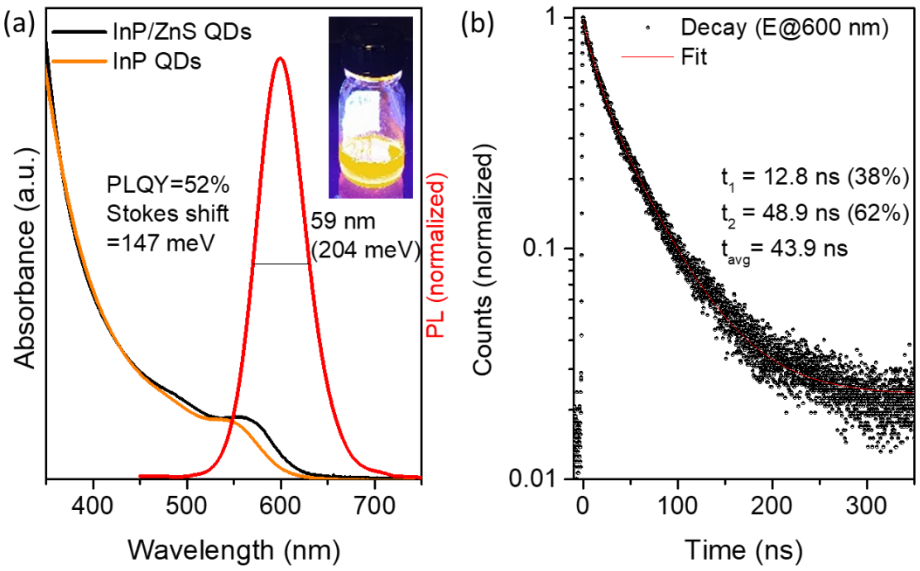

Figure 2.16: (a) Absorption and PL spectra of InP/ZnS QDs synthesized using the optimized conditions. (b) PL decay curve of the obtained InP/ZnS QDs.

Next, we carried out time-resolved photoluminescence (TRPL) measurements of the InP/ZnS to study the PL decay kinetics. For the TRPL measurements, the sample were excited by a pulsed NanoLED with a wavelength of 350 nm, and the decay was monitored at the 600 nm emission wavelength. The PL decay curves were fitted with a bi-exponential function:

$$Y(t) = A_1 \, exp\left(-\frac{t}{\tau_1}\right) + A_2 \, exp\left(-\frac{t}{\tau_2}\right) \qquad \textit{Eq. 2.4}$$

where τ_1 and τ_2 correspond to decay time constants and A_1 and A_2 are the respective amplitudes. The average lifetime (τ_{avg}) was calculated using the following equation (*Eq. 2.5*).[115]

$$\tau_{avg} = \frac{A_1{\tau_1}^2 + A_2{\tau_2}^2}{A_1\tau_1 + A_2\tau_2} \qquad \textit{Eq. 2.5}$$

It is evident from Figure 2.16b that the decay follows a bi-exponential nature combining a shorter decay (12.9 ns) and longer decay pathway (48.9 ns). The shorter decay is indicative of surface trap decay channels whereas longer decay time is assigned to intrinsic band-edge transitions.[116] The calculated average lifetime (43.9 ns) is in agreement with the previous studies of InP/ZnS QDs.[113]

2.4 Continuous flow synthesis of InP QDs

Continuous flow synthesis of InP QDs was attempted applying the batch-optimized protocol using $P(NHR)_3$ as the P precursor and ODE as the solvent. The continuous flow setup is shown in Figure 2.1 (section 2.2.3.). Before moving to larger (gram-) scale-scale production, we performed several tests at smaller scale (2 mL synthesis volume) to further optimize the reaction conditions in the flow synthesis. In this case, two automated injectors were used to feed the In and P precursors. Previously degassed

ODE was filled in the pressurized bottles connected to the pumps and a 20-bar argon line was attached to the system to insure the inert conditions and provide the required pressure (used values in these experiments: 0-10 bar). We used ODE for cleaning the system before and after each experiment. Next, the In and P precursor were injected into the tubular stainless steel heater (inner diameter: 1 mm) after insuring the molar ratio of both precursors (In:P = 1:4). All the experiments were performed in the automatic mode where the system automatically adjusts the flow rate depending on the programmed residence time (= reaction time).

2.4.1. Effect of the flow configuration

As shown in Figure 2.16a and 2.16b, two types of configurations (1 and 2) can be chosen for the flow syntheses. In configuration 1, the indium and phosphorous precursors are premixed and then the mixed solution is injected into the heater in a single flow pipe (heat-up method). In configuration 2, both precursors are mixed within the heater (hot-injection method). We found that flow configuration 2 requires a high flow rate to achieve good mixing. As an example, in the case where the In and P precursors were prepared with same the concentration, the flow rate for P was reduced by 4 times to ensure the P:In = 4:1 ratio, which is needed for high chemical yield. In this case, very broad and blue-shifted absorption spectra were observed due to the insufficient mixing of the precursors. To avoid this problem, we pre-prepared the In and P precursors with a 1:4 ratio of concentrations and maintained the same flow rate for each of them. For both configurations, the solubility of the In and P precursors was controlled prior to the flow synthesis to avoid any clogging in the flow pipes. Figure 2.16c shows the absorption spectra of the InP QDs prepared using configuration 1 and configuration 2. In both cases, well-defined excitonic peaks and dark red products were observed characteristic of InP QDs (Figure 2.16d). We found that in the case of configuration 2 a slightly better size distribution was observed as the FWHM of the first excitonic was reduced from 63 to 61 nm. Moreover, we observed that the first excitonic peak position was blue shifted from 516 nm to 480 nm in configuration 2, indicative of the formation of smaller-sized particles. This behavior can be attributed to the precursor mixing at high temperature where a burst nucleation occurred leading to smaller-sized QDs.

The above results also suggest that adequate mixing of the precursors was achieved with our continuous flow system, which has been reported to be problematic in flow syntheses.[99-101]

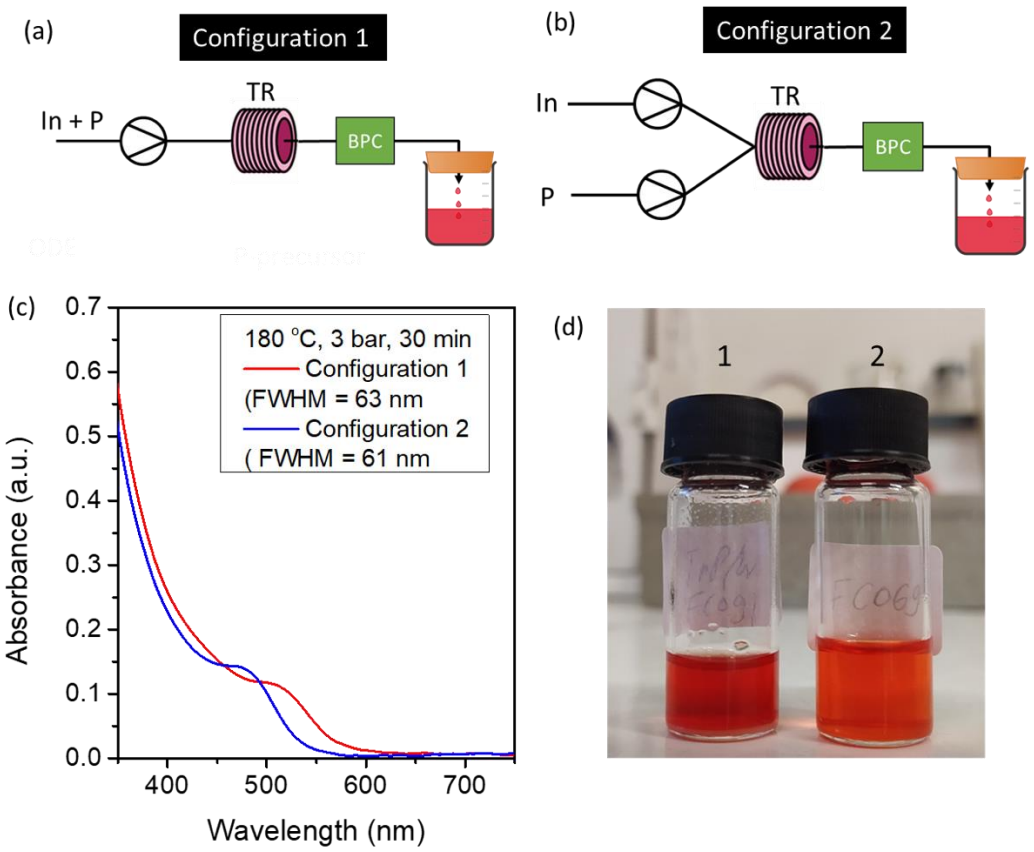

Figure 2.16: (a) and (b) Flow charts of configurations 1 and 2, respectively (TR: tubular reactor, BPC: back pressure controller). (c) Absorption spectra of InP QDs obtained using flow configurations 1 and 2 using a temperature of 180 °C and a pressure of 3 bar. (d) Photograph of as-prepared InP QDs under normal light.

2.4.2. Effect of the reaction conditions

Next, we investigated the effect of temperature on the reaction kinetics of the InP QDs. The InP QDs synthesis was tested at 160-220 °C while keeping the same residence time and pressure. We found that higher temperature promotes larger particle sizes as the corresponding absorption spectra red-shifted with the increase in the temperature (Figure 2.17a). However, at the same time, a broadening of the absorption spectra was observed due to a rapid nucleation rate at the higher temperature (>200 °C) followed by rapid dissolution of the formed QDs and leading to ripening-type growth.[80] Therefore the optimal temperature of 180 °C as optimized for batch experiments was chosen for further studies. Next, we tested the effect of the pressure on the reaction kinetics. It should be noted that this parameter has not been possible to be studied in batch. Figure 2.17b shows the absorption spectra of the InP QDs synthesized under 0-9 bar at 180 °C and 30 min of residence time. To our surprise, we only observed a slight red shift in the absorption spectra with an increase in the pressure. The size distribution remained unaffected suggesting that pressure does not play a significant role in the reaction kinetics of the InP QDs. Figures 2.17c and 2.17d show typical heating and pressure profiles during the flow synthesis, exhibiting great uniformity.

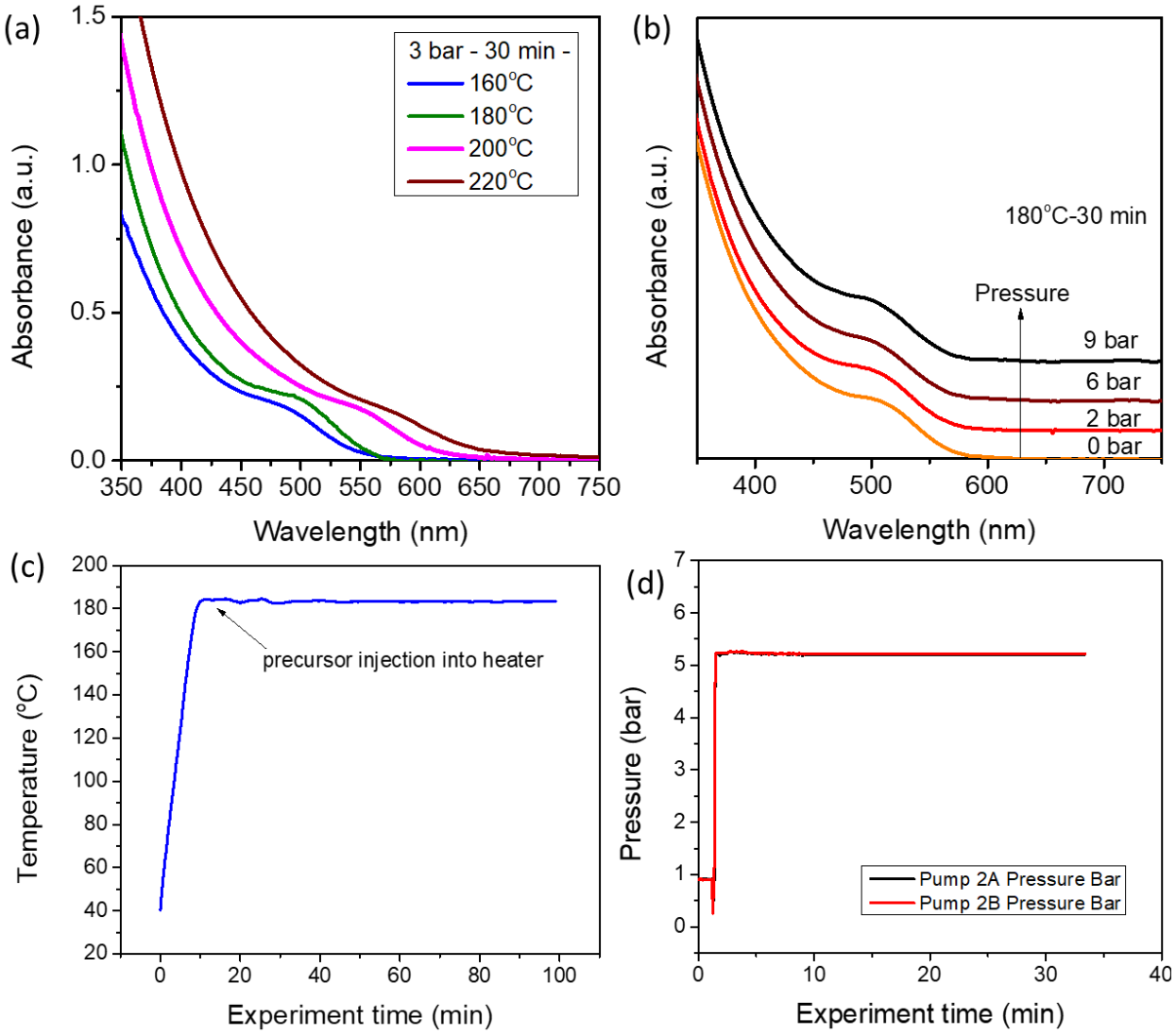

Figure 2.17: (a) Absorption spectra of InP QDs synthesized at 160-220 °C. (b) Absorption spectra of InP QDs synthesized using a pressure of 0-9 bar. (c) and (d) temperature and pressure profiles recorded during the continuous flow synthesis of the InP QDs.

2.4.3. Effect of In to Zn ratio

Similar to the batch synthesis, we also tested the influence of the Zn addition during the core synthesis in the continuous flow synthesis of the InP QDs. The sample prepared without zinc addition shows a very broad absorption shoulder (Figure 2.18). As we increased the amount of zinc from Zn:In = 1:1 and 3:1, a clear improvement of the first excitonic peak feature can be observed demonstrating a better size distribution. These results are similar to what we have observed in the batch reactions. It should be noted, however, that higher ratios than Zn:In = 1:3 could not be prepared due to the saturation of the mixture where Zn starts to settle down at the bottom of the bottle at room temperature. We have seen in the batch synthesis that, in accordance with the literature, a Zn:In ratio of 6:1 is required for obtaining the best results in terms of size distribution.

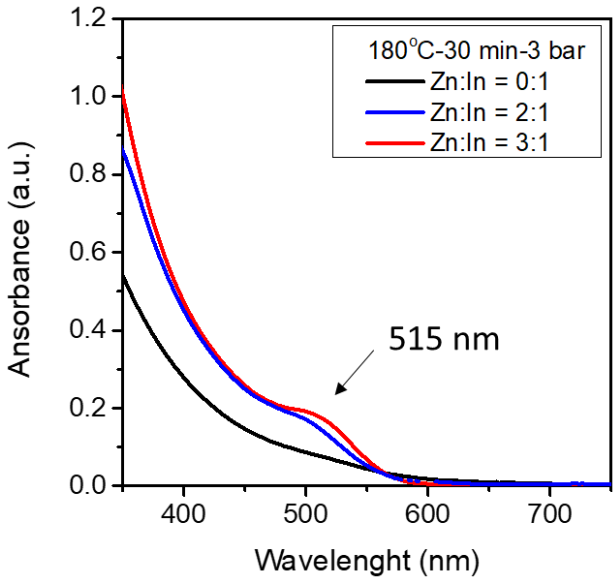

Figure 2.18: Absorption spectra of InP QDs synthesized using different ratios of Zn and In; Zn:In = 0:1 (black), Zn:In = 2:1 (blue) and Zn:In = 3:1 (red).

2.4.4. Dilution and reproducibility

To study the influence of the concentration on the size, we prepared two precursors; one with the same concentration as in the batch synthesis (0.04 mol/mL) and another with a dilution to the half of this concentration (0.02 mol/mL) by adding ODE. Similarly, two concentrations of the phosphorous precursors were also prepared. Figure 2.19a shows the absorption spectra of the InP QDs synthesized using the above-mentioned dilutions. By comparing the absorption spectra, we observe that the first excitonic peak is slightly blue shifted suggesting smaller-sized particles formation in the case of the diluted precursors. Moreover, in the case of the dilution a size broadening was observed as the absorption peak become less defined. Next, we checked the reproducibility of the synthesis, which was not easy to achieve in the batch synthesis due to poorer control of the reaction temperature. Figure 2.19b shows the absorption spectra of two different syntheses performed while keeping all reaction parameters the same, demonstrating the high reproducibility of the flow synthesis.

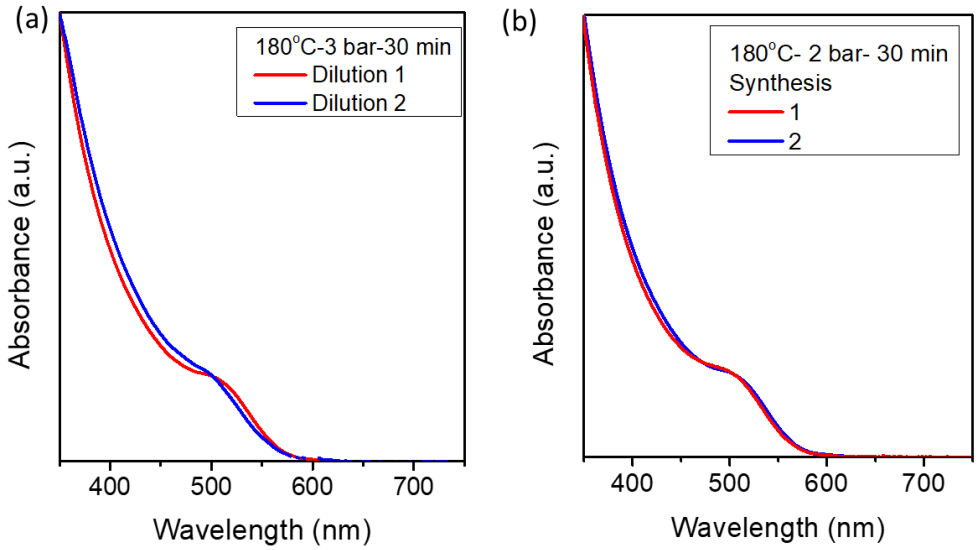

Figure 2.19: (a) Absorption spectra of InP QDs synthesized using two different dilutions of the precursors (dilution 1: standard conditions; dilution 2: diluted by a factor of 2). (b) Absorption spectra of two different batches of InP QDs synthesized using the same reaction conditions with the continuous flow setup, demonstrating high reproducibility.

2.4.5. Optimized continuous flow synthesis of InP QDs

After optimizing the flow configuration, pressure and temperature, we tuned the particle size by varying the residence time/flow rate. Figure 2.20a shows the UV-vis spectra of the InP QDs prepared by changing the residence time from 10-120 min. With the change in the residence time, the excitonic peak can be tuned from 466 nm (10 min) to 562 nm (120 min) similar to the batch synthesis. Figure 2.20b shows the X-ray diffractogram of the obtained InP QDs. The XRD peak positions corresponding to the (111), (200), (220), and (311) planes are in agreement with the bulk InP reference confirming that the InP QDs exhibit the zinc blende crystal structure. The observed broadening of the peaks is expected due to the significantly smaller crystallite size in the QDs compared to the bulk reference. Figure 2.20c and 20d show TEM images of the synthesized InP QDs exhibiting a spherical shape. The size analysis from TEM (Figure 2.20e) reveals that the obtained size distribution is with 17% (3.5±0.6 nm) slightly broader than with the batch synthesis (14%), in agreement with the slightly broader features in the absorption data.

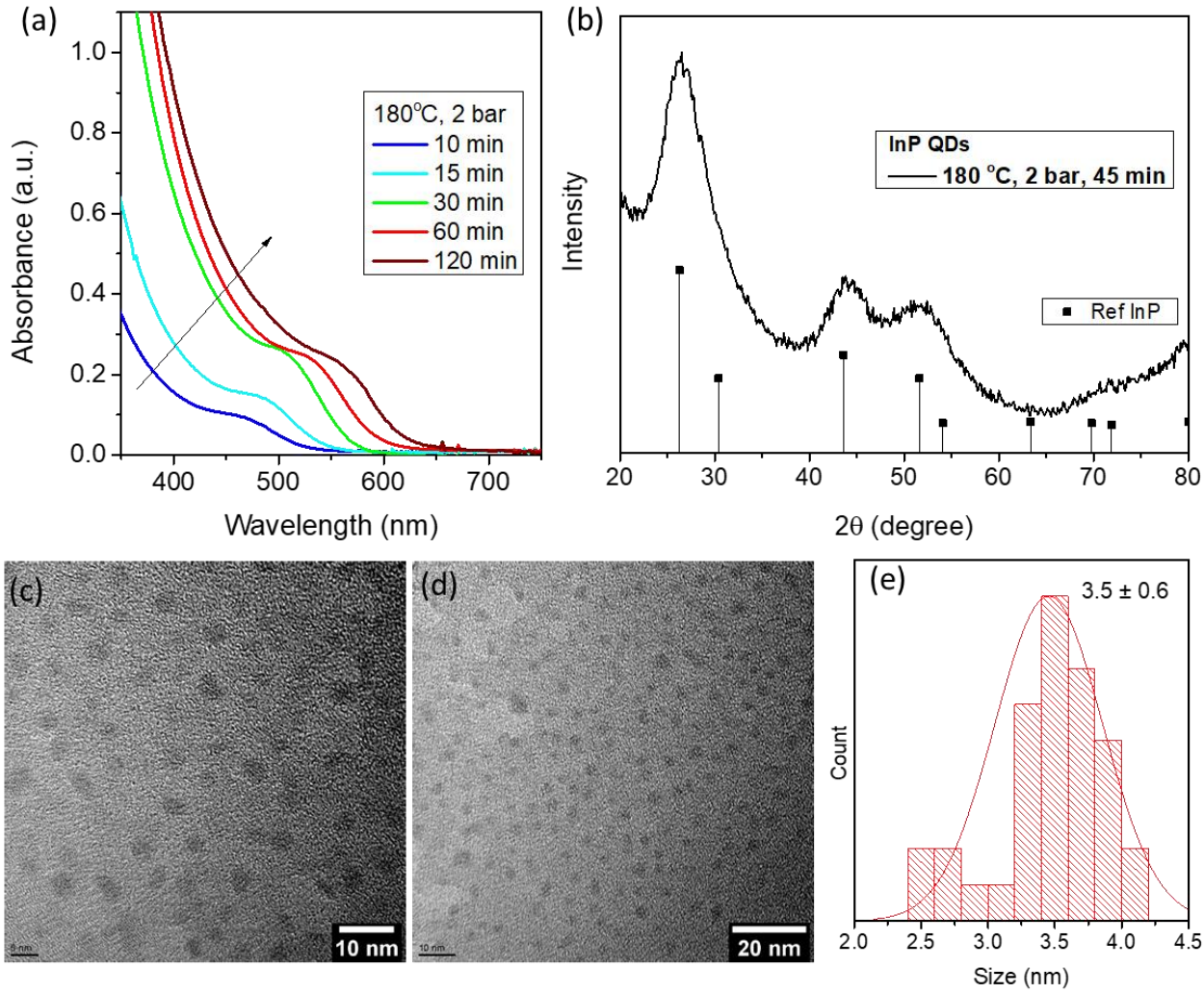

Figure 2.20: Absorption spectra of InP QDs synthesized with optimized conditions via the continuous flow route. (b) X-ray diffraction pattern of the obtained InP QDs after 120 min. The data of bulk InP (PDF # 00-032-0452, vertical lines) is given as reference. (c), (d) and (e) TEM images and size histogram of the as-prepared InP QDs.

2.4.6. Optimization of the ZnS shelling in flow synthesis

Similar to the batch synthesis, InP/ZnS QDs were synthesized using the $Zn(DDTC)_2$ precursor. InP/ZnS QDs were prepared in flow using configuration 2 where the shell precursor and the InP core QDs were separately injected into the heater. We targeted to develop the InP/ZnS core/shell structure in fully continuous manner for the large-scale production. Figure 2.21a shows that the emission intensity increased with the shelling time similar to the batch. Figure 2.21b shows the absorption and normalized PL spectra of InP/ZnS QDs. A redshift in the absorption spectra from 472 nm to 488 nm was observed after one hour of the ZnS shell growth and strong green emission was detected under UV-vis light. In the PL spectra, an emission peak at 528 nm with FWHM of 63 nm/278 meV was observed. We also observed a less intense peak around 425 nm, which probably originated from the defect emission of separately formed ZnS NPs or from the ZnS shell.[116] An increase in the absorbance of the InP/ZnS QDs can also be observed at higher energy, which can be due to the growth of the ZnS shell but would also

be observed due to the formation of ZnS NPs. The latter may be favored by the addition of the $Zn(DDTC)_2$ precursor into the heater at high temperature. To avoid this problem, a T-shape connector was added just before the heater to premix the InP core and the $Zn(DDTC)_2$ precursor. However, due to the high viscosity of the $Zn(DDTC)_2$ precursor incomplete mixing was observed resulting in poor PLQY (<10%) and significantly broad emission line widths (> 100 nm). Therefore we decided to mix the InP and $Zn(DDTC)_2$ precursor directly into heater for further experiments.

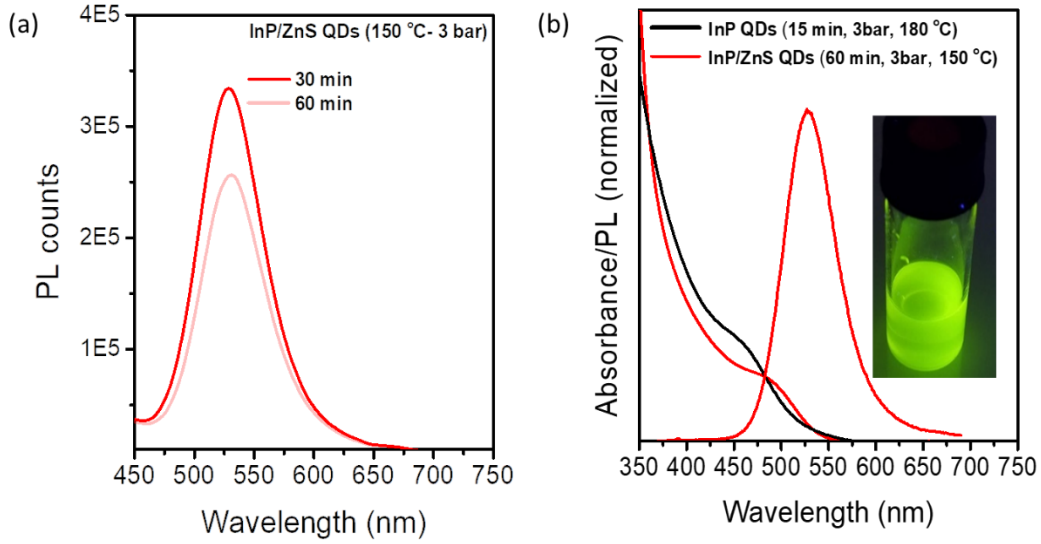

Figure 2.21: (a) Photoluminescence spectra of InP/ZnS core-shell QDs prepared with different shelling residence times. (b) Absorption and PL spectra of InP/ZnS QDs synthesized with configuration 2 along with a photograph of the InP/ZnS QDs (60 min shelling time) sample under UV light.

2.4.7. Larger-scale synthesis of InP/ZnS quantum dots

Finally, after the described optimizations of the flow synthesis of InP QDs and InP/ZnS QDs, we moved towards the gram-scale synthesis of InP/ZnS QDs in a fully continuous manner. To do so, a third configuration was installed where the automated injectors were replaced by pumps to be able to inject larger volumes continuously, and with respect to the core synthesis setup, an additional pump and heater were installed for the subsequent shell synthesis. The stock solutions of the precursors were directly added into pressurized bottles connected to the pumps. Figure 2.22 shows the configuration 3, in which first two pumps containing indium and phosphorous precursors were connected to the first heater 1, which was connected to another heater 2. Between both, another pump containing the $Zn(DDTC)_2$ precursor was added. In this way, the formed InP core QDs and the $Zn(DDTC)_2$ precursor were directly injected into heater 2 for the shell growth.

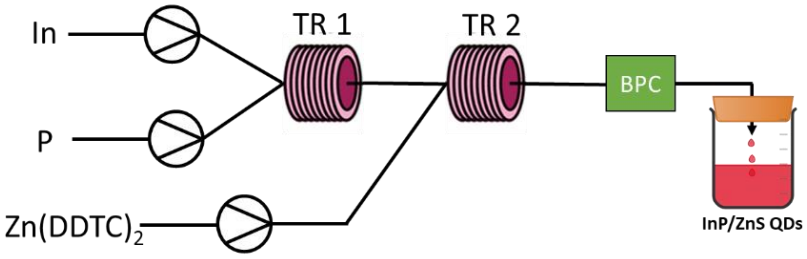

Figure 2.22: Flowchart of configuration 3 for the synthesis of InP/ZnS QDs at a larger scale.

The core synthesis was performed at 180 ºC, 3 bar and 33 mins of residence time/120 µL/min of flow rate and the InP/ZnS QDs were prepared at 160 ºC, 1 bar and 66 minutes of residence time/240 µL/min of flow rate (Figure 2.23a). Figure 2.23b shows the UV-vis and PL spectra of the obtained InP/ZnS QDs. A red shift from 516 to 535 nm can be observed in the first excitonic peak. The synthesized InP/ZnS QDs show an emission peak at 574 nm with a FWHM of 68 nm/261 meV, a Stokes shift of 157 meV and a PLQY of 54%. Figure 2.23c shows the strong yellow emission of InP/ZnS QDs under UV light. For the production analysis, 100 mL of InP QDs were prepared. To record the weight, InP/ZnS QDs were purified several times with a mixture of methanol/chloroform and acetone to remove organics and unreacted precursors. The obtained red powder was kept under vacuum for drying overnight. The continuous synthesis of InP/ZnS QDs (30 min InP core and 60 min ZnS shelling) yielded 6.2 grams of InP/ZnS QDs in 9.54 hours.

TEM and XRD measurements were performed for the size and structural analysis of the InP/ZnS QDs. Figure 2.23d shows the XRD pattern of the InP/ZnS QDs along with the bulk ZnS and InP references confirming the zinc blende structure. A small shift toward higher angles was observed in the peaks corresponding to (111), (220), and (311) planes of InP after ZnS shell growth, which is expected due to the smaller lattice parameter of ZnS. The TEM analysis (Figure 2.23e and 2.23f) revealed that the size of the InP/ZnS increased from 3.5 (core) to 4.3 nm after ZnS shell formation, confirming a ~1-2 monolayers thick ZnS shell. It should be noted that the ZnS shell thickness is generally underestimated from TEM analysis due to the low contrast of ZnS. A thicker shell can be deposited by increasing the ZnS shelling time (3-4 h).

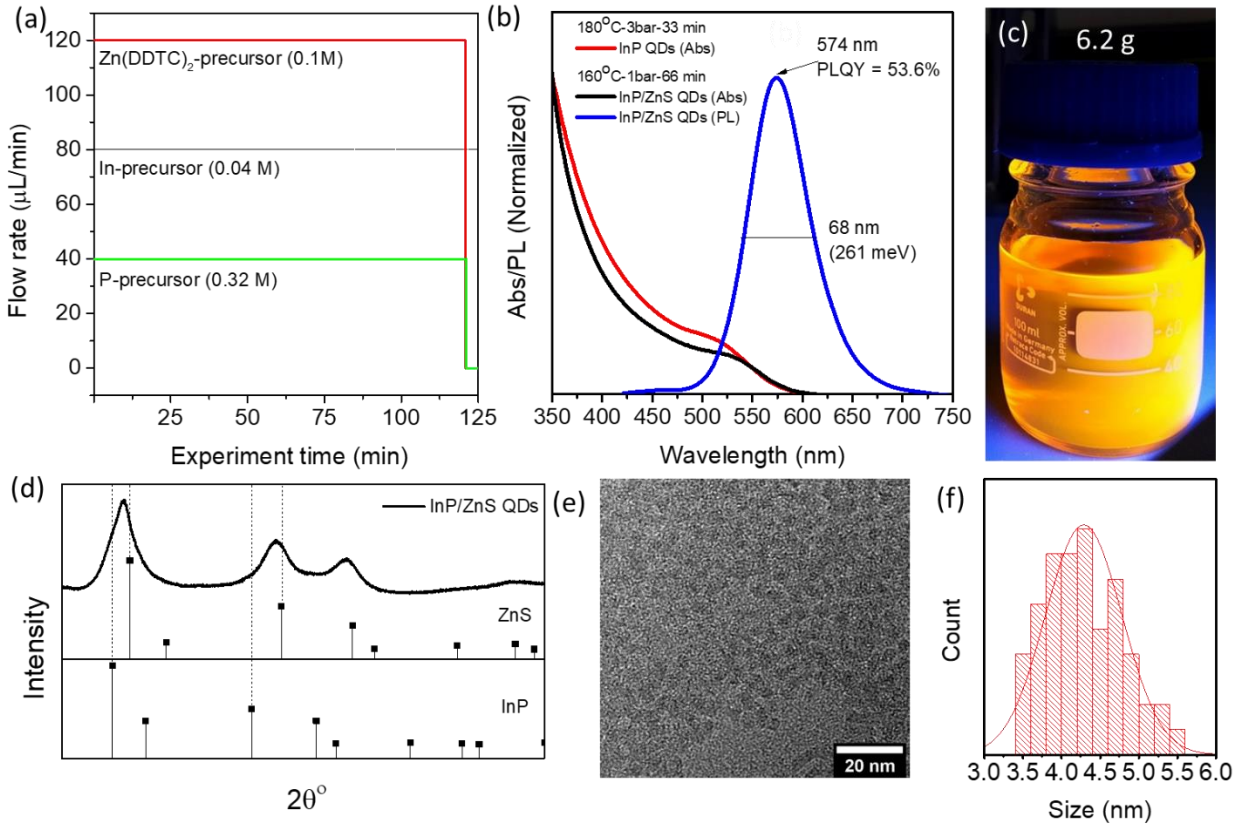

Figure 2.23: (a) Flow rate for synthesizing InP core and InP/ZnS core-shell QDs. (b) Absorption and photoluminescence spectra of the InP/ZnS QDs prepared at larger scale. (c) Photograph of 100 mL colloidal solution of the as-prepared yellow/orange-emitting InP/ZnS QDs under UV light. (d) XRD pattern of the InP/ZnS QDs. The reference of bulk ZnS (JCPDS # 01-071-5976) and InP (JCPDS # 00-032-0452 are given for comparison (vertical lines). (e) and (f) TEM image and size histogram of the InP/ZnS QDs, respectively.

2.4. Conclusion

In conclusion, we optimized the continuous flow synthesis of size-tunable InP QDs using transaminated tris(oleylamino)phosphine ($P(NHR)_3$) as the phosphorus precursor replacing tris(diethylamino)phosphine to avoid *in situ* gas formation (diethylamine) during the reaction, which would lead to an uncontrolled preasure increase in the flow setup. We first optimized the reaction conditions in batch syntheses using $P(NHR)_3$. To obtain a narrow size distribution, a mixture of both tri- and bi-substituted phosphine was required, which led to the separation of nucleation and growth due to the different reactivity of both precursors. The addition of $ZnCl_2$ in the InP core QDs synthesis was found to be crucial to improve the size distribution. We also developed a novel synthesis route to prepare InP QDs in non-coordinating solvent (ODE) via the aminophosphine route with a size dispersity similar to the classical route using $P(DEA)_3$. This batch-optimized synthesis was successfully implemented in the continuous flow synthesis of the InP QDs. Using optimized conditions, the first excitonic peak could be tuned from 450 to 580 nm by varying the residence time and temperature. A slightly broader size distribution was observed compared to the batch due to the viscosity-induced inability of using a higher

amount of zinc chloride in the core synthesis. We also demonstrated the efficiency of the continuous flow platform for the gram-scale production of InP/ZnS core/shell QDs. We achieved a line width of 64-68 nm (FWHM) and a PLQY of up to 54% while continuously producing more than 6 g of InP/ZnS QDs. We emphasize that in this study, the core/shell synthesis was not fully optimized. A multishell structure of InP/ZnSeS/ZnS can be developed to further improve the PLQY. Overall, the continuous flow platform exhibits great potential for the large-scale and highly reproducible production of InP QDs with well-defined optical properties.

Chapter III

Synthesis of zinc-free InP quantum dots covering a large size range

3.1. Introduction

In more recent studies, safer and more economical aminophosphine-based phosphorus precursors have been explored as alternatives to $P(TMS)_3$ in the synthesis of InP QDs.[78-80] In 2013, Song et al. first reported the synthesis of InP QDs with tunable PL emission in the green-red range (532-610 nm) by introducing tris(dimethylamino)phosphine $P(NMe_2)_3$ in a mixture of $InCl_3$, $ZnCl_2$, and oleylamine at 220°C.[79] Recently, after overgrowth with multiple shells up to 95% PLQY has been reached with InP QDs synthesized via the aminophosphine route,[16] albeit the PL linewidth (45 nm FWHM at 607 nm emission/151 meV)[84] was broader than the best values reported with $P(TMS)_3$-based syntheses (35 nm at 630 nm emission/110 meV).[98] Furthermore, zinc chloride is generally added in significant amounts (more than 6 equivalents to In) to aminophosphine-based syntheses of InP QDs since it has been noted that it strongly reduces the size distribution and improves the PL properties.[78] $ZnCl_2$ has been shown to influence the synthesis reaction kinetics, generally leading to smaller-sized InP QDs of lower-size dispersion.[60, 117] It can also play the role of a Z-type (Lewis acid) ligand for the QD surface improving its passivation.[117-119] The localization of Zn^{2+} either on the QD surface or in its volume depends on several parameters, such as temperature, concentration and ligation governing the reactivity of the Zn precursor during the reaction.[119-120] Therefore, in some conditions, Zn^{2+} can also act as a p-type dopant for InP QDs introducing shallow defects which lead to spectral broadening.[114] Talapin and coworkers demonstrated that Zn-doping in InP QDs leads to lattice disorder generating localized hole states close to the valence band edge, which are responsible for the observed red-shifted emission and large Stokes shift as well as the anomalous broadening of the photoluminescence excitation (PLE) spectra.[121] Moreover, the same study demonstrated that O^{2-}, acting as an interstitial dopant, leads to a similar net effect as substitutional Zn^{2+} doping, inducing shallow hole traps above the valence band with the same detrimental consequences on the optical properties.

In parallel to the flow synthesis of InP QDs as discussed in the previous chapter, we decided to develop a zinc-free aminophosphine-based synthesis method aiming at reducing the emission line width and getting access to larger InP QD sizes. To achieve this goal, we investigated indium (I) halides (In(I)X, X= Cl, Br, I), which can serve as both the In source and reducing agent for aminophosphines. Indium (I) halides are readily commercially available and well-known reducing agents in organic synthesis.[122] Moreover, In(I)Cl has been recently applied in the synthesis of InAs QDs using tris(dimethylamino)arsine as the As source.[123]

In this chapter, we developed the synthesis of InP QDs using indium (I) chloride and optimized the reaction parameters to improve the optical properties. Then we investigated the effect of different reaction parameters such as the effect of the nature of the halide, reaction temperature, amount of aminophosphine, etc. We performed X-ray diffraction (XRD) and transmission electron microscopy (TEM) analyses to understand the crystal structure and morphology of the synthesized particles and intermediates. We further studied the reaction kinetics of the formation of InP QDs using ^{31}P NMR spectroscopy and mass spectrometry.

3.2. Experimental Section

3.2.1. Materials

Indium monochloride In(I)Cl, metal basis 99.99%, indium trichloride $InCl_3$, 99.99%), indium monobromide In(I)Br, metal basis 99.99%), Indium monoiodide In(I)I, metal basis 99.999%), trioctylphosphine (TOP, 97%), octadecene (ODE, 90 %), oleylamine (OLA, 90%), zinc diethyldithiocarbamate $Zn(DDTC)_2$, 97%), and tris(diethylamino)phosphine [$P(NEt_2)_3$, 97%] were purchased from Sigma Aldrich and used without any purification. All anhydrous solvents were degassed before usage and were stored inside an Ar-filled glove box.

3.2.2. Synthesis of InP QDs using In(I)Cl

In a 50 mL three-necked round bottom flask, 75 mg (0.5 mmol) of InCl, 0.3 mL (0.7 mmol) of trioctylphosphine and 7.2 mL (22 mmol) of oleylamine were added. The flask was evacuated at 50 °C for 25 minutes. During this step, the reaction mixture color changed from light green to deep brown. Afterward, the solution was quickly heated to 220 °C (30 °C/min) under Argon. After reaching 220 °C, $P(NEt_2)_3$ (2 mmol) diluted in 0.5 mL ODE was rapidly injected. The reaction temperature was maintained at 220 °C for 30 minutes. After 30 minutes, the reaction color turned black and the reaction was quenched by cooling it down. Before purification, InP QDs were centrifuged at 4000 rpm to remove any unreacted precursor present. For purification, the synthesized InP QDs were precipitated by centrifugation at 8000 RPM after adding dry acetone (10 times) and were redispersed in toluene for further characterization.

3.2.3. Synthesis of InP QDs using In(I)Br and In(I)I

In a 50 mL three-necked round bottom flask, 0.5 mmol of In(I)Br (or In(I)I), 0.3 mL (0.7 mmol) of trioctylphosphine and 7.2 mL (22 mmol) of oleylamine were added. The flask was kept under vacuum at 50 °C for 25 minutes. After 25 minutes, the reaction mixture was switched under argon and quickly heated to 220 °C (30 °C/min). After reaching 220 °C, $P(NEt_2)_3$ (1 mmol) diluted in 0.5 mL ODE was rapidly injected. The reaction temperature was maintained at 220 °C for 30 minutes. After 30 minutes, the reaction color turned deep red and the reaction was quenched by cooling it down. Synthesized InP QDs were purified using similar procedure as given in the previous section.

3.2.4. Synthesis of InP QDs using In(III)Cl_3

In a 50 mL round bottom flask, 0.5 mmol $InCl_3$, 0.3 mL TOP and 7.2 mL oleylamine were added. The reaction mixture was degassed at 100 ^oC for 30 minutes. After that, the reaction temperature was increased to 220 ^oC (30 ^oC/min) under argon. At 220 ^oC, 2mmol of $P(NEt_2)_3$ diluted in 0.5 mL of ODE was injected swiftly. Shortly, bubbling was observed inside the reaction flask, suggesting the formation of dimethylamine gas. The reaction mixture was changed from colorless to deep red color. The synthesized InP QDs were then precipitated by centrifugation at 8000 RPM after adding methanol/chloroform/acetone (1/1/2) and redispersed in dry toluene for further characterization.

3.2.5. In-situ HF etching of the InP QDs

The etching procedure was adapted from a recently reported method[124] and was optimized for our as-prepared InP QDs. In a typical room temperature etching procedure, 20 nmol of purified InP QDs were added in 10 mL of vial containing 880 mL of mesitylene. Further 30 μL of $ZnCl_2$-TBP solution (0.64M) and 150 μL of octylamine/mesitylene (0.64M) were added. Then 150 μL of benzoyl fluoride/mesitylene (0.64 M) were added to the solution. During the etching process, HF bubbles can be observed. InP QDs prepared with In(I)Cl were etched for 60 min, samples prepared with In(I)Br were etched for 20 min and those obtained from In(I)I for 10 min. All the procedures were performed at room temperature and inside the glove box, the exhaust of which is connected to the extraction.

3.2.6. Preparation of 0.2 M $Zn(DDTC)_2$ stock solution

To prepare a stock solution of 0.2 M $Zn(DDTC)_2$, 361.93 mg (1 mmol) of $Zn(DDTC)_2$ powder and 5 ml of oleylamine (degassed previously) were added in a 10 mL vial and were stirred overnight inside a glove box. The obtained clear solution was stored inside the glove box for further utilization.

3.2.7. Synthesis of InP/ZnS core/shell QDs

For ZnS shelling, 1 mL of the as-prepared InP core QDs (unetched) were taken in a 50 mL three-necked round bottom flask. 1 mL of $Zn(DDTC)_2$ (0.2 M) stock solution and 2 mL of ODE were added at room temperature. The reaction mixture was heated to 140 °C for 2-5 hours under argon flow and a slow heating rate (2 °C/min) was maintained to avoid any secondary nucleation of ZnS NPs. After completion, InP/ZnS QDs were precipitated with a mixture of methanol, chloroform and acetone (1/1/2) and centrifuged at 8000 RPM (5 min). The purified InP QDs were then redispersed in toluene for further characterization.

3.2.8. Characterization

Absorption spectra were measured on a Hewlett Packard 8452A UV-VIS spectrometer. The emission spectra were obtained using a Fluorolog FL3-22 spectrometer, which was equipped with 150 W xenon lamps (for steady-state measurements). A NanoLED laser diode from Horiba with a wavelength of 455 or 350 nm (1 MHz repetition rate) was used for time-correlated single-photon counting (TCSPC). The

PL decay for all three samples was fitted by a bi-exponential function as follows. The PL decay curves were fitted with a bi-exponential function:

$$Y(t) = A_1 \, exp\left(-\frac{t}{\tau_1}\right) + A_2 \, exp\left(-\frac{t}{\tau_2}\right) \qquad \textit{Eq. 3.1}$$

where τ_1 and τ_2 correspond to decay time constants and A_1 and A_2 are the respective amplitudes [X^2=0.99]. The average lifetime (τ_{avg}) was calculated using the following equation.[115]

$$\tau_{avg} = \frac{A_1{\tau_1}^2 + A_2{\tau_2}^2}{A_1\tau_1 + A_2\tau_2} \qquad \textit{Eq. 3.2}$$

Absolute photoluminescence quantum yield (PLQY) measurements were performed at room temperature using an integrated sphere, Hamamatsu Quantaurus. Powder X-ray diffraction (XRD) patterns were recorded using a Bruker powder diffractometer equipped with a copper anode (lKa1=1.5406 A, lKa2=1.5444 A) and an X'Celerator 1D detector. The elemental compositions were analyzed using a Zeiss Ultra 55+ scanning electron microscope equipped with a Bruker QUANTAX energy dispersive X-ray (EDX) probe. The samples for XRD and EDX measurements were prepared by drop-casting concentrated InP QDs dispersed in toluene on a cleaned silicon substrate (disoriented Si for XRD). The substrate was kept under argon and toluene was allowed to evaporate. TEM grids were prepared by drop-casting nanocrystal suspensions onto a 400-mesh copper transmission electron microscopy grid covered with an ultrathin carbon film and the solvent was allowed to evaporate. Transmission electron microscopy was performed at cryogenic temperature and images were collected with an FEI Tecnai F20 microscope. For ^{31}P NMR spectroscopy, in a typical preparation, 300 µL of the sample, 5.2 mg (0.02 mmol) triphenylphosphine (external reference, δ = -5 ppm), and 300 µL of toluene *d8* were added to the NMR tube. Proton-coupled ^{31}P spectra were collected on a Bruker NEO nanobay spectrometer at a frequency of 161.9MHz (50 scans, relaxation delay = 3 sec). Chemical shifts were internally referenced to H_3PO_4 (δ = 0 ppm). For MALDI-TOF analysis, 10 µL of the reaction solution (without any purification) was diluted in 1 mL of acetonitrile. Then, 1 to 2 mg of pyrene matrix was added and 1 µL of this solution is deposited on a MALD grid.

3.3. Results and Discussion

3.3.1. Influence of aminophosphine amount

InP QDs were synthesized using indium (I) chloride and tris(diethylamino)phosphine in oleylamine acting as a coordinating solvent without adding zinc halides or fatty acids. It should be noted that in the previous aminophosphine-based syntheses, an excess of 2-6 equivalents of zinc chloride was introduced, [78-80] which was found mandatory for achieving a low size distribution.[78, 125] In the present study, we chose not to use zinc or any oxygen-containing precursors in the core synthesis to be able to

assess the optical properties of the prepared InP QDs without the influence of volume or surface trap states induced by these ions.[121] In particular, it can be expected that the large Stokes shift and PL linewidth reported for InP QDs can be significantly reduced in Zn- and O-free syntheses.

Theoretically, the minimum stoichiometric ratio needed for the complete reduction of P^{3+} to P^{3-} by In(I)X is P:In = 1:3. However, with this ratio we only obtained <10% reaction yield regardless of the reaction temperature (180 – 270 °C). This low reaction yield demonstrates that *in situ* formed tris(oleylamino)phosphine was not completely reduced by the In(I)Cl. Therefore, we first investigated if the larger P:In ratios increase the chemical yield of InP QDs. To answer this question, we increased the aminophosphine amount while keeping all other reaction parameters constant. Figure 3.1a/b/c shows the absorption spectra of InP QDs synthesized with different aminophosphine amounts (0.5 - 2 mmol) while keeping the amount of In(I)Cl constant (0.5 mmol). The aliquots were collected at different reaction times ranging from 1 to 30 minutes. A clear excitonic shoulder characteristic of InP NCs was observed in all three cases. However, the excitonic peak exhibits a strong redshift with an increase in the P:In ratio, indicative of larger particle size. This behavior contrasts with that reported for the $InCl_3$-based aminophosphine synthesis of InP QDs, in which a slight blue shift in the absorption spectra was observed when the P:In ratio was increased from around 0.6 to 2.[79] Figure 3.1d shows the change in the first excitonic peak position of InP QDs synthesized with InCl. The first excitonic peak is visible as a shoulder evolving from 603 to 700 nm with reaction time, i.e., in a much higher wavelength range than that reported for the synthesis with $InCl_3$ (480-580 nm).[78] Figure 3.1e shows the change in the chemical yield with the change in the P:In ratio. Indeed, an increase of the P:In ratios strongly improved the reaction yield reaching up to 80% in the case of a ratio of 4:1.

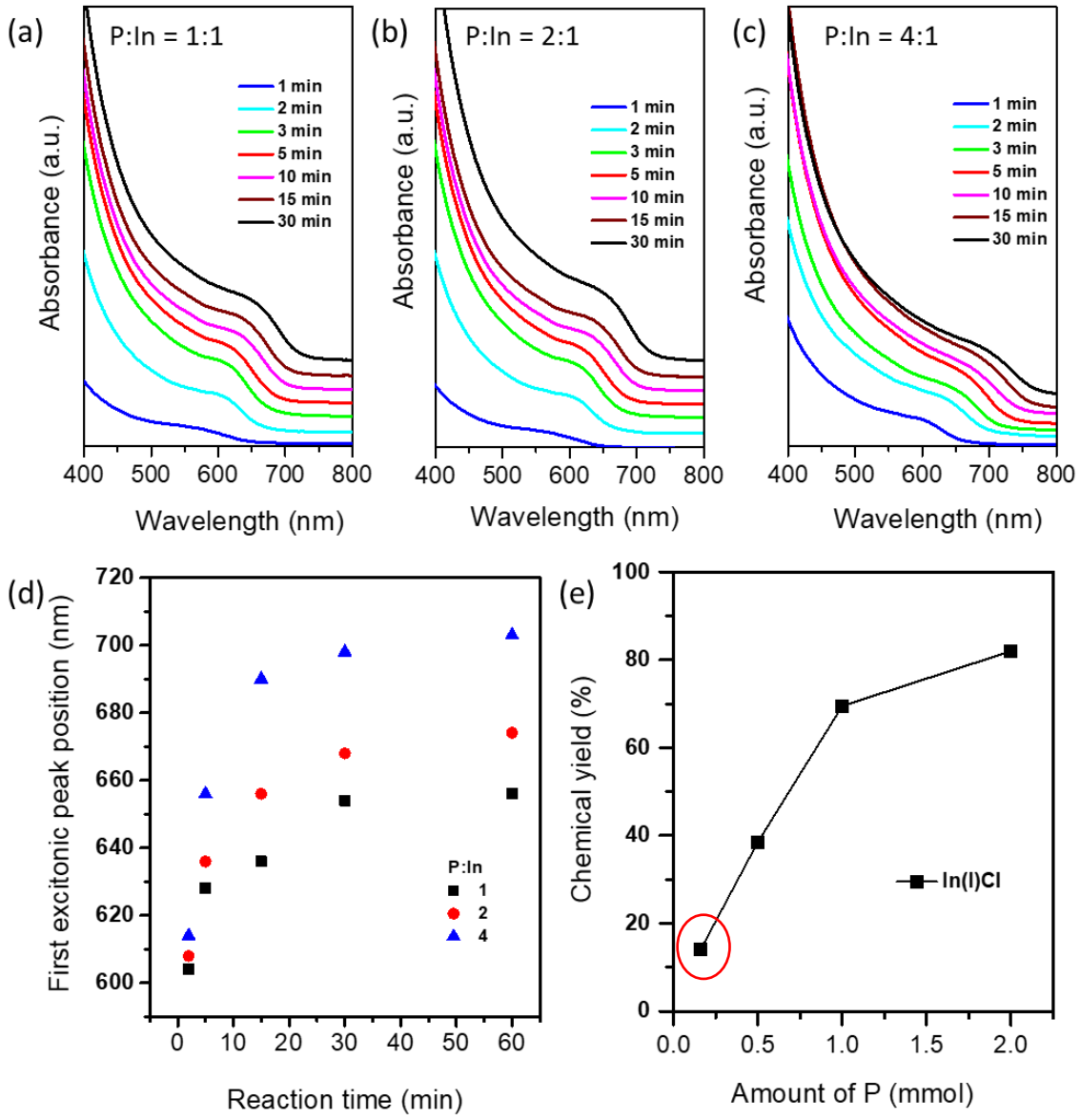

Figure 3.1: Absorption spectra of InP QDs synthesized using different ratios of aminophosphine and In(I)Cl (a) P:In = 1/1, (b) P:In = 2/1, (c) P:In = 4:1. Aliquots were collected at various reaction times and the spectra are vertically shifted for clarity. (d) Influence of P:In ratio on the first excitonic peak position of InP QDs. (e) Change in the reaction yield as a function of the P:In ratio (reaction time: 30 min). The red circle depicts the reaction yield for P:In = 1:3, which is the ratio theoretically needed for the complete reduction of phosphorus by In(I).

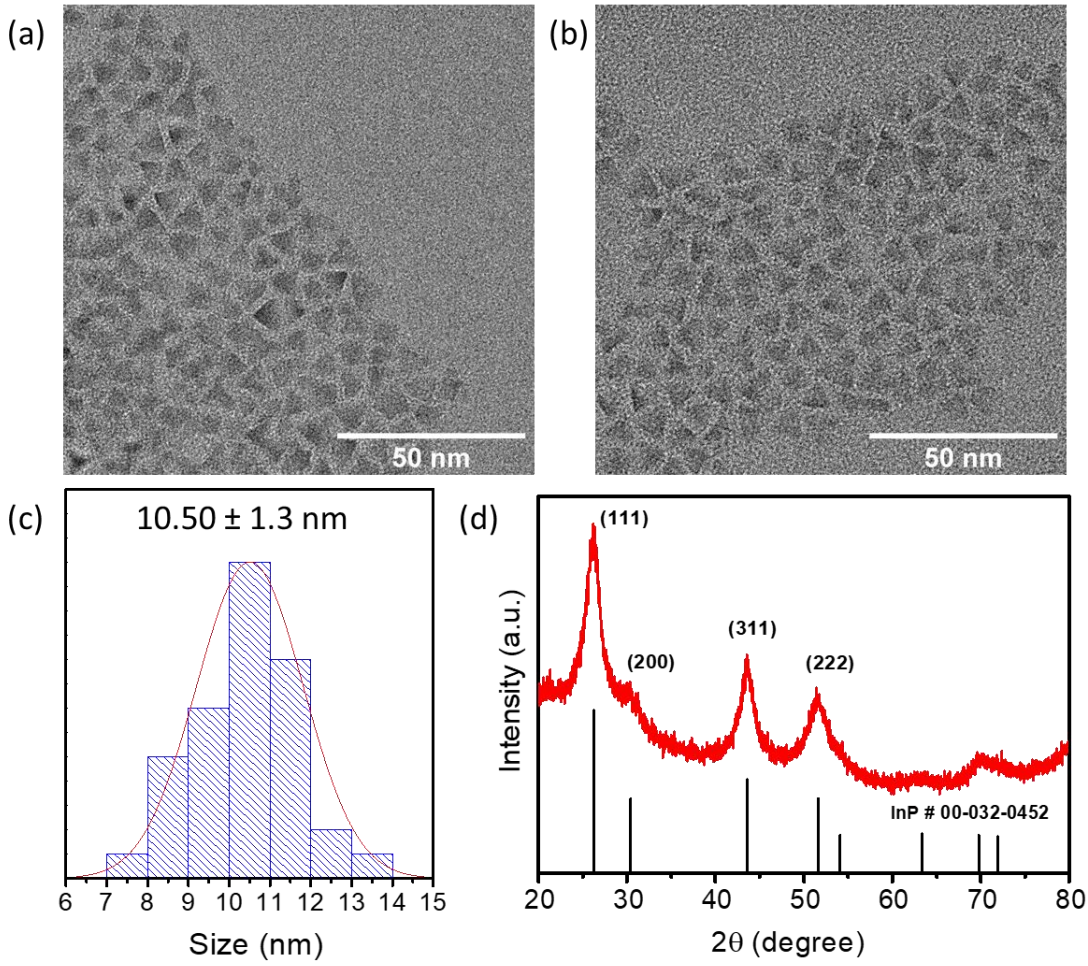

Figure 3.2: (a) and (b) TEM images of InP QDs synthesized with P:In = 4:1 ratio with In(I)Cl (reaction time: 30 min). (c) Statistical analysis of the size of the same QDs (edge length of the tetrahedra). (d) X-ray diffractogram; the cubic InP bulk reference is indicated as vertical black lines for comparison (JPCDS# 00-032-0452).

TEM images of the QDs (Figure 3.2a and 3.2b) obtained after 30 min reveal that the InP QDs are tetrahedral shaped with an average of 10.5 ± 1.3 nm (size distribution: 12.4% Figure 3.2c). This value represents to the best of our knowledge the largest-sized InP QDs reported so far synthesized in a single-injection reaction without the secondary addition of precursors. Our result shows a great improvement in the aminophosphine-based synthesis in terms of size distribution and band gap tunability. Powder X-ray diffraction analysis (Figure 3.2d) shows the characteristic (111), (220), and (311) peaks corresponding to the cubic zinc blende crystal structure of InP.

3.3.2. Effect of the indium (I) halides

To study the effect of the different indium halide precursors, In(I)Cl was replaced by InBr and InI. Figure 3.3a shows a series of UV-vis absorption spectra of InP QDs synthesized with InBr in similar conditions as InCl and with the ratio of P:In = 2:1. The absorption spectra were measured by analysis of the aliquots collected between 1 to 30 minutes of reaction. The first excitonic peak is visible as a shoulder evolving from 530 to 610 nm with reaction time. A significant blue shift of 90 nm in the

absorption peak can be observed for 30 min reaction time compared to InCl. Similarly, a further systematic blue shift of the first excitonic peak compared to InBr was observed when InI is used (Figure 3.3b and 3.3c). Furthermore, similar to the InCl case, a red shift in the peak was observed with an increase in the amount of aminophosphine. The evolution of the first excitonic peaks with change in aminophosphine amount is depicted in Figures 3.3d and 3.3e for InBr and InI respectively. Contrary to the case of In(III) halides (chapter 1), which show fast growth in the first 5-7 min before reaching a plateau, with the In(I) halides this plateau is reached for longer reaction times (around 20-30 min). This suggests that In(I)X provides better size tunability compared to In(III)halides.

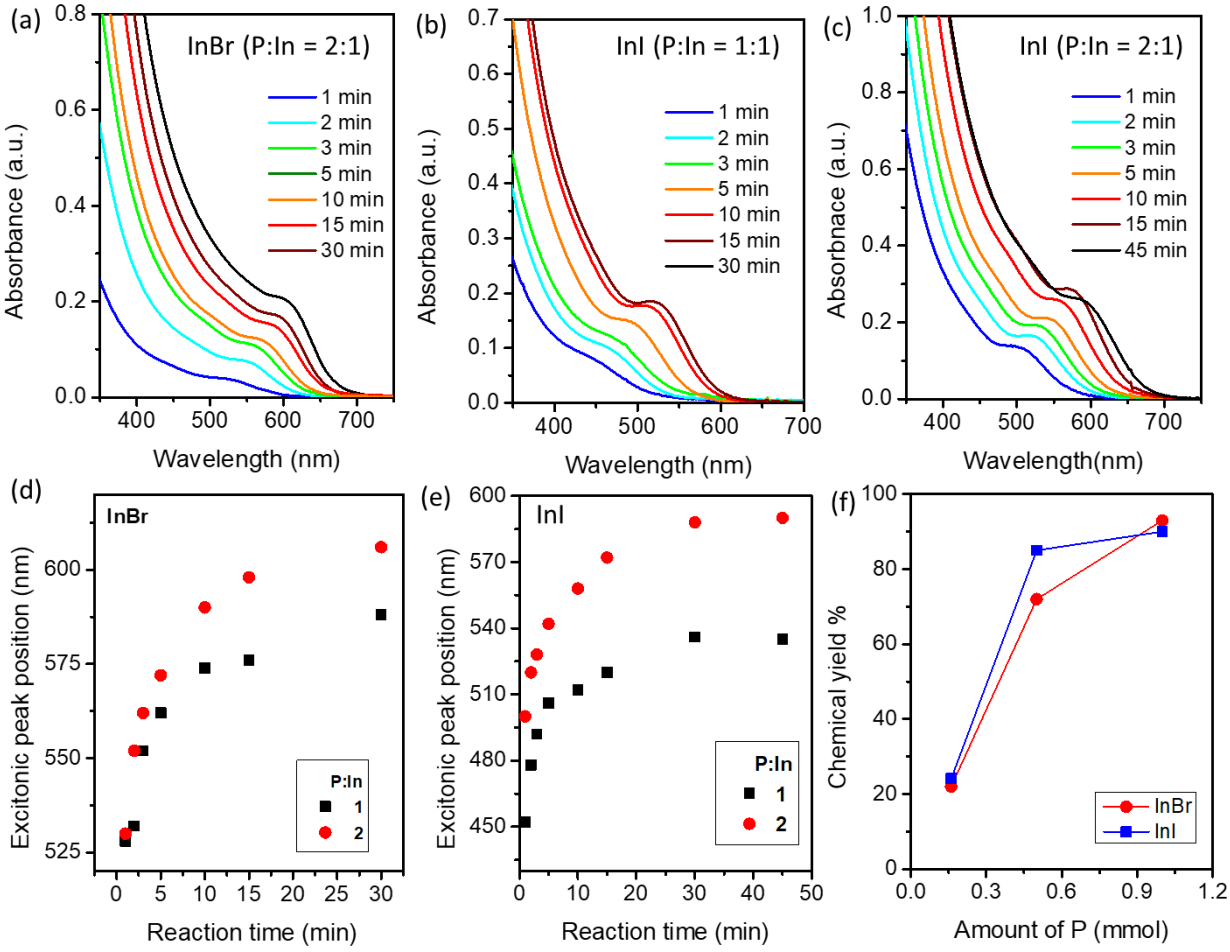

Figure 3.3: (a) Absorption spectra of InP QDs synthesized using InBr (P:In = 2:1). Absorption spectra of InP QDs synthesized using InI (b) with P:In = 1:1 and (c) with P:In = 2:1 Influence of P:In ratio on the first excitonic peak position of InP QDs synthesized using (d) InBr and (e) InI. (f) Change in the reaction yield as a function of the P:In ratio and indium (I) halide used (reaction time: 30 min, amount of indium precursor: 0.5 mmol).

A similar trend as with InCl was observed when InBr or InI was used as the In(I) source (Figure 3.3f). Concomitant with the size increase, the higher P:In ratios afforded a strongly improved reaction yield. Figure 3.3f shows that with InI and InBr, reactions using P:In = 2:1 already resulted in a reaction yield exceeding 90%, while in the case of InCl, a ratio of 4:1 was required to push the yield to 80%. We underline that even at a low P:In ratio of 1:1 reaction yields of 40–85% (depending on the halide) have

been obtained. These values unambiguously show that the reaction pathway implying aminophosphine reduction by In(I)X is either predominant (with InI and InBr) or at least strongly involved in the reaction (with InCl) because at a low P:In ratio of 1:1, the maximum theoretically achievable reaction yield via pure aminophosphine disproportionation would be 25%.

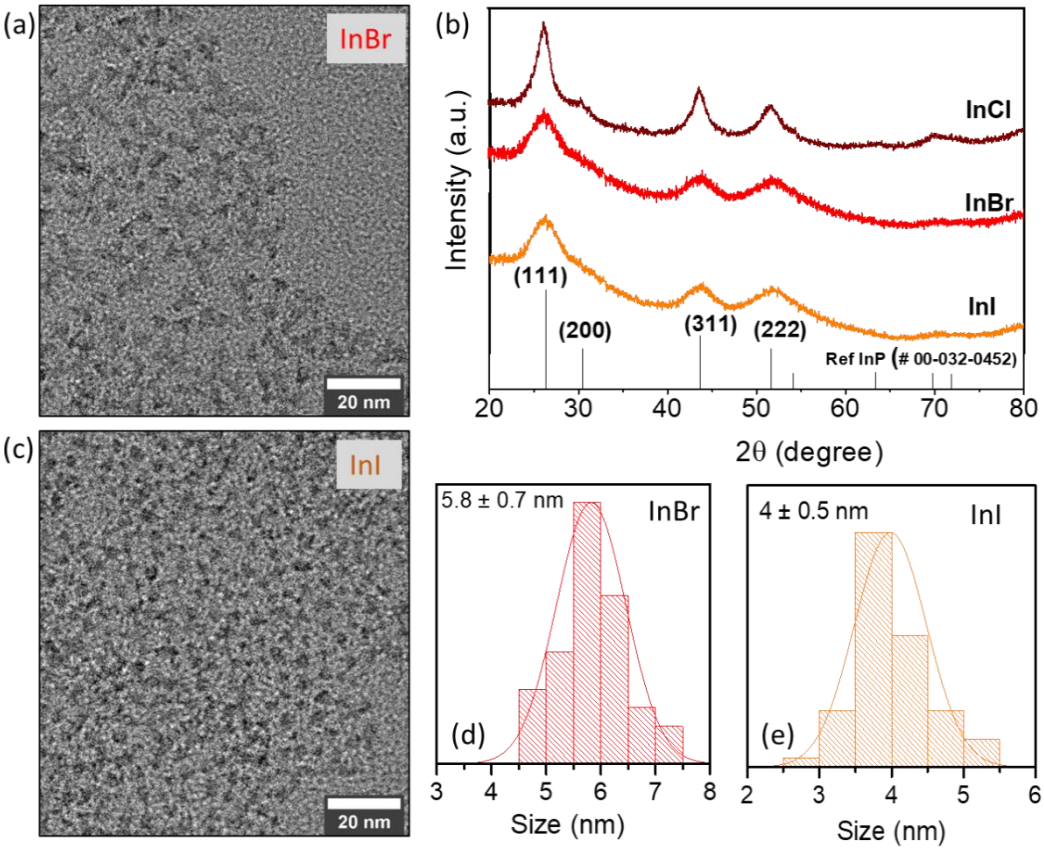

Figure 3.4: TEM images of InP QDs synthesized InBr (a) and InI (c) precursors (reaction time: 30 min). (b) XRD patterns of the InP QDs obtained with the different In(I) halides (reaction time: 30 min). The cubic bulk InP reference is indicated as vertical black lines for comparison (JPCDS# 00-032-0452). Statistical analysis of the size of the InP QDs synthesized with InBr (d) and InI (e) precursors (reaction time: 30 min).

Figure 3.4a/c shows TEM images of the InP QDs obtained after 30 min of the reaction, with InBr (5.8 ± 0.7 nm), and with InI (4.0 ± 0.5 nm), demonstrating the size tunability in a wide range by simply changing the In(I) precursor. Moreover, the size distribution remained similar (12-13%) irrespective of the halides used (Figure 3.4d-e). XRD analysis (Figure 3.4b) shows the characteristic (111), (220), and (311) peaks corresponding to the cubic zinc blende crystal structure of InP. In case of InI and InBr XRD peak broadening is attributed to smaller-sized particle.

Summarizing, by changing the nature of halides, the first excitonic peak position can be tuned from the visible to near-infrared (450 – 700 nm) while maintaining a narrow size dispersion of 12 – 13%. Unlike reported procedures relying on the continuous or multiple injections of precursors to push the first

excitonic beyond 600 nm, the present approach gives access to the near-infrared spectral region in a single-step reaction and without deteriorating the size dispersion.

A variety of kinetic growth models has been developed to explain the nanoparticles' formation, growth, and resulting size dispersion. Based on both theoretical and experimental predictions, growth of the nanoparticles is controlled by the diffusion of the monomers to the surface (diffusion-limited growth) or by the surface reaction of the monomers (reaction-limited growth) or by both diffusion and reaction at the surface at the same time.[54] Recently a mechanistic investigation performed by Owen et al. revealed that the growth of InP QDs via the aminophosphine route is controlled by the surface reaction of the monomers.[126] In our case, the observed effect of the indium halides on the QD size can be correlated with their reactivity, where the surface reaction rate is limited by the reactivity of the indium halide precursors. The observed size reduction when going to heavier halides has already been reported for InP and other metal phosphide QDs.[76, 78, 127] In the present case, we have to consider that the halides are involved in the stabilization of the growing nanocrystals, in particular by coordinating to the (111) facets of the tetrahedral particles.[128] Considering the bond enthalpies of the three halides InCl: 439; InBr: 418; InI 331 $kJ \cdot mol^{-1}$), InI is the most reactive one leading to the formation of the largest number of seeds in the nucleation burst, as confirmed by analyzing the number of InP units formed in the initial reaction stages (vide infra). A second effect of the stronger In–Cl bond is the decreased reactivity of the QD surface towards incoming monomers. Jeong and coworkers showed that the halides are involved in the stabilization of the growing nanocrystals by coordinating preferentially the (111) facets of tetrahedral particles.[129] In the elemental analysis of the purified InP QDs we detected indeed a significant fraction of halides whose amount followed the reverse order of their ionic radii: Cl > Br > I (cf. Table 3.1). This hypothesis is supported by the significant amount of halide we find in the elemental analysis of the InP QDs (Table 3.1).

Table 3.1: Elemental composition analysis of InP QDs synthesized with InCl, InBr, and InI.

In precursor used (reaction time 30 min)	Atomic % of In in EDX	Atomic % of P in EDX	Atomic % of halide in EDX
InCl	48	40	12
InBr	56	34	10
InI	50	43	7

3.3.3. Influence of different reaction parameters

In solution, In(I)Cl is in equilibrium with its disproportionation products In(0) and $In(III)Cl_3$.[130] The formation of In(0) particles could indeed be observed in the early aliquots and samples synthesized at lower temperatures (<200 °C) or with a low pre-nucleation heating rate (Figure 3.5).

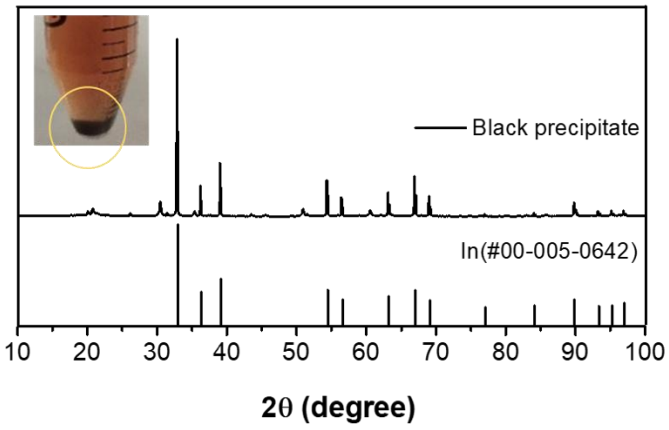

Figure 3.5: X-ray diffractogram of the black precipitate obtained in early aliquots (<5 min) of the reaction between InCl and aminophosphine. The diffraction pattern of indium is also given for comparison (# 00-005-0642).

These findings indicate the shift of the equilibrium towards disproportionation in the abovementioned conditions, while in the optimized conditions for InP QD synthesis no formation of In(0) was detected. The polydispersity of the particles considerably improved as evidenced by sharper first excitonic peak features when the pre-nucleation heating rate was increased from 10 to 30 °C/min (Figure 3.6a).

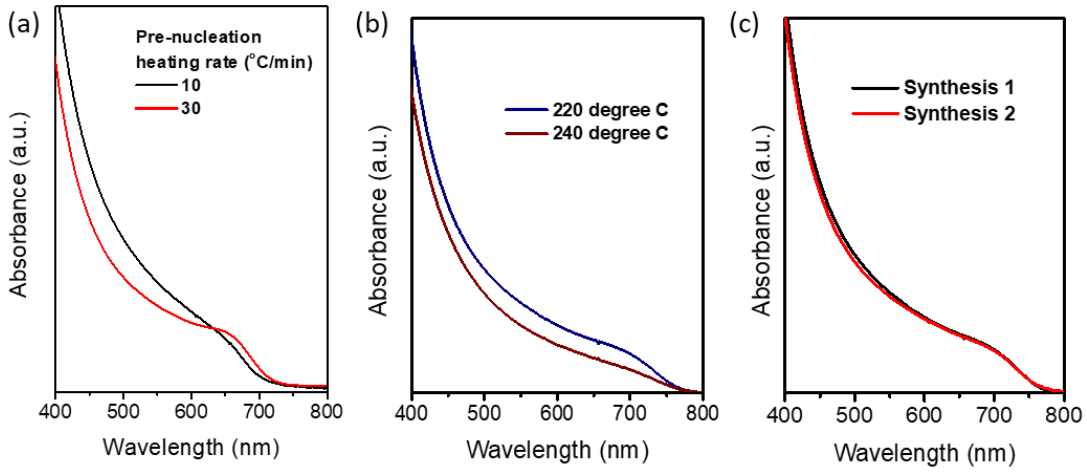

Figure 3.6: (a) Absorption spectra of InP QDs synthesized with 10 ºC/min (black) and 30 ºC/min (red) pre-nucleation heating rate. (b) Absorption spectra of InP QDs synthesized at different reaction temperatures; 220 ºC (blue) and 240 ºC (brown). (c) Absorption spectra of InP QDs of two different batches synthesized using the optimized reaction conditions.

Figure 3.6b shows the absorption spectra of InP QDs synthesized at 240 °C. It can be observed that at higher temperature absorption spectra became broader suggesting a larger size distribution than at 220°C (Figure 3.6b). Two syntheses were performed in the optimized conditions to confirm the reproducibility of the developed protocol. As can be judged from the absorption spectra shown in Figure 3.6c, the synthesis of InP QDs using In(I)X halides and aminophosphine is highly reproducible.

3.3.4. Study of the intermediates

Figure 3.7a-d show the transmission electron microscopy (TEM) images of the aliquots collected at 5 and 15 min of the reaction of InP QDs synthesized using different P:In ratios. We found that at the early stage of the reaction (5min), tetrapod-like InP nanocrystal intermediate were formed which subsequently grew into tetrahedral shaped particles. For higher P:In ratio we can already observe tetrahedra at 15 min of the reaction. Figure 3.7e shows the XRD pattern of the tetrapod intermediates synthesized using P:In = 2:1. The tetrapods appear crystalline and in the zinc blende crystal structure similar to the tetrahedra. A small peak at 35° was observed corresponding to In_2O_3 which was attributed to surface oxidization during the washing procedure. Figure 3.7f shows the proposed reaction pathway for the formation of InP tetrahedra synthesized using In(I)Cl and aminophosphine. We propose that after injection of $P(DEA)_3$, nuclei grow into anisotropic tetrapods which finally grow into tetrahedra with (111) indium-rich facets stabilized by amines and halides.[129]

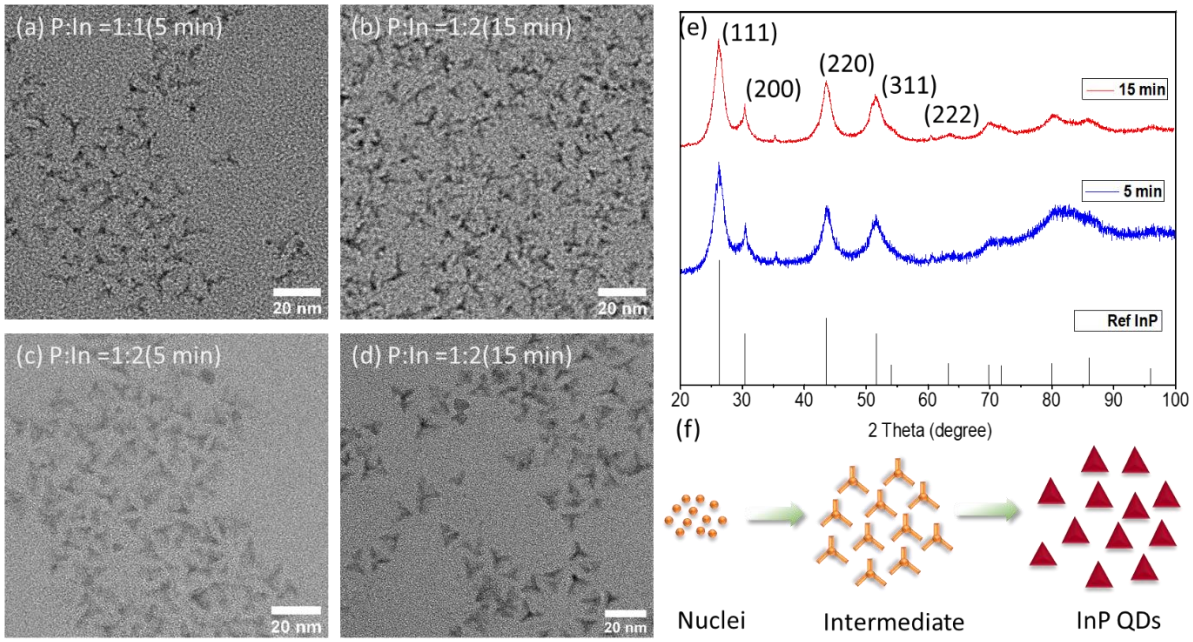

Figure 3.7: TEM images of aliquots taken at early reaction stages of InP QDs synthesized with (a) P:In = 1:1 (5min), (b) P:In = 1:1 (15 min), (c) P:In = 2:1 (5min) (d) P:In = 2:1 (15min) ratios using InCl. (d) XRD pattern of the InP tetrapods intermediate at 5 and 15 min of the synthesis. The pattern of bulk InP reference is given as vertical black lines for comparison (JPCDS# 00-032-0452).

The InP tetrapods can be isolated by using strong ligands. Figure 3.8a shows the absorption spectra of the InP tetrapods prepared with the addition of myristic acid in optimized conditions. We can observe an evolution of the excitonic peak from 580 to 605 nm which is significantly blue-shifted as compared to the tetrahedra (700 nm). Unlike the latter, the optical properties of the InP tetrapods are governed by their arm width. Figure 3.8b shows a TEM image of the synthesized InP tetrapods with an arm length of 7 ± 0.8 nm and width of 2.5 ± 0.4 nm. These preliminary results demonstrate that using In(I)X and aminophosphine, anisotropic growth of InP QDs can be achieved which has been challenging for

P(TMS)$_3$-based synthesis. Further development in the aminophosphine-based synthesis might be helpful to develop other morphologies such as InP nanoplatelets (NPLs), whose optical properties could be particularly interesting.

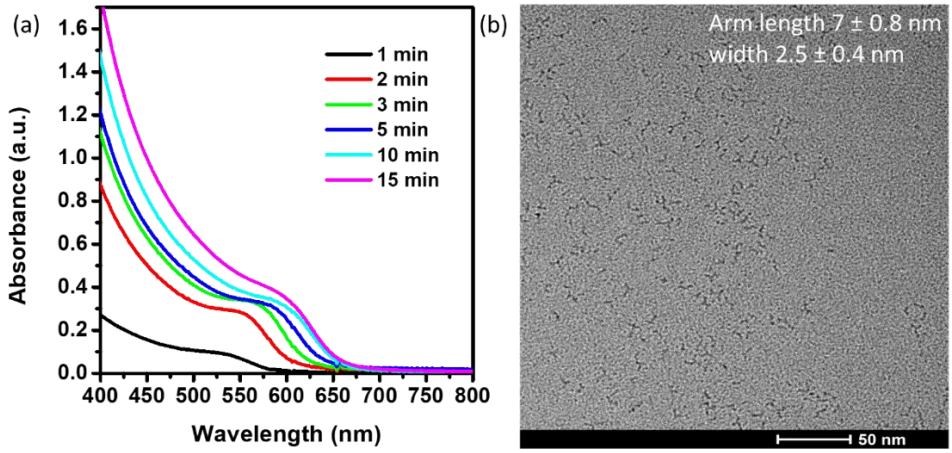

Figure 3.8: (a) Absorption spectra and (b) TEM image of InP tetrapods synthesized using InCl, aminophosphine and myristic acid.

3.3.5. Reaction mechanism

In the first step, we performed a systematic mechanistic study using ^{31}P NMR spectroscopy along with mass spectrometry for the case of In(I)Cl. In these experiments, triphenylphosphine (TPP) was used as an external reference to calculate the amount of different P species formed during the reaction by integrating their ^{31}P NMR peaks with respect to the known amount of TPP used. After 20 sec of P(NEt$_2$)$_3$ injection into the hot indium precursor solution at 220 °C, triply transaminated P(NHR)$_3$ **1** was detected at 97 ppm (R = $C_{18}H_{35}$) along with a small quantity (2–5%) of its tautomer H–P=NR(NHR)$_2$ **1'** at 10-13 ppm (Figure 3.9a/3.11).[80] Furthermore, the oleylimido-bridged species (RHN)$_2$P–NR–P(NHR)$_2$ **2** at 111 ppm and a small amount (<5%) of heterocyclic [(RHN)P–NR]$_2$ **2'** at 183 ppm could be identified (Figure 3.9a/3.11). The amount of these species strongly depends on the initial P:In ratio and hence the total amount of aminophosphine with respect to oleylamine; for the fraction of **2** with respect to **1** is 32% (1:1), 40% (2:1) and 75% (4:1). This behavior is consistent with the study of Buffard et al.[80] who demonstrated that the formation of **2** is favored by lowering the oleylamine:aminophosphine ratio. For longer reaction times, the P(V) compound tetra(oleylamino)phosphonium chloride [(RHN)$_4$P$^+$]Cl$^-$ **3** appeared at 29 ppm under concomitant reduction of the signals related to **1** and **2**, similar to the reaction using InCl$_3$. However, for lower P:In ratios the amount of **3** is very low (P:In = 2:1) or not detectable (P:In = 1:1), indicating that the disproportionation mechanism is not the predominant pathway of aminophosphine transformation in this case. At the same time, a novel peak at 16 ppm (**4**) is observed, in particular for low P:In ratios (Figure 3.9b/c/ 3.11). Recent studies on copper phosphide nanocrystals revealed the same signal which was attributed to transaminated aminophosphine tautomers,[131] while in the works on the aminophosphine synthesis of InP QDs this 16-ppm peak has not been discussed. To

isolate the corresponding product, a reaction with the 1:1 P:In ratio was used and the formed InP QDs were separated by precipitation. Mass spectrometry on the supernatant (Figure 3.12) gave in addition to the phosphonium salt **3** (m/z 1096.11) a compound with the hypothetical composition $[(NHR)_2P–NR]_2O$ (m/z: 1674.64), corresponding to the oxidation product of the dimerized aminophosphine tautomer. Accordingly, we can assign the NMR peak of **4** to the deprotonated tautomer of $P(NHR)_3$ (Figure 3.11). This interpretation is corroborated by the analysis of the evolution of the different NMR peaks with reaction time, plotted in Figure 3.9c-e. For the lowest P:In ratio of 1:1 (Figure 3.9c), compound **4** is the major species formed during the reaction, while the disproportionation product **3** characteristic of the $InCl_3$ synthesis remains at a very low amount (<2%). Furthermore, we note a clear correlation between the rise of **4** and the fading of **1**. At a 2:1 P:In ratio (Figure 3.9d), after an initial rise in the first 15 min of the reaction, the amount of **3** is decreasing until around 30 min and then remains stable, while the evolution of **4** follows a similar behavior as before with its rise correlated to the drop of **1**. The observed decrease of the P(V) compound **3** is tentatively assigned to its reduction through In(I) or In(0) in the reaction medium. Finally, for the 4:1 ratio (Figure 3.9e), the phosphonium salt **3** becomes the main product, while still a significant amount of **4** is formed. Strikingly, the amount of **4** formed for all P:In ratios after 60 min is roughly the same (0.3–0.45 mmol) in In(I)Cl-syntheses and its evolution with reaction time follows the same trend. Therefore, we can deduce that the formation of **4** is related to the interaction of the transaminated aminophosphine with the In(I) precursor as the initial concentration of In(I) was kept constant in all experiments (0.5 mmol).

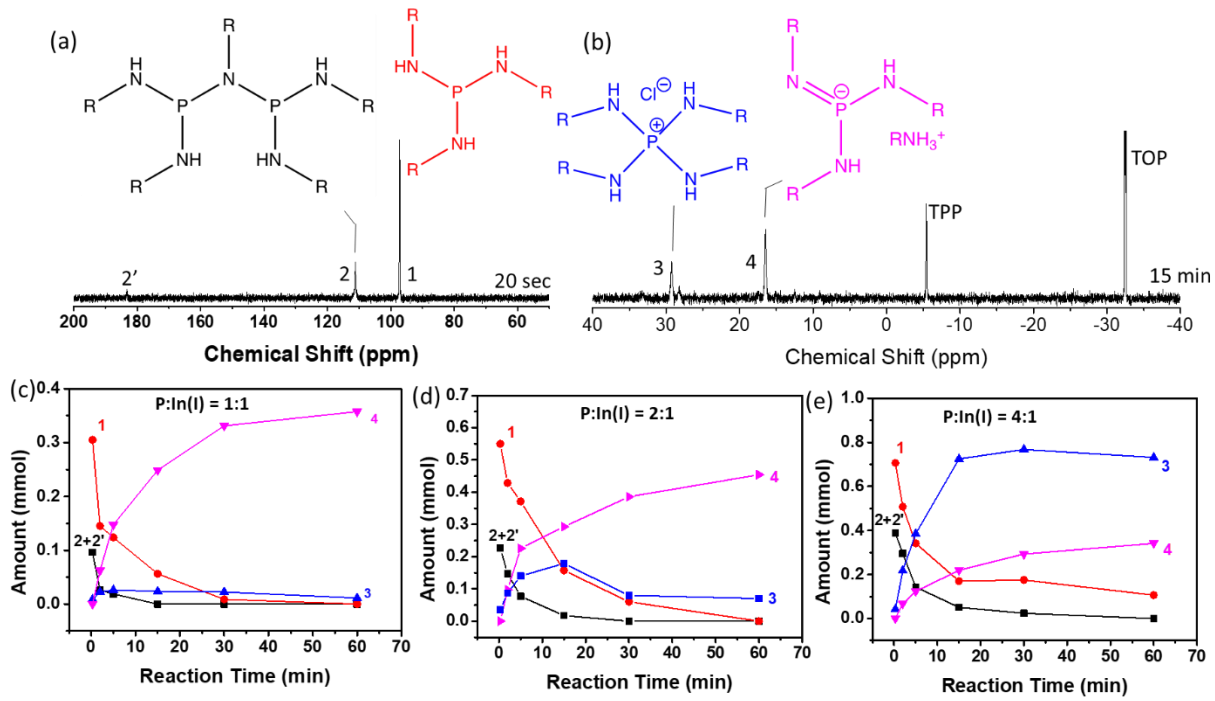

Figure 3.9: (a) $^{31}P\{^{1}H\}$ NMR spectrum of the reaction mixture after 20 sec of the reaction at 220°C using (P:In=1:1) and attribution to the compounds **1, 2** and **2'**. (b) $^{31}P\{^{1}H\}$ NMR spectrum of the reaction mixture after 15 min at 220 °C using a 2:1 P:In ratio and attribution to the compounds **3, 4,** TPP(external reference) and TOP. Evolution of the amount of the different P-containing species with reaction time determined by $^{31}P\{^{1}H\}$ NMR: (c) P:In =1:1,(d) P:In =2:1, (e) P:In =4:1. For all reactions an indium concentration of 0.5 mmol was used.

Next, we compared the reported standard aminophosphine synthesis using $InCl_3$ (P:In = 4:1) with a reaction applying In(I)Cl under identical conditions to study the reaction kinetics. Figure 3.10a depicts the UV-vis absorption spectra obtained for both cases. The first excitonic peak features of the different aliquots are better pronounced in the case of In(I)Cl than of $InCl_3$ suggesting a narrower size distribution. Moreover, the synthesis with In(I)Cl (Figure 3.10a) follows a LaMer-like behavior, with a nucleation burst at short reaction times (0-5 min) and subsequent growth from solution(10-60 min).[132] It is noteworthy that when InCl is employed as the In precursor, a better reaction yield (78 vs 46%) is achieved than with $InCl_3$ after 60 min, once again supporting the involvement of the In(I) induced reduction pathway. As shown in Figure 3.10b-c, in the 4:1 P:In case, the reaction kinetics is slower with InCl than with $InCl_3$ as only 25 vs. 43% of phosphorus is consumed during 2 min of reaction but more InP units were formed. These results further support that the reduction of P by In(I) is the dominating mechanism at early reaction times (0-5 min). Additionally, we observed unreacted P precursor (10-15%) at the end of the InCl reaction likely due to the complete consumption of the In precursor.

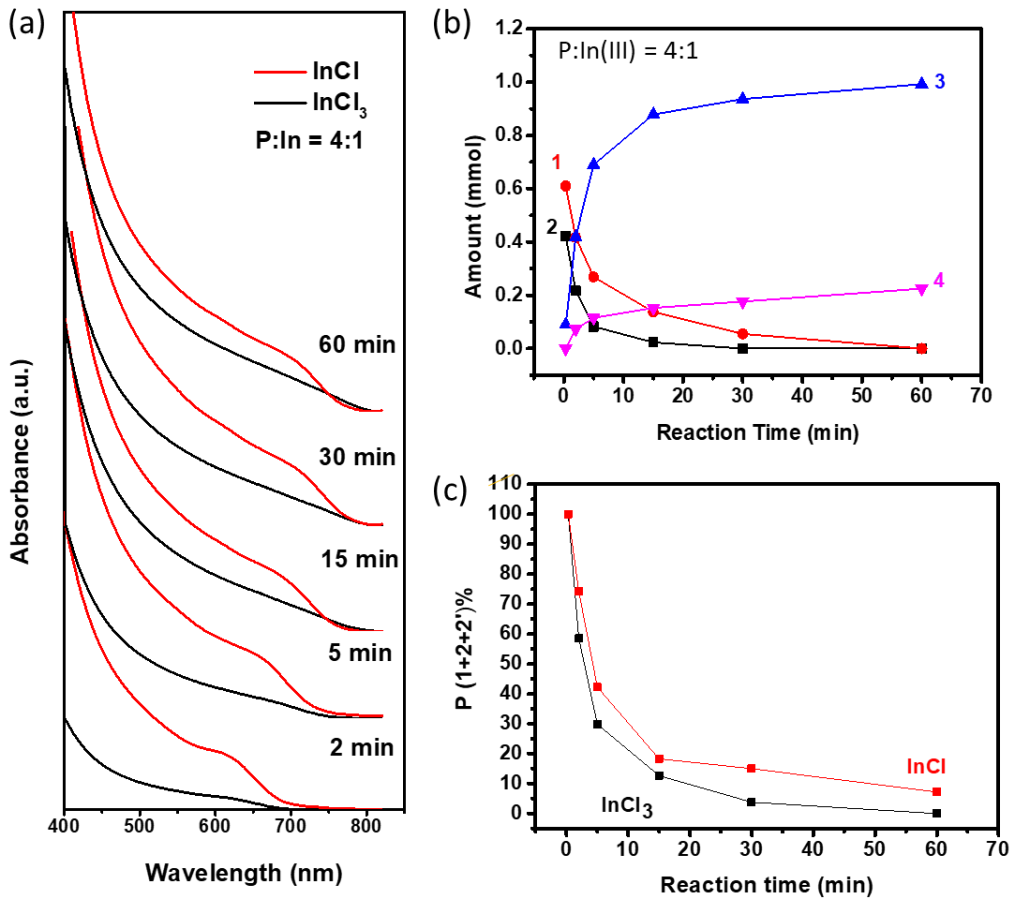

Figure 3.10: (a) Absorption spectra of InP QDs synthesized using InCl (red) and $InCl_3$ (black) with an excess of phosphorous (P:In = 4:1) (the spectra are vertically shifted for clarity). (b) Formation of the different P species with reaction time in the case of $InCl_3$ (black). Synthesis with $InCl_3$ is performed in similar reaction condition as InCl (c) Consumption of the P amount (%) during the synthesis with InCl (red) and $InCl_3$ (black) (P:In ratio = 4:1). The amount of P (reactant) is calculated from adding transaminated aminophosphine 1 (97 ppm), 2(111 ppm) and 2'(181ppm) (vide infra).

The InP formation reaction implying In(I)X and aminophosphine is not yet well understood. Nevertheless, the analysis of the above-described evolution of the different P-containing species allows us to draw a few conclusions about the reaction mechanism. As stated before, the full conversion of $P(NHR)_3$ would require a P:In ratio of 1:3, however, this condition resulted in a very low reaction yield (Figure 3.1d). Therefore, a higher amount of P is required to activate the In–X bond, in particular for X=Cl. At the 1:1 P:In ratio almost no phosphonium salt **3** is formed (Figure 3.11), and assuming that this compound is the only P(V) species, it can be concluded that reduction via In(I) is the largely predominant reaction pathway, which is also supported by the good match of the measured and theoretical reaction yield (around 40%).

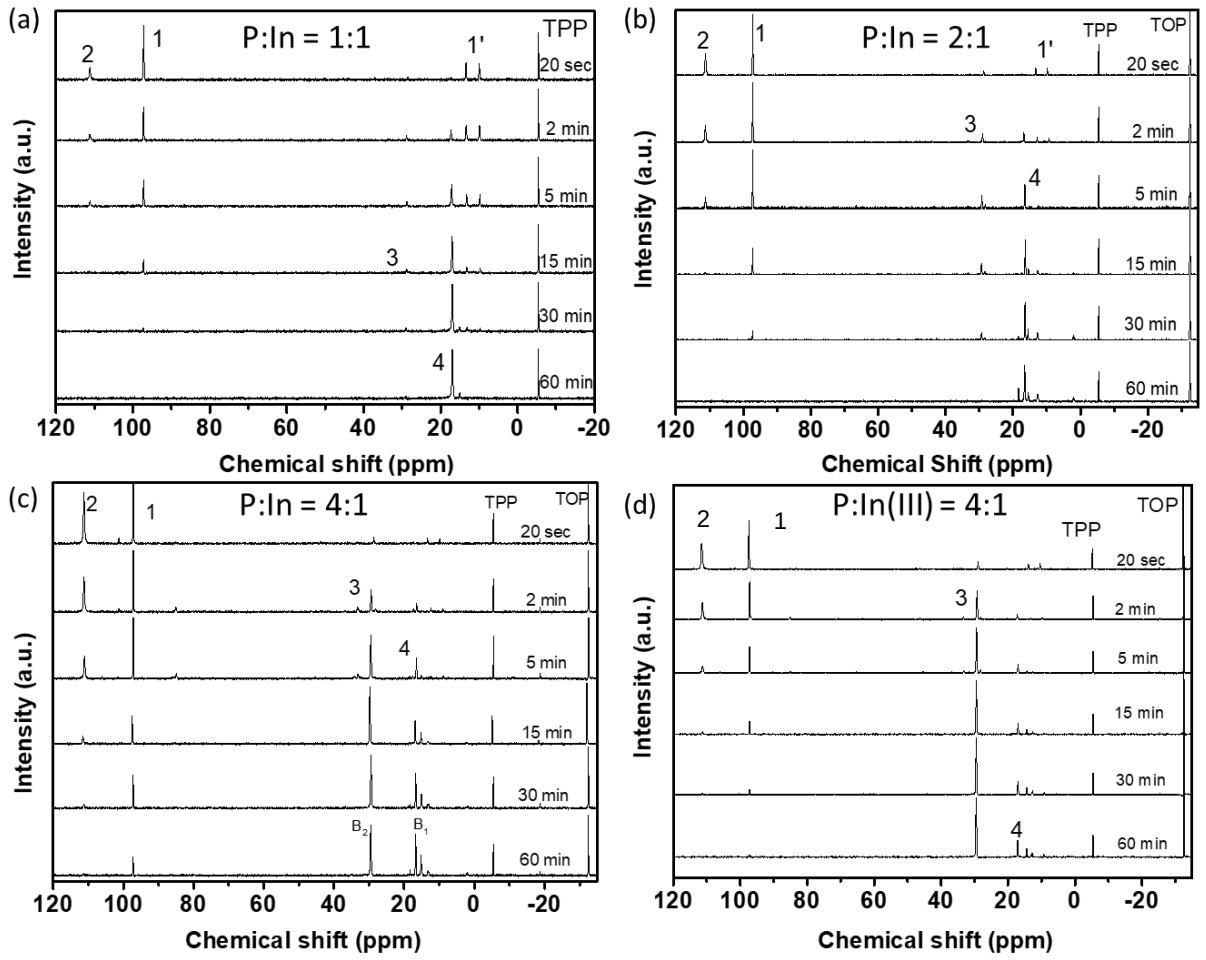

Figure 3.11: Proton-coupled ^{31}PNMR spectra of as-synthesized InP QDs obtained with different ratios of $P(NEt_2)_3$ and InCl; (a) P:In = 1:1 (b) P:In = 2:1 (c) P:In = 4:1. (d) Control experiment using $InCl_3$ instead of InCl with a P:In ratio of 4:1.

As shown by Buffard et al.,[80] the formation of a $(RHN)_2P–InCl_2$ fragment is the rate-determining step in the formation of the first In–P bond in the synthesis based on $InCl_3$ and aminophosphine. This step comprises the required redox reaction and necessitates an additional $P(NHR)_3$ unit. In the case of low P:In ratios in the In(I)Cl reaction, this step is either suppressed (P:In=1:1) or of minor contribution (P:In=2:1) in the overall reaction, showing that the involved intermediate adduct complex between $P(NHR)_2NR^-$ and In halide cannot react further like in the In(III)-based synthesis. This situation leads to the release of compound **4** (which corresponds indeed to $P(NHR)_2NR^-$) over the course of the reaction. Its almost constant appearance for all P:In ratios (vide supra), allows us to conclude that the adduct of $P(NHR)_2NR^-$ and In halide is an important reaction intermediate in the In(I) reaction pathway, activating the In–X bond and leading to a fast formation of InP units even at low P:In ratios. At higher ratios, the disproportionation pathway becomes competitive as seen by the evolution of compound **3** with the reaction time. In the cases of In(I)Br and In(I)I, the higher reaction yields already obtained for P:In ratios of 1:1 and 2:1 evidence the stronger contribution of the disproportionation pathway, which is kinetically favored by the lower In–X bond dissociation enthalpies.

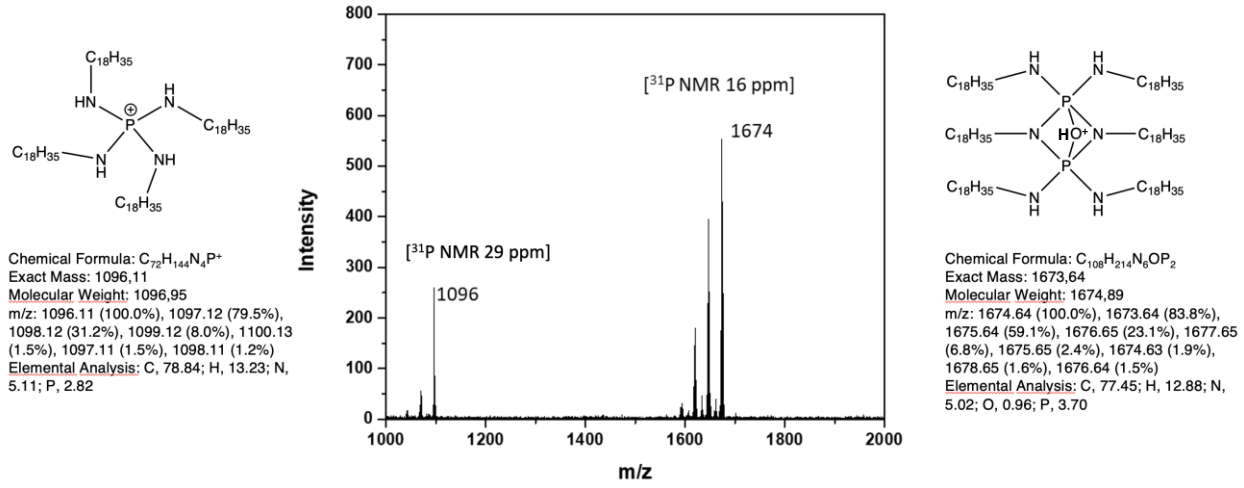

Figure 3.12: Mass spectrum of the supernatant obtained from the reaction using P:In = 1:1 after 60 min, in which the species giving rise to the 16 ppm peak in ^{31}P NMR is predominant. Oxidation of the cyclic dimer occurred presumably during the analysis, which was carried out under air.

3.3.6. In situ HF etching of InP QDs

As in reported aminophosphine syntheses using In(III)Cl_3,[78-80] the obtained core InP QDs via the In(I)Cl route do not show PL emission. The quenching of PL is generally attributed to surface trap states or surface oxidation (in the case of PTMS-based synthesis).[78, 98] HF treatments have been widely used to improve the PLQY of InP and In(Zn)P core QDs eventually followed by the subsequent overgrowth with an inorganic shell.[98, 133-136] However, most of the reported methods involve the use of aqueous hydrofluoric acid, which is extremely dangerous. Very recently, Houtepen and coworkers reported a post-synthetic method relying on a safer way of generating HF *in situ* using benzoyl fluoride in presence of octylamine and successfully etched InP QDs at temperatures between 150 °C and 200 °C (Scheme 3.1).[124] They achieved high PLQY values of 40 – 70% with some broadening of the line width (FWHM around 70 nm). The PLQY could be further enhanced up to 85% by adding a Z-type ligand ($ZnCl_2$) at the beginning of the etching process to assure the passivation of phosphorus dangling bonds at the QD surface. Inspired by this work, we subjected the InP QDs synthesized with the In(I)X – aminophosphine approach to a similar benzoyl fluoride/$ZnCl_2$ treatment, comparing different temperatures and ratios.

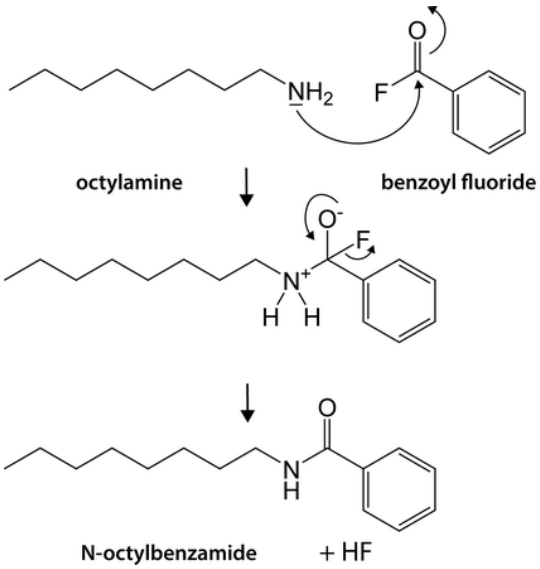

Scheme 3.1: Reaction mechanism of *in situ* HF generation.[124]

3.3.6.1. Effect of temperature

First, we have tested the effect of temperature in our study since it is one of the critical parameters for the etching process. The experimental details of the etching process are presented in the experimental section. We prepared three samples by etching at 150 °C, 100 °C and RT (Figure 3.13a) and found that the etching process was very fast for the samples kept at high temperature, requiring only 5-10 min. Figure 3.13a shows the photographs under UV light for samples etched for 5 min at higher temperature exhibiting a strong red emission. Surprisingly, we found that room temperature etching is possible in our case as the sample etched at RT exhibited a strong emission after 40-60 min of etching. Figure 3.13 shows the absorption spectra of InP QDs etched at different temperatures. A blue shift of 25-30 nm was observed in the absorption peak due to reduction of the particle size. Moreover, the PL spectra (Figure 3.13b) also confirm that the etching is faster in case of high temperature resulting in a more blue-shifted PL. We can also see that etching is more controlled in case of room temperature producing the narrowest line width (43 nm/119 meV at 668 nm) reported for the aminophosphine route so far. These results are in stark contrast with the reported etching procedure,[124] which leads to a significant broadening of the absorption features. We hypothesize that the use of room temperature etching is at the origin of this behavior and that the reported elevated temperatures (150-200 °C) are not required in our case due to the absence of an oxide layer on the InP core QDs. This assumption is supported by the comparison of both synthesis methods: in the present study no oxygen-containing precursors are applied, while in the reported study $P(TMS)_3$ was reacted with *in situ* prepared indium palmitate at 260 °C. These conditions can favor the ketonization of the fatty acid molecules under the release of water, inducing oxidation of the InP QD surface.[137]

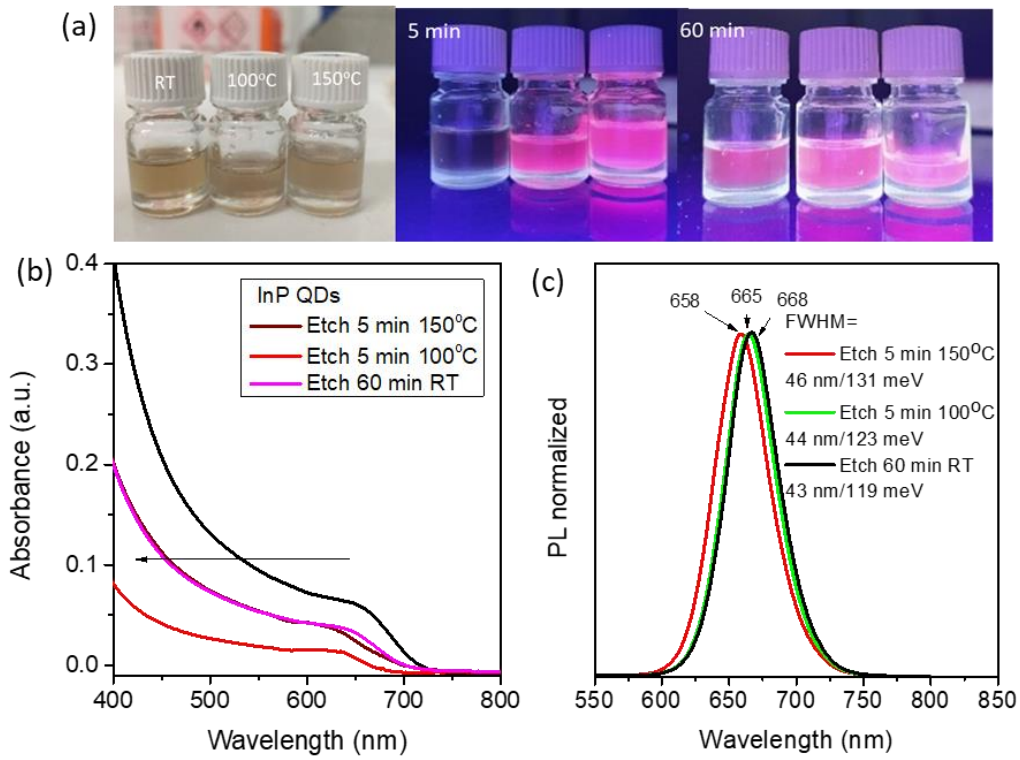

Figure 3.13: (a) Photograph of in-situ etched InP QDs before and after 5 and 60 min of etching at different temperatures. (b) Absorption and (c) photoluminescence spectra of InP QDs after etching at 150 °C (5min), 100 °C (5 min) and RT (60 min).

3.3.6.2. Effect of $ZnCl_2$ addition

Figure 3.14 shows the PL spectra of the etched InP QDs with or without addition of $ZnCl_2$ before the etching. Both samples were etched at room temperature under otherwise identical conditions. We can see that the PL was blue shifted (657 vs. 667 nm) when $ZnCl_2$ was not added before the etching. Moreover, after comparing the emission line width for both cases, we found that the addition of $ZnCl_2$ leads to a slightly smaller value (136 meV vs. 141 meV).

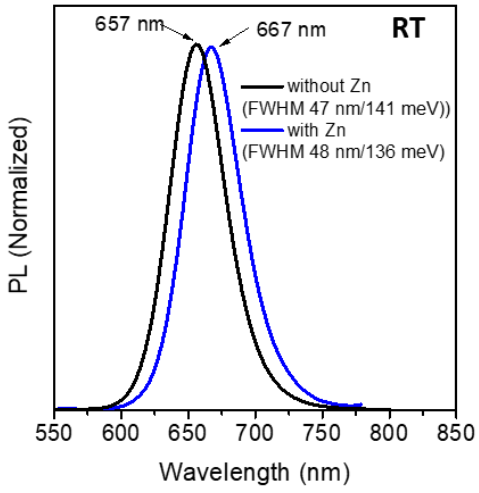

Figure 3.14: PL spectra of InP QDs prepared with or without $ZnCl_2$ addition before the RT etching process.

3.3.6.3. Room temperature etching under the optimized conditions

InP QDs prepared with InI were etched for 10 minutes at room temperature while InP QDs synthesized using InBr and InCl were etched for 20 and 60 minutes, respectively. Washing the InP QDs before the etching was found to be important to remove oleylamine, which was used as the solvent for the InP synthesis. As mentioned before, the best results in terms of PLQY and line width were obtained by simply carrying out the etching process at room temperature, which has the further advantage of slowing it down and thus making it better controllable. The UV-vis absorption spectra of the QDs obtained with the three different halides showed a blue shift of 20-45 nm (Figure 3.15a-c). While the spectral shape remained essentially unchanged in the case of the QDs prepared with InI, a marked (slight) enhancement of the excitonic peak features is visible in the case of InBr (InCl).

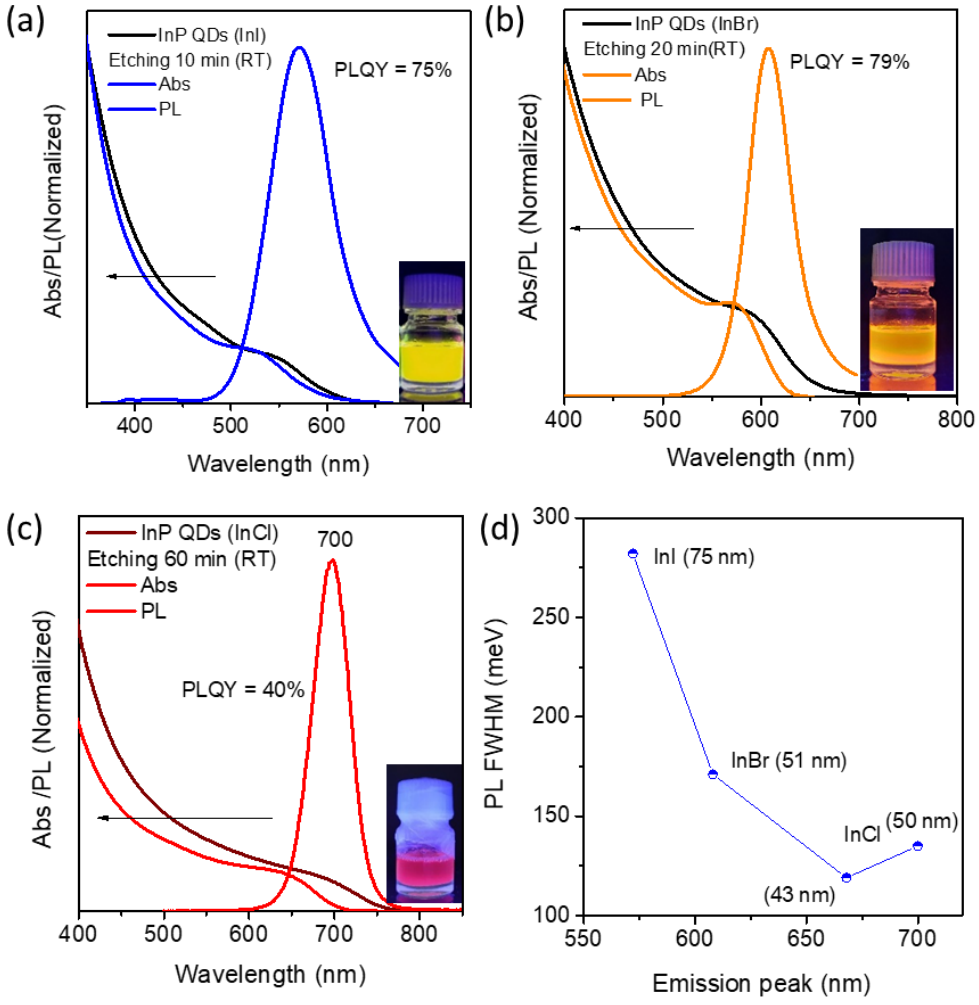

Figure 3.15: Room temperature etching of the purified InP QDs using benzoyl fluoride and octylamine. Comparison of the UV-vis absorption spectra before and after etching and PL spectra after etching of QDs synthesized with InI (a), InBr (b), and InCl (c). The insets show photographs of the etched samples under UV light. (d) PL line width (FWHM) and emission peak position of the etched samples

For all three indium (I) halides cases, strong PL emission is detectable under UV light and the PLQY reached up to 79% for the QDs etched under optimized conditions. As an example, yellow emitting InP QDs obtained with InI exhibit 75% PLQY after 5 min of the etching. It is noteworthy that the etching process is considerably faster for smaller particles as the emission changes from yellow to green in only 10 min. The yellow emitting InP QDs exhibit an emission linewidth of 75 nm (282 meV) (Figure 3.15a), which is rather broad but similar to the reported case (70 nm/300 meV),[124] and increases with the etching time. The orange emitting samples prepared with InBr exhibit a much narrower emission line width of 53 nm (160 meV) with the highest PLQY of 79%. Deep-red emitting QDs prepared with InCl show the narrowest emission line width with a FWHM of 43 nm (119 meV) for an emission at 670 nm and 50 nm (131 meV) for an emission at 700 nm with 40 % PLQY (Figure 3.15c-d/16a).

Table 3.2: Stokes shift of in-situ HF-etched InP QDs prepared with InCl, InBr and InI.

Emission Peak (nm)	**Energy (eV)**	**InX (X=Cl,Br,I)**	**Stokes shift (meV)**
570	2.17	InI	186
607	2.04	InBr	121
668	1.85	InCl	118
700	1.78	InCl	125

The same trend as for the line widths is observed for the Stokes shift of the etched QDs prepared with the different halides (Table 3.2). While the InP QDs synthesized with InI exhibit a large Stokes shift of 186 meV, the QDs prepared with the other two halides show much smaller values in the range of 118-125 meV. Figure 3.16b shows the PL decay analysis of InP QDs after etching at room temperature for 60 min. The average lifetime is significantly reduced (37.2 ns) compared to previous studies (>100 ns),[124] which can be attributed to the successful removal of surface traps in our case.

In conclusion, our results show that room temperature in situ HF etching is a convenient post-synthetic surface treatment for the In(I)X and aminophosphine-route obtained InP core QDs leading to high PLQY without negatively affecting their size distribution. However, it should be noted that all the experiments were done in very low concentration (nmol/mL). We did not test the scalability of this method during our optimization.

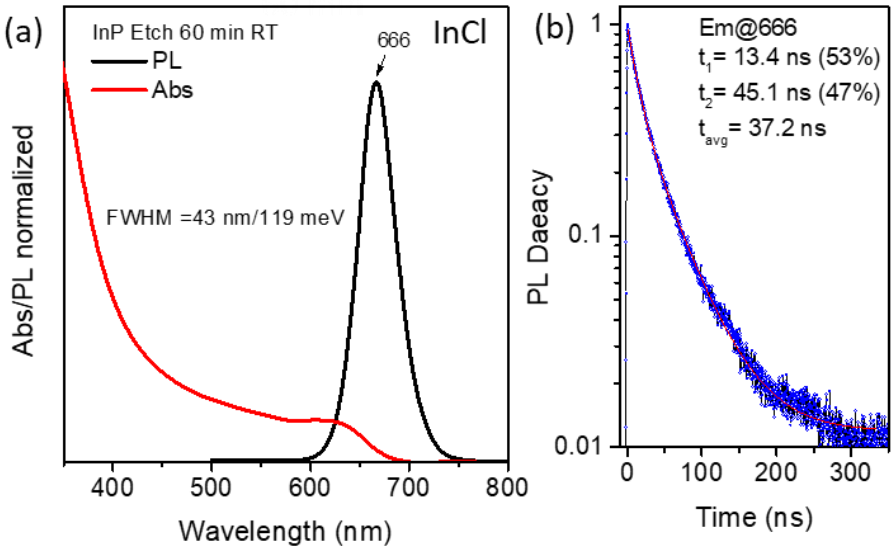

Figure 3.16: (a) Absorption and PL spectra (normalized) of in-situ HF etched InP QDs (60 min, RT) prepared with InCl. (b) TRPL decay profile of the etched QDs (emission peak: 666 nm).

3.3.7. InP/ZnS core/shell QDs

As a second way of enhancing the PL efficiency, we used the traditional method of overgrowing the core with a larger band gap semiconductor to create a core/shell structure. Typical choices for InP are ZnS, ZnSe, or combinations thereof,[88] and meanwhile, PLQYs of virtually 100% have been obtained in fully optimized systems with cores from $P(TMS)_3$ or aminophosphine based syntheses.[15, 134] In our approach, using a zinc- and oxygen-free core QD synthesis, we wanted to avoid high temperatures to prevent from ripening and alloying with Zn, which could induce PL line broadening as discussed in the introduction.[121] Moreover, we also aimed at avoiding oxidation processes induced by the *in-situ* transformation of the carboxylate precursors during the shelling process, such as amide formation or ketonization.[138] As an alternative, single-source precursors such as zinc diethyldithiocarbamate [$Zn(DDTC)_2$] or zinc ethylxanthate are characterized by low thermal decomposition temperatures (<200 °C) and are therefore suitable monomolecular sources for ZnS shelling under mild conditions.[139-140]

As shown in the schematic in Figure 3.17a, InP/ZnS core-shell QDs were prepared at 140 °C using $Zn(DDTC)_2$ in a simple one-pot heat-up approach. We observed the appearance of luminescence followed by a significant increase in PL intensity with ZnS shelling time (0-5 h), no further evolution was noted for longer times (Figure 3.17b). As an example, a sample emitting at 695 nm obtained with InCl exhibited a PLQY of 16% and a PL linewidth of 53 nm/123 meV after 5h of shelling. Figure 3.17c shows TEM images of core/shell QDs having size of 11.5 ± 1.6 nm after ZnS shelling of 9.4 ± 1.4 nm-sized core particles corresponding to a ZnS shell thickness of around 2.1 nm (~3 monolayers). The InP/ZnS QDs retained the same tetrahedral shape as the core particles.

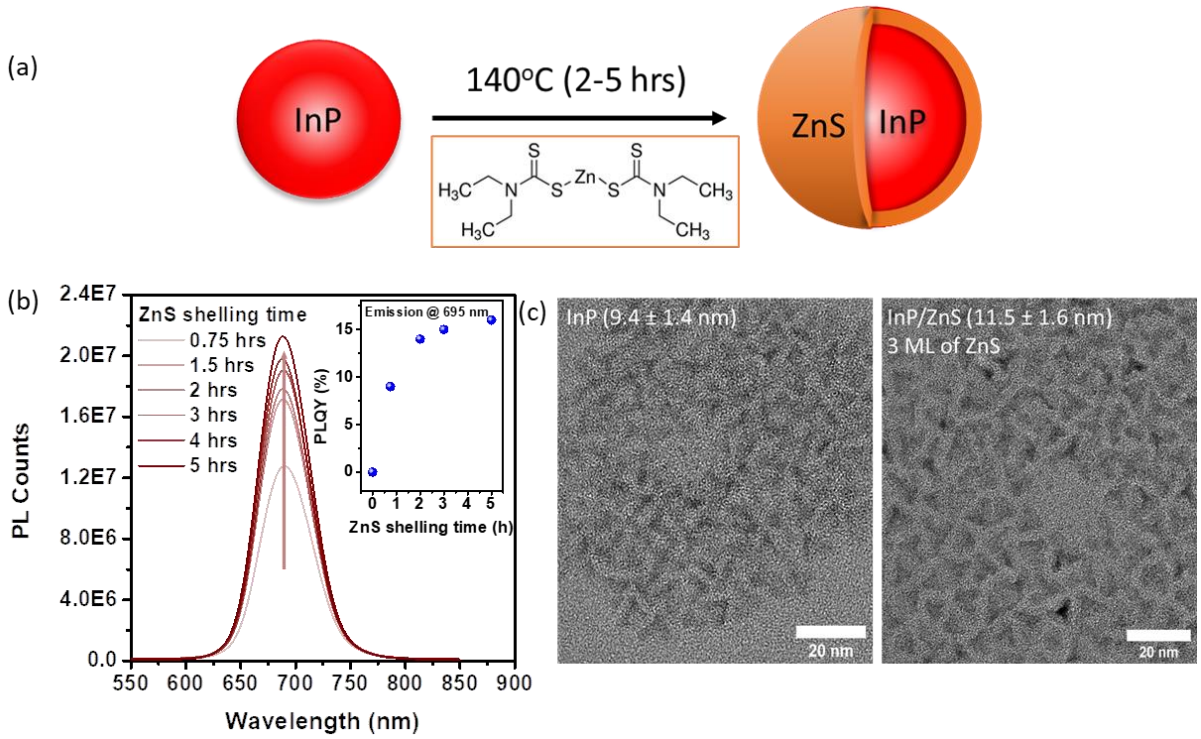

Figure 3.17: (a) Schematic of the synthesis of InP/ZnS core/shell QDs at low temperature using the single-source precursor $Zn(DDTC)_2$. (b) Evolution of the PL spectra of the obtained InP/ZnS QDs with shelling time. (c) TEM images of InP QDs and InP/ZnS QDs.

No detectable redshift of the first excitonic peak occurred upon ZnS shelling (Figure 3.18). However, in the case of InP QDs prepared with InI and InBr, the absorption features became better resolved during the ZnS overgrowth (Figure 3.18a-b), which is opposite to most reported shelling procedures. We attribute this effect to the low shelling temperature of 140 °C used, which minimizes ripening processes, and the passivation of shallow surface trap states with ZnS leading to the sharpening of the spectral features and diminution of the red tail in the absorption spectra.

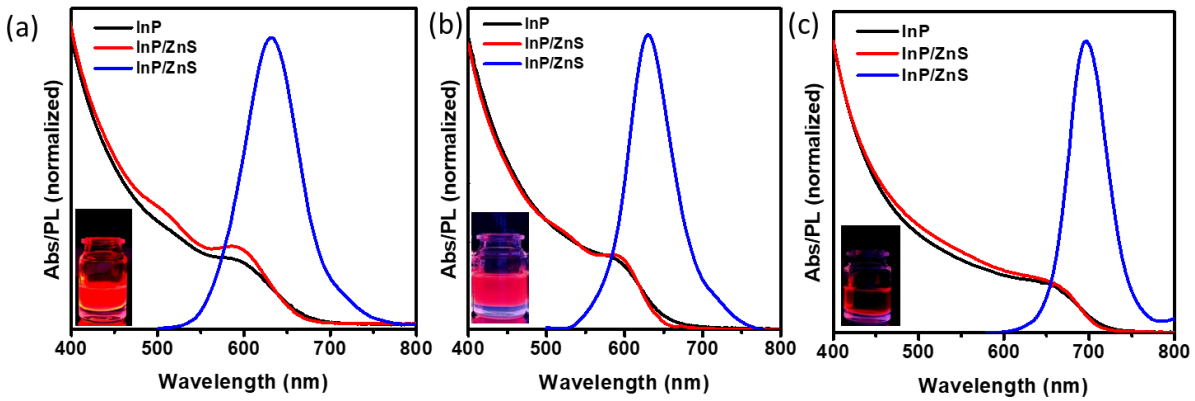

Figure 3.18: UV-vis absorption spectra of the InP core (blue) and InP/ZnS core/shell (black) QDs along with their PL spectra (red) for InP core QDs prepared with InI (a), InBr (b) or InCl (c).

Powder X-ray diffraction (Figure 3.19) shows a systematic shift to larger angles of all diffraction peaks towards the positions of ZnS in the zinc blende structure. This behavior is generally observed when overcoating different types of QDs with ZnS due to the lower lattice parameter of the shell material and the resulting compressive strain exerted on the core.[141]

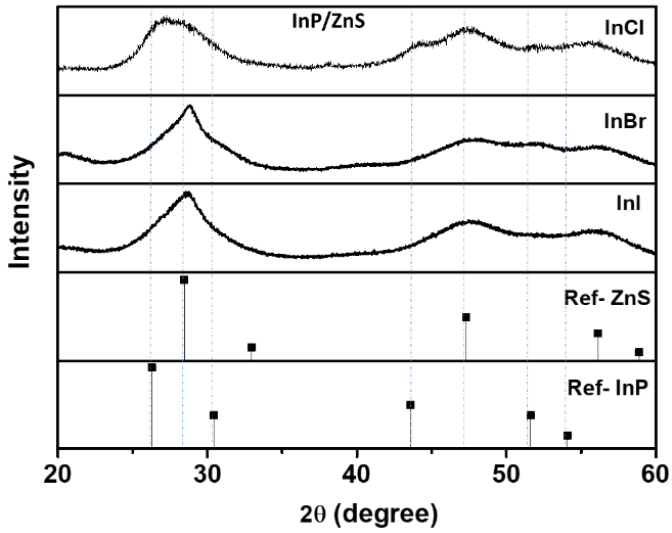

Figure 3.19: (a) X-ray diffraction patterns of InP/ZnS QDs synthesized using InCl, InBr, and InI. The vertical black lines represent InP Bulk reference (# 00-032-0452) and ZnS bulk reference (# 01-071-5976) patterns.

Figure 3.20a depicts the emission spectra of InP/ZnS QDs obtained with cores using different indium (I) halides, which results in a tunable emission in the range of 594–728 nm. The evolution of the line width (FWHM) and PLQYs of the InP/ZnS QDs are shown in Figure 3.20b. It should be noted that no efforts have been made at this stage to optimize the emission efficiency, which would very likely necessitate the introduction of a ZnSe and/or GaP intermediate shell to adapt the large lattice mismatch between the InP core and the ZnS outer shell (7.7%). For the same crystallographic reasons, it was not

possible to grow much thicker ZnS shells on the InP core QDs without degrading their emission properties: as the cores are already of large diameter and with flat surfaces in the tetrahedral-shaped particles, low lattice mismatch is becoming a more stringent requirement than in the case of much smaller spherical QDs.

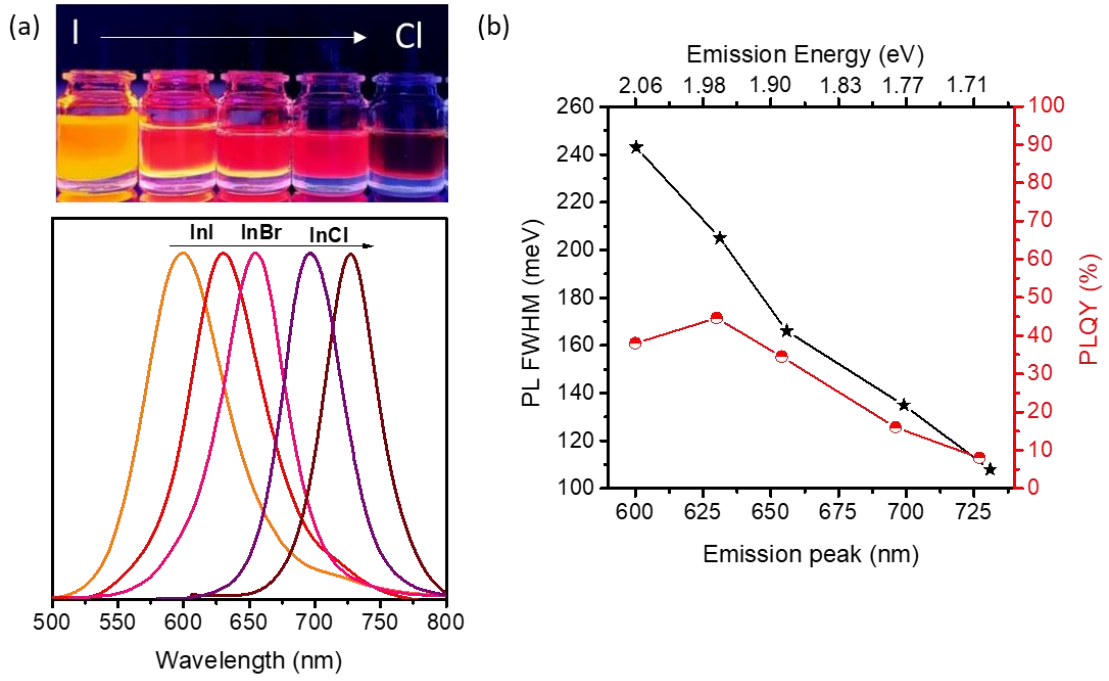

Figure 3.20: (a) PL spectra of the obtained InP/ZnS QDs using cores synthesized with different In(I) halides. (b) Line width (FWHM, black curve) and PLQY (red curve) as a function of the emission wavelength.

The emission line width decreased as expected with increasing PL wavelength, due to the fact that the large particles obtained with InCl are in a weaker confinement regime than the smaller nanocrystals synthesized with the other halides. By consequence, the same size distribution induces a significantly lower energy dispersion in the case of the bigger particles. Notably, the line width of the biggest QDs emitting at 728 nm is with 48 nm (112 meV) FWHM the narrowest reported for InP QDs in the NIR range and comparison with the values obtained in the etching experiments demonstrates that the ZnS shell growth did not induce any broadening. A relatively small Stokes shift of 108 meV (Table 3.3) was observed as in the HF-treated samples (118 meV) in our study, which is much lower than that of previously reported HF-treated InP QDs (188 meV) or In(I)X_3-based In(Zn)P/ZnS QDs (165 meV).[121] This behavior can be attributed to the fact that in our case the samples exhibit lower structural disorder due to the absence of doping and of oxygen- and/or zinc-containing species at the surface.

Table 3.3: Stokes shift of InP/ZnS QDs using InP cores prepared with InCl, InBr and InI.

Emission peak (nm)	Energy (eV)	InX	Stokes shift (meV)
633	1.95	InI	140
630	1.96	InBr	126
697	1.78	InCl	108

Time-resolved photoluminescence (TRPL) measurements were carried out for the InP/ZnS QDs obtained with the different core particles to study the excited-state dynamics and PL decay kinetics. Figure 3.21 shows the PL decay curves of the InP/ZnS QDs measured for yellow (604 nm), red (650 nm), and deep red (720 nm) emitting samples, which were fitted using bi-exponential functions (Table 3.4). The shorter component (5-10 ns) is generally attributed to the recombination at surface states, while the longer component (48-52 ns) corresponds to the intrinsic excitonic transition. Both decay times are significantly shorter than those observed for alloyed In(Zn,S)P and In(Zn)P QDs (34-38 ns and 75-85 ns).[60, 142] The average lifetimes of 40-48 ns are similar to the values reported for non-alloyed red-emitting InP-based QDs[98, 113] and slightly higher than in the case of the HF-etched QDs (37 ns) of this study.

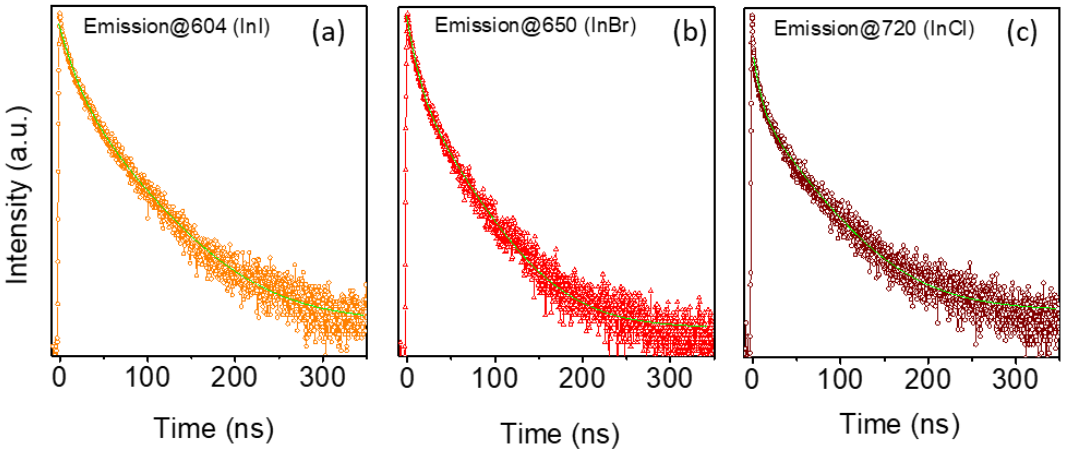

Figure 3.21: PL decay curves measured at the emission peaks of 720 nm (brown), 650 nm (red), and 604 nm (orange).

Table 3.4*:* PL lifetimes of InP/ZnS QDs calculated from TRPL data.

Indium (I) halide	**Peak emission (nm)**	**τ_1 (ns) (A_1%)**	**τ_2 (ns) (A_2%)**	**τ_{avg}(ns)**	**PLQY (%)**
InI	604	8 (54)	52 (46)	45.3	41
InBr	650	9 (55)	48 (45)	40.7	35
InCl	720	5 (59)	53 (41)	47.3	8

Finally, photoluminescence excitation (PLE) spectroscopy was carried out to investigate the relaxation of excitons for ensemble InP QDs emitting at 604 nm (InI), 650 nm (InBr), and 728 nm (InI). Figure 3.22a/b/c shows the PLE spectra for samples prepared using the different In (I) halides. The PLE spectra are in good accordance with the absorption profiles showing multiple transitions irrespective of the halide used. Moreover, the line width (FWHM) of the excitonic feature in the PLE spectra is considerably smaller than that of the fitted first excitonic peak, especially in the case of InCl (Figure 3.22c). Figure 3.22d shows the PLE spectra of the 630 nm emitting sample at various detection energy across the PL profile. No significant broadening in the PLE spectra was observed when detection energy was shifted to the lower energy side. Figure 3.22e summarizes the differences in the ensemble absorption and PLE spectrum line widths. The latter reach for the samples prepared with InBr and InCl values close to that reported by Talapin and coworkers for pure InP QDs (114 meV).[121] In these cases, the observed reduction in the PLE line width compared to the absorption spectra suggests that the size distribution of the InP QDs is the main cause for the PL broadening in the ensemble spectra. For the InI sample, however, the PLE line width is significantly larger (241 meV) than for the InCl and InI samples. Therefore, the broad PL emission of this sample cannot stem from an ensemble of narrow single emitters. We hypothesize that InI (or InI_3) is a less efficient Z-type ligand than InCl or InBr for passivating undercoordinated anionic sites on the QD surface.[143] Therefore, trap states at the InP/ZnS interface can lead to carrier localization and stronger electron-phonon coupling.

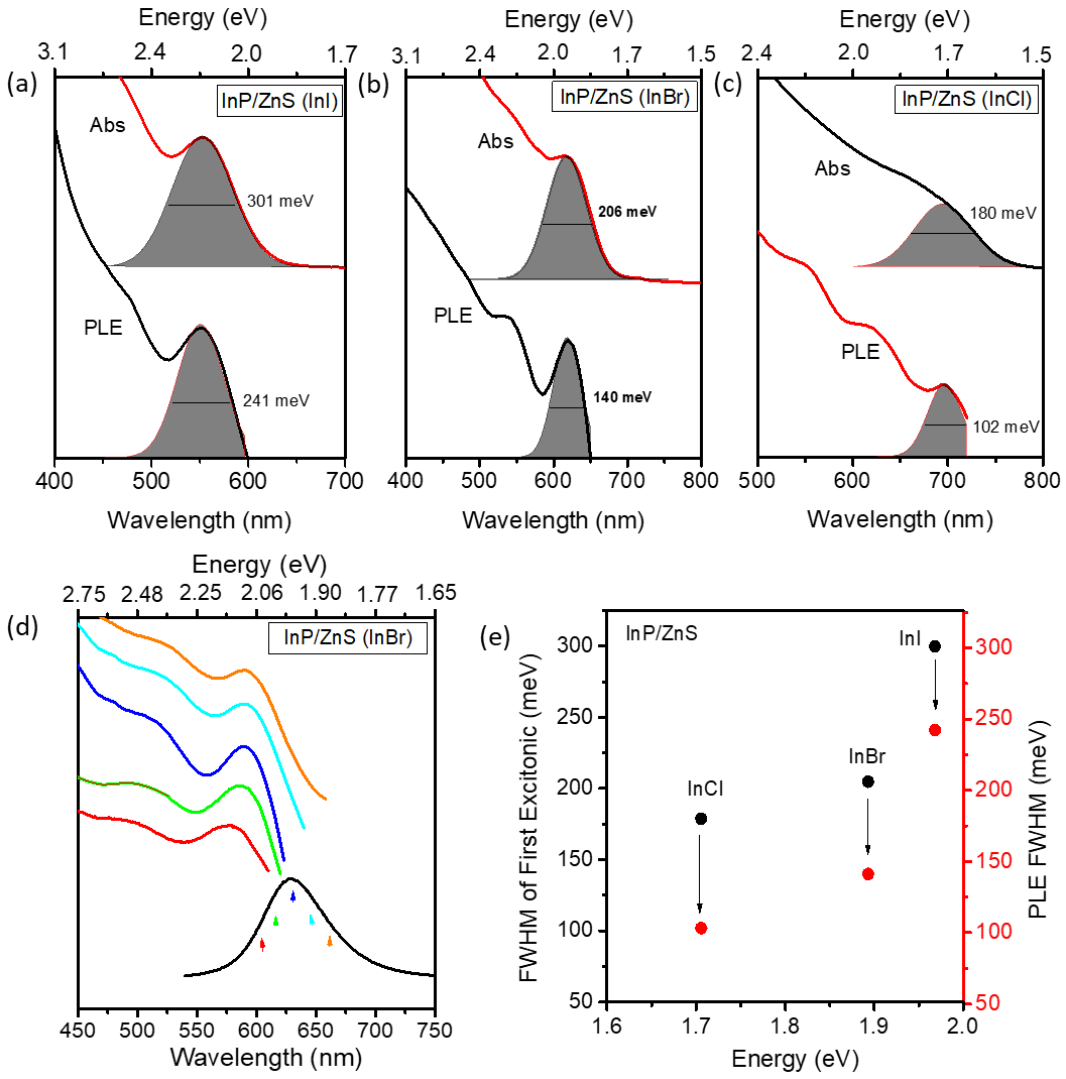

Figure 3.22: Comparison of FWHM of the excitonic peak feature in the PLE and absorption spectra. The PLE is recorded at the peak emission values of (a) 603 nm, (b) 654 nm, (c) 728 nm. The FWHM is calculated from Gaussian fits (shaded area) for both the PLE and absorption spectra. (d) PL spectrum (black) and PLE spectra of InP/ZnS QDs where the PLE is recorded across the emission range (marked with arrows). (e) Representation of the change in FWHM obtained from the PLE spectra (red circles) with respect to the absorption data (black circles).

3.4. Conclusion

We developed a novel synthesis protocol for obtaining size-focused and size-tunable InP QDs using indium (I) halides and aminophosphine. The In(I)X precursors have the dual role as the In source and reducing agent for aminophosphine. As the halide was varied from I over Br to Cl, the size of the obtained InP QDs could be controlled in a large range from 3-11 nm while the size distribution remained unaffected (12-13%). InI is more reactive compared with InBr or InCl resulting in the smallest InP QDs. For InCl, a higher P:In feed ratio (4:1) was needed to achieve high reaction yield than with InBr and InI, for which a ratio of 2:1 was sufficient. These differences could be explained by the different

contributions of the two reduction mechanisms, via In (I) halide and via aminophosphine disproportionation, as revealed by phosphorus NMR spectroscopy. To improve the PLQY, the InP QDs were etched at room temperature using *in-situ* generated HF. The first excitonic absorption peaks of InP QDs exhibited a blue-shift of 20-48 nm as a result of etching and their PL intensity increased significantly up to 79% showing a narrow emission line width of 43-50 nm FWHM (119-135 meV), low Stokes shift (125 meV for an emission at 700 nm), and comparably short PL lifetime (37.2 ns). Furthermore, we synthesized InP/ZnS core/shell QDs using $Zn(DDTC)_2$ at low temperature (140 °C). The obtained core/shell QDs showed a PLQY up to 44%, once again with narrow emission line width (112 meV at 728 nm) and low Stokes shift (108 meV). The PL line width in our study is the lowest value reported for aminophosphine-based syntheses and quasi-identical with the best reported linewidth obtained with $P(TMS)_3$ (110 meV at 630 nm).[25] Taken together, these results confirm that the emission properties of InP-based QDs can indeed be improved and a larger size range accessed by avoiding Zn addition during the core synthesis. These results present the groundwork for preparing high-quality InP QDs with wide tunability of their optical properties from the visible to the near NIR range.

Chapter IV

Trial synthesis of InP nanoplatelets

4.1. Introduction

In the past decade, colloidal synthesis of semiconductor nanocrystals (NCs) has shown remarkable development with ever-growing demands for their application in various fields.[4, 26, 90-91] One of the main advantages of colloidal synthesis is the ability to control the shape or the morphology of NCs.[67, 144] Many semiconductor NCs show very interesting shape-dependent optoelectronic properties such as a modified charge carrier distribution within the NCs, polarized emission, modulable Stokes shift and so on.[145-146] Depending on their confinement dimension, various anisotropic structures can be formed such as one-dimensional nanorods (NRs),[144] two-dimensional nanoplatelets (NPLs)[67, 144] and more complicated branched structures such as tetrapods.[147] Compared with 0D quantum dots, atomically flat 2D NPLs made from ZnSe,[148] CdSe, and CdS[22] have shown a unique influence of their thickness on their electrical and optical properties, leading to extremely sharp absorption and emission profiles. Additionally, the planar surface improves the linear and nonlinear absorption coefficients and suppresses the non-radiative recombinations.[149]

The II-VI group of semiconductor NCs including CdSe, CdTe, CdS, ZnSe, and ZnS has been largely explored to generate anisotropic nanostructures.[144, 148] In the majority of cases, structure-directing agents (e.g., organic acids or amines) are used to synthesize anisotropic structures. These agents show higher affinity towards a particular facet, and as a result, the crystal growth is suppressed in the direction perpendicular to this facet. In comparison to the II-VI compounds, the In–P bond is more covalent in nature and thus shows less reactivity towards structure-directing agents. Moreover, InP crystallizes in the cubic zinc blende structure and does not show the zinc blende/wurtzite polytypism characteristic of the mentioned II-VI compounds. For these reasons, it is highly challenging to achieve symmetry breaking and anisotropic growth in the case of InP. This largely explains why there are only a few reports on the anisotropic growth of InP NCs via the colloidal route. In a recent study, Kim et al. synthesized InP tetrapods by isolating the InP intermediate and then thermodynamically controlling the growth of specific facets.[128] InP NPLs were synthesized using a cation exchange-based method where anisotropic Cu_3P NPLs were used as a template due to a similar anion framework.[67, 150] In the systematic study, Manna et al. found that $Cu_{3-x}P$ NPLs were easily formed wurtzite InP NPLs via cation exchange process.[150] It was found that the exchange between Cu^+ and In^{3+} ions started from the peripheral corners of the $Cu_{3-x}P$ NPLs and slowly evolved toward the center. Very recently, Banin et al. reported a method to synthesize wurtzite InP NPLs by cation exchange from Cu_xP NPLs.[67] They obtained up to 44% PLQY

and down to 80 meV emission line width after surface etching of as-prepared InP NPLs with $NOBF_4$. However, they found that the complete exchange of Cu with In was not possible and Cu impurities remained in the InP NPLs during the cation-exchange process. To date, there no direct synthesis method has been reported for preparing InP NPLs.

Herein, we report our attempt to synthesize InP NPLs in a template-mediated growth using preformed ZnSe NPLs for synthesizing a ZnSe/InP NPLs inverted type-I heterostructure. As discussed in chapter 1, seed-mediated or template-mediated growth favours the deposition of the monomers on the template due to the reduction in the energy barrier compared to homogeneous nucleation. Additionally, in our case, the ZnSe template offers two advantages: (i) ZnSe has a higher band gap and type 1 alignment with respect to InP, hence both carriers will be localized in the InP shell, and (ii) the lattice mismatch between ZnSe and InP is low (3.4%) which has been shown to be extremely important for governing the final morphology of the NCs[151] and reducing the number of interfacial defects. We first studied the surface reactivity of ZnSe NPLs towards the indium and phosphorous precursors used. Next, we explored the possibility of ligand exchange while maintaining the ZnSe NPLs morphology. Finally, we extended our study to the ZnSe/InP heterostructure.

4.2. Experimental section

4.2.2. Materials

Zinc stearate ($Zn(St)_2$, technical grade), tris(trimethylsilyl)phosphine ($P(TMS)_3$, 97%), indium acetate ($In(Ac)_3$, 99.99%), indium chloride ($InCl_3$, 99.9%), Se powder (99.99%), oleylamine (OLA, 98%), octylamine (Oct, 99%), octadecene (ODE, 90%), Trimethyloxonium tetrafluoroborate (Me_3OBF_4, 95%) and trioctylphosphine (TOP, 90%) were purchased from Sigma-Aldrich and used without further purification.

4.2.3. Preparation of indium oleate

Indium oleate (0.2 M) was prepared by reacting indium acetate (584 mg, 2 mmol) and oleic acid (2.3 mL, 7 mmol) in ODE (7.7 mL). The mixture was heated at 120 ^oC under vacuum for 1 h with constant stirring. During the process, vigorous bubbling was observed in the solution due to the release of acetic acid. To ensure the full conversion, the reaction mixture was heated at 160 ^oC for 30 min under argon and again degassed under vacuum at 100 ^oC for 30 min. The purity of the final product was controlled by FTIR and it was stored in a glove box.

4.2.4. Synthesis of ZnSe NPLs template

ZnSe NPLs were synthesized by following a reported method.[148] In a typical synthesis of ZnSe NPLs, 187 mg (0.3 mmol) of zinc stearate, 48 mg (0.6 mmol) of Se and 10 mL of oleylamine were added into a three-neck round bottom flask. The reaction mixture was then degassed under a vacuum at 100 ^oC for

2 h. After this stage, the reaction mixture was backfilled with argon and 5 mL of octylamine was added. The flask was then kept at 170 ^{o}C for 6 h resulting in a turbid light yellow solution. Subsequently, the temperature was lowered to 70 ^{o}C and 2 mL of TOP was injected into the mixture to quench the unreacted Se. After 30 min, the reaction mixture was cooled to room temperature. Then, the ZnSe NPLs were precipitated by centrifugation at 8000 rpm (5 min) after a mixture of toluene and ethanol (1:1 vol:vol) was added to the reaction flask. The purified ZnSe NPLs were dispersed in hexane and stored in the glove box.

4.2.5. Native ligand stripping using Meerwein's salt

The ligand stripping process was inspired by previously reported work with slight modifications.[152] In a 10 mL vial, 5 mg of purified ZnSe NPLs were dispersed in 1 mL of hexane. Then, 1 mL of Me_3OBF_4 (0.01M) in acetonitrile was added to the suspension creating two liquid phases. This mixture was vortexed for 5 min and then NPLs were precipitated using centrifugation (4000 rpm). The precipitate was washed with dry chloroform and redispersed in DMF.

4.2.6. Ligand exchange

To exchange surface amine ligands with oleate, in a glass vial, 10 mg of the purified ZnSe NPLs were dispersed in 2 mL of hexane. Subsequently, 1.5 mL of oleic acid (excess) and 0.4 mL of TOP were added to the vial. This mixture was vortexed for 15 min at room temperature. The product was precipitated by centrifugation (8000 rpm, 5 min). The precipitate was washed with dry ethanol/acetone mixture to remove the excess oleic acid and redispersed in toluene.

4.2.7. Trial syntheses of ZnSe-InP NPLs

The successive ionic layer adsorption and reaction (SILAR) method was followed to deposit InP on the ZnSe NPLs template. In a 50 mL round bottom flask, 10 mg of washed ZnSe NPLs (after ligand exchange) were dispersed in ODE (4 mL). The temperature of the reaction was raised to 150 ^{o}C and indium oleate (0.032 mmol, for 1 monolayer) was added and the reaction was kept for 60 min. After this step, 0.032 mmol of $P(TMS)_3$ in 1 mL ODE was added dropwise resulting in a color change from colorless to yellow. A similar method was followed for the second monolayer formation of InP while increasing the amount of In and P precursors accordingly. The same synthesis conditions were followed when the In precursor was changed to indium amidinate or In-TOP complex.

In the case of synthesizing ZnSe-InP NPLs without ligand exchange, the P precursor was added to the reaction mixture first, followed by the In precursor using the same synthesis procedure as in the ligand exchange case.

4.3. Results and discussion

4.3.1. Characterization of the ZnSe nanoplatelets template

Figure 4.1a shows the photograph of the reaction flask containing the as-prepared ZnSe NPLs synthesized using a heat-up method in an oil bath (cf. experimental section). The TEM image (Figure 4.1b) confirms that the ZnSe particles have platelet morphology. The thickness of the ZnSe NPLs can be calculated using an image where the NPLs are stacked on each other (Figure 4.1c). The calculated thickness of ZnSe NPLs is 1.4 nm after subtracting the length of amine ligands (0.8 nm) which are attached to both sides of the NPLs as shown in the Figure 4.1d. The XRD pattern (Figure 4.1e) of the ZnSe NPLs shows that the peak positions are well-matched with the hexagonal wurtzite structure of ZnSe. Amongst the diffraction peaks, the (100) and (002) peaks are the sharpest and most intense, implying a preferential growth in the directions of length and the width as shown in the schematic (Figure 4.1d). The broad peak of (110) corresponds to planes in the direction of NPLs thickness (confined direction). 1.4 nm thick ZnSe NPLs contain eight planes of (110) or four monolayers of ZnSe in the direction of thickness.

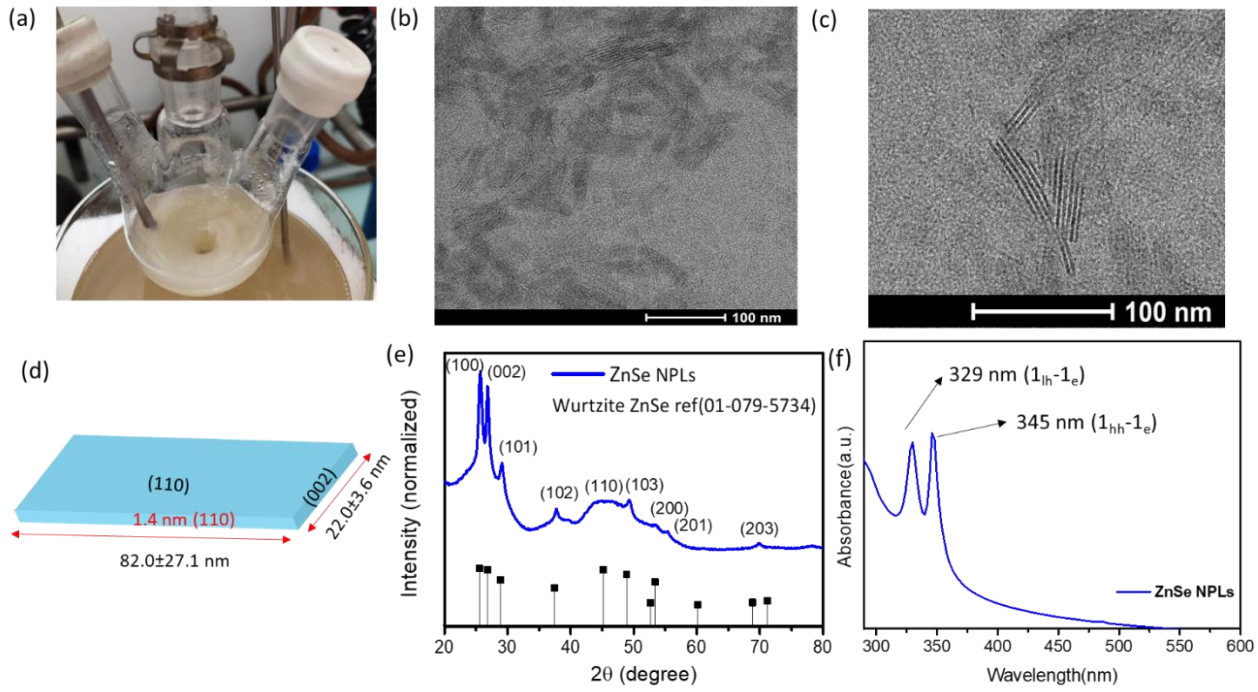

Figure 4.1: (a) Photograph of the reaction mixture containing as-prepared ZnSe NPLs. (b) and (c) TEM images of the ZnSe NPLs showing different orientations on the substrate. (d) Schematic of the obtained ZnSe NPLs representing their length, width and height. (e) XRD pattern of the ZnSe NPLs along with the bulk wurtzite ZnSe reference (vertical black lines). (f) Absorption spectrum of the ZnSe NPLs obtained after 6 hours of growth.

Figure 4.1f shows the absorption spectrum of the ZnSe NPLs revealing two narrow peaks at 345 nm (3.59 eV) and 329 nm (3.76 eV) assigned to the light hole-electron and heavy hole-electron transitions, respectively. The position of the peaks is strongly blue-shifted compared to that of the bulk (2.8 eV)

indicating strong quantum confinement of the excitons. Additionally, the narrow absorption linewidth (7 nm at 345 nm) confirms that the ZnSe NPLs are uniform in thickness.

4.3.2. Separate nucleation of InP QDs

To grow InP on the ZnSe template NPLs, we used the successive ion layer adsorption and reaction (SILAR) method as presented in the experimental section. We expected that the SILAR method could provide a nice strategy to control precisely the thickness of the InP shell by adding a phosphide layer on the zinc-terminated facets of ZnSe NPLs, followed by a layer of indium and so on.

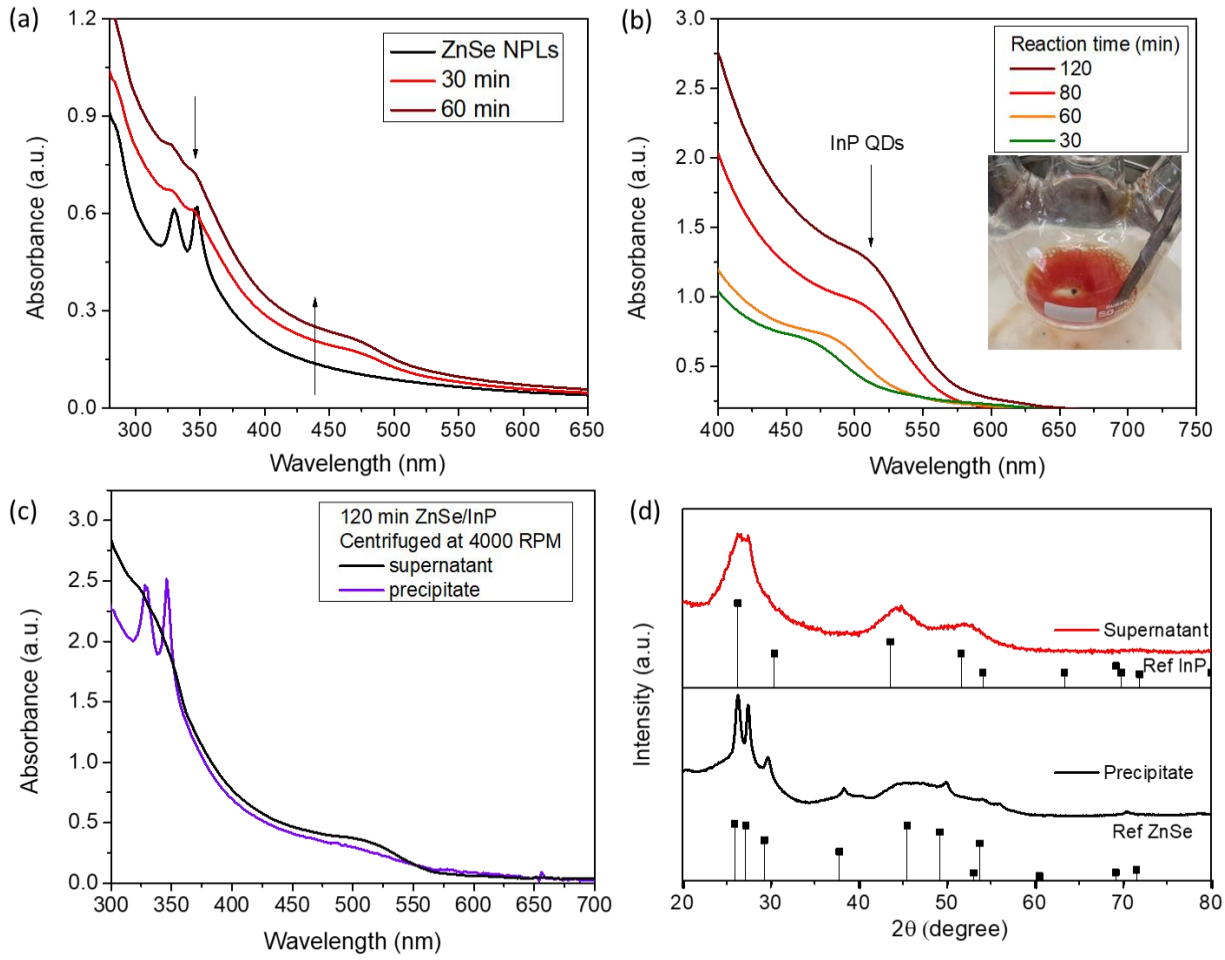

Figure 4.2: (a) Absorption spectra of the aliquots collected at different reaction times after injecting In and P precursors into ZnSe NPLs suspension at 170 ^{0}C. (b) Absorption spectra of InP QDs formed during the reaction. (c) Absorption spectra of the supernatant and the precipitate after centrifugation of the ZnSe-InP NPLs. (d) XRD patterns of the supernatant and the precipitate after centrifugation of ZnSe-InP NPLs.

Figure 4.2a shows the absorption spectra of aliquots collected at 30 and 60 min of reaction time after addition of the In and P precursors needed for the first monolayer formation. The excitonic peaks corresponding to the ZnSe template NPLs started to disappear and a new broad peak was observed at 470 nm. Figure 4.2b shows that the peak at 470 nm shifted towards higher wavelengths with longer reaction time. Additionally, the color of the reaction mixture changed from colorless to red, indicating the formation of separate InP QDs. Indeed, when the final sample was centrifuged at 4000 RPM and

the absorption spectra were recorded for the precipitate and supernatant, we found that the precipitate mostly contained ZnSe NPLs and the supernatant contained InP QDs (Figure 4.2c). XRD analysis shows that the InP QDs were in the zinc blende crystal structure while the ZnSe NPLs retained the wurtzite structure (Figure 4.2d). Next, we tried to change the reaction temperature to control the reactivity of the precursors. However, separate nucleation of InP particles was favored at all temperatures investigated (150 – 220 ^{o}C), indicating that already the first step, functionalization of the ZnSe surface with the P precursor, failed.

4.3.3. Room-temperature native ligand stripping using Meerwein's salt

As discussed in the previous section, the P precursor does not seem to adsorb on or react with the ZnSe surface. A possible reason is that the amine ligands passivating the ZnSe NPLs template hinder the surface binding of P with Zn. To test this hypothesis, we performed ligand stripping of the surface amines. In the literature, either $NOBF_4$ or strong acids such as HBF_4 have been explored for metal oxides and a few semiconductor NCs.[152-153] While these chemicals are effective etching agents, the process is often not well-controlled resulting in particle aggregation. Therefore, we used the milder stripping agent Meerwein's salt (Me_3OBF_4) which has been shown to be a universal reagent for stripping carboxylate, phosphonate and amine ligands while passivating the bare nanocrystal surface with BF_4^- weakly coordinating through electrostatic interaction.[152]

Figure 4.3a shows a schematic for native amine ligand stripping and stabilization of the ZnSe NPLs. Figure 4.3b depicts the absorption spectra of the ZnSe NPLs before and after the ligand stripping. The first excitonic peak was slightly red-shifted from 345 nm to 351 nm probably due to the change in the polarity of the solvent as after ligand stripping, the ZnSe NPLs were dissolved in DMF. DMF is a coordinating solvent that also may weakly coordinate with Zn. Afterward, $P(TMS)_3$ was added for re-passivation/functionalization of the ZnSe NPLs surface at different temperatures (RT-150 ^{o}C). Figure 4.3c shows the absorption spectra of the ZnSe NPLs before and after addition of $P(TMS)_3$. We found that during the repassivation process, the ZnSe NPLs aggregated and quickly precipitated at the bottom of the vial probably due to lack of the surface ligands.

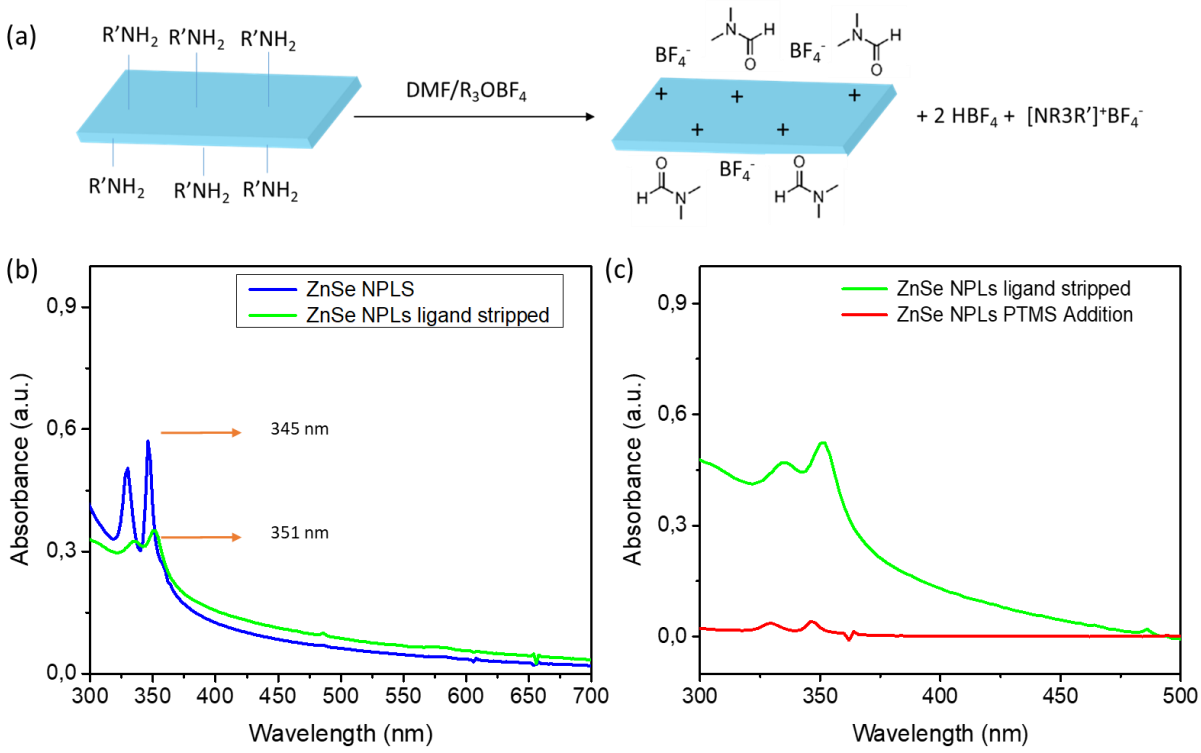

Figure 4.3: (a) General scheme for native ligand (amines) stripping using Meerwein's salt (R=C_2H_5, R'=$C_{18}H_{35}$). (b) Absorption spectra of ZnSe NPLs before (blue) and after (green) ligand stripping. (c) Absorption spectra of the ligand-stripped ZnSe NPLs before (green) and after (red) repassivation with $P(TMS)_3$ (precipitation occurred).

4.3.4. Room temperature ligand exchange from amine to carboxylate

As the repassivation after ligand stripping was unsuccessful due to the aggregation upon addition of the P precursor, another possibility we explored was to exchange the surface ligands while maintaining the NPLs morphology and colloidal stability, which we could not achieve in the ligand stripping process. As-prepared ZnSe NPLs are passivated by amines which can be replaced by carboxylate ligands through proton exchange (Scheme 1). It has been shown for CdSe nanobelts that protic acid (HX) can displace bound amine ligands by protonation, forming surface-bound ion pairs between X^- and the free protonated amine.[154]

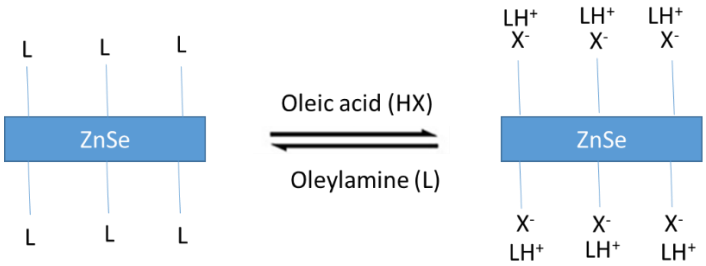

Scheme 1: Proposed schematic for the surface ligand exchange process in ZnSe NPLs. Neutral donor and anionic ligands are classified as L-type ligands and X-type ligands respectively.[155]

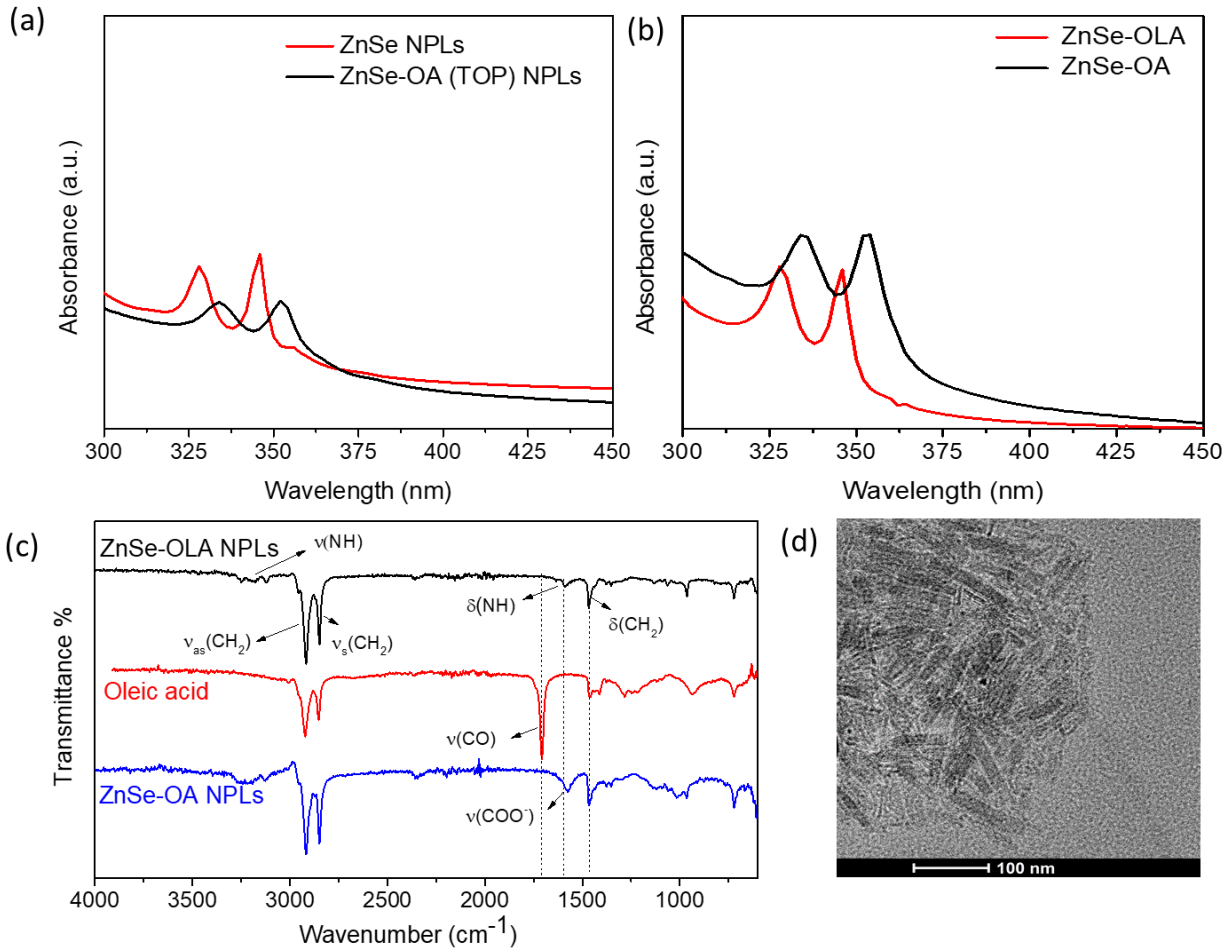

Figure 4.4: (a) Absorption spectra of the ZnSe NPLs before (red) and after (black) ligand exchange with oleic acid (OA). (b) Absorption spectra of the OA-passivated NPLs before (red) and after (black) re-passivation with oleylamine (OLA). (b) IR spectra of the pristine ZnSe NPLs and after ligand exchange with oleate ligands; the spectrum of free oleic acid is also given for comparison. (c) TEM image of the ZnSe NPLs after ligand exchange with oleic acid.

We choose to use oleic acid for the ligand exchange because oleate ligands can favor the subsequent surface reaction with $P(TMS)_3$. Since $P(TMS)_3$ is used as an anionic precursor, it can selectively react with the oleate ligands at the surface of the template and displace them while coordinating to surface Zn atoms.[156] The ligand exchange with oleate was performed at room temperature with the addition of an excess of oleic acid. Figure 4.4a shows the absorption spectra after ligand exchange with oleate. The absorption peak shifted from 345 nm to 355 nm. During ligand exchange, the absorption spectral features remained the same, consistent with the literature.[154] We found that the ligand exchange process is reversible and the absorption peak shifted back to 345 nm after the introduction of an excess of oleylamine in the colloidal solution fo the ZnSe-OA NPLs (Figure 4.4b). FTIR spectra of the ZnSe NPLs before and after ligand exchange are recorded in Figure 4.4c. After the reaction with oleic acid, C=O stretching signal at 1712 cm^{-1} disappeared and O-C-O^- stretching signal appeared at 1576 cm^{-1}. No trace of free oleic acid was observed. In the final sample, the broad peak 3100-3300 cm^{-1} could be

attributed to O-H stretching originating from ethanol which was used for the purification of NPLs after the ligand exchange process. It should be noted that meaningful NMR spectra could not be recorded due to presence of a significant amount of hexane (solvent). Multiple washing of the ZnSe-OA NPLs resulted in aggregation of the NPLs. TEM image (Figure 4.4d) suggests that the stability and morphology of the NPLs were retained after ligand exchange.

4.3.5. Formation of InP islands

Similar to the previous section, we followed the SILAR method for the growth of InP NCs on oleate-capped ZnSe NPLs. First, $P(TMS)_3$ was introduced into the oleate-capped ZnSe NPLs suspension, the NPLs precipitated, impeding subsequent addition steps. However, when indium oleate was introduced first into the ZnSe-OA solution at 150 ^oC, the reaction mixture color changed from colorless to light yellow without visible signs of precipitation. This indicates that In was bound to ZnSe NPLs surface probably by replacing the surface Zn atoms.

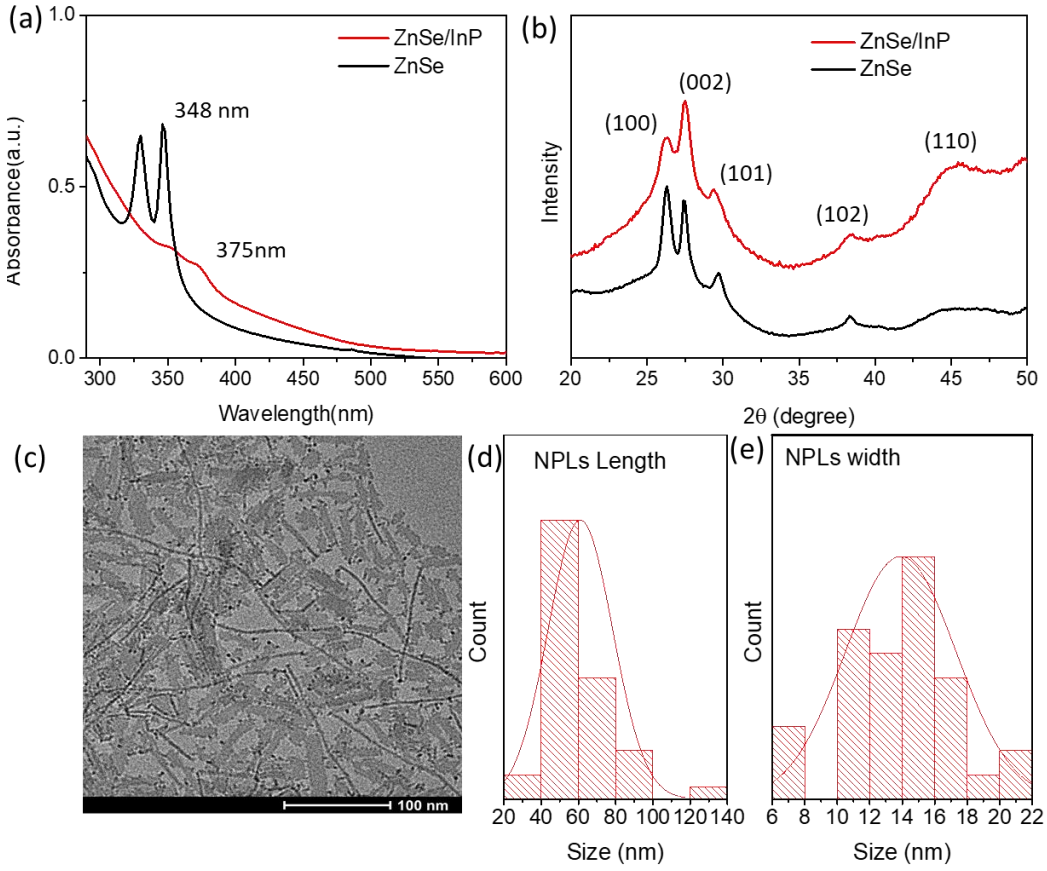

Figure 4.5: (a) Absorption spectra of ZnSe/InP NPLs (red) and the pristine ZnSe-OLA NPLs (black). (b) XRD patterns of the two samples. (c) TEM image of the obtained ZnSe/InP NPLs. (d) Length, (e) width histogram of the ZnSe/InP NPLs.

Figure 4.5a shows the absorption spectra of the reaction mixture aliquot collected at 15 minutes after indium oleate (In-OA) and $P(TMS)_3$ required for 1 monolayer (ML) were introduced into a colloidal solution of oleate-ligated ZnSe NPLs. The absorption peak was shifted from 348 to 375 nm after the

injection of In-OA and $P(TMS)_3$. The broadening of the first excitonic peak suggests some aggregation of the NPLs. XRD (Figure 4.5b) reveals that the crystal structure remained the same. However, an increase in the intensity of the (002) peak was noted in the XRD. Further TEM analysis (Figure 4.5c) shows that the formation of InP (darker in color) is not homogeneous. Instead, InP islands are formed preferably on the edges of the ZnSe NPL template which was further confirmed by EDX where 9-10% of In and P were recorded. Also, a broad absorption shoulder around 430 nm corresponding to the InP QDs could be observed. Alongside InP islands on ZnSe NPLs, ZnSe nanowires (width 5.2 nm) were also visible. After size analysis from TEM (Figure 4.5c-e) of the final samples, we found that the length and width of NPLs were significantly reduced. This suggests that during the addition of In-OA, ZnSe NPLs were degraded and slowly transformed into ZnSe nanowires which are responsible for the increase in the (002) peak relative intensity in the XRD analysis (Figure 4.5b). Comparison with the absorption peak of ZnSe nanowires in the literature, strongly suggests that the formed nanowires are ZnSe.[157] It has been shown that ZnSe nanowires can be formed at a low temperature of 150 °C, further supporting our assumption.

4.4. Conclusion

We have successfully synthesized ZnSe nanoplatelets which were used as a template for our attempt to synthesize ZnSe/InP core/shell NPLs. InP growth was tested using the SILAR method by successively adding calculated amounts of indium oleate and $P(TMS)_3$ to the template NPLs. However, the formation of separate InP QDs was observed in all the trials demonstrating the low reactivity of the amine-passivated ZnSe surface. For surface activation, we performed ligand exchange of the ZnSe NPLs and showed that the amine ligands can be exchanged for carboxylate ligands at room temperature and this process is reversible. Such exchanges may become useful for manipulating the surface functionalization of the NPLs. Again, InP deposition was tested on the oleate-ligated ZnSe NPLs but in all the synthesis attempts, the formation of InP islands was observed. We also found that some ZnSe NPLs dissolved during the synthesis and transformed into ZnSe nanowires. Homogeneous InP NPLs may be synthesized using a more reactive indium precursor which could also allow performing the synthesis at lower temperatures to avoid the transformation of the ZnSe NPLs into other morphologies.

Chapter V

Synthesis of Ga_2S_3 nanocrystals for blue LEDs applications

5.1. Introduction

Binary and ternary semiconductor nanocrystals (NCs) have gained vast attention in recent research due to their wide range of applications.[34-36, 91] Predominantly studied cadmium and lead-based semiconductor NCs exhibit excellent optical properties but their toxicity remains a concern for their applications in daily life.[92] Amongst Cd-free replacements, III-VI materials such as Ga_2S_3, GaSe, GaS, In_2S_3, In_2Se_3, and Ga_2Se_3 nanocrystals are potential candidates, especially selenium-free sulfide chalcogenides due to their lower intrinsic toxicity.[158-160]

Owing to its wide direct band gap of 3.05 eV,[158] Ga_2S_3 provides a promising alternative to CdS-based NCs for blue light-emitting devices. However, to date, theoretical and experimental studies have mainly explored Ga_2S_3 in the form of thin films and single crystals. Unlike other binary compounds such as InP or CdSe, the misvalancy between Ga and S can result in different crystal structures such as hexagonal, cubic, and monoclinic depending on the stoichiometry of Ga and S.[158, 161] Moreover, owing to this misvalancy, the crystal structure generally contains a high number of defects.[158] In a study to understand the origin of the emission in single crystals, Aydinli et al. found that the blue-green photoluminescence (PL) arises from the recombination of defect donor and defect acceptor levels caused by S and Ga vacancies, respectively.[159] To improve the blue emission coming from the defects, Yoon et al. doped Fe^{2+} into the gallium sulfide single crystals, however, they observed that the emission was only detectable below a temperature of 10 K.[161] Recently, Zhang et al. reported a one-pot method to synthesize phase-pure Ga_2S_3 quantum dots.[162] They obtained a photoluminescence yield of up to 25.7%. In addition, they were able to tune the emission from 420-535 nm by varying the Ga:S feed ratio. However, a very broad emission linewidth (110 nm/640 meV) was observed due to insufficient control over the defect emission. In the literature, thus far, this is the only method reported for the synthesis of Ga_2S_3 at the nanoscale.

Besides Ga_2S_3, amorphous GaS_x has recently been studied as a shell material for improving the optical properties of $AgInS_2$ QDs.[163] These ternary chalcopyrite materials are characterized by a very broad PL line width of 300-500 meV due to the underlying emission mechanism involving localized hole states arising from defect states close to the valence band edge.[164] Unexpectedly, the emission linewidth of

$AgInS_2$ NPs was significantly reduced down to around 100 meV when coated with an amorphous GaS_x shell; the detailed mechanism of this improvement is still under investigation.[163] As demonstrated for ternary QDs, we expected that the amorphous shell formation may open new possibilities for the design of new core/shell structures based on InP QDs. It is in this respect, the study in this chapter was conducted. We divided our study into three parts; i) first we investigated gallium sulfide as a potential shell material for InP QDs, ii) we developed a novel colloidal route for the synthesis of Ga_2S_3 QDs and performed their detailed characterization to study their defect-related emission, and iii) we developed a Ga_2S_3/ZnS core/shell structure leading to PL emission at 400 and 460 nm. Part of this work (core/shell optimization and characterization) was performed by Dr. Avijit Saha.

5.2. Experimental section

5.2.1. Materials

Gallium (III) acetylacetonate ($Ga(acac)_3$, 99.99%), elemental sulfur (S, 99.99%) indium (III) acetate ($In(OAc)_3$, 99.99%), zinc stearate (technical grade), myristic acid (MA, 99%), octadecene (ODE, 90%), and trioctylphosphine(TOP, 90% technical grade) were purchased from Sigma Aldrich and were used without further purification. The synthetic procedure of gallium sulfide QDs was carried out using a Schlenk line and under Argon atmosphere.

5.2.2. Preparation of indium myristate ($In(MA)_3$)

For indium myristate [$In(MA)_3$] preparation, 10 mmol of $In(OAc)_3$ and 30 mmol of myristic acid (MA) were added in a three-neck round bottom flask containing 20 mL of ODE. The mixture was heated to 110 °C for 1 h under vacuum. Afterward, it was backfilled with argon and kept for 2 h at the same temperature. After 2 h, the reaction mixture was again switched to vacuum for 30 min. After cooling to room temperature, the product was purified using dry hexane (two times), dried under vacuum for 2 h and stored in a glove box for further utilization.

5.2.3. Synthesis of InP core quantum dots

In a round bottom flask, 79.6 mg (0.1 mmol) $In(MA)_3$, 126 mg (0.2 mmol) $ZnSt_2$ and 8.5 ml of ODE were added. The reaction flask was heated at 100 ^oC under vacuum for 1 hr. After the dissolution of all the precursors, a clear solution was observed. The temperature of the mixture was raised to 130 ^oC and 29.1 µL of $P(TMS)_3$ diluted in 1 mL of ODE was swiftly injected. The temperature of the reaction mixture was then quickly raised to 250 ^oC. Shortly after the injection, a color change was observed from colorless to deep red. After 20 minutes, the reaction was quenched using a water bath. The prepared InP QDs were purified by precipitation using a mixture of chloroform/methanol (1:1 vol:vol) and 2 volume equivalents of acetone and centrifugation at 8000 rpm (10 min). The InP precipitate was dispersed in toluene for further characterization.

5.2.4. Synthesis of the GaS_x shell

2 mL of the as-prepared InP QDs were mixed with 36.7 mg (0.1 mmol) of $Ga(acac)_3$, 3.2 mg (0.1 mmol) of elemental sulfur and 7 ml of ODE along with 0.5 mL of TOP. The reaction mixture was heated at 200 ºC for 10 min and then the temperature was raised to 300 ºC at the rate of 2 ºC/min. The mixture was cooled to room temperature after 1 hour. The same purification steps were followed as mentioned for the InP core QDs.

5.2.5. Synthesis of gallium sulfide quantum dots

Ga_2S_3 QDs were synthesized using a one-pot colloidal synthetic method. In a three-neck round bottom flask, 92 mg (0.25 mmol) of $Ga(acac)_3$, 32 mg (1 mmol) of elemental sulfur, 5 mL of ODE, and 1.1 mL of trioctylphosphine (TOP) were taken. The reaction mixture was kept under constant magnetic stirring and vacuum at 100 ºC for 20 min to remove any moisture if present. After obtaining a clear solution, the temperature of the reaction mixture was raised to 280 ºC at 2 ºC/min under argon flow and kept at this temperature for 30 min before cooling to room temperature. The Ga_2S_3 QDs were precipitated with an excess of dry ethanol and centrifuged at 10000 RPM (10 min). The purified Ga_2S_3 QDs were redispersed in toluene for further characterization.

5.2.6. Synthesis of zinc oleate (ZnOA)

0.33 g (1.5 mmol) of $Zn(OAc)_2.2H_2O$, 1.5 mL (4.8 mmol) of oleic and 6 mL of ODE were added in a 25 mL round-bottom flask connected to a Schlenk line. The reaction mixture was degassed at 50 ºC for 30 min under vigorous stirring. The temperature was increased to 180 ºC under Ar atmosphere and then lowered to 100 ºC as soon as a clear solution formed. Finally, while maintaining the temperature at 100 ºC, ZnOA was transferred into a degassed vial for future use. The compound solidifies at room temperature, therefore, prior to its use it was heated inside a vial using a heat gun.

5.2.7. Synthesis of Ga_2S_3/ZnS core/shell quantum dots

To synthesize Ga_2S_3/ZnS core/shell QDs, the growth of the core QDs was stopped after 2 min at 280 ºC by decreasing the temperature to 230 ºC. At this temperature, the reaction was maintained for 5-6 min. At this stage, PL emission due to the band edge recombination near 400 nm can be observed and no trace of trap-state related emission at lower energy/higher wavelength can be detected. The previously prepared ZnOA complex was used as the Zn precursor while an excess amount of elemental sulfur, present in the reaction mixture, acts as the S precursor. At 230 ºC, 800 µL of the preheated ZnOA complex was slowly injected into the reaction mixture. The reaction mixture was kept at 230°C for 80 min and sample aliquots were collected at different stages of the ZnS shell growth. Following the same procedure in a different reaction, Ga_2S_3/ZnS core/shell QDs were also synthesized using a Ga_2S_3 core after 30 min of reaction time at 280 ºC.

5.2.8. Characterization

UV-VIS absorption spectra of the samples were recorded using a Hewlett Packard 8452A spectrometer. The steady-state and time-resolved PL spectra were obtained using a Horiba Fluorolog FL1057 spectrophotometer, while the absolute PLQY was determined using an integrating sphere introduced in the same equipment. X-ray diffraction patterns of the nanocrystals were recorded on a Bruker diffractometer using Cu-K□ (l = 1.5406 Å) radiation. Transmission electron microscopy was performed on an FEI Polara microscope operating at 300 kV and the images were recorded using a Gatan K2 camera. Chemical characterization by XPS was carried out using a Versaprobe II ULVAC-PHI spectrometer. All XPS measurements were performed by Dr. Dmitry Aldakov and carried out in an ultra-high vacuum chamber (7.10−8 mbar). The samples for XPS were prepared on silicon substrates by spin-coating the QDs and washing them with ethanol to remove the extra ligands. Curve fitting and background subtraction were accomplished using Casa XPS software.

5.3. Results and discussion

5.3.1. Investigation of GaS_x as a shell material for InP

For InP NCs, generally, ZnS has been investigated as the shell material to improve the emission and stability.[15, 17, 23] As discussed in the first chapters, the lattice mismatch between InP and ZnS is comparably large (7.7%). This large lattice misfit creates interfacial defects between the core and the shell reducing the ensemble photoluminescence. To overcome the problem of lattice mismatch the use of amorphous shells could be an option, similar to the aforementioned case of ternary Ag-In-S QDs. To the best of our knowledge, this approach has not yet been explored for improving the optical properties of InP QDs. In such a view, we attempted to develop an InP/GaS_x core/shell structure.

Figure 5.1a and 5.1b show the UV-vis absorption and PL spectra of InP core QDs and InP/GaS_x core/shell QDs, respectively. In the absorption spectrum, the excitonic peak corresponding to InP core QDs can be observed at 487 nm whereas two blue-shifted absorption features at 446 nm and 370 nm, respectively, were observed after gallium sulfide shell growth. As shown in Figure 5.1b, the emission spectrum also blue-shifted from 545 nm to 455 nm after the shell growth procedure. Such a drastic change in the PL and UV–vis spectra can only appear in the case of alloy formation (InGaP) or through etching (particle size reduction), resulting in an increase of the band gap. We also speculated that the separate nucleation of GaS_x QDs may occur. In order to have a clear understanding, a control experiment was performed using only the Ga and S precursors. Surprisingly, we observed very similar absorption and PL features as for the supposed core/shell structure (a detailed study is presented in the next part). Several attempts were undertaken to deposit the gallium sulfide shell by changing the reaction temperature and precursor reactivity, but in all cases similar optical properties were obtained. Hence, we concluded that during the attempts of InP/GaS_x core/shell QDs synthesis, there was a formation of

separate GaS_x nanoparticles, possibly along with InGaP alloy. Since the reaction with gallium requires high temperatures (> 300 °C), it is very hard to control the reactivity of the precursors.

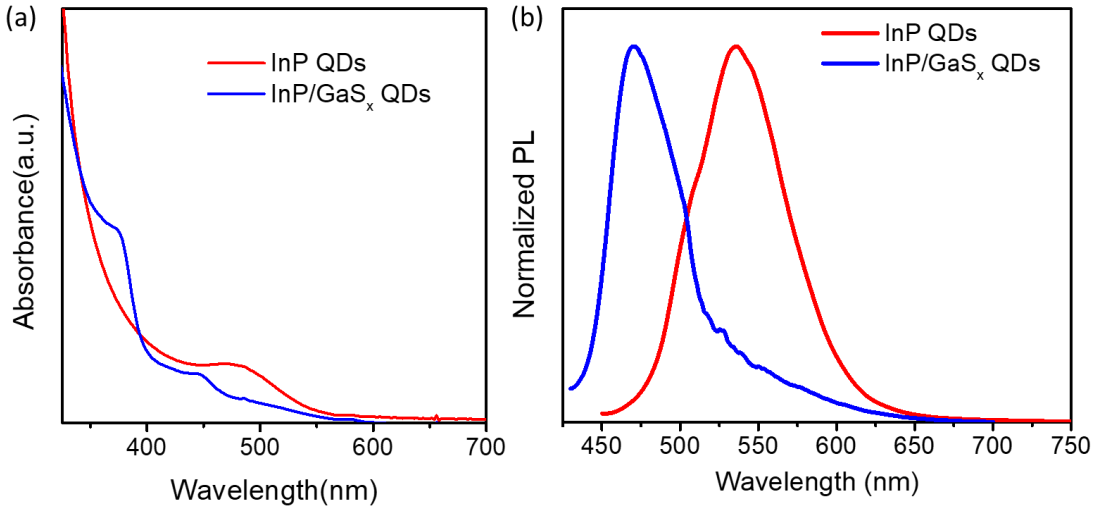

Figure 5.1: (a) Absorption and (b) PL spectra of the InP core QDs before (red) and after (blue) the attempt to deposit an amorphous GaS_x shell.

After observing a strong blue emission for the control experiment, we were interested in investigating further the gallium sulfide QDs as they can be a potential candidate for blue-emitting devices, which is highly desirable as the choice of efficient blue emitters is very restricted.

5.3.2. Synthesis of Ga_2S_3 nanocrystals: study of the reaction parameters

5.3.2.1. Effect of temperature

Ga_2S_3 nanocrystals (NCs) were synthesized using a heat-up method where the gallium and sulfur precursors were added at room temperature and heated to 300 °C. First, we investigated the effect of temperature on the formation of Ga_2S_3 QDs. Notably, no formation of Ga_2S_3 NCs was observed below 250 °C suggesting that the nucleation temperature is situated in this range, consequently, no absorption peak or shoulder was observed for the aliquots collected below 250 °C. Figure 5.2a shows the absorption spectra of the aliquots collected from 260 to 300 °C. A sharp excitonic peak at 370 nm was observed for the aliquot collected at 260 °C. However, no noticeable change in the 370 nm excitonic peak was observed when the reaction temperature was increased to 280 °C. This can be possibly due to the smaller Bohr radius (< 2 nm), and since particles are already in the weak confinement regime the change in the band gap is not dramatic. The optical band gap calculated from the first excitonic peak is 3.39 eV which is in line with the values reported in the literature.[158] For the aliquot collected at 300 °C, two absorption peaks were observed. One sharp peak at 370 nm similar to the previous case and a second absorption shoulder at 445 nm attributed to defect states. Figure 5.2b shows the PL spectra of the collected aliquots. An emission peak at 390 nm was observed for the aliquot collected at 260 °C. As the temperature was increased to 280 °C, two emission peaks at 393 nm and 460 nm appeared. Moreover, as the temperature

reached 300 °C, a single broad emission peak at 516 nm was observed which seemed to originate from multiple emission sites. Based on the literature concerning bulk Ga_2S_3 (cf. section 5.3.3.2), we speculate that the 390 nm emission is related to the band-edge transition and the 460 nm and 510 nm emissions are arising from defect states. A detailed study regarding the origin of the different emissions is presented in the next section.

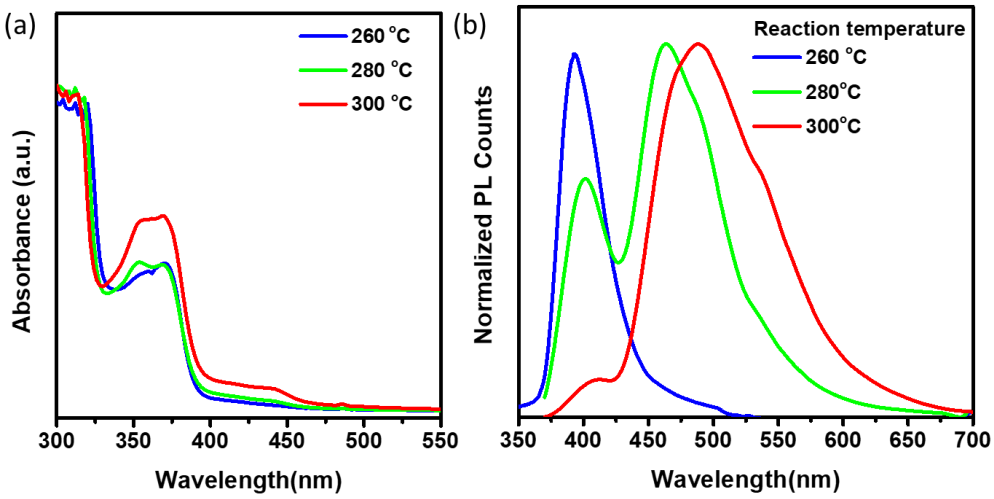

Figure 5.2: (a) Absorption and PL spectra of Ga_2S_3 NCs prepared at different temperatures.

5.3.2.2. Effect of the Ga:S ratio

As shown in a previous study, the ratio between gallium and sulfur strongly influences the defect emission dynamics and the band gap.[162] To investigate the effect of the S/Ga ratio on the reaction kinetics, two samples were prepared by varying the amount of sulfur while keeping the amount of gallium and the other reaction conditions constant. Figure 5.3a shows the absorption and the PL spectra of Ga_2S_3 QDs prepared with S:Ga = 1.5:1 (stoichiometric ratio) and S:Ga = 4:1 (excess of S), respectively. In both cases, a sharp excitonic peak at 374 nm was observed. We do not observe any distinguishable shift in the excitonic peak position with the change in the feed molar ratio. However, the second excitonic peak at 445 nm seems more pronounced in the case of excess sulfur along with a small shoulder at 510 nm which is absent for the lower ratio. Figure 5.3b shows the emission spectra for both cases. For the higher ratio, an emission peak at 460 nm with fairly narrow linewidth (FWHM = 38 nm) was observed whereas for the lower ratio, a broad emission at 530 was observed.

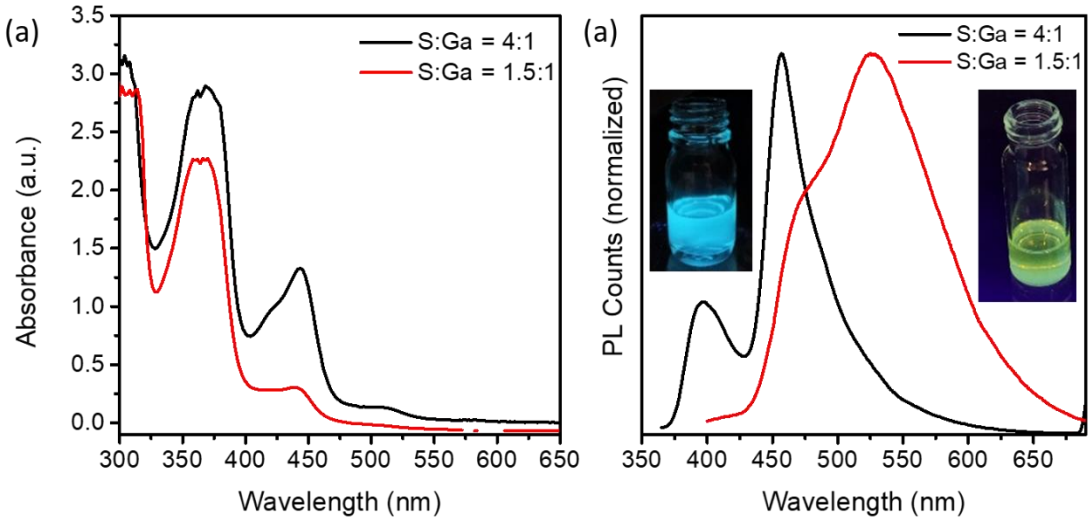

Figure 5.3: (a) Absorption and (b) PL spectra of Ga_2S_3 QDs prepared with different ratios of gallium and sulfur.

EDX analysis (Table 5.1) confirms the presence of Ga and S as the main elements in both cases. However, we found a drastic contrast in the Ga:S feed ratio and the experimentally determined ratio. In EDX, Ga:S = 1:0.70 was observed for the feed ratio of Ga:S = 1:1.5 (theoretical stoichiometric ratio). For samples prepared with a higher amount of sulfur, Ga:S = 1:1.32 was analyzed for a feed ratio of 1:4. These results from EDX suggest that an excess of S is needed to obtain the stoichiometric ratio in the Ga_2S_3 QDs synthesis.

Table 5.1: EDX analysis of the Ga_2S_3 QDs synthesized with different Ga/S ratios.

Feed ratio of Ga:S	Ga (Atomic %)	S (Atomic %)	Ga/S ratio
1:1.5	59	41	1:0.70
1:4	43	57	1:1.32

5.3.2.3. Effect of oleylamine addition

Figure 5.4a shows the absorption spectra of Ga_2S_3 NCs synthesized while adding oleylamine as a ligand along with TOP. An excitonic shoulder was observed at 374 nm, which remained constant with the reaction time. The final sample could not be precipitated probably due to the very small size of the Ga_2S_3 NCs. Because of the issue of purification, no other characterization could be performed for the Ga_2S_3 NCs prepared with oleylamine addition. In addition to oleylamine, we also investigated 1-dodecanethiol (DDT) as a ligand. We followed a similar synthesis procedure and replaced oleylamine with DDT. However, the final product was colloidally unstable and formed a muddy yellow mixture.

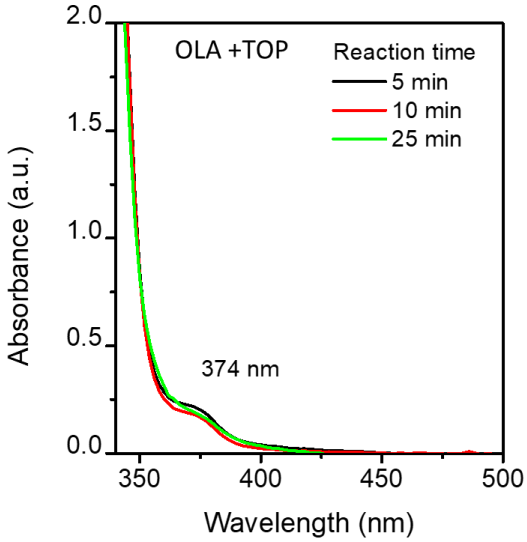

Figure 5.4: Absorption spectra of GaS_x NCs prepared with a mixture of oleylamine and TOP ligands.

5.3.3. Optimized synthesis of Ga_2S_3 NCs

5.3.3.1. Optical properties

The absorption and PL spectra of various Ga_2S_3 QDs dispersed in toluene are depicted in Figure 5.5a. It is evident from Figure 5.5a, that there is an evolution of three different types of transitions resulting in PL emissions near 400 nm, 460 nm, and 520 nm, respectively, depending on the reaction time. At the initial stage of the growth (up to 1-2 min at 280 ºC), the sharp band edge peak at 395 nm dominates over other peaks suggesting the insignificant presence of vacancy-related midgap states. However, with increasing reaction time, the peak at 460 nm along with a shoulder at 520 nm slowly evolve under the concomitant decrease of the band-edge peak as depicted in Figures 5.5c. It is noteworthy that with reaction time both the absorption peak and the highest energy PL peak (near 400 nm) show a slight redshift under quasi-constant Stokes shift: the absorption peak from 370 nm to 376 nm, the PL peak from 395 nm to 402 nm. However, the PL peak positions at 460 nm and 520 nm remain unaltered. This behavior further supports our hypothesis that the highest energy peak is due to band-edge emission, which shows a small redshift as a result of weaker quantum confinement due to QD growth with the reaction time, while the peaks at 460 nm and 520 nm arise from localized mid-gap states, whose energy levels are insensitive to size variation.

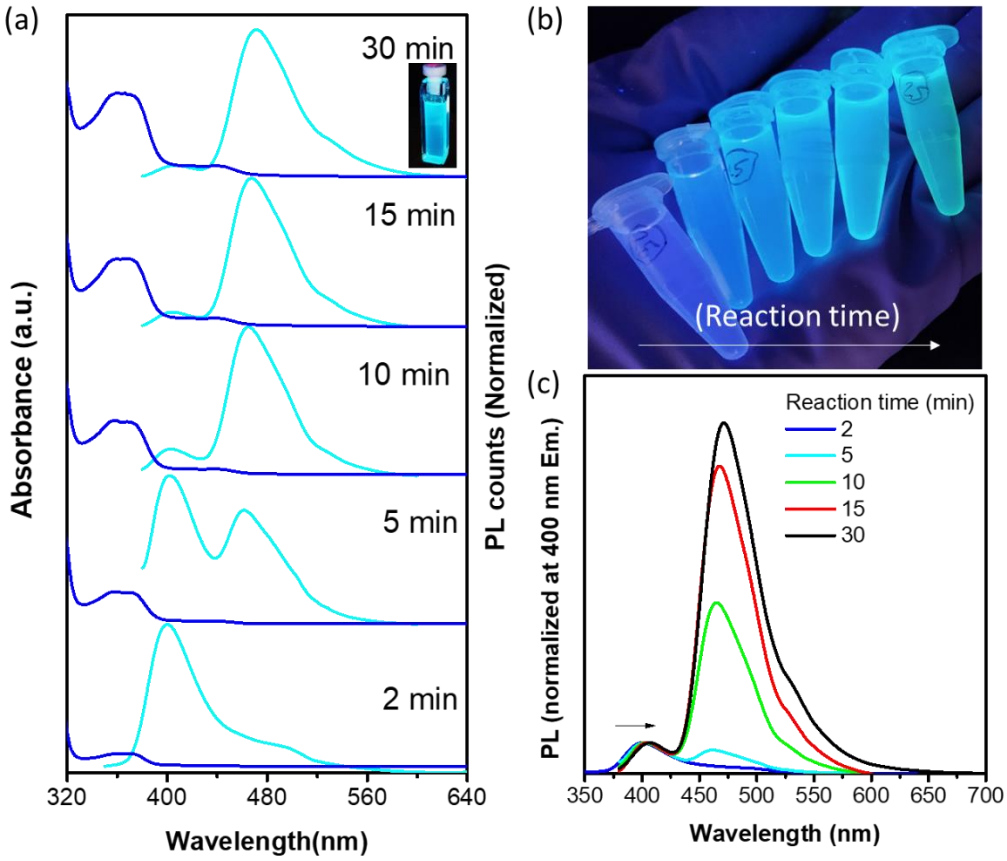

Figure 5.5: (a) Absorption spectra and PL spectra of aliquots of Ga_2S_3 NCs taken at different reaction times. (b) Photograph of the as-prepared the Ga_2S_3 QD under UV light. (c) Evolution of the 460-nm peak intensities with respect to the peak 400-nm emission peak.

5.3.3.2. Origin of photoluminescence

Figure 5.6 shows a schematic of the proposed recombination pathways of the photogenerated carriers involving the three different transitions. As explained in previous reports, gallium sulfide crystals contain a high density of defect states.[158, 162] These defect states are caused by sulfur and gallium vacancies which behave like donor (D) sites and accepter (A) sites, respectively. The emission at 400 nm, which is supposed to be associated with band edge emission but with reaction time, this peak starts to decrease and a broad blue emission centered at 460 nm arises from the exciton recombination from a donor (D) site to an acceptor (A) site, commonly known as donor–acceptor pair (DAP) recombination process. The gallium vacancies are formed due to the requirement of electroneutrality/charge equilibrium. It is apparent that the PL peak near 400 nm is due to band edge emission while the peaks at 460 nm and 520 nm are the results of mid-gap related transitions (donor-acceptor pair recombination).

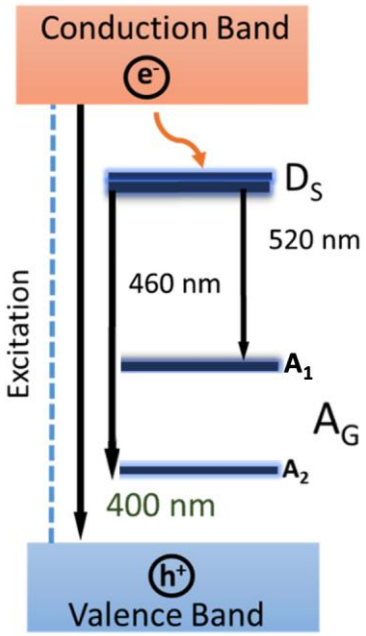

Figure 5.6: Schematic energy band diagram illustrating possible transitions in Ga_2S_3 QDs. D_S and A_{Ga} represent sulfur and gallium vacancy related donor and acceptor states, respectively.

5.3.3.3. Excited states dynamics

The PL excitation (PLE) spectrum of the QDs can provide more insights into the origin of sub-band-gap and band-gap transitions and the mechanisms of the radiative processes. Figure 5.7a shows the PLE scan of the 30 min sample, which exhibits the PL emission shown in Figure 5.7b. The PLE spectra were measured at the PL emission wavelengths of 410 nm and 470 nm, respectively. The PLE spectrum of the 410-nm emission peak looks very similar to the corresponding absorption spectrum, further confirming the assignment of band edge emission to this transition. On the contrary, in the case of the 460-nm emission, the absorption in the 400-460 nm range is much lower than the PLE signal. This behavior suggests that while emission occurs through the mid-gap states, light absorption is dominated by the host semiconductor, followed by fast charge or energy transfer to the Ga and S defects. To understand the exciton decay dynamics and the recombination pathways inside the QDs, we used time-resolved PL (TRPL) spectroscopy (Figure 5.7c). For this measurement, the samples were excited by a pulsed NanoLED with a wavelength of 350 nm, and the decay was monitored at the 400 and 460 nm emission wavelengths. It is evident from the Figure 5.7c that mid-gap emission has multiple decay pathways resulting in bi-exponential decay, whereas band-edge emission is single-exponential in nature. The lifetime of the 400-nm signal is with 0.95 ns very short compared to other types of QDs.

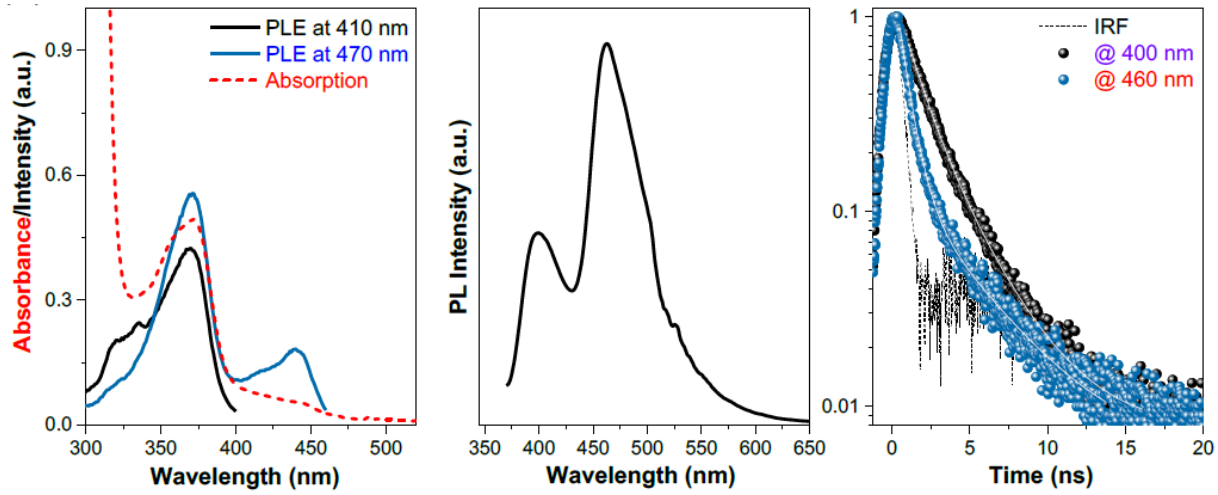

Figure 5.7: (a) PLE spectra of Ga_2S_3 QDs monitored at 410 nm (black) and 470 nm (blue) emission. Red dotted line absorption spectrum. (b) PL emission spectrum for the corresponding Ga_2S_3 QDs. (c) Time-resolved PL spectra measured at the 400 nm and 460 nm peaks, respectively. IRF is the decay of the lamp.

5.3.3.4. Crystal structure and morphology

Figure 5.8a displays the XRD pattern of Ga_2S_3 NCs revealing three broad peaks between 10° and 100° (2 theta). Due to their small size and probably partially amorphous nature, the diffraction peaks of the NCs are very broad. Nonetheless, the diffraction pattern can be tentatively assigned to the monoclinic Ga_2S_3 phase (ICSD# 00-050-0811). The monoclinic symmetry of the as-synthesized gallium sulfide QDs is in accordance with previous XRD results obtained with Ga_2S_3 single crystals.[158, 160-161, 165]

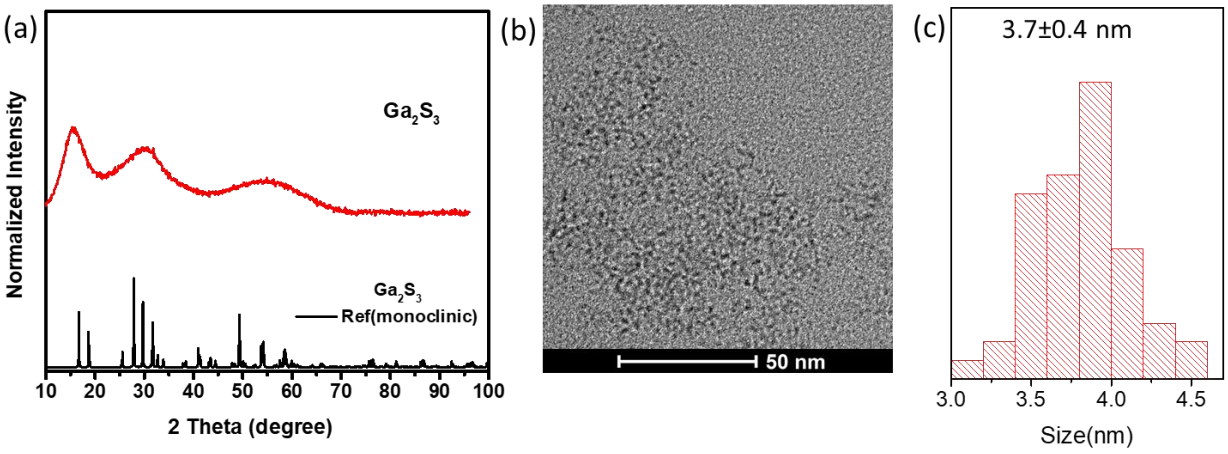

Figure 5.8: (a) X-ray diffractogram of Ga_2S_3 NCs and reference pattern of monoclinic Ga_2S_3. (b) and (c) TEM image and size histogram of the obtained Ga_2S_3 NCs, respectively.

Figure 5.8b represents a TEM image of the obtained Ga_2S_3 NCs having an average diameter of 3.7±0.6 nm revealing a narrow size distribution and spherical shape. The EDX analysis results in a composition of $Ga_2S_{2.8}$, i.e., almost stoichiometric for a feed ratio of 1:4.

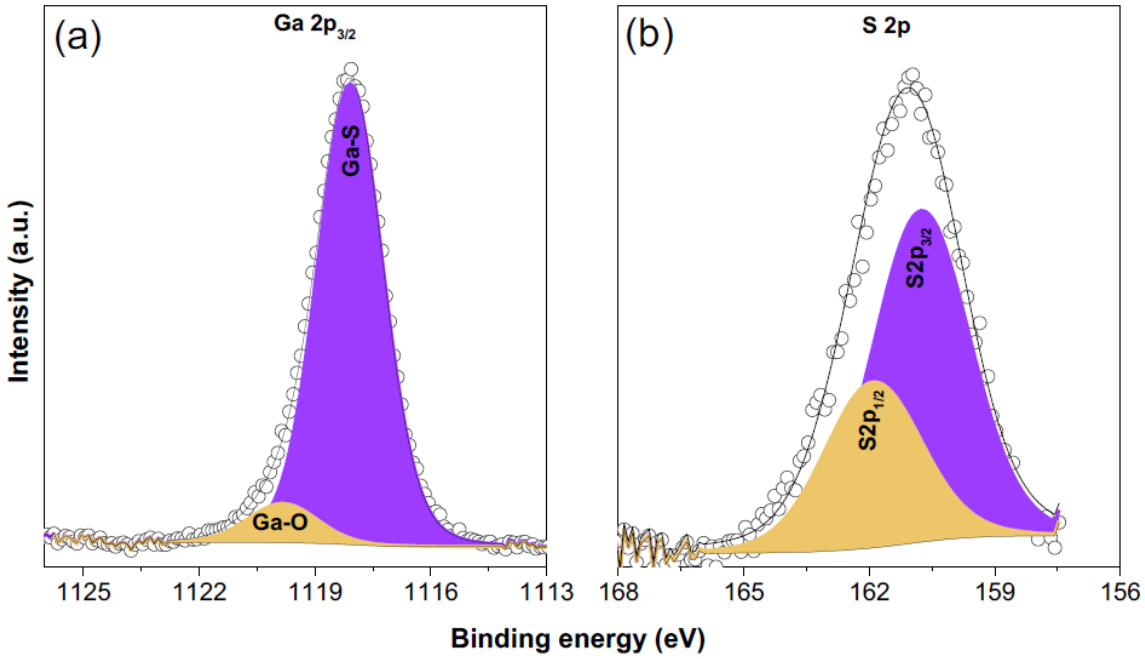

Figure 5.9: High-resolution XPS spectra of the (a) $Ga2p_{3/2}$ and (b) S2p peaks of the Ga_2S_3 NCs.

XPS analysis has been performed to investigate the chemical states of the constituent elements and the chemical composition of the Ga_2S_3 NCs. Figures 5.9a and 5.9b represent the high-resolution XPS spectra of the Ga $2p_{3/2}$ component of the Ga 2p region and the S2p peak, respectively. The ratio between the integrated intensity of Ga2p and S2p = 2:3.5 which suggests the formation of Ga_2S_3 NCs with a slightly sulfur-rich surface. For further analysis, the spectra have been deconvoluted considering the spin-orbit splitting where the binding energy differences, full width at half maximum (FWHM), and area under the curve are fixed with standard database literature. The Ga $2p_{3/2}$ signal can be deconvoluted into two doublet peaks due to the Ga-S and Ga-O bond. The small contribution of Ga-O is due to the oxidation of Ga, most likely on the bare surface. In the S2p spectrum (Figure 5.9b), the deconvoluted doublet peaks are located at 160.73 and 161.89 eV with a peak separation of 1.16 eV, consistent with the expected S in the sulfide phase confirming the formation of gallium sulfide QDs.

5.3.4. Formation of ZnS shell

After the optimization of the Ga_2S_3 core NCs photophysical properties using different reaction times, we proceeded toward the passivation of their surface using a ZnS shell. ZnS was chosen due to i) its successful widespread use as shell material on many types of QDs; ii) its large bandgap enabling type-I band alignment in a Ga_2S_3/ZnS core/shell system; iii) the structural similarity: in both materials, the metal atoms are tetrahedrally coordinated by 4 sulfur atoms; iv) the common-anion heterostructure improves the core/shell interface quality. As discussed above, it is possible to have two distinguished emissions (near 400 nm and at 460 nm) from Ga_2S_3 core NCs depending on the reaction time. Therefore, in two separate experiments, we have grown ZnS shells on the two different cores of Ga_2S_3 QDs, in

which the core has either intense band-edge emission or emission involving mid-gap states; they will be referred to as Ga_2S_3-400 and Ga_2S_3-460 respectively.

5.3.4.1. Ga_2S_3-400/ZnS core/shell formation

The synthesis technique of Ga_2S_3-400/ZnS core/shell QDs was achieved by reacting excess sulfur in the reaction medium with zinc oleate, injected at lower temperature (230°C) than for the core synthesis. Figures 5.10a and 5.10b show the evolution of UV-VIS absorption and PL spectra respectively at various stages of ZnS shell growth. The shoulder peak in the UV-VIS absorption spectra of Ga_2S_3 QDs is suppressed after ZnS shell growth. The absorption peak does not show any redshift suggesting the formation of a type-I semiconductor heterostructure with large band offsets, where the core Ga_2S_3 levels (maximum of valence band and minimum of conduction band) lie in between the band gap of the ZnS shell. All NCs emit near 400 nm. The observed PL spectra were normalized for their absorption at the excitation wavelength (350 nm), to compare the change in intensity. It is clear from the PL spectra that the PLQY significantly improved with the growth of the ZnS shell reaching up to 32% compared to 12.6% for the core. Moreover, bare Ga_2S_3 QDs have poor colloidal and optical stability, while the core/shell QDs retain both colloidal as well as PL stability for several months.

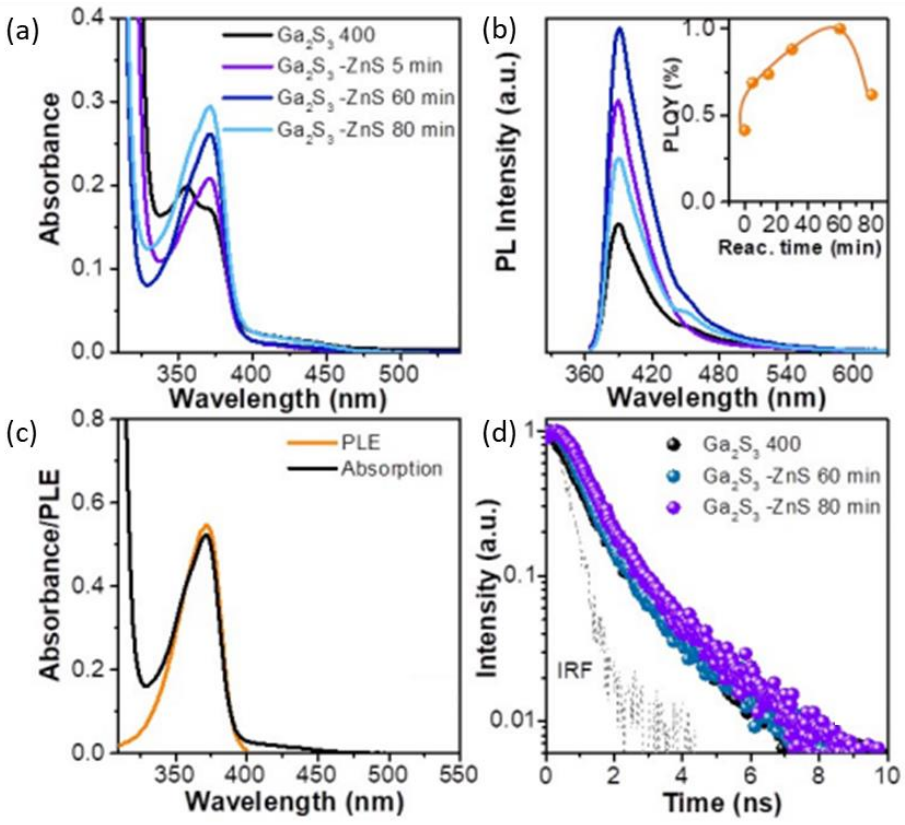

Figure 5.10: (a) Absorption and (b) PL spectra of the Ga_2S_3 QD core and Ga_2S_3-400/ZnS core/shell NCs with different shell thicknesses. (c) Overlaid PLE and absorption spectra of the core/shell NCs. (d) TRPL spectra of the core and core/shell NCs with different shell growth times.

The PL linewidths (FWHM) of these QDs are comparably low (38 nm/255 meV) and invariant to the ZnS shell growth as depicted in Figure 5.10b. Figure 5.10b inset illustrates the variation of the PLQY (normalized) which shows a slow decrease for ZnS growth times longer than 60 min, probably due to the increase of interfacial strain. Figure 5.10c depicts the PLE scan of Ga_2S_3-ZnS core/shell QD after 60 min of ZnS growth monitored at the 400-nm PL emission. As for the core QDs, the PL excitation spectrum looks very similar to their absorption spectrum. [We note that the decrease of the PLE spectrum at wavelengths below 300 nm is caused by the Xenon lamp, used for PL excitation, which has a very poor intensity in this range.] Furthermore, TRPL (Figure 5.10d) was studied to understand the effect of the ZnS shell growth on the excitation decay dynamics of the QDs. However, we do not observe any significant change in the PL decay when comparing the core and the core/shell QDs with average lifetimes of 0.95 ns and 1.05 ns, respectively.

5.3.4.2. Ga_2S_3-460/ZnS core/shell formation

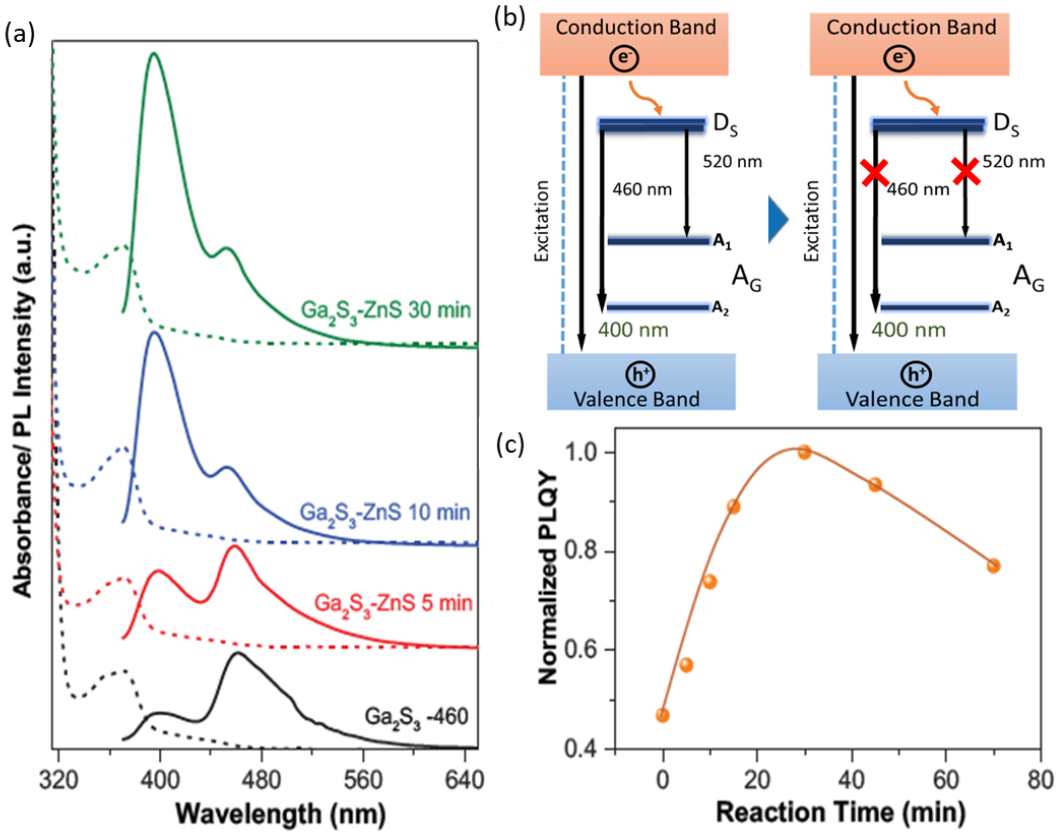

Figure 5.11: (a) Absorption (dashed line) and corresponding PL (solid line) spectra of Ga_2S_3-460/ZnS QDs dispersed in toluene with different ZnS growth times. (b) Scheme of the exciton dynamics before and after ZnS shelling on Ga_2S_3 QDs. (c) Variation of the PLQY normalized with respect to the highest PLQY sample.

The detailed synthesis protocol for Ga_2S_3-460/ZnS QDs is presented in the experimental section. Different from the previous case, we annealed the core at a high temperature (280 ºC) for 30 min to obtain strong emission at 460 nm due to the mid-gap transition from the starting Ga_2S_3 NCs. Figure

5.11a shows the evolution of absorption and emission spectra, following the same procedure of ZnS growth as for the 400 nm emitting QDs. While the absorption spectra do not show any significant shift, the PL spectra exhibit the continuous suppression of the 460 nm peak and the enhancement of the 400 nm peak. After 30 min of ZnS shell growth, we observe a strong emission at 400 nm with a shoulder-like small peak at 460 nm. The origin of the observed change in the PL emission can be explained by the scheme shown in Figure 5.11b. The growth of the ZnS shell leads to the suppression of surface states, which are responsible for the mid-gap state emission in Ga_2S_3 as shown in Figure 5.6c. This behavior suggests that the mid-gap states due to Ga and S vacancies form predominantly on the surface rather than in the bulk of the Ga_2S_3 NCs. Figure 5.11c shows the variation of the PLQY with the growth of the ZnS shell. While the PLQY of the core Ga_2S_3 QDs was 12.2 ± 0.6%, it improved with the growth of the ZnS layer up to 29.8 ± 1.5 %. However, it is noteworthy that the 460 nm shoulder does not disappear completely even after 80 min of ZnS growth. This can be due to the presence of some Ga and S vacancies inside the bulk of the QDs or to a small fraction of QDs with insufficient shelling. Similar to Ga_2S_3-400/ZnS NCs, the PLQY of Ga_2S_3-460/ZnS also enhanced significantly with the ZnS shell growth up to 30 min and then slowly decayed for longer shell growth times.

5.3.4.3. Structural analysis of the Ga_2S_3/ZnS core/shell NCs

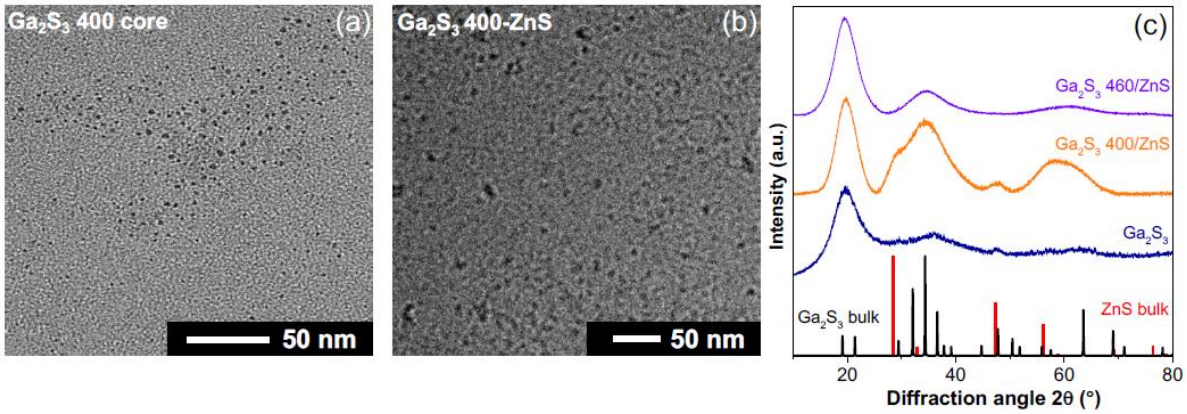

Figure 5.12: Bright-field TEM images of (a) Ga_2S_3-400 core and (b) Ga_2S_3-400/ZnS core/shell NCs. (c) XRD patterns of Ga_2S_3 core Ga_2S_3-400/ZnS, and Ga_2S_3-460/ZnS core/shell NCs. The reference patterns of monoclinic Ga_2S_3 and zinc blende ZnS are also given for comparison.

Figure 5.12a and 5.12b show low magnification TEM images of Ga_2S_3-400 core and Ga_2S_3-400/ZnS core/shell NCs after 60 min of ZnS growth, respectively. It can be observed from the TEM image that the particles have a nearly spherical morphology. The average particle size increased from 2.8 nm to about 4.2 nm from the core to the core/shell NCs. The unaltered morphology, uniform growth of the QDs, and the absence of any other separate size distribution supports the formation of a ZnS shell on the Ga_2S_3 core NCs. The crystal structure and compositional purity of the Ga_2S_3 core and Ga_2S_3/ZnS core/shell NCs have been studied using XRD. A comparison of the XRD patterns between the core and

the two types of core/shell NCs is depicted in Figure 5.12c. After 60 min of ZnS growth on Ga_2S_3-400 QDs, we observe the signals characteristic of zinc blende ZnS along with the Ga_2S_3 diffraction peaks due to the existence of the core/shell structure. However, we do not observe a ZnS signature peak in the case of the Ga_2S_3-460 NCs, which might be due to the larger size of the core NCs and hence the larger core:shell volume ratio.

Figures 5.13a, 5.13b, and 5.13c show the high-resolution XPS spectra for $Ga2p_{3/2}$, S2p, and Zn $2p_{3/2}$ respectively. All the spectra have been deconvoluted considering the spin-orbit splitting where the binding energy differences, full width at half maximum (FWHM), and area under the curve are fixed with standard database data. We note that unlike the Ga 2p spectra of Ga_2S_3 QDs (Figure 5.9a), Ga_2S_3/ZnS core/shell NCs (Figure 5.13a) do not display any presence of a Ga-O peak. This suggests that the in-situ formation of the ZnS shell has stopped the surface oxidation of the Ga_2S_3 core NCs. The similar splitting of the $S2p_{3/2}$ and S $2p_{1/2}$ signals with a peak separation energy of 1.16 eV indicates the presence of S in the sulfide phase from both the core and shell constituents. Finally, the presence of the Zn $2p_{3/2}$ peak (Figure 5.13c) further confirms the formation of ZnS. Thus, the presence of ZnS detected by XPS and XRD, along with the uniform size growth from TEM images, confirms the formation of a ZnS shell on top of the Ga_2S_3 NCs, which gives rise to the superior optical properties and enhanced colloidal stability.

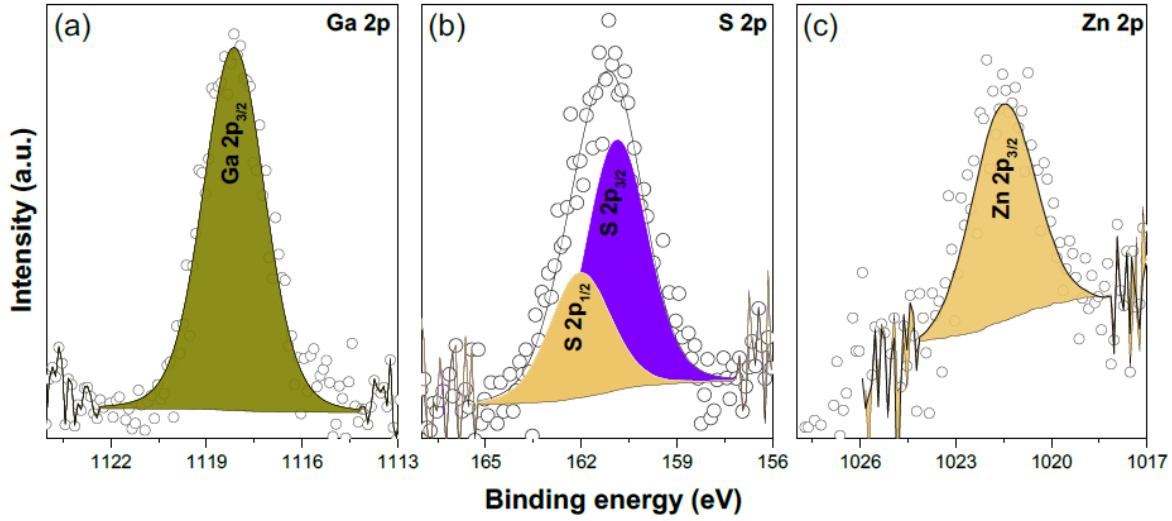

Figure 5.13: High-resolution XPS spectra of the Ga_2S_3/ZnS core/shell NCs, showing (a) $Ga2p_{3/2}$ (b) S2p, and (c) Zn $2p_{3/2}$.

5.4. Conclusion

Summarizing this part, a robust synthetic method for producing violet and blue luminescent, environmentally friendly Ga_2S_3 NCs has been developed. The study of their photophysical properties revealed that the emission from these NCs can occur through band edge transition and/or vacancy (Ga and S vacancy) mediated emission involving mid-gap states. However, by controlling the synthesis

parameters, we successfully demonstrated that it is possible to obtain selective emission in only one range. The luminescence color can be altered from 400 to 460 nm by changing the reaction time and controlling the mid-gap defect states. Furthermore, we have grown a ZnS shell on top of the Ga_2S_3 NCs, which passivates the surface of the core and gives rise to a strong enhancement of the band edge emission. Studying the optical properties of the core/shell NCs starting from two different types of cores, we have proven that the Ga and S vacancies are mostly located on the surface of the NCs rather than in their bulk volume. From a fundamental perspective, we have revealed the role of vacancy-related mid-gap states in the PL emission of these novel III-VI group semiconductor nanocrystals and devised a way to obtain defect-free band edge emission by developing a core/shell heterostructure. This work paves a new pathway for deep-blue emitting QDs using non-toxic and environmentally friendly compositions.

Chapter VI

General conclusion and perspectives

6.1. General conclusion

This thesis focused on developing the continuous flow synthesis of InP-based quantum dots (QDs) with improved optical properties for their application in the fields of optoelectronics and biological imaging. We first explored novel chemistries for the InP QDs preparation to make it compatible with the requirements of the flow synthesis. On the way of achieving these goals, we found that the use of novel indium (I) halide precursors gave access to a larger range of sizes and a narrower emission line width of the InP QDs than traditionally used In (III) halides. While exploring the possibility of using amorphous shells to passivate the QD surface, we discovered that Ga_2S_3 nanocrystals exhibit a high potential as efficient blue emitters. Finally, the gram-scale, fully automated flow synthesis of highly luminescent InP/ZnS core/shell QDs was achieved.

Concerning the synthetic development of InP core QDs, we first explored a batch route to prepare InP QDs using the inexpensive and non-pyrophoric phosphorus precursor tris(oleylamino)phosphine $P(NHR)_3$ and $InCl_3$ as the indium precursor (Chapter 2). We found that for controlled nucleation and growth, both bi- and trisubstituted oleylaminophosphine were needed where the former was mainly implied in the nucleation burst, whereas the latter acted as the phosphorus reservoir for the growth of the nuclei. This study allowed us to provide a better understanding of the nucleation and growth of InP QDs via the aminophosphine route. We confirmed that in this synthetic scheme, the addition of $ZnCl_2$ improved the size dispersity of the InP QDs by modifying the reaction kinetics. Furthermore, we developed a novel synthesis route to prepare InP QDs and InP/ZnS QDs in the non-coordinating solvent ODE resulting in optical properties comparable with the state of the art. Replacing oleylamine, which is ubiquitously used as the solvent in the aminophosphine synthesis of InP, by ODE can greatly enhance the reproducibility. Finally, we carried out the continuous flow synthesis using the batch-optimized protocol. Several parameters such as different flow configurations, the effect of temperature, pressures, and residence time (flow rate) were studied in detail. Under optimized conditions, the excitonic peak position of the obtained InP NCs could be adjusted in a wide spectral range (466-562 nm) by simply varying the reaction time (residence time in the reactor). We successfully produced InP/ZnS core/shell QDs in the continuous flow reactor at large scale (6.2 grams) with high reproducibility. Nevertheless, the optical properties in terms of PL line width were slightly inferior to those of batch-synthesized InP QDs. Since the size distribution is strongly influenced by the amount of added $ZnCl_2$, we attributed the

broader size dispersity to the inability of using higher concentrations than Zn:In = 3:1 during flow synthesis due to the precipitation of excess $ZnCl_2$ at room temperature.

In Chapter 3, we developed a novel Zn- and oxygen-free aminophosphine route to prepare InP QDs using indium monohalides. We found that indium (I) halide precursors played a dual role as both the In source and reducing agent for aminophosphines. The kinetic studies on the formation of InP QDs using ^{31}P-NMR revealed the coexistence of the two pathways: i) reduction of aminophosphine by In (I) and ii) reduction of aminophosphine by redox disproportionation. The contribution of each pathway strongly depended on the amount of phosphorus precursor and impacted the final size and shape of the particles. The size of the InP QDs could tuned in an unprecedentedly wide range from 3 to 11 nm just by changing the halide while maintaining a narrow size distribution (11-13%). To improve the PLQY, two methods were followed. First, InP QDs were etched using *in situ* generated HF at room temperature resulting in a PLQY up to 79% and a narrow emission linewidth of 43-50 nm FWHM (119-135 meV). Second, we followed the traditional epitaxial shell growth route using the single-molecular precursor $Zn(DDTC)_2$ at low temperature (140 °C). InP/ZnS core/shell QDs showed up to 44% PLQY with narrow emission linewidth (112 meV at 728 nm), the lowest value reported for aminophosphine-based syntheses and identical with the best-reported linewidth obtained with $P(TMS)_3$ (110 meV at 630 nm). Finally, PLE studies revealed that the PL broadening in the In(I)X-prepared InP QDs mainly originated from the size distribution and not from intra-band gap defect states arising from Zn- or O-impurities.

In another strategy to improve the optical properties and to reduce the emission line width significantly, we attempted the synthesis of InP nanoplatelets (NPLs), which can be atomically-flat and exhibit quantum confinement in only one direction (Chapter 4). Therefore, by precisely controlling the thickness, ultra-narrow PL emission line widths can be achieved. As InP crystallizes in the cubic zinc blende phase and no evident ways for symmetry breaking could be identified, we followed a template-mediated approach for synthesizing ZnSe/InP core/shell NPLs. After reproducing the synthesis of ZnSe NPLs, several attempts were made for their overcoating with InP using the SILAR method, however, in all cases, separate nucleation of InP QDs was observed. Stripping of the native amine ligands from the ZnSe template using Meerwein's salt before growing InP resulted in the irreversible agglomeration of the ZnSe NPLs. Finally, for the surface activation of the ZnSe NPLs template, we exchanged the native amine ligands for carboxylate ligands at room temperature. In this case, we observed the formation of InP islands at the edges of the ZnSe NPLs, while at the same time some ZnSe NPLs dissolved and transformed into ZnSe nanowires.

In Chapter 5, we explored the possibility to grow an amorphous shell of gallium sulfide (GaS_x) on the surface of InP core QDs to improve their optical properties (emission line width, PLQY) and photostability. However, it turned out challenging to control the gallium precursor's reactivity and avoid the formation separate GaS_x nanoparticles and/or In(Ga)P alloys. At the same time, the Ga_2S_3 formed in some reactions exhibited intense blue emission, and therefore, their synthesis was optimized in a

side-project. The blue emission arose from transitions involving the band edge and/or donor accepter mid-gap states caused by Ga and S vacancies, respectively. We demonstrated that it is possible to obtain pure and narrow band edge emission at around 400 nm by controlling the reaction parameters. Furthermore, Ga_2S_3/ZnS NCs were successfully prepared, giving rise to a strong enhancement of the band edge emission thanks to surface passivation. The present results show that Ga_2S_3/ZnS NCs have a high potential for application in blue-emitting devices, in particular as a more environment-friendly replacement of Cd-based QDs.

6.2. Outlook

InP NCs are in huge demand in the lighting and display industry.[4, 166] For commercial use, their optical properties need to be optimized in terms of emission wavelength, line width, PLQY, photo- and thermal stability, while using low-cost and reproducible large-scale methods for their fabrication. This thesis opens several perspectives for the development of InP-based QDs for commercial applications as well as for fundamental studies.

Continuous flow synthesis of InP QDs using indium (I) halides

As part of some preliminary studies, we have investigated In(I)X (X = Cl, Br, I) in the continuous flow synthesis. Figure 6.1 shows the absorption spectra of InP QDs synthesized using InI in flow. An absorption shoulder at 528 nm can be observed corresponding to InP QDs. However, further optimization of the synthesis parameters is needed to improve the optical properties. In addition, a full understanding of the reaction mechanism involving indium monohalides and aminophosphines is needed. NIR-emitting (>700 nm) InP QDs obtained using InCl can be very interesting for in vivo biological imaging applications.

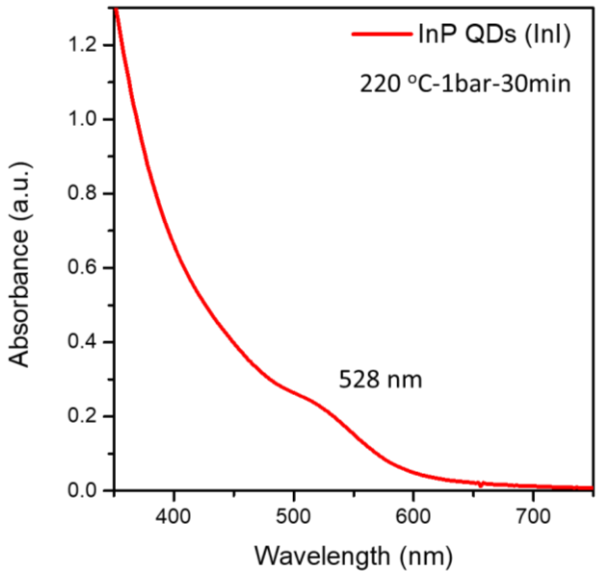

Figure 6.1: Absorption spectrum of InP QDs synthesized via the continuous flow route using InI and $P(NHR)_3$.

Development of InP/ZnSe/ZnS or other types of multi-shell structures

The results obtained from room temperature HF etching are promising for improving the PLQY (Chapter 3). Future work should focus on improving the scalability of the etching process and further developing other core/shell structures to improve the PLQY and stability of the InP QDs. The development of InP/ZnSe/ZnS multi-shell structure in the continuous flow route is particularly interesting due to the reduced lattice mismatch between InP and ZnSe. Furthermore, PLQYs virtually 100% have already been obtained in the literature using this type of heterostructure.[134] As a first challenge, continuous flow-compatible precursors for the synthesis of the ZnSe shell need to be identified. The single-molecular precursor zinc bis(diethyldiselenocarbamate) could be a promising candidate in this respect.[167] As an alternative, a GaP intermediate shell is envisioned, which could be advantageous for eliminating shallow trap states in the InP band gap induced by zinc leading to spectral broadening.[168] Finally, to drastically enhance the chemical stability of the core/shell systems, the overcoating with a ceramic-type material such as alumina, titania or zirconia can be envisioned. Promising results have already been obtained with an amorphous alumina shell on InP/ZnSe/ZnS QDs.[169]

References

1. Feynman, R., There's Plenty of Room at the Bottom. 1, Ed. 2002; p 14.
2. Taniguchi, N. In *On the Basic concept of Nanotechnology*, ICPE, 1974.
3. Pokropivny, V. V.; Skorokhod, V. V., New dimensionality classifications of nanostructures. *Physica E: Low-dimensional Systems and Nanostructures* **2008,** *40* (7), 2521-2525.
4. Chen, B.; Li, D.; Wang, F., InP Quantum Dots: Synthesis and Lighting Applications. *Small* **2020,** *16* (32), e2002454.
5. Kovalenko, M. V.; Manna, L.; Cabot, A.; Hens, Z.; Talapin, D. V.; Kagan, C. R.; Klimov, V. I.; Rogach, A. L.; Reiss, P.; Milliron, D. J.; Guyot-Sionnnest, P.; Konstantatos, G.; Parak, W. J.; Hyeon, T.; Korgel, B. A.; Murray, C. B.; Heiss, W., Prospects of nanoscience with nanocrystals. *ACS Nano* **2015,** *9* (2), 1012-57.
6. Schaming, D.; Remita, H., Nanotechnology: from the ancient time to nowadays. *Foundations of Chemistry* **2015,** *17* (3), 187-205.
7. Bayda, S.; Adeel, M.; Tuccinardi, T.; Cordani, M.; Rizzolio, F., The History of Nanoscience and Nanotechnology: From Chemical-Physical Applications to Nanomedicine. *Molecules* **2019,** *25* (1).
8. Dargaud, O.; Stievano, L.; Faurel, X., A new procedure for the production of red gold purples at the “Manufacture nationale de Céramiques de Sèvres”. *Gold Bulletin* **2007,** *40* (4), 283-290.
9. Padovani, S.; Puzzovio, D.; Sada, C.; Mazzoldi, P.; Borgia, I.; Sgamellotti, A.; Brunetti, B. G.; Cartechini, L.; D’Acapito, F.; Maurizio, C.; Shokoui, F.; Oliaiy, P.; Rahighi, J.; Lamehi-Rachti, M.; Pantos, E., XAFS study of copper and silver nanoparticles in glazes of medieval middle-east lustreware (10th–13th century). *Applied Physics A* **2006,** *83* (4), 521-528.
10. Walter, P.; Welcomme, E.; Hallegot, P.; Zaluzec, N. J.; Deeb, C.; Castaing, J.; Veyssiere, P.; Breniaux, R.; Leveque, J. L.; Tsoucaris, G., Early use of PbS nanotechnology for an ancient hair dyeing formula. *Nano Lett* **2006,** *6* (10), 2215-9.
11. Montanarella, F.; Kovalenko, M. V., Three Millennia of Nanocrystals. *ACS Nano* **2022**, *16* (4) 5085–5102.
12. Brus, L. E., Electron–electron and electron-hole interactions in small semiconductor crystallites: The size dependence of the lowest excited electronic state. *The Journal of Chemical Physics* **1984,** *80* (9), 4403-4409.
13. Ekimov, A. I.; Efros, A. L.; Onushchenko, A. A., Quantum size effect in semiconductor microcrystals. *Solid State Communications* **1985,** *56* (11), 921-924.
14. Einevoll, G. T., Confinement of excitons in quantum dots. *Phys Rev B Condens Matter* **1992,** *45* (7), 3410-3417.

15. Won, Y. H.; Cho, O.; Kim, T.; Chung, D. Y.; Kim, T.; Chung, H.; Jang, H.; Lee, J.; Kim, D.; Jang, E., Highly efficient and stable InP/ZnSe/ZnS quantum dot light-emitting diodes. *Nature* **2019,** *575* (7784), 634-638.
16. Liu, P.; Lou, Y.; Ding, S.; Zhang, W.; Wu, Z.; Yang, H.; Xu, B.; Wang, K.; Sun, X. W., Green InP/ZnSeS/ZnS Core Multi-Shelled Quantum Dots Synthesized with Aminophosphine for Effective Display Applications. *Advanced Functional Materials* **2021,** *31* (11), 2008453.
17. Lim, J.; Bae, W. K.; Lee, D.; Nam, M. K.; Jung, J.; Lee, C.; Char, K.; Lee, S., InP@ZnSeS, Core@Composition Gradient Shell Quantum Dots with Enhanced Stability. *Chemistry of Materials* **2011,** *23* (20), 4459-4463.
18. Rogach, A., Quantum dots still shining strong 30 years on. *ACS Nano* **2014,** *8* (7), 6511-2.
19. Murray, C. B.; Norris, D. J.; Bawendi, M. G., Synthesis and characterization of nearly monodisperse CdE (E = sulfur, selenium, tellurium) semiconductor nanocrystallites. *Journal of the American Chemical Society* **1993,** *115* (19), 8706-8715.
20. LaMer, V. K.; Dinegar, R. H., Theory, Production and Mechanism of Formation of Monodispersed Hydrosols. *Journal of the American Chemical Society* **1950,** *72* (11), 4847-4854.
21. Hines, M. A.; Guyot-Sionnest, P., Synthesis and Characterization of Strongly Luminescing ZnS-Capped CdSe Nanocrystals. *The Journal of Physical Chemistry* **1996,** *100* (2), 468-471.
22. Peng, X.; Schlamp, M. C.; Kadavanich, A. V.; Alivisatos, A. P., Epitaxial Growth of Highly Luminescent CdSe/CdS Core/Shell Nanocrystals with Photostability and Electronic Accessibility. *Journal of the American Chemical Society* **1997,** *119* (30), 7019-7029.
23. Haubold, S.; Haase, M.; Kornowski, A.; Weller, H., Strongly Luminescent InP/ZnS Core-Shell Nanoparticles. *ChemPhysChem* **2001,** *2* (5), 331-334.
24. Sashchiuk, A.; Langof, L.; Chaim, R.; Lifshitz, E., Synthesis and characterization of PbSe and PbSe/PbS core–shell colloidal nanocrystals. *Journal of Crystal Growth* **2002,** *240* (3-4), 431-438.
25. Balet, L. P.; Ivanov, S. A.; Piryatinski, A.; Achermann, M.; Klimov, V. I., Inverted Core/Shell Nanocrystals Continuously Tunable between Type-I and Type-II Localization Regimes. *Nano Letters* **2004,** *4* (8), 1485-1488.
26. Shariati, M. R.; Samadi-Maybodi, A.; Colagar, A. H., Dual cocatalyst loaded reverse type-I core/shell quantum dots for photocatalytic antibacterial applications. *Journal of Materials Chemistry A* **2018,** *6* (41), 20433-20443.
27. Eren, G. O.; Sadeghi, S.; Bahmani Jalali, H.; Ritter, M.; Han, M.; Baylam, I.; Melikov, R.; Onal, A.; Oz, F.; Sahin, M.; Ow-Yang, C. W.; Sennaroglu, A.; Lechner, R. T.; Nizamoglu, S., Cadmium-Free and Efficient Type-II InP/ZnO/ZnS Quantum Dots and Their Application for LEDs. *ACS Appl Mater Interfaces* **2021,** *13* (27), 32022-32030.

28. Dorfs, D.; Hickey, S.; Eychmüller, A., Type-I and Type-II Core-Shell Quantum Dots: Synthesis and Characterization. **2011**.
29. Kim, S.; Fisher, B.; Eisler, H. J.; Bawendi, M., Type-II quantum dots: CdTe/CdSe(core/shell) and CdSe/ZnTe(core/shell) heterostructures. *J Am Chem Soc* **2003,** *125* (38), 11466-7.
30. Zhu, H.; Song, N.; Rodriguez-Cordoba, W.; Lian, T., Wave function engineering for efficient extraction of up to nineteen electrons from one CdSe/CdS quasi-type II quantum dot. *J Am Chem Soc* **2012,** *134* (9), 4250-7.
31. Wu, K.; Liang, G.; Kong, D.; Chen, J.; Chen, Z.; Shan, X.; McBride, J. R.; Lian, T., Quasi-type II CuInS(2)/CdS core/shell quantum dots. *Chem Sci* **2016,** *7* (2), 1238-1244.
32. Reiss, P.; Protiere, M.; Li, L., Core/Shell semiconductor nanocrystals. *Small* **2009,** *5* (2), 154-68.
33. Dupont, D.; Tessier, M. D.; Smet, P. F.; Hens, Z., Indium Phosphide-Based Quantum Dots with Shell-Enhanced Absorption for Luminescent Down-Conversion. *Adv Mater* **2017,** *29* (29).
34. Sargent, E. H., Colloidal quantum dot solar cells. *Nature Photonics* **2012,** *6* (3), 133-135.
35. Sun, Q.; Wang, Y. A.; Li, L. S.; Wang, D.; Zhu, T.; Xu, J.; Yang, C.; Li, Y., Bright, multicoloured light-emitting diodes based on quantum dots. *Nature Photonics* **2007,** *1* (12), 717-722.
36. Shirasaki, Y.; Supran, G. J.; Bawendi, M. G.; Bulović, V., Emergence of colloidal quantum-dot light-emitting technologies. *Nature Photonics* **2012,** *7* (1), 13-23.
37. Colvin, V. L.; Schlamp, M. C.; Alivisatos, A. P., Light-emitting diodes made from cadmium selenide nanocrystals and a semiconducting polymer. *Nature* **1994,** *370* (6488), 354-357.
38. Kim, S.; Kim, T.; Kang, M.; Kwak, S. K.; Yoo, T. W.; Park, L. S.; Yang, I.; Hwang, S.; Lee, J. E.; Kim, S. K.; Kim, S. W., Highly luminescent InP/GaP/ZnS nanocrystals and their application to white light-emitting diodes. *J Am Chem Soc* **2012,** *134* (8), 3804-9.
39. Liu, J.; Zhang, H.; Selopal, G. S.; Sun, S.; Zhao, H.; Rosei, F., Visible and Near-Infrared, Multiparametric, Ultrasensitive Nanothermometer Based on Dual-Emission Colloidal Quantum Dots. *ACS Photonics* **2019,** *6* (10), 2479-2486.
40. Chen, S.; Tang, M.; Jiang, Q.; Wu, J.; Dorogan, V. G.; Benamara, M.; Mazur, Y. I.; Salamo, G. J.; Smowton, P.; Seeds, A.; Liu, H., InAs/GaAs Quantum-Dot Superluminescent Light-Emitting Diode Monolithically Grown on a Si Substrate. *ACS Photonics* **2014,** *1* (7), 638-642.
41. Ramasamy, P.; Kim, N.; Kang, Y.-S.; Ramirez, O.; Lee, J.-S., Tunable, Bright, and Narrow-Band Luminescence from Colloidal Indium Phosphide Quantum Dots. *Chemistry of Materials* **2017,** *29* (16), 6893-6899.
42. Li, Y.; Hou, X.; Dai, X.; Yao, Z.; Lv, L.; Jin, Y.; Peng, X., Stoichiometry-Controlled InP-Based Quantum Dots: Synthesis, Photoluminescence, and Electroluminescence. *J Am Chem Soc* **2019,** *141* (16), 6448-6452.

43. Saran, R.; Curry, R. J., Lead sulphide nanocrystal photodetector technologies. *Nature Photonics* **2016,** *10* (2), 81-92.
44. Yin, X.; Zhang, C.; Guo, Y.; Yang, Y.; Xing, Y.; Que, W., PbS QD-based photodetectors: future-oriented near-infrared detection technology. *Journal of Materials Chemistry C* **2021,** *9* (2), 417-438.
45. Howes, P. D.; Chandrawati, R.; Stevens, M. M., Bionanotechnology. Colloidal nanoparticles as advanced biological sensors. *Science* **2014,** *346* (6205), 1247390.
46. Sukhanova, A.; Devy, J.; Venteo, L.; Kaplan, H.; Artemyev, M.; Oleinikov, V.; Klinov, D.; Pluot, M.; Cohen, J. H.; Nabiev, I., Biocompatible fluorescent nanocrystals for immunolabeling of membrane proteins and cells. *Anal Biochem* **2004,** *324* (1), 60-7.
47. Dahan, M.; Levi, S.; Luccardini, C.; Rostaing, P.; Riveau, B.; Triller, A., Diffusion dynamics of glycine receptors revealed by single-quantum dot tracking. *Science* **2003,** *302* (5644), 442-5.
48. Mallick, S.; Kumar, P.; Koner, A. L., Freeze-Resistant Cadmium-Free Quantum Dots for Live-Cell Imaging. *ACS Applied Nano Materials* **2019,** *2* (2), 661-666.
49. Zhang, Y.; Lv, Y.; Li, L. S.; Zhao, X. J.; Zhao, M. X.; Shen, H., Aminophosphate precursors for the synthesis of near-unity emitting InP quantum dots and their application in liver cancer diagnosis. *Exploration* **2022,** *2* (4), 20220082.
50. DIRECTIVE 2002/95/EC OF THE EUROPEAN PARLIAMENT AND OF THE COUNCIL.
51. Chibli, H.; Carlini, L.; Park, S.; Dimitrijevic, N. M.; Nadeau, J. L., Cytotoxicity of InP/ZnS quantum dots related to reactive oxygen species generation. *Nanoscale* **2011,** *3* (6), 2552-9.
52. Reiss, P.; Carriere, M.; Lincheneau, C.; Vaure, L.; Tamang, S., Synthesis of Semiconductor Nanocrystals, Focusing on Nontoxic and Earth-Abundant Materials. *Chem Rev* **2016,** *116* (18), 10731-819.
53. Yong, K. T.; Ding, H.; Roy, I.; Law, W. C.; Bergey, E. J.; Maitra, A.; Prasad, P. N., Imaging pancreatic cancer using bioconjugated InP quantum dots. *ACS Nano* **2009,** *3* (3), 502-10.
54. Thanh, N. T.; Maclean, N.; Mahiddine, S., Mechanisms of nucleation and growth of nanoparticles in solution. *Chem Rev* **2014,** *114* (15), 7610-30.
55. Healy, M. D.; Laibinis, P. E.; Stupik, P. D.; Barron, A. R., The reaction of indium(III) chloride with tris(trimethylsilyl)phosphine: a novel route to indium phosphide. *Journal of the Chemical Society, Chemical Communications* **1989,** (6), 359.
56. Wells, R. L.; Aubuchon, S. R.; Kher, S. S.; Lube, M. S.; White, P. S., Synthesis of Nanocrystalline Indium Arsenide and Indium Phosphide from Indium(III) Halides and Tris(trimethylsilyl)pnicogens. Synthesis, Characterization, and Decomposition Behavior of I3In.cntdot.P(SiMe3)3. *Chemistry of Materials* **2002,** *7* (4), 793-800.
57. Guzelian, A. A.; Katari, J. E. B.; Kadavanich, A. V.; Banin, U.; Hamad, K.; Juban, E.; Alivisatos, A. P.; Wolters, R. H.; Arnold, C. C.; Heath, J. R., Synthesis of Size-Selected,

Surface-Passivated InP Nanocrystals. *The Journal of Physical Chemistry* **1996,** *100* (17), 7212-7219.

58. Battaglia, D.; Peng, X., Formation of High Quality InP and InAs Nanocrystals in a Noncoordinating Solvent. *Nano Letters* **2002,** *2* (9), 1027-1030.
59. Li, L.; Reiss, P., One-pot Synthesis of Highly Luminescent InP/ZnS Nanocrystals without Precursor Injection. *Journal of the American Chemical Society* **2008,** *130* (35), 11588-11589.
60. Thuy, U. T. D.; Reiss, P.; Liem, N. Q., Luminescence properties of In(Zn)P alloy core/ZnS shell quantum dots. *Applied Physics Letters* **2010,** *97* (19), 193104.
61. Koh, S.; Eom, T.; Kim, W. D.; Lee, K.; Lee, D.; Lee, Y. K.; Kim, H.; Bae, W. K.; Lee, D. C., Zinc–Phosphorus Complex Working as an Atomic Valve for Colloidal Growth of Monodisperse Indium Phosphide Quantum Dots. *Chemistry of Materials* **2017,** *29* (15), 6346-6355.
62. Gary, D. C.; Glassy, B. A.; Cossairt, B. M., Investigation of Indium Phosphide Quantum Dot Nucleation and Growth Utilizing Triarylsilylphosphine Precursors. *Chemistry of Materials* **2014,** *26* (4), 1734-1744.
63. Harris, D. K.; Bawendi, M. G., Improved precursor chemistry for the synthesis of III-V quantum dots. *J Am Chem Soc* **2012,** *134* (50), 20211-3.
64. Joung, S.; Yoon, S.; Han, C. S.; Kim, Y.; Jeong, S., Facile synthesis of uniform large-sized InP nanocrystal quantum dots using tris(tert-butyldimethylsilyl)phosphine. *Nanoscale Res Lett* **2012,** *7* (1), 93.
65. Ramasamy, P.; Ko, K.-J.; Kang, J.-W.; Lee, J.-S., Two-Step "Seed-Mediated" Synthetic Approach to Colloidal Indium Phosphide Quantum Dots with High-Purity Photo- and Electroluminescence. *Chemistry of Materials* **2018,** *30* (11), 3643-3647.
66. Beberwyck, B. J.; Alivisatos, A. P., Ion exchange synthesis of III-V nanocrystals. *J Am Chem Soc* **2012,** *134* (49), 19977-80.
67. Stone, D.; Koley, S.; Remennik, S.; Asor, L.; Panfil, Y. E.; Naor, T.; Banin, U., Luminescent Anisotropic Wurtzite InP Nanocrystals. *Nano Lett* **2021,** *21* (23), 10032-10039.
68. Gerbec, J. A.; Magana, D.; Washington, A.; Strouse, G. F., Microwave-enhanced reaction rates for nanoparticle synthesis. *J Am Chem Soc* **2005,** *127* (45), 15791-800.
69. Ashley, B.; Vakil, P. N.; Lynch, B. B.; Dyer, C. M.; Tracy, J. B.; Owens, J.; Strouse, G. F., Microwave Enhancement of Autocatalytic Growth of Nanometals. *ACS Nano* **2017,** *11* (10), 9957-9967.
70. Li, Y.; Huang, H.; Xiong, Y.; Kershaw, S. V.; Rogach, A. L., Revealing the Formation Mechanism of CsPbBr(3) Perovskite Nanocrystals Produced via a Slowed-Down Microwave-Assisted Synthesis. *Angew Chem Int Ed Engl* **2018,** *57* (20), 5833-5837.
71. Lovingood, D. D.; Strouse, G. F., Microwave induced in-situ active ion etching of growing InP nanocrystals. *Nano Lett* **2008,** *8* (10), 3394-7.

72. Lignos, I.; Protesescu, L.; Stavrakis, S.; Piveteau, L.; Speirs, M. J.; Loi, M. A.; Kovalenko, M. V.; deMello, A. J., Facile Droplet-based Microfluidic Synthesis of Monodisperse IV–VI Semiconductor Nanocrystals with Coupled In-Line NIR Fluorescence Detection. *Chemistry of Materials* **2014,** *26* (9), 2975-2982.
73. Nightingale, A. M.; de Mello, J. C., Controlled synthesis of III-V quantum dots in microfluidic reactors. *Chemphyschem* **2009,** *10* (15), 2612-4.
74. Vikram, A.; Kumar, V.; Ramesh, U.; Balakrishnan, K.; Oh, N.; Deshpande, K.; Ewers, T.; Trefonas, P.; Shim, M.; Kenis, P. J. A., A Millifluidic Reactor System for Multistep Continuous Synthesis of InP/ZnSeS Nanoparticles. *ChemNanoMat* **2018,** *4* (9), 943-953.
75. Yan, P.; Xie, Y.; Wang, W.; Liu, F.; Qian, Y., A low-temperature route to InP nanocrystals. *Journal of Materials Chemistry* **1999,** *9* (8), 1831-1833.
76. Li, L.; Protière, M.; Reiss, P., Economic Synthesis of High Quality InP Nanocrystals Using Calcium Phosphide as the Phosphorus Precursor. *Chemistry of Materials* **2008,** *20* (8), 2621-2623.
77. Liu, Z.; Kumbhar, A.; Xu, D.; Zhang, J.; Sun, Z.; Fang, J., Coreduction colloidal synthesis of III-V nanocrystals: the case of InP. *Angew Chem Int Ed Engl* **2008,** *47* (19), 3540-2.
78. Tessier, M. D.; Dupont, D.; De Nolf, K.; De Roo, J.; Hens, Z., Economic and Size-Tunable Synthesis of InP/ZnE (E = S, Se) Colloidal Quantum Dots. *Chem. Mater.* **2015,** *27* (13), 4893-4898.
79. Song, W.-S.; Lee, H.-S.; Lee, J. C.; Jang, D. S.; Choi, Y.; Choi, M.; Yang, H., Amine-derived synthetic approach to color-tunable InP/ZnS quantum dots with high fluorescent qualities. *Journal of Nanoparticle Research* **2013,** *15* (6).
80. Buffard, A.; Dreyfuss, S.; Nadal, B.; Heuclin, H.; Xu, X.; Patriarche, G.; Mézailles, N.; Dubertret, B., Mechanistic Insight and Optimization of InP Nanocrystals Synthesized with Aminophosphines. *Chemistry of Materials* **2016,** *28* (16), 5925-5934.
81. McVey, B. F. P.; Swain, R. A.; Lagarde, D.; Tison, Y.; Martinez, H.; Chaudret, B.; Nayral, C.; Delpech, F., Unraveling the role of zinc complexes on indium phosphide nanocrystal chemistry. *J Chem Phys* **2019,** *151* (19), 191102.
82. Tessier, M. D.; De Nolf, K.; Dupont, D.; Sinnaeve, D.; De Roo, J.; Hens, Z., Aminophosphines: A Double Role in the Synthesis of Colloidal Indium Phosphide Quantum Dots. *J Am Chem Soc* **2016,** *138* (18), 5923-9.
83. Kim, Y.; Ham, S.; Jang, H.; Min, J. H.; Chung, H.; Lee, J.; Kim, D.; Jang, E., Bright and Uniform Green Light Emitting InP/ZnSe/ZnS Quantum Dots for Wide Color Gamut Displays. *ACS Applied Nano Materials* **2019,** *2* (3), 1496-1504.
84. Van Avermaet, H.; Schiettecatte, P.; Hinz, S.; Giordano, L.; Ferrari, F.; Nayral, C.; Delpech, F.; Maultzsch, J.; Lange, H.; Hens, Z., Full-Spectrum InP-Based Quantum Dots with Near-Unity Photoluminescence Quantum Efficiency. *ACS Nano* **2022**, 16(6), 9701-9712.

85. Jo, J. H.; Jo, D. Y.; Choi, S. W.; Lee, S. H.; Kim, H. M.; Yoon, S. Y.; Kim, Y.; Han, J. N.; Yang, H., Highly Bright, Narrow Emissivity of InP Quantum Dots Synthesized by Aminophosphine: Effects of Double Shelling Scheme and Ga Treatment. *Advanced Optical Materials* **2021,** *9* (16), 2100427.
86. Yu, P.; Shan, Y.; Cao, S.; Hu, Y.; Li, Q.; Zeng, R.; Zou, B.; Wang, Y.; Zhao, J., Inorganic Solid Phosphorus Precursor of Sodium Phosphaethynolate for Synthesis of Highly Luminescent InP-Based Quantum Dots. *ACS Energy Letters* **2021,** *6* (8), 2697-2703.
87. Choi, S.-W.; Kim, H.-M.; Yoon, S.-Y.; Jo, D.-Y.; Kim, S.-K.; Kim, Y.; Park, S. M.; Lee, Y.-J.; Yang, H., Aminophosphine-derived, high-quality red-emissive InP quantum dots by the use of an unconventional in halide. *Journal of Materials Chemistry C* **2022,** *10* (6), 2213-2222.
88. Tamang, S.; Lincheneau, C.; Hermans, Y.; Jeong, S.; Reiss, P., Chemistry of InP Nanocrystal Syntheses. *Chemistry of Materials* **2016,** *28* (8), 2491-2506.
89. Steinhagen, C.; Panthani, M. G.; Akhavan, V.; Goodfellow, B.; Koo, B.; Korgel, B. A., Synthesis of Cu(2)ZnSnS(4) nanocrystals for use in low-cost photovoltaics. *J Am Chem Soc* **2009,** *131* (35), 12554-5.
90. Wang, X.; Sun, G.; Li, N.; Chen, P., Quantum dots derived from two-dimensional materials and their applications for catalysis and energy. *Chem Soc Rev* **2016,** *45* (8), 2239-62.
91. Garcia de Arquer, F. P.; Talapin, D. V.; Klimov, V. I.; Arakawa, Y.; Bayer, M.; Sargent, E. H., Semiconductor quantum dots: Technological progress and future challenges. *Science* **2021,** *373* (6555).
92. Reiss, P.; Carrière, M.; Lincheneau, C.; Vaure, L.; Tamang, S., Synthesis of Semiconductor Nanocrystals, Focusing on Nontoxic and Earth-Abundant Materials. *Chem Rev* **2016,** *116* (18), 10731-819.
93. Hendricks, M. P.; Campos, M. P.; Cleveland, G. T.; Jen-La Plante, I.; Owen, J. S., NANOMATERIALS. A tunable library of substituted thiourea precursors to metal sulfide nanocrystals. *Science* **2015,** *348* (6240), 1226-30.
94. Owen, J. S.; Chan, E. M.; Liu, H.; Alivisatos, A. P., Precursor conversion kinetics and the nucleation of cadmium selenide nanocrystals. *J Am Chem Soc* **2010,** *132* (51), 18206-13.
95. Franke, D.; Harris, D. K.; Xie, L.; Jensen, K. F.; Bawendi, M. G., The Unexpected Influence of Precursor Conversion Rate in the Synthesis of III-V Quantum Dots. *Angew Chem Int Ed Engl* **2015,** *54* (48), 14299-303.
96. Allen, P. M.; Walker, B. J.; Bawendi, M. G., Mechanistic insights into the formation of InP quantum dots. *Angew Chem Int Ed Engl* **2010,** *49* (4), 760-2.
97. Clark, M. D.; Kumar, S. K.; Owen, J. S.; Chan, E. M., Focusing nanocrystal size distributions via production control. *Nano Lett* **2011,** *11* (5), 1976-80.

98. Won, Y.-H.; Cho, O.; Kim, T.; Chung, D.-Y.; Kim, T.; Chung, H.; Jang, H.; Lee, J.; Kim, D.; Jang, E., Highly efficient and stable InP/ZnSe/ZnS quantum dot light-emitting diodes. *Nature* **2019,** *575* (7784), 634-638.
99. Nightingale, A. M.; Demello, J. C., Segmented flow reactors for nanocrystal synthesis. *Adv Mater* **2013,** *25* (13), 1813-21.
100. Xu, S.; Kumar, S.; Nann, T., Rapid synthesis of high-quality InP nanocrystals. *J Am Chem Soc* **2006,** *128* (4), 1054-5.
101. Lignos, I.; Mo, Y.; Carayannopoulos, L.; Ginterseder, M.; Bawendi, M. G.; Jensen, K. F., A high-temperature continuous stirred-tank reactor cascade for the multistep synthesis of InP/ZnS quantum dots. *Reaction Chemistry & Engineering* **2021,** *6* (3), 459-464.
102. Rivaux, C.; Akdas, T.; Yadav, R.; El-Dahshan, O.; Moodelly, D.; Ling, W. L.; Aldakov, D.; Reiss, P., Continuous Flow Aqueous Synthesis of Highly Luminescent AgInS2 and AgInS2/ZnS Quantum Dots. *The Journal of Physical Chemistry C* **2022,** *126* (48), 20524-20534.
103. Akdas, T.; Reiss, P., "Safer-by-design" synthesis of quantum dots in flow reactors. *Journal of Physics: Conference Series* **2019,** *1323* (1), 012007.
104. Adam, S.; Talapin, D. V.; Borchert, H.; Lobo, A.; McGinley, C.; de Castro, A. R.; Haase, M.; Weller, H.; Moller, T., The effect of nanocrystal surface structure on the luminescence properties: photoemission study of HF-etched InP nanocrystals. *J Chem Phys* **2005,** *123* (8), 084706.
105. Kirkwood, N.; De Backer, A.; Altantzis, T.; Winckelmans, N.; Longo, A.; Antolinez, F. V.; Rabouw, F. T.; De Trizio, L.; Geuchies, J. J.; Mulder, J. T.; Renaud, N.; Bals, S.; Manna, L.; Houtepen, A. J., Locating and Controlling the Zn Content in In(Zn)P Quantum Dots. *Chemistry of Materials* **2019,** *32* (1), 557-565.
106. Pietra, F.; De Trizio, L.; Hoekstra, A. W.; Renaud, N.; Prato, M.; Grozema, F. C.; Baesjou, P. J.; Koole, R.; Manna, L.; Houtepen, A. J., Tuning the Lattice Parameter of InxZnyP for Highly Luminescent Lattice-Matched Core/Shell Quantum Dots. *ACS Nano* **2016,** *10* (4), 4754-62.
107. Mourdikoudis, S.; Liz-Marzán, L. M., Oleylamine in Nanoparticle Synthesis. *Chemistry of Materials* **2013,** *25* (9), 1465-1476.
108. Baranov, D.; Lynch, M. J.; Curtis, A. C.; Carollo, A. R.; Douglass, C. R.; Mateo-Tejada, A. M.; Jonas, D. M., Purification of Oleylamine for Materials Synthesis and Spectroscopic Diagnostics for trans Isomers. *Chemistry of Materials* **2019,** *31* (4), 1223-1230.
109. Xu, Z.; Li, Y.; Li, J.; Pu, C.; Zhou, J.; Lv, L.; Peng, X., Formation of Size-Tunable and Nearly Monodisperse InP Nanocrystals: Chemical Reactions and Controlled Synthesis. *Chemistry of Materials* **2019,** *31* (14), 5331-5341.
110. Zhang, X.; Lv, H.; Xing, W.; Li, Y.; Geng, C.; Xu, S., Trioctylphosphine accelerated growth of InP quantum dots at low temperature. *Nanotechnology* **2021,** *33* (5).

111. Singh, A.; Chawla, P.; Jain, S.; Sharma, S. N., Tapping the potential of trioctylphosphine (TOP) in the realization of highly luminescent blue-emitting colloidal indium phosphide (InP) quantum dots. *Physica E: Low-dimensional Systems and Nanostructures* **2017,** *90*, 175-182.
112. Kim, Y.; Yang, K.; Lee, S., Highly luminescent blue-emitting In1−xGaxP@ZnS quantum dots and their applications in QLEDs with inverted structure. *Journal of Materials Chemistry C* **2020,** *8* (23), 7679-7687.
113. Lian, L.; Li, Y.; Zhang, D.; Zhang, J., Synthesis of Highly Luminescent InP/ZnS Quantum Dots with Suppressed Thermal Quenching. *Coatings* **2021,** *11* (5), 581.
114. Cho, H.; Jung, S.; Kim, M.; Kwon, H.; Bang, J., Effects of Zn impurity on the photoluminescence properties of InP quantum dots. *Journal of Luminescence* **2022,** *245*, 118647.
115. Lakowicz, J. R., *Principles of Fluorescence Spectroscopy*. 3rd ed.; Springer New York, NY: 2006.
116. Thuy, U. T. D.; Thuy, P. T.; Liem, N. Q.; Li, L.; Reiss, P., Comparative photoluminescence study of close-packed and colloidal InP/ZnS quantum dots. *Applied Physics Letters* **2010,** *96* (7), 073102.
117. McVey, B. F. P.; Swain, R. A.; Lagarde, D.; Tison, Y.; Martinez, H.; Chaudret, B.; Nayral, C.; Delpech, F., Unraveling the role of zinc complexes on indium phosphide nanocrystal chemistry. *J. Chem. Phys.* **2019,** *151* (19), 191102.
118. Xu, S.; Ziegler, J.; Nann, T., Rapid synthesis of highly luminescent InP and InP/ZnS nanocrystals. *J. Mater. Chem.* **2008,** *18* (23), 2653-2656.
119. Kirkwood, N.; Monchen, J. O. V.; Crisp, R. W.; Grimaldi, G.; Bergstein, H. A. C.; du Fosse, I.; van der Stam, W.; Infante, I.; Houtepen, A. J., Finding and Fixing Traps in II-VI and III-V Colloidal Quantum Dots: The Importance of Z-Type Ligand Passivation. *J Am Chem Soc* **2018,** *140* (46), 15712-15723.
120. Kim, Y.; Lee, S., Investigating the role of zinc precursor during the synthesis of the core of III–V QDs. *Chem. Commun.* **2022,** *58* (6), 875-878.
121. Janke, E. M.; Williams, N. E.; She, C.; Zherebetskyy, D.; Hudson, M. H.; Wang, L.; Gosztola, D. J.; Schaller, R. D.; Lee, B.; Sun, C.; Engel, G. S.; Talapin, D. V., Origin of Broad Emission Spectra in InP Quantum Dots: Contributions from Structural and Electronic Disorder. *J Am Chem Soc* **2018,** *140* (46), 15791-15803.
122. Shen, Z. L.; Wang, S. Y.; Chok, Y. K.; Xu, Y. H.; Loh, T. P., Organoindium reagents: the preparation and application in organic synthesis. *Chem Rev* **2013,** *113* (1), 271-401.
123. Ginterseder, M.; Franke, D.; Perkinson, C. F.; Wang, L.; Hansen, E. C.; Bawendi, M. G., Scalable Synthesis of InAs Quantum Dots Mediated through Indium Redox Chemistry. *J Am Chem Soc* **2020,** *142* (9), 4088-4092.

124. Ubbink, R. F.; Almeida, G.; Iziyi, H.; du Fossé, I.; Verkleij, R.; Ganapathy, S.; van Eck, E. R. H.; Houtepen, A. J., A Water-Free In Situ HF Treatment for Ultrabright InP Quantum Dots. *Chem. Mater.* **2022**, DOI: 10.1021/acs.chemmater.2c02800.
125. Huang, K.; Demadrille, R.; Silly, M. G.; Sirotti, F.; Reiss, P.; Renault, O., Internal structure of InP/ZnS nanocrystals unraveled by high-resolution soft X-ray photoelectron spectroscopy. *ACS Nano* **2010,** *4* (8), 4799-805.
126. McMurtry, B. M.; Qian, K.; Teglasi, J. K.; Swarnakar, A. K.; De Roo, J.; Owen, J. S., Continuous Nucleation and Size Dependent Growth Kinetics of Indium Phosphide Nanocrystals. *Chemistry of Materials* **2020,** *32* (10), 4358-4368.
127. Mundy, M. E.; Ung, D.; Lai, N. L.; Jahrman, E. P.; Seidler, G. T.; Cossairt, B. M., Aminophosphines as Versatile Precursors for the Synthesis of Metal Phosphide Nanocrystals. *Chemistry of Materials* **2018,** *30* (15), 5373-5379.
128. Kim, Y.; Choi, H.; Lee, Y.; Koh, W. K.; Cho, E.; Kim, T.; Kim, H.; Kim, Y. H.; Jeong, H. Y.; Jeong, S., Tailored growth of single-crystalline InP tetrapods. *Nat Commun* **2021,** *12* (1), 4454.
129. Kim, K.; Yoo, D.; Choi, H.; Tamang, S.; Ko, J. H.; Kim, S.; Kim, Y. H.; Jeong, S., Halide-Amine Co-Passivated Indium Phosphide Colloidal Quantum Dots in Tetrahedral Shape. *Angew Chem Int Ed Engl* **2016,** *55* (11), 3714-8.
130. Goggin, P. L.; McColm, I. J., Lower valent indium compounds. *Journal of Inorganic and Nuclear Chemistry* **1966,** *28* (11), 2501-2505.
131. Rachkov, A. G.; Schimpf, A. M., Colloidal Synthesis of Tunable Copper Phosphide Nanocrystals. *Chem. Mater.* **2021,** *33* (4), 1394-1406.
132. LaMer, V. K.; Dinegar, R. H., Theory, Production, and Mechanism of Formation of Monodispersed Hydrosols. *J. Am. Chem. Soc.* **1950,** *72*, 4847.
133. Adam, S.; Talapin, D. V.; Borchert, H.; Lobo, A.; McGinley, C.; de Castro, A. R. B.; Haase, M.; Weller, H.; Möller, T., The effect of nanocrystal surface structure on the luminescence properties: Photoemission study of HF-etched InP nanocrystals. *J. Chem. Phys.* **2005,** *123* (8), 084706.
134. Van Avermaet, H.; Schiettecatte, P.; Hinz, S.; Giordano, L.; Ferrari, F.; Nayral, C.; Delpech, F.; Maultzsch, J.; Lange, H.; Hens, Z., Full-Spectrum InP-Based Quantum Dots with Near-Unity Photoluminescence Quantum Efficiency. *ACS Nano* **2022,** *16* (6), 9701-9712.
135. Talapin, D. V.; Gaponik, N.; Borchert, H.; Rogach, A. L.; Haase, M.; Weller, H., Etching of colloidal InP nanocrystals with fluorides: Photochemical nature of the process resulting in high photoluminescence efficiency. *J. Phys. Chem. B* **2002,** *106* (49), 12659-12663.
136. Micic, O. I.; Sprague, J.; Lu, Z.; Nozik, A. J., Highly efficient band-edge emission from InP quantum dots. *Appl. Phys. Lett.* **1996,** *68* (22), 3150-3152.

137. Cros-Gagneux, A.; Delpech, F.; Nayral, C.; Cornejo, A.; Coppel, Y.; Chaudret, B., Surface Chemistry of InP Quantum Dots: A Comprehensive Study. *Journal of the American Chemical Society* **2010,** *132* (51), 18147-18157.
138. Virieux, H.; Le Troedec, M.; Cros-Gagneux, A.; Ojo, W.-S.; Delpech, F.; Nayral, C.; Martinez, H.; Chaudret, B., InP/ZnS Nanocrystals: Coupling NMR and XPS for Fine Surface and Interface Description. *Journal of the American Chemical Society* **2012,** *134* (48), 19701-19708.
139. Chen, D.; Zhao, F.; Qi, H.; Rutherford, M.; Peng, X., Bright and Stable Purple/Blue Emitting CdS/ZnS Core/Shell Nanocrystals Grown by Thermal Cycling Using a Single-Source Precursor. *Chemistry of Materials* **2010,** *22* (4), 1437-1444.
140. Protiere, M.; Reiss, P., Facile synthesis of monodisperse ZnS capped CdS nanocrystals exhibiting efficient blue emission. *Nanoscale Res. Lett.* **2006,** *1* (1), 62-67.
141. Ithurria, S.; Guyot-Sionnest, P.; Mahler, B.; Dubertret, B., ${\mathrm{Mn}}^{2+}$ as a Radial Pressure Gauge in Colloidal Core/Shell Nanocrystals. *Phys. Rev. Lett.* **2007,** *99* (26), 265501.
142. Ung, T. D. T.; Pham, T. T.; Nguyen, Q. L.; Li, L.; Reiss, P., Comparative photoluminescence study of close-packed and colloidal InP/ZnS quantum dots. *Appl. Phys. Lett.* **2010,** *96* (7), 073102.
143. Kirkwood, N.; Monchen, J. O. V.; Crisp, R. W.; Grimaldi, G.; Bergstein, H. A. C.; du Fossé, I.; van der Stam, W.; Infante, I.; Houtepen, A. J., Finding and Fixing Traps in II–VI and III–V Colloidal Quantum Dots: The Importance of Z-Type Ligand Passivation. *Journal of the American Chemical Society* **2018,** *140* (46), 15712-15723.
144. Peng, X.; Manna, L.; Yang, W.; Wickham, J.; Scher, E.; Kadavanich, A.; Alivisatos, A. P., Shape control of CdSe nanocrystals. *Nature* **2000,** *404* (6773), 59-61.
145. Hikmet, R. A. M.; Chin, P. T. K.; Talapin, D. V.; Weller, H., Polarized-Light-Emitting Quantum-Rod Diodes. *Adv Mater* **2005,** *17* (11), 1436-1439.
146. Hu, J.; Li, L.; Yang, W.; Manna, L.; Wang, L.; Alivisatos, A. P., Linearly polarized emission from colloidal semiconductor quantum rods. *Science* **2001,** *292* (5524), 2060-3.
147. Kwon, Y.; Bang, G.; Kim, J.; Agnes, A.; Kim, S., Synthesis of InP branched nanostructures by controlling the intermediate nanoclusters. *Journal of Materials Chemistry C* **2020,** *8* (3), 1118-1124.
148. Park, H.; Chung, H.; Kim, W., Synthesis of ultrathin wurtzite ZnSe nanosheets. *Materials Letters* **2013,** *99*, 172-175.
149. Scott, R.; Achtstein, A. W.; Prudnikau, A.; Antanovich, A.; Christodoulou, S.; Moreels, I.; Artemyev, M.; Woggon, U., Two Photon Absorption in II-VI Semiconductors: The Influence of Dimensionality and Size. *Nano Lett* **2015,** *15* (8), 4985-92.
150. De Trizio, L.; Gaspari, R.; Bertoni, G.; Kriegel, I.; Moretti, L.; Scotognella, F.; Maserati, L.; Zhang, Y.; Messina, G. C.; Prato, M.; Marras, S.; Cavalli, A.; Manna, L., Cu(3-x) P

Nanocrystals as a Material Platform for Near-Infrared Plasmonics and Cation Exchange Reactions. *Chem Mater* **2015,** *27* (3), 1120-1128.

151. Carbone, L.; Nobile, C.; De Giorgi, M.; Sala, F. D.; Morello, G.; Pompa, P.; Hytch, M.; Snoeck, E.; Fiore, A.; Franchini, I. R.; Nadasan, M.; Silvestre, A. F.; Chiodo, L.; Kudera, S.; Cingolani, R.; Krahne, R.; Manna, L., Synthesis and micrometer-scale assembly of colloidal CdSe/CdS nanorods prepared by a seeded growth approach. *Nano Lett* **2007,** *7* (10), 2942-50.
152. Rosen, E. L.; Buonsanti, R.; Llordes, A.; Sawvel, A. M.; Milliron, D. J.; Helms, B. A., Exceptionally mild reactive stripping of native ligands from nanocrystal surfaces by using Meerwein's salt. *Angew Chem Int Ed Engl* **2012,** *51* (3), 684-9.
153. Dong, A.; Ye, X.; Chen, J.; Kang, Y.; Gordon, T.; Kikkawa, J. M.; Murray, C. B., A generalized ligand-exchange strategy enabling sequential surface functionalization of colloidal nanocrystals. *J Am Chem Soc* **2011,** *133* (4), 998-1006.
154. Zhou, Y.; Buhro, W. E., Reversible Exchange of L-Type and Bound-Ion-Pair X-Type Ligation on Cadmium Selenide Quantum Belts. *J Am Chem Soc* **2017,** *139* (37), 12887-12890.
155. Anderson, N. C.; Hendricks, M. P.; Choi, J. J.; Owen, J. S., Ligand exchange and the stoichiometry of metal chalcogenide nanocrystals: spectroscopic observation of facile metal-carboxylate displacement and binding. *J Am Chem Soc* **2013,** *135* (49), 18536-48.
156. Mahler, B.; Nadal, B.; Bouet, C.; Patriarche, G.; Dubertret, B., Core/shell colloidal semiconductor nanoplatelets. *J Am Chem Soc* **2012,** *134* (45), 18591-8.
157. Cunningham, P. D.; Coropceanu, I.; Mulloy, K.; Cho, W.; Talapin, D. V., Quantized Reaction Pathways for Solution Synthesis of Colloidal ZnSe Nanostructures: A Connection between Clusters, Nanowires, and Two-Dimensional Nanoplatelets. *ACS Nano* **2020,** *14* (4), 3847-3857.
158. Ho, C. H.; Chen, H. H., Optically decomposed near-band-edge structure and excitonic transitions in Ga(2)S(3). *Sci Rep* **2014,** *4*, 6143.
159. Aydinli, A.; Gasanly, N. M.; Gökşen, K., Donor–acceptor pair recombination in gallium sulfide. *Journal of Applied Physics* **2000,** *88* (12), 7144-7149.
160. Aono, T.; Kase, K., Green photoemission of a-Ga2S3 crystals. *Solid State Communications* **1992,** *81* (4), 303-305.
161. Yoon, C.-S.; Medina, F. D.; Martinez, L.; Park, T.-Y.; Jin, M.-S.; Kim, W.-T., Blue photoluminescence of α-Ga2S3 and α-Ga2S3:Fe2+ single crystals. *Applied Physics Letters* **2003,** *83* (10), 1947-1949.
162. Hu, Z. M.; Fei, G. T.; Zhang, L. D., Synthesis and tunable emission of Ga2S3 quantum dots. *Materials Letters* **2019,** *239*, 17-20.
163. Uematsu, T.; Wajima, K.; Sharma, D. K.; Hirata, S.; Yamamoto, T.; Kameyama, T.; Vacha, M.; Torimoto, T.; Kuwabata, S., Narrow band-edge photoluminescence from AgInS2 semiconductor nanoparticles by the formation of amorphous III–VI semiconductor shells. *NPG Asia Materials* **2018,** *10* (8), 713-726.

164. Moodelly, D.; Kowalik, P.; Bujak, P.; Pron, A.; Reiss, P., Synthesis, photophysical properties and surface chemistry of chalcopyrite-type semiconductor nanocrystals. *Journal of Materials Chemistry C* **2019,** *7* (38), 11665-11709.
165. Ho, C.-H.; Lin, M.-H.; Wang, Y.-P.; Huang, Y.-S., Synthesis of In2S3 and Ga2S3 crystals for oxygen sensing and UV photodetection. *Sensors and Actuators A: Physical* **2016,** *245*, 119-126.
166. Jalali, H. B.; Sadeghi, S.; Dogru Yuksel, I. B.; Onal, A.; Nizamoglu, S., Past, present and future of indium phosphide quantum dots. *Nano Research* **2022,** *15* (5), 4468-4489.
167. Malik, M. A.; Zulu, M. M.; O'Brien, P.; Wakefield, G., Single-source molecular precursors for the deposition of zinc selenide quantum dots. *Journal of Materials Chemistry* **1998,** *8* (8), 1885-1888.
168. Janke, E. M.; Williams, N. E.; She, C.; Zherebetskyy, D.; Hudson, M. H.; Wang, L.; Gosztola, D. J.; Schaller, R. D.; Lee, B.; Sun, C.; Engel, G. S.; Talapin, D. V., Origin of Broad Emission Spectra in InP Quantum Dots: Contributions from Structural and Electronic Disorder. *Journal of the American Chemical Society* **2018,** *140* (46), 15791-15803.
169. Wegner, K. D.; Dussert, F.; Truffier-Boutry, D.; Benayad, A.; Beal, D.; Mattera, L.; Ling, W. L.; Carrière, M.; Reiss, P., Influence of the Core/Shell Structure of Indium Phosphide Based Quantum Dots on Their Photostability and Cytotoxicity. *Frontiers in Chemistry* **2019,** *7*, 466.

Abbreviations

1. AU : Absorbance unit
2. CSQD : Core-shell quantum dots
3. EDX: Energy dispersive X-ray spectroscopy
4. FTIR: Fourier transform infrared (spectroscopy)
5. FWHM: Full width at half maximum
6. HRTEM : High-resolution transmission electron microscopy
7. HA: Hexadecylamine
8. Ga_2S_3: Gallium sulphide
9. InP: Indium phosphide
10. MA: Myristic acid
11. NPLs: Nanoparticles
12. NCs: Nanocrystals
13. NMR: Nuclear magnetic resonance
14. NIR: Near-infrared
15. ODE: Octadecene
16. OCA: Octylamine
17. OA: Oleic acid
18. OLA: Oleylamine
19. PL: Photoluminescence
20. PLQY: Photoluminescence quantum yield
21. $P(TMS)_3$: Tris(trimethylsilyl)phosphine
22. $P(DEA)_3$: Tris(diethylaminophosphine)
23. $P(OLA)_3$: Tris(oleylamino)phosphine
24. $P(OCA)_3$: Tris(octylamino)phosphine
25. $P(Pyrr)_3$: Tris(pyrrolidinyl)phosphine
26. Pyrr: Pyrollidine
27. QDs: Quantum dots
28. RPM: Rotation per minute
29. RT: Room temperature
30. TEM: Transmission electron microscopy
31. TOP: Trioctylphosphine
32. TOA: Trioctylamine
33. UV: Ultra-violet
34. UV-Vis: Ultra-violet-visible

35. XRD: X-ray diffraction
36. XPS : X-ray photoelectron spectroscopy
37. ZnSe: Zinc selenide
38. ZnS: Zinc sulfide
39. $Zn(DDTC)_2$: Zinc diethyldithiocarbamate

Title: Continuous flow synthesis of semiconductor nanocrystals

Colloidal semiconductor quantum dots (QDs) exhibit unique photophysical properties such as narrow and size-tunable fluorescence emission, broadband absorption, and high photostability. They are used in diverse applications such as biological imaging and detection or as color converters in displays and TVs. Indium phosphide (InP) QDs are in compliance with EU regulations and have been identified as the most promising candidate for substituting toxic CdSe-based QDs. In this thesis, we developed the continuous flow synthesis of high-quality indium phosphide-based QDs. Continuous flow synthesis has many advantages compared to conventional batch synthesis due to the better mass and heat transfers in tubular reactors and the higher reproducibility related to the automated system. A novel continuous flow synthesis route was developed to prepare InP QDs using In-trioctylphosphine complexes as the In precursor and tris(oleylamino)phosphine as the P precursor in a non-coordinating solvent (octadecene). In parallel, a novel synthetic approach relying on the use of indium (I) halides was developed, which act as both the indium source and reducing agent for aminophosphine. This reaction pathway gave access to unprecedented large-sized InP QDs showing a narrow size distribution and a large tunability of the excitonic peak position from 450 nm to 700 nm. Kinetic studies using ^{31}P NMR revealed the contribution of two different reduction pathways of transaminated aminophosphine. To improve the photoluminescence quantum yield (PLQY) two methods were followed. i) The surface of the InP QDs was etched at room temperature using *in-situ* generated HF leading up to 79% PLQY. ii) InP/ZnS core/shell QDs were developed by overgrowth of the InP core with zinc diethyldithiocarbamate. This method is compatible with flow synthesis and was used to prepare highly luminescent InP/ZnS QDs on the gram-scale in a fully automated way. To further reduce the emission linewidth of the InP QDs, the synthesis of ZnSe/InP core/shell nanoplatelets (NPLs) was explored. Native ligand stripping and surface ligand exchange procedures were performed for the surface activation of the ZnSe NPLs acting as a template for the InP growth. Finally, the use of an amorphous GaS_x shell was investigated to improve the emission properties of InP QDs, which led to the discovery of strongly blue-emitting Ga_2S_3 nanocrystals.

Titre : Synthèse en flux continu de nanocristaux de semi-conducteurs

Les nanocristaux semi-conducteurs colloïdaux (quantum dots, QDs) présentent des propriétés photophysiques uniques telles qu'une fluorescence étroite et ajustable avec la taille, une absorption large bande et une photostabilité élevée. Ils sont utilisés dans diverses applications telles que l'imagerie et la détection biologiques ou comme convertisseurs de couleurs dans les écrans et les téléviseurs. Les QDs de phosphure d'indium (InP) ont été identifiés comme le candidat le plus prometteur pour remplacer les QDs toxiques à base de cadmium. Dans cette thèse, nous avons développé la synthèse en flux continu de QDs à base de phosphure d'indium. La synthèse en flux continu présente de nombreux avantages par rapport à la synthèse conventionnelle par batch en raison des meilleurs transferts de masse et de chaleur dans les réacteurs tubulaires et de la meilleure reproductibilité liée au système automatisé. Une nouvelle voie de synthèse en flux continu a été développée pour préparer des QDs d'InP en utilisant des complexes In-trioctylphosphine comme précurseur d'In et de la tris(oleylamino)phosphine comme précurseur de P dans un solvant non-coordonnant (octadécène). En parallèle, une nouvelle approche synthétique reposant sur l'utilisation d'halogénures d'indium (I) a été développée, qui agissent à la fois comme source d'indium et comme agent réducteur pour l'aminophosphine. Cette voie de réaction a donné accès à des QDs d'InP de grande taille, présentant une distribution de taille étroite et la possibilité d'ajuster la position du pic excitonique de 450 nm à 700 nm. Des études cinétiques utilisant la RMN du phosphore ont révélé la contribution de deux voies de réduction différentes de l'aminophosphine transaminée. Pour améliorer le rendement quantique de photoluminescence (RQ), deux méthodes ont été suivies. i) La surface des QDs d'InP a été attaquée chimiquement à température ambiante en utilisant du HF généré in-situ, ce qui a permis d'obtenir un RQ de 79%. ii) Des QDs cœur/coquille InP/ZnS ont été développés par croissance du ZnS sur les QDs coeur d'InP en utilisant du diéthyldithiocarbamate de zinc. Cette méthode est compatible avec la synthèse en flux continu et a été utilisée pour préparer des QDs InP/ZnS fortement luminescents à l'échelle du gramme de manière entièrement automatisée. Pour réduire davantage la largeur de raie d'émission des QDs d'InP, la synthèse de nanoplaquettes cœur/coquille ZnSe/InP a été explorée. La surface des nanoplaquettes de ZnSe servant de support pour la croissance de l'InP a été activée par différentes méthodes. Enfin, l'utilisation d'une coquille amorphe en GaS_x a été étudiée pour améliorer les propriétés d'émission des QDs d'InP, ce qui a conduit à la découverte de nanocristaux de Ga_2S_3 présentant une forte émission bleue.